

AFRL-SN-HS-TR-2005-016, Vol I

PROCEEDINGS OF THE 2004 ANTENNA APPLICATIONS SYMPOSIUM

**Volume I of II
Pages 1-244**

Daniel Schaubert et al.

Final Report: September 2004

APPROVED FOR PUBLIC RELEASE



**AIR FORCE RESEARCH LABORATORY
Sensors Directorate
Electromagnetics Technology Division
80 Scott Drive
Hanscom AFB MA 01731-2909**

DTIC ONLY

20050408 049

TECHNICAL REPORT

Proceedings of the 2004 Antenna Applications Symposium, Vol I

Unlimited, Statement A

NOTICE

USING GOVERNMENT DRAWINGS, SPECIFICATIONS, OR OTHER DATA INCLUDED IN THIS DOCUMENT FOR ANY PURPOSE OTHER THAN GOVERNMENT PROCUREMENT DOES NOT IN ANY WAY OBLIGATE THE US GOVERNMENT. THE FACT THAT THE GOVERNMENT FORMULATED OR SUPPLIED THE DRAWINGS, SPECIFICATIONS, OR OTHER DATA DOES NOT LICENSE THE HOLDER OR ANY OTHER PERSON OR CORPORATION; OR CONVEY ANY RIGHTS OR PERMISSION TO MANUFACTURE, USE, OR SELL ANY PATENTED INVENTION THAT MAY RELATE TO THEM.

THIS TECHNICAL REPORT HAS BEEN REVIEWED AND IS APPROVED FOR PUBLICATION.

//signature//

Livio D. Poles
Chief, Antenna Technology Branch

//signature//

Michael N. Alexander
Technical Advisor
Electromagnetics Technology Division

REPORT DOCUMENTATION PAGE					Form Approved OMB No. 0704-0188	
<small>The public reporting burden for this collection of information is estimated to average 1 hour per response, including the time for reviewing instructions, searching existing data sources, gathering and maintaining the data needed, and completing and reviewing the collection of information. Send comments regarding this burden estimate or any other aspect of this collection of information, including suggestions for reducing the burden, to Department of Defense, Washington Headquarters Services, Directorate for Information Operations and Reports (0704-0188), 1215 Jefferson Davis Highway, Suite 1204, Arlington, VA 22202-4302. Respondents should be aware that notwithstanding any other provision of law, no person shall be subject to any penalty for failing to comply with a collection of information if it does not display a currently valid OMB control number.</small> PLEASE DO NOT RETURN YOUR FORM TO THE ABOVE ADDRESS.						
1. REPORT DATE (DD-MM-YYYY) 30 November 2004		2. REPORT TYPE Final			3. DATES COVERED (From - To) 15-17 Sept 2004	
4. TITLE AND SUBTITLE Proceedings of the 2004 Antenna Applications Symposium Vol I				5a. CONTRACT NUMBER ATESRD F33615-02-D-1283		
				5b. GRANT NUMBER		
				5c. PROGRAM ELEMENT NUMBER		
6. AUTHOR(S) Daniel Schaubert et, al				5d. PROJECT NUMBER		
				5e. TASK NUMBER		
				5f. WORK UNIT NUMBER		
7. PERFORMING ORGANIZATION NAME(S) AND ADDRESS(ES) University of Massachusetts 149 Aubinwood Road Amherst, MA 01002					8. PERFORMING ORGANIZATION REPORT NUMBER	
9. SPONSORING/MONITORING AGENCY NAME(S) AND ADDRESS(ES) Air Force Research Laboratory 80 Scott Rd Electromagnetics Technology Division Sensors Directorate Hanssom AFB, MA 01731					10. SPONSOR/MONITOR'S ACRONYM(S) AFRL-SN-HS-TR-2005-016	
					11. SPONSOR/MONITOR'S REPORT NUMBER(S)	
12. DISTRIBUTION/AVAILABILITY STATEMENT APPROVED FOR PUBLIC RELEASE; DISTRIBUTION UNLIMITED. ESC 05-0109, 21 JAN 2005						
13. SUPPLEMENTARY NOTES Volume I contains Pages 1-244, Volume II 245-473						
14. ABSTRACT The Proceedings of the 2004 Antenna Applications Symposium is a collection of state-of-the art papers relating to antenna arrays, millimeter wave antennas, simulation and measurment of antennas, integrated antennas, and antenna bandwidth and radiation improvements.						
15. SUBJECT TERMS Antennas, phased arrays, digital beamforming, millimeter waves, antenna measurements						
16. SECURITY CLASSIFICATION OF:			17. LIMITATION OF ABSTRACT UL	18. NUMBER OF PAGES 244	19a. NAME OF RESPONSIBLE PERSON Livio Poles	
a. REPORT UL	b. ABSTRACT UL	c. THIS PAGE UL			19b. TELEPHONE NUMBER (Include area code) 781-377-4087	

2004 ANTENNA APPLICATIONS SYMPOSIUM
(Volume I)

15 – 17 September 2004
Monticello, Illinois

Applications of the Coaxial Cavity Antenna in Time and Frequency Tim Holzheimer	1
Small Ultra Wideband Planar Antenna V.I. Litvinov, R. Webb, M. Felman, M. Aretskin and L.S. Sadovnik	20
Wireless Embedded Rust Monitoring Systems K. Hietpas, B. Ervin, D.A. Kuchma, H. Reis and J.T. Bernhard	27
Parameter Study of a Single Isolated and Infinite Arrays of Balanced Antipodal Vivaldi Antennas M.W. Elsallal and D.H. Schaubert	45
Log-Periodic Networks of Resonant Circuits: Models for Wideband, Electrically Small Antennas P.E. Mayes and P.W. Klock	70
Efficient Pattern and Impedance Bandwidth Analysis of Reactively Steered Arrays David Kelly and Samuel Reier	99
A Performance Comparison of Various Ultra Wideband Antennas Using the 3-Antenna Method Akihiko Maeda and Takehiko Kobayashi	117
2nd-Mode Four-Arm Slot Spiral Antennas Nathan Stutzke, Neill Kefauver and Dejan Filipovic	133
Coupled Sectorial Loop Antenna (CSLA) for Ultra-Wideband Applications Nader Behdad and Kamal Sarabandi	159

A Circularly Polarized Metamaterial and Dielectric Resonator Antenna with Enhanced Bandwidth Amelia Buerkle and Kamal Sarabandi	169
Analysis of a Radiation and Frequency Reconfigurable Microstrip Antenna G.H. Huff and J.T. Bernhard	175
32-Channel X-Band Digital Beamforming Receive Array Hardware William H. Weedon, David D.Curtis, Ryan W. Thomas, John Burroughs, Daniel Spendley and Joseph D. Rosal	192
Non-Foster Coupling and Matching in Arrays R.C. Hansen	203
Polarization Characterization of Wideband Array Elements Joel C. Roper and R.Thomas Dover	229

Identifiers for Proceedings of Symposia

The USAF Antenna Research and Development Program

Year	Symp. No.	Identifier
1951	First	
1952	Second	ADB870006
1953	Third	ADB283180
1954	Fourth	AD63139
1955	Fifth	AD90397
1956	Sixth	AD114702
1957	Seventh	AD138500
1958	Eighth	AD301151
1959	Ninth	AD314721
1960	Tenth	AD244388 (Vol. 1) AD319613 (Vol. 2)
1961	Eleventh	AD669109 (Vol. 1) AD326549 (Vol. 2)
1962	Twelfth	AD287185 (Vol. 1) AD334484 (Vol. 2)
1963	Thirteenth	AD421483
1964	Fourteenth	AD609104
1965	Fifteenth	AD474238L
1966	Sixteenth	AD800524L
1967	Seventeenth	AD822894L
1968	Eighteenth	AD846427L
1969	Nineteenth	AD860812L
1970	Twentieth	AD875973L
1971	Twenty-First	AD888641L
1972	Twenty-Second	AD904360L
1973	Twenty-Third	AD914238L

Antenna Applications Symposium

		TR#	ADA#
1977	First	None	955413
1978	Second	None	955416
1979	Third		077167
1980	Fourth		205907
1981	Fifth		205816
1982	Sixth		129356
1983	Seventh		142003; 142754
1984	Eighth	85-14	153257; 153258
1985	Ninth	85-242	166754; 165535
1986	Tenth	87-10	181537; 181536
1987	Eleventh	88-160	206705; 206704
1988	Twelfth	89-121	213815; 211396
1989	Thirteenth	90-42	226022; 226021
1990	Fourteenth	91-156	237056; 237057
1991	Fifteenth	92-42	253681; 253682
1992	Sixteenth	93-119	268167; 266916
1993	Seventeenth	94-20	277202; 277203
1994	Eighteenth	95-47	293258; 293259
1995	Nineteenth	96-100	309715; 309723
1996	Twentieth	97-189	341737
1997	Twenty First	1998-143	355120
1998	Twenty Second	1999-86	364798
1999	Twenty Third	2000-008 (I) (II)	386476; 386477
2000	Twenty Fourth	2002-001 Vol I & II	
2001	Twenty Fifth	2002-002 Vol I & II	
2002	Twenty Sixth	2005-001 Vol I & II	
2003	Twenty Seventh		

Applications of the Coaxial Cavity Antenna in Time and Frequency

Dr. Tim Holzheimer, P.E.
Raytheon
Tactical Systems
Garland, Texas 75042

Abstract:

A Coaxial Cavity antenna, developed and patented by Raytheon, exhibits low dispersion over wide field-of-view (FOV) and multiple octaves. This antenna is typically fabricated as a four point feed design. The antenna has now been developed for use in the low frequency bands, for example 100 to 500 MHz, which is the frequency application of this paper. Measured data is shown that illustrates the Coaxial Cavity antenna performance in the lower frequencies. This is shown for both a single Coaxial Cavity and for a dual Coaxial Cavity antenna. A second application uses a Coaxial Cavity antenna in the time domain, which is the time application of this paper. This antenna uses a single Coaxial Cavity for an instantaneous bandwidth of approximately 5 GHz. Performance is discussed as compared to the performance of a measured TEM Horn. The antenna design is still scaleable over multiple frequency ranges, and antennas have been built covering frequency ranges from 20 MHz to as high as 44 GHz, with bandwidths on the order of four and one-half octaves. Multiple polarizations can still be implemented.

1.0 Introduction:

The Coaxial Cavity antenna is one of numerous antennas that attain multi-octave bandwidth. Other examples include spirals, sinuous, TEM type structures and other variations such as Zig-Zags and Interlogs.[1-3] Extensive work with regard to wide band or wide bandwidth antennas operating over multiple octaves has been performed by numerous researchers such as Mayes, and others. The designs have accomplished multi-octave frequency coverage, typically in the 2 to 18 GHz or 6 to 18 GHz frequency bands. Unlike the Coaxial Cavity antenna these structures are generally traveling wave type structures.[4] However, they are complimentary just like the Coaxial Cavity antenna.

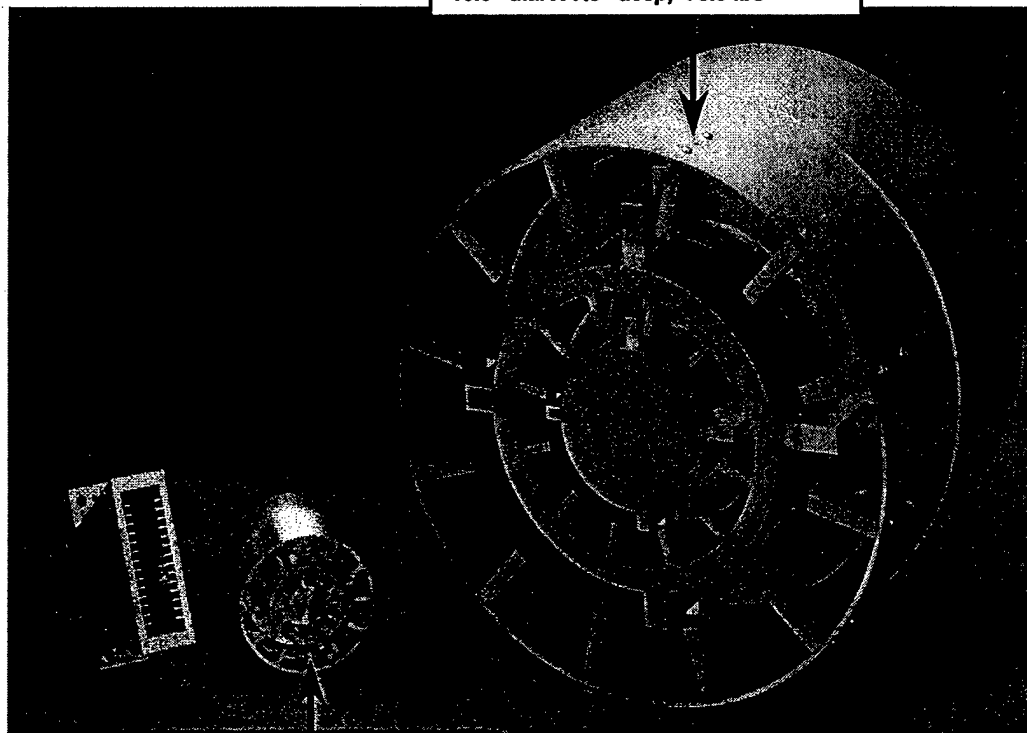
The Coaxial Cavity Antenna was initially presented at the Antenna Applications Symposium 2000.[5] This was the first time a published paper had been presented describing the Raytheon patented Coaxial Cavity Antenna, which is shown in figure 1. This antenna is fully scalable over any octave or multi-octave frequency range and has been demonstrated over the 400 MHz to 40 GHz frequency range. This antenna design is a balanced complimentary structure that has N discrete feed points, is light weight, and generally is unloaded, i.e. no dielectrics are introduced into the cavity structure.

Applications that have been previously discussed include the incorporation of these various coaxial cavity elements into systems such as interferometers, direction finding arrays, tracking systems and various types of phased array antennas.[6-9]

Low Frequency designs, typically below 500 MHz, have not been reported until now. It is desirable to have a coaxial cavity antenna that can operate all the way into the high frequency bands. This paper will show results for a design that works to at least 100 MHz and potentially lower, but not verified below 100 MHz due to existing antenna range limitations.

In the same context, an extremely broadband design was attempted that allowed the reception of a fast pulse in time. This requires that the antenna be low dispersion in order to minimize time distortion. The Coaxial Cavity antenna is a low dispersion device where the phase center remains stationary at the center of the face of the antenna. This is the reason that this antenna was designed initially for polarimetry.

0.5 to 2.0 GHz (0.5 - 1, 1 - 2)
Dual Polarized Coaxial Antenna
10.5" dia. X 7.5" deep, < 5.5 lbs



2.0 to 8.0 GHz (2 - 4, 4 - 8)
Dual Polarized Coaxial Antenna
2.75" dia. X 2.0" deep, < 0.5 lbs

Figure 1. Raytheon patented coaxial cavity antennas illustrating scaling.

2.0 Low Frequency Coaxial Cavity Antenna:

The Coaxial Cavity antenna is normally built in four-port configuration for most applications. The use of symmetric feed ports allows for the application of different phasing relationships that result in the formation of different radiation modes and control of polarization reception.

The lowest frequency that the Coaxial Cavity antenna has been used was 400 MHz. This has now changed with a scaled design that performs to 100 MHz at a minimum. The antenna that was built and tested is 12 inches in diameter and 8 inches in depth with a weight of approximately 15 pounds. The targeted frequency band of operation was 100 to 1 GHz for this antenna. It is noted that the Coaxial Cavity antenna is a scalable design where design have been developed and tested that cover 500 MHz to 40 GHz in a single aperture (This design is not discussed in this paper). With these designs the aperture phase center stays at the center of the antenna and on the face of the antenna. This allows the antenna to function in a polarimeter application outside the designed band of operation, but only on the lower frequency side.

The Single Coaxial Cavity antenna that was fabricated and tested is shown in figures 2-4. This is a single cavity antenna operating over a frequency band less than 1 GHz and is 12 inches in diameter.

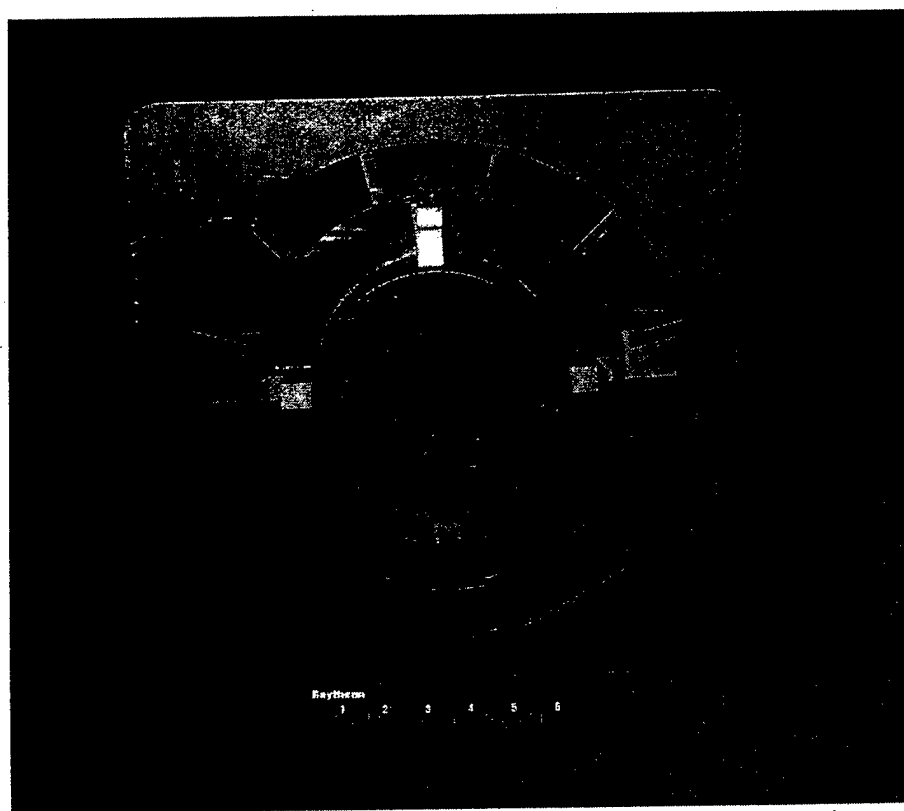


Figure 2. Fabricated low band coaxial cavity antenna, front view.



Figure 3. Fabricated low band coaxial cavity antenna, 45 degree view.

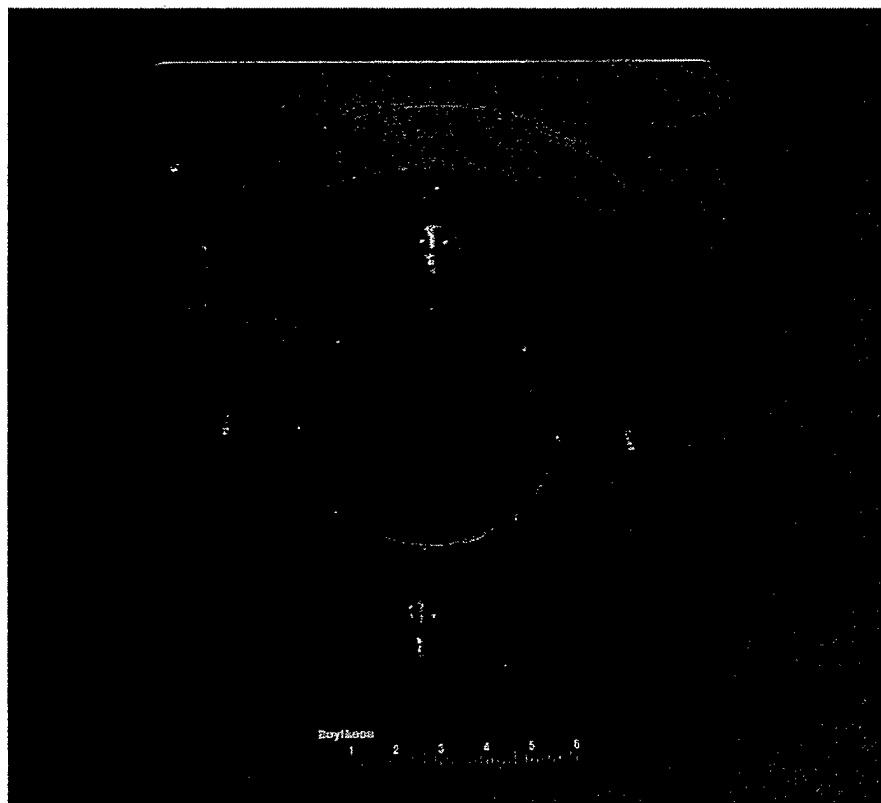


Figure 4. Fabricated low band coaxial cavity antenna, rear view.

The Low band Coaxial Cavity antenna was tested from 100 MHz to 2 GHz. The In-Band frequency range is approximately 550 MHz to 1.1 GHz. Radiation patterns are not shown above 1.1 GHz as the antenna becomes multimodal with bifurcation of the radiation pattern and major skewing of the beam peak. However, at the frequencies below the In-Band operational band, the radiation patterns are well behaved. The radiation patterns become wider and harder to differentiate the backlobe from the mainlobe due to the aperture size being too small. The aperture size for this effort was locked at 12 inches. Figures 5 through 8 are measured radiation patterns from 100 MHz to 1 GHz. These patterns illustrate the discussion on the radiation patterns.

The question that then becomes important is, what does the antenna gain look like? This is shown in figure 9. The gain is highest in the In-Band area, bounces around in the high side of the Out-of-Band area and rolls off in the low side Out-of-Band area. The gain is useable from approximately 1.1 to 1.2 GHz down to 100 MHz at a minimum. It is noted that the size of the aperture was locked at 12 inches and the measured data implies that the antenna could easily be used outside of the In-Band frequency range by approximately 3 octaves.

An additional investigation was made as to the feed size that should be used for maximum performance. Two Coaxial feed lines were investigated that are 0.141 inch and 0.25 inch diameter coax. The 0.25 inch coax used for feeds had better performance both on the low side and In-Band frequency band of operation, with opposite effects on the high side of the In-Band frequency of operation. This is illustrated in figure 9 by looking at the gain plots that verify the above findings.

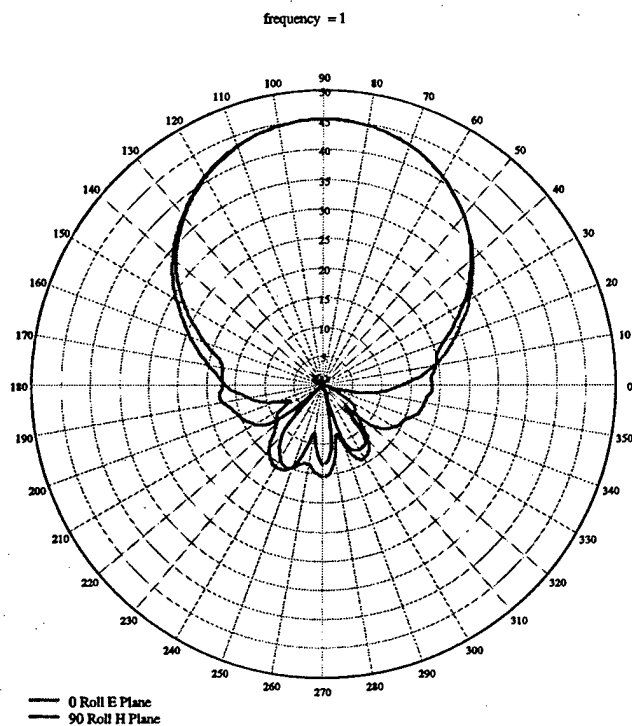


Figure 5. Fabricated low band coaxial cavity antenna principle plane radiation patterns at 1 GHz.

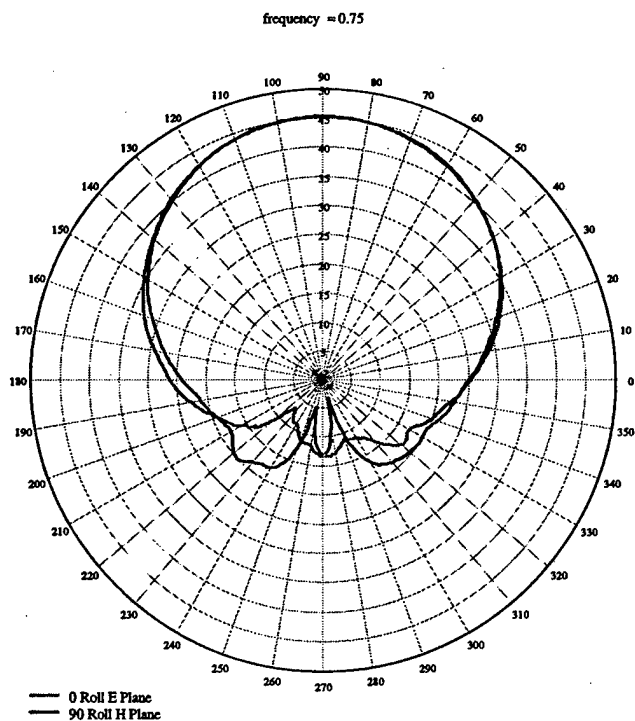


Figure 6. Fabricated low band coaxial cavity antenna principle plane radiation patterns at 750 MHz.

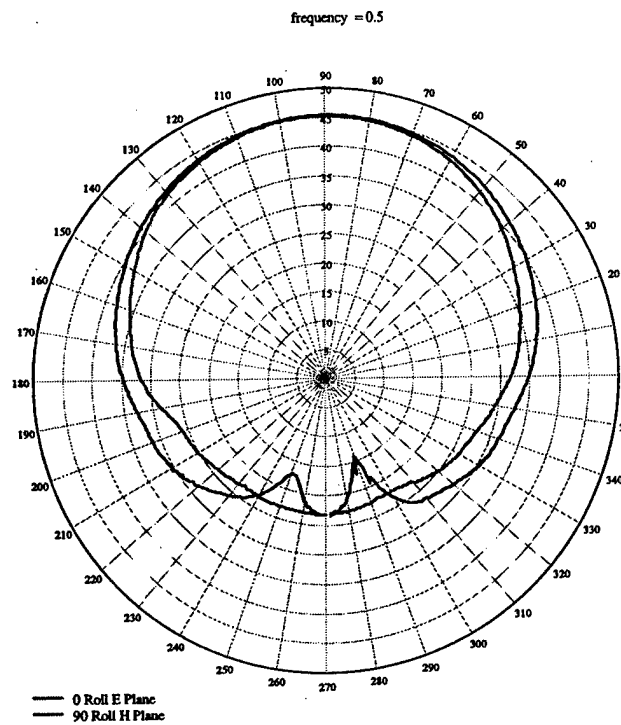


Figure 7. Fabricated low band coaxial cavity antenna principle plane radiation patterns at 500 MHz.

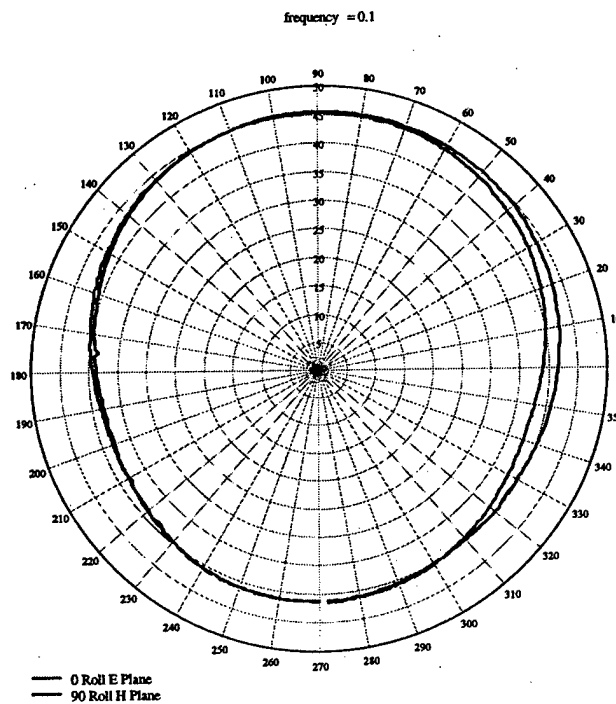


Figure 8. Fabricated low band coaxial cavity antenna principle plane radiation patterns at 100 MHz.

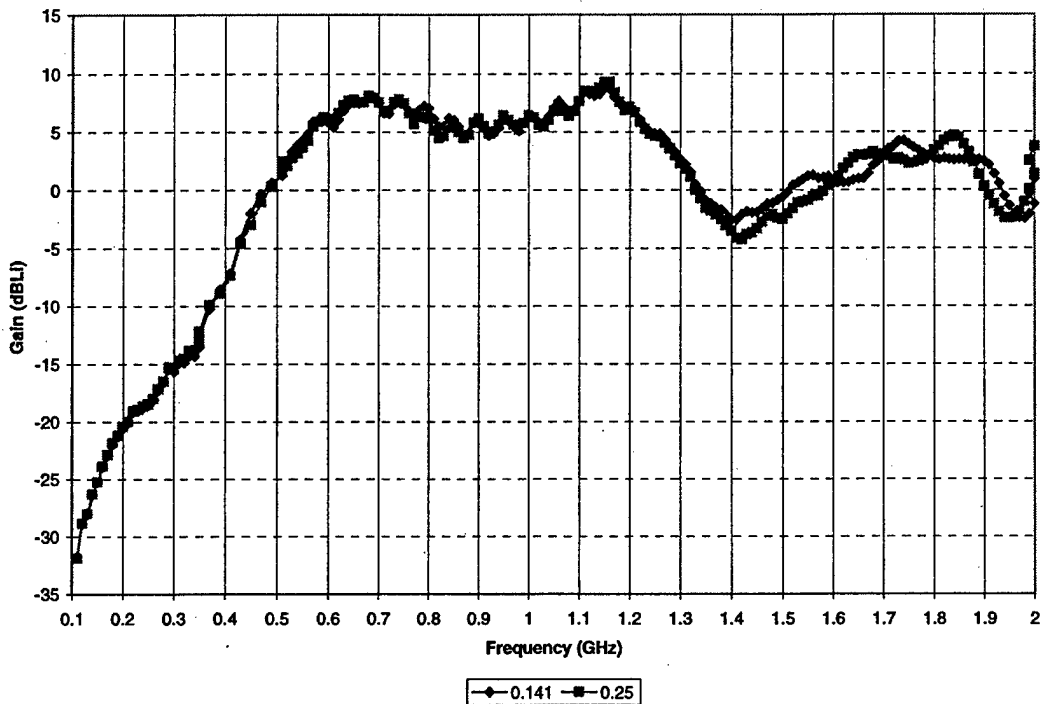


Figure 9. Fabricated low band coaxial cavity antenna gain 100 MHz. to 2 GHz.

A modification was made to the single Coaxial Cavity antenna by adding a second coaxial cavity in the center. The outer dimensions of the antenna did not change. The radiation patterns are as expected, that is equal in principle planes with no dips. The radiation patterns are presented in figures 10 through 12 and the additional cavity gain is shown in figure 13 for the additional band that covers approximately 1.2 to 2 GHz. The patterns do show effects from ground reflections on the low frequency outdoor antenna range that is seen in the cross-polarization results. Figures 14 and 15 show the measured beamsquint. Figure 14 is for the 100 MHz to 1 GHz band where the big dip is due to a ground reflection on the outdoor antenna range and thus is not real. Figure 15 is beamquint measured in the 1 to 2 GHz frequency band. The beam squint is negligible up to approximately 1.8 GHz, but it is only 3 degrees or less up to 2 GHz. Part of this was determined to be the result of a test fixture to antenna mount problem that was later corrected with the resulting beamsquint more closely following the measured data from 1 to 1.8 GHz.

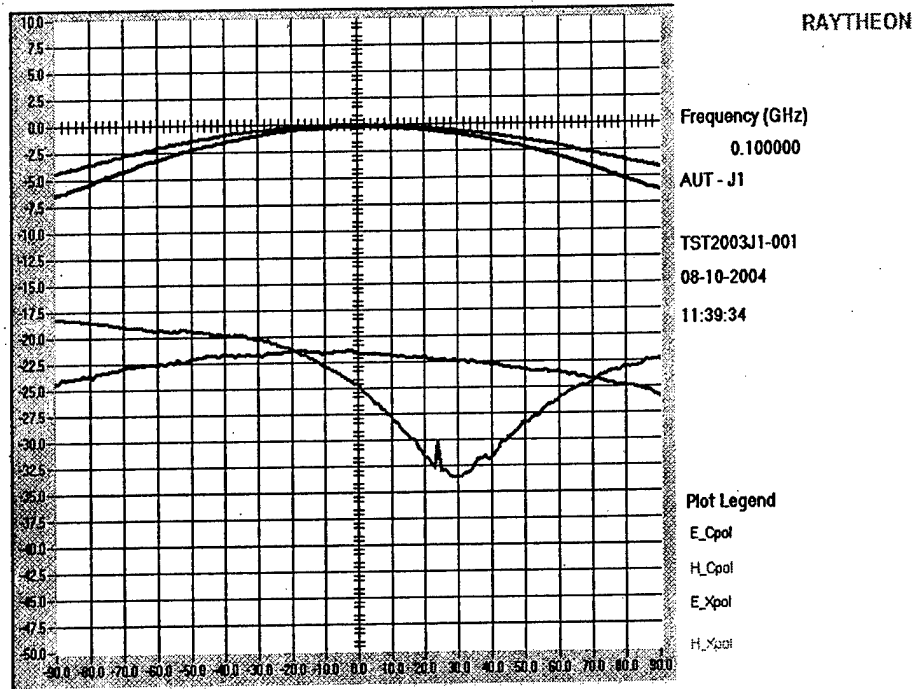


Figure 10. Measured radiation patterns low band coaxial cavity, two cavities, at 100 MHz.

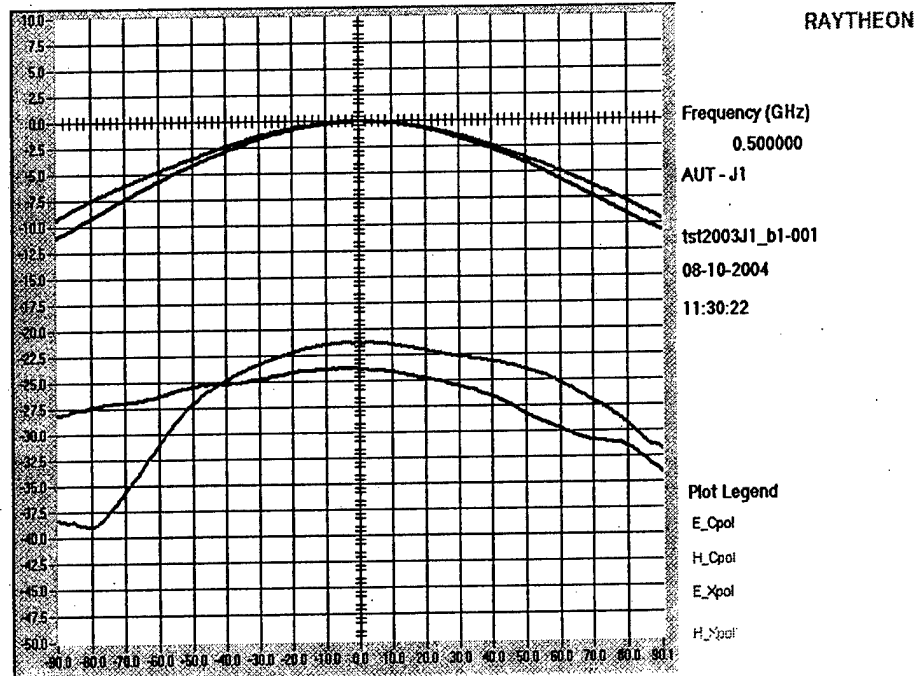


Figure 11. Measured radiation patterns low band coaxial cavity, two cavities, at 500 MHz.

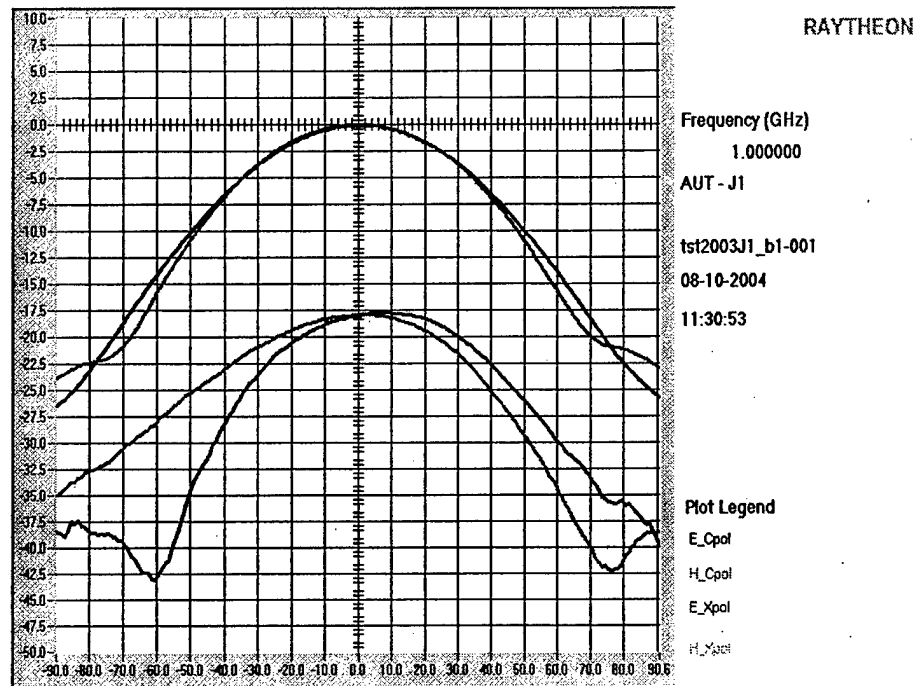


Figure 12. Measured radiation patterns low band coaxial cavity, two cavities, at 1 GHz.

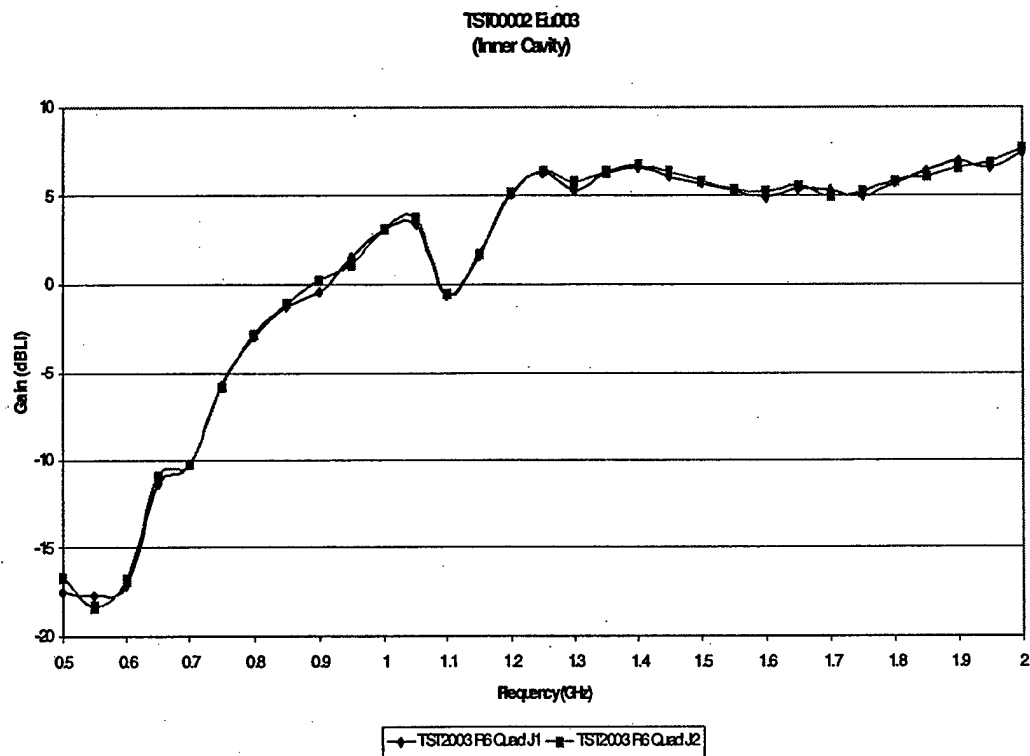


Figure 13. Fabricated low band coaxial cavity antenna gain for the additional center cavity in-band from 1.2. to 2 GHz.

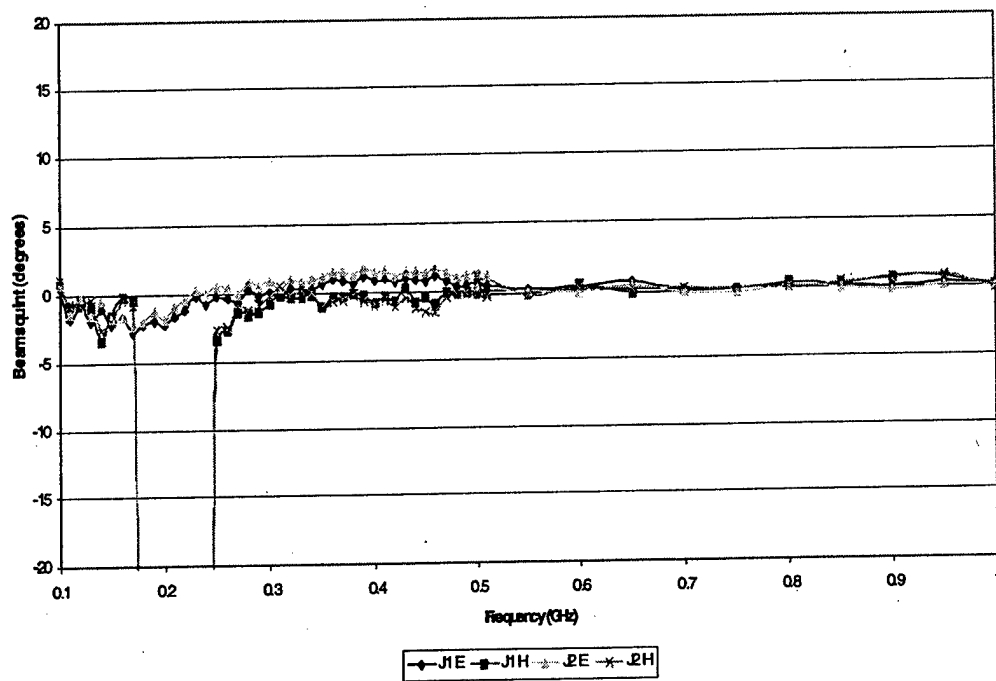


Figure 14. Fabricated low band coaxial cavity antenna beamsquint from 100 MHz to 1 GHz.

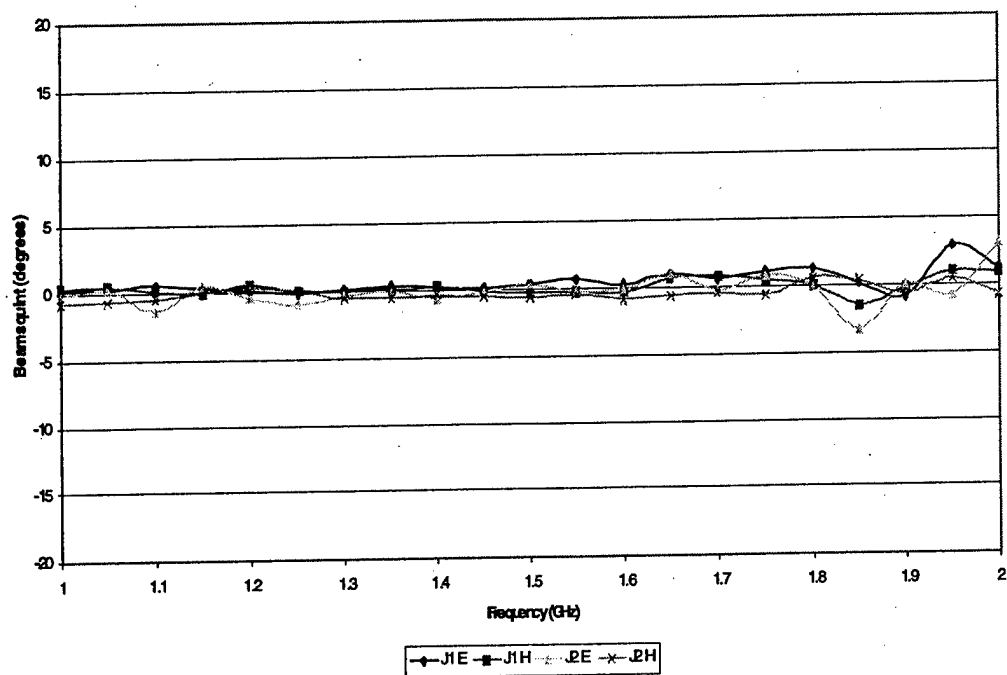


Figure 15. Fabricated low band coaxial cavity antenna beamsquint from 1 GHz to 2 GHz.

3.0 Low Dispersion, Wide Instantaneous Bandwidth, Coaxial Cavity Antenna:

A version of the Coaxial Cavity antenna was built for large instantaneous bandwidth for use in transient systems. The antenna is pictured in figure 16 and is only 2.75 inches in diameter and a maximum of 2 inches in total depth weighing approximately 8 ounces. This Raytheon Coaxial cavity antenna (patent pending) is used both In-band and out-of-band over the 100 MHz to approximately 5 GHz frequency range. The VSWR is acceptable down to 100 MHz where the maximum is 12:1. Figures 17 and 18 show measured VSWR data for this antenna both as a reference and where the antenna was not quite assembled correctly. Figure 17 is In-Band for this antenna which is 2 to 5 GHz. Figure 18 is Out-of-Band for this antenna which is 100 MHz to 2 GHz. Based on this data and the knowledge that this design is low dispersion it was then applied to a transient system. Figure 19 shows the measured impulse that is fed into the antenna with an approximately 70 picosecond risetime. Figure 20 shows the received doublet with a slight ringing after transmission through the transmit antenna and then received through a secondary antenna.

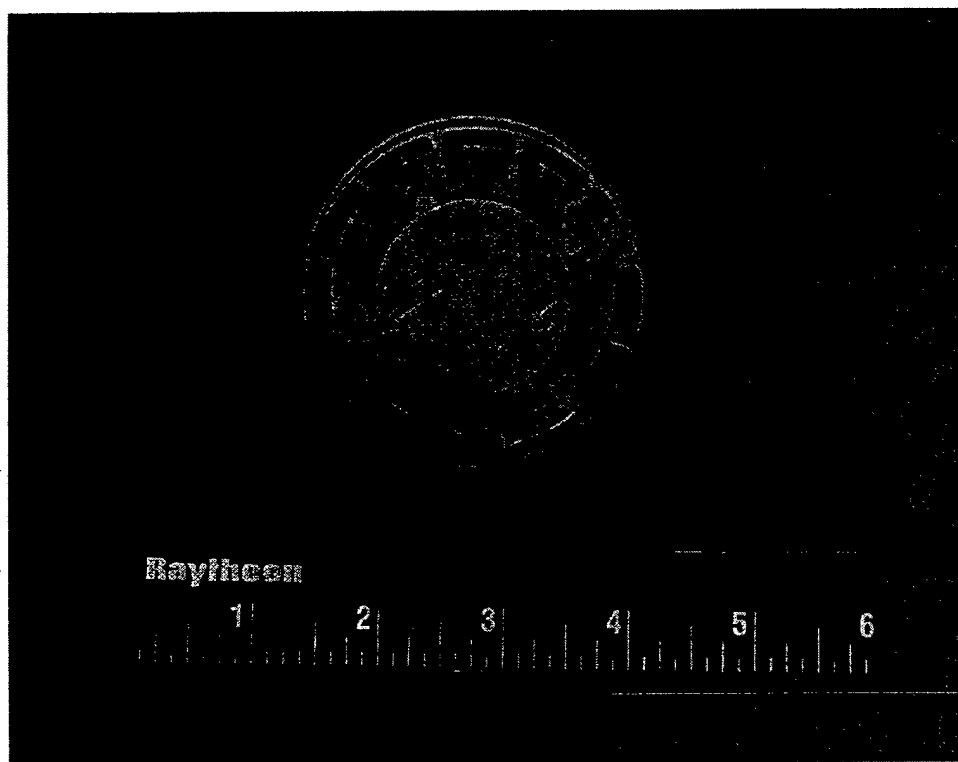


Figure 16. Fabricated impulsive coaxial cavity antenna with instantaneous bandwidth from 100 MHz to 5 GHz.

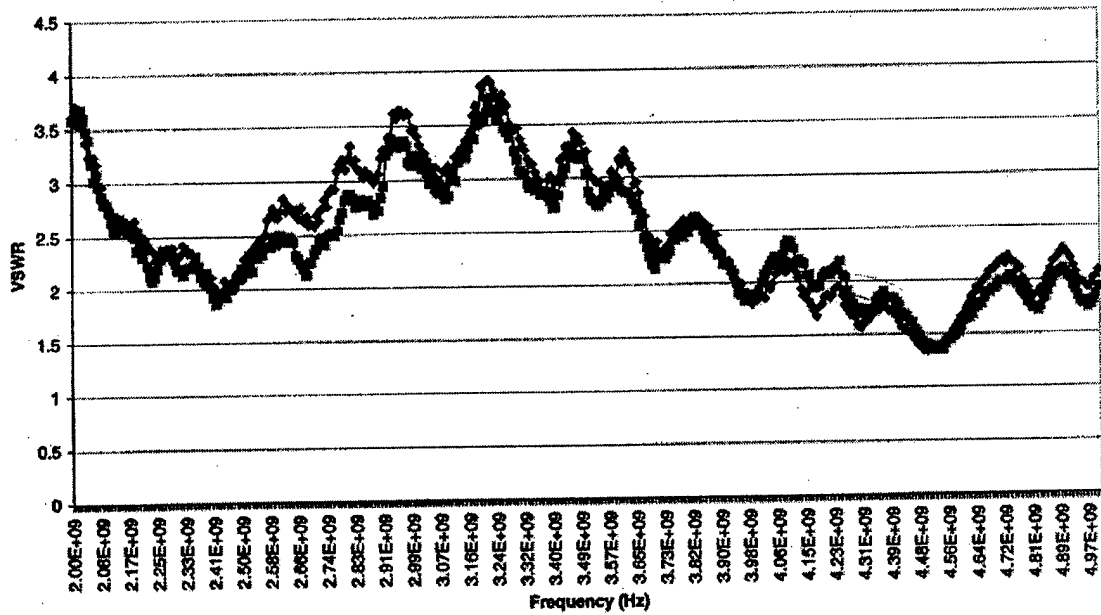


Figure 17. VSWR of fabricated impulsive coaxial cavity antenna from 2 GHz to 5 GHz.

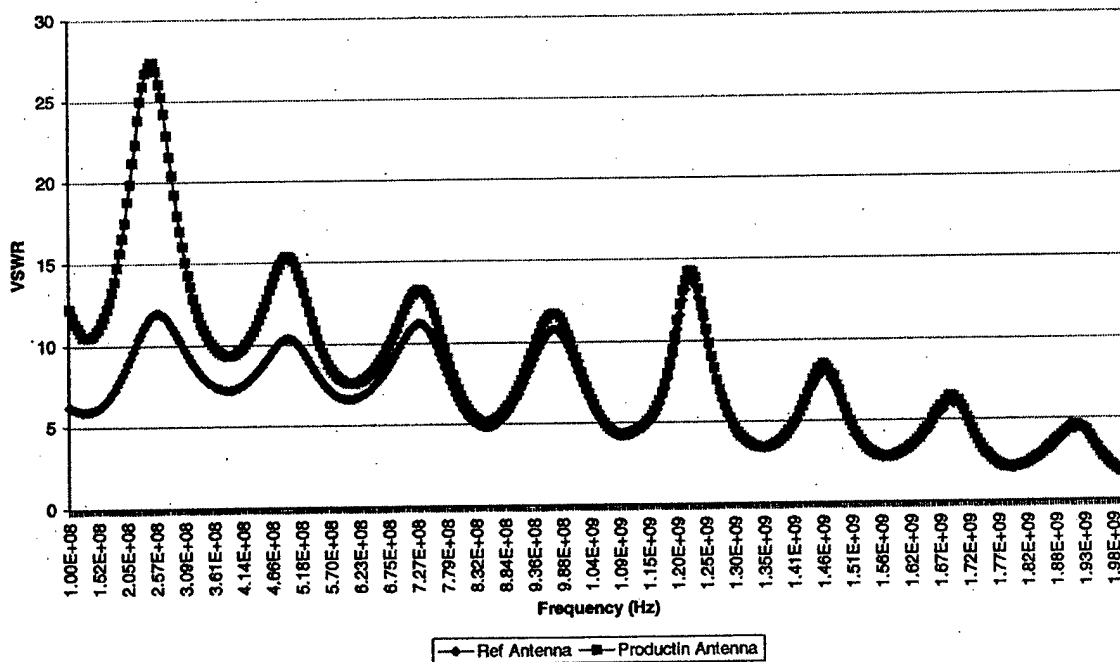


Figure 18. VSWR of fabricated impulsive coaxial cavity antenna from 100 MHz to 2 GHz.

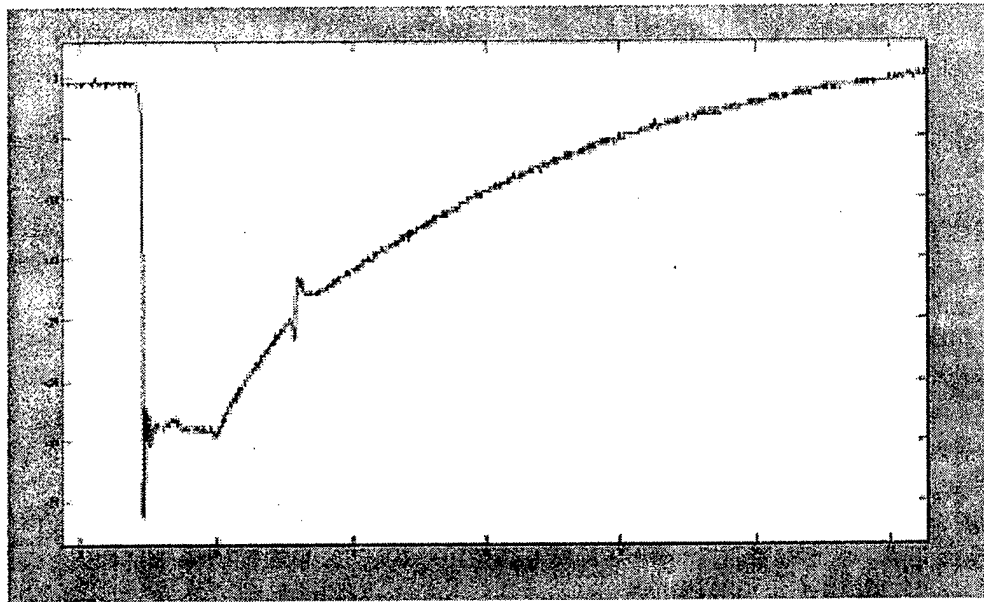


Figure 19. Impulse to be transmitted through Raytheon coaxial cavity antenna.

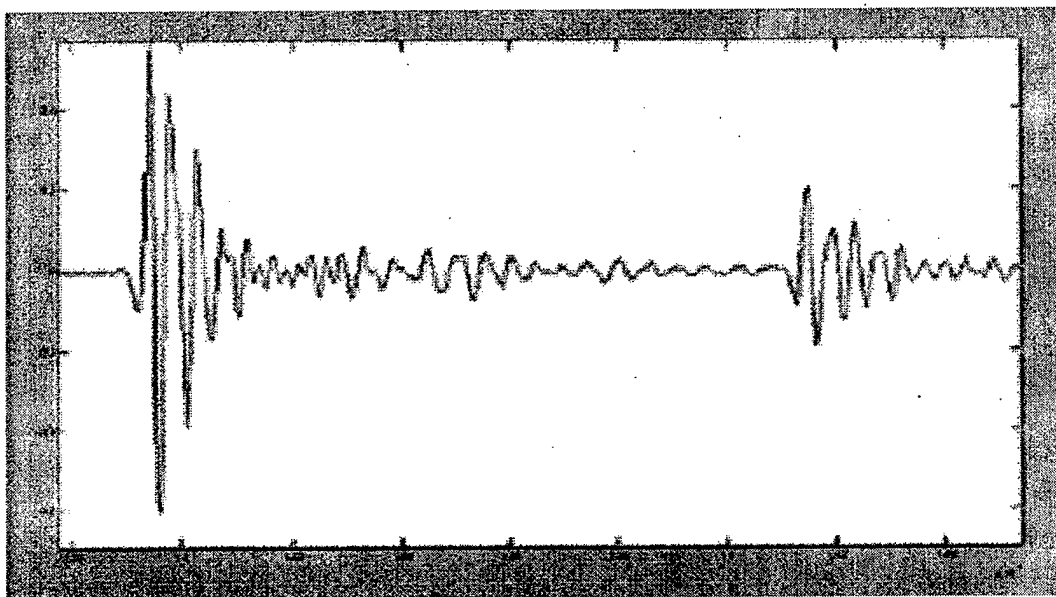


Figure 20. Received pulse through Raytheon coaxial cavity antenna.

It should be noted that figure 20 shows a late time response that is typical in these types of systems. The amplitude on the received doublet pulse shape is slightly off since the antennas were not completely aligned to each other in height. However, this is still useable in a transient system. Other data has since been collected where the doublet amplitudes are correct, but are not included in this paper.

A TEM horn also exhibits similar VSWR over large bandwidths with low dispersion. However, This type of antenna has open sidewalls that can receive energy in real world applications. In addition, the TEM horn is extremely large when used for low frequencies. This is unlike the smaller Coaxial Cavity antenna described.

4.0 Additional Applications:

Typical applications for these types of antennas, regardless of whether they are spirals, horns or coaxial cavity antennas, are in use as interferometer elements, direction finders, radar warning receiver (RWR) antennas, phased array elements, polarimeters and others. The interferometer and the polarimeter place the most stringent requirements on the antennas of the applications listed above. They require flat amplitude and phase over both field of view and frequency of operation. Stated another way, if the antenna can radiate an exact duplicate of an impulse then it will have the desired properties for use as an interferometer and polarimeter antenna element.

The elements described can be used at lower frequencies with a reasonable size for installation. Using the antennas out of band affords small direction finders at the lower frequencies as an example. The transient response of the impulsive coaxial cavity antenna lends itself for use in an imaging system. Preliminary data is shown in figures 21 and 22 where these antennas are used for both transmission and reception of impulses in an imaging system.

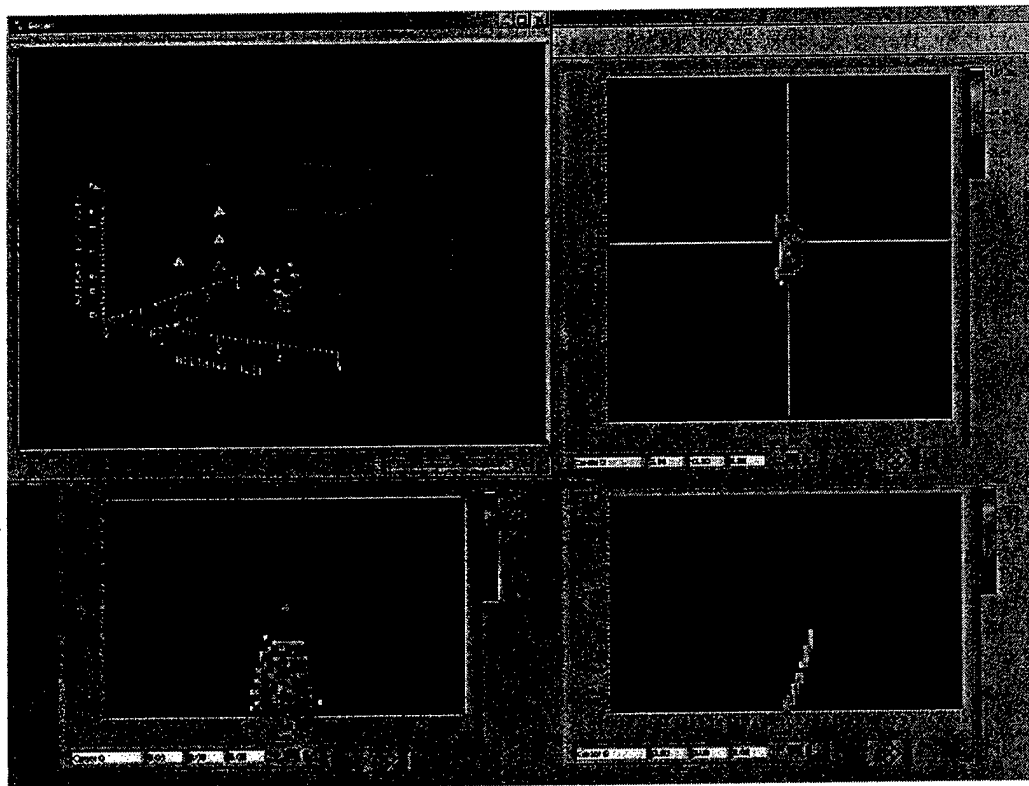


Figure 21. Impulsive image of electrical conduit using Raytheon impulsive coaxial cavity antenna.

3 Inch Sphere Buried 9 Inches Below Ground

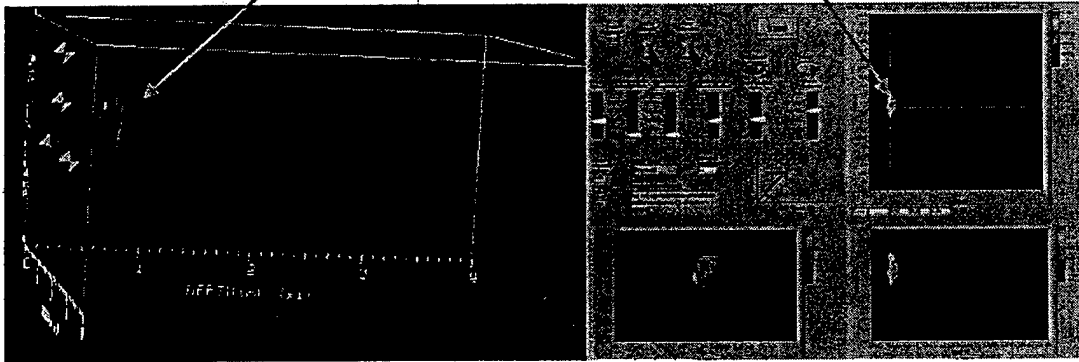


Figure 22. Impulsive image of buried 3 inch sphere using Raytheon impulsive coaxial cavity antenna.

The Capability to detect and image pipes and buried spheres provides numerous applications of the Raytheon Impulsive Coaxial Cavity antenna. Details for further use in imaging is the subject of a future paper.

5.0 Conclusions:

The coaxial cavity antenna has been fabricated, tested and described with data illustrating its low dispersion performance in previous papers. The coaxial cavity antenna is scaleable over octave, multi-octave and any other desired frequency band. Numerous aperture sizes can be determined based on desired operating frequency bands and desired gain. The self-complimentary structure of the coaxial cavity antenna provides the capability for both transmission and reception of any polarization. The Coaxial Cavity antenna is completely scalable to any frequency band of interest.

Several Low Frequency designs, typically below 500 MHz, have been described. It is desirable to have a coaxial cavity antenna that can operate all the way into the high frequency bands. This paper showed acceptable results for a design that works to at least 100 MHz and potentially lower, but not verified below 100 MHz due to existing antenna range limitations.

In the same context, an extremely broadband design was described that allowed the reception of a fast pulse in time. This required that the antenna be low dispersion in order to minimize time distortion. The Raytheon Impulsive Coaxial Cavity antenna is a low dispersion device where the phase center remains stationary at the center of the face of the antenna. This is the reason that this antenna was designed initially for polarimetry.

The Capability to detect and image pipes and buried spheres provides numerous applications of the Raytheon Impulsive Coaxial Cavity antenna.

6.0 References:

1. R. G. Corzine and J. A. Mosko, Four-Arm Spirals, Artech House, Norwood, MA, 1990.
2. C. H. Walter, Traveling Wave Antennas, Dover Publications, Inc., New York, 1965.
3. Y. Mushiake, Self-Complimentary Antennas: Principle of Self-Complementary for Constant Impedance, Springer-Verlag, New York, 1996.
4. R. Jaeger, T. Holzheimer, R. Rudd and R. Ackerman, "Coaxial Cavity Antenna," Patent No. 6,356,241, 12 March, 2002.
5. T. R. Holzheimer A Coaxial Cavity Antenna Exhibiting Low Dispersion Over a Wide Field of View," 2000 Antenna Applications Symposium, Allerton Park, Monticello, Illinois, 20-22 September, 1995, pp. 281-310.
6. T. R. Holzheimer, "An Implementation of a 0.5 to 2.0 GHz Circular 360 Degree Direction Finding Antenna," 1999 Antenna Applications Symposium, Allerton Park, Monticello, Illinois, 17-19 September, 1999, pp. 374-404.
7. T. R. Holzheimer, "High Accuracy DF Antenna Using COTS Hardware," 1995 Antenna Applications Symposium, Allerton Park, Monticello, Illinois, 20-22 September, 1995, pp. 12-1-12-30.
8. T. R. Holzheimer and S. Schneider, "Performance Enhancements with Applications of the Coaxial Cavity Antenna," 2001 Antenna Applications Symposium, Allerton Park, Monticello, Illinois, 19-21, September, 2001, pp. 171-193.
9. T. R. Holzheimer, "The Low Dispersion Coaxial Cavity as an Ultra Wideband Antenna," 2002 IEEE Conference on Ultra Wideband Systems and Technologies, Baltimore, Maryland, 21-23 May, 2002, pp. 333-336.

Small Ultra Wideband Planar Antenna

V.I. Litvinov, R. Webb, M. Felman, M. Aretskin, and L.S. Sadovnik

WaveBand Corporation,
17152 Armstrong ave, Irvine CA, 92614

We designed the log-periodic type antenna and associated feed network for optimum radiation pattern characteristics and good impedance match across a wide frequency range. The design was founded on general principles of frequency independent and electrically small antennas and then enhanced through simulation with the Ansoft 9 HFSS. We found good agreement between the measured and simulated return loss. The 19" diameter antenna has good matching characteristics over the extremely wide frequency band of 40 to 6000 MHz, can be used for transmission as well as reception, is semi-transparent to a visible light and can be rolled and stored in a small diameter tube.

1. INTRODUCTION.

Most antennas are inherently narrow-band devices. For a fixed antenna size, the main antenna parameters (gain, input impedance, pattern shape, and secondary lobe level and distribution) will vary with frequency. The frequency dependence also implies that to operate efficiently, an antenna must be larger than a certain minimum size relative to the wavelength. That is, given a particular frequency, the antenna cannot be made arbitrarily small, having to maintain a minimum size, typically on the order of a quarter of a wavelength. Despite the size-operating wavelength relation is still a problem in practical antenna designs, the electrically small antenna is feasible as a result of some tradeoff between size and performance depending on an application scenario.

Frequency independent antennas may be less demanding as for the size-wavelength constraint. There are general design principles the antenna should obey to be frequency independent: radiating elements of the antenna should be symmetric and self-similar with respect to center. We studied an antenna with self-similar shape of the radiation surface—planar log-periodic antenna that is expected to have flat electromagnetic response in a wide frequency range [1]. Metal coating and substrate material were chosen to provide as much visible transparency as possible when antenna is applied to a window. The maximal geometrical dimension of the antenna shown in Fig. 1 is 19".

2. ANTENNA CHARACTERIZATION

Simulation. Simulation of the antenna was performed with Ansoft HFSS 8.5 and 9. The antenna comprises two wings connected by a metal frame as shown in Fig. 1. Feed port was arranged at the end of 75 Ohm coaxial cable. The center conductor of the coaxial cable is attached to the antenna through a metal pad and a frame. The outer conductor is connected to a ground at a close distance to the antenna terminal (not further than the quarter of a shortest wavelength).

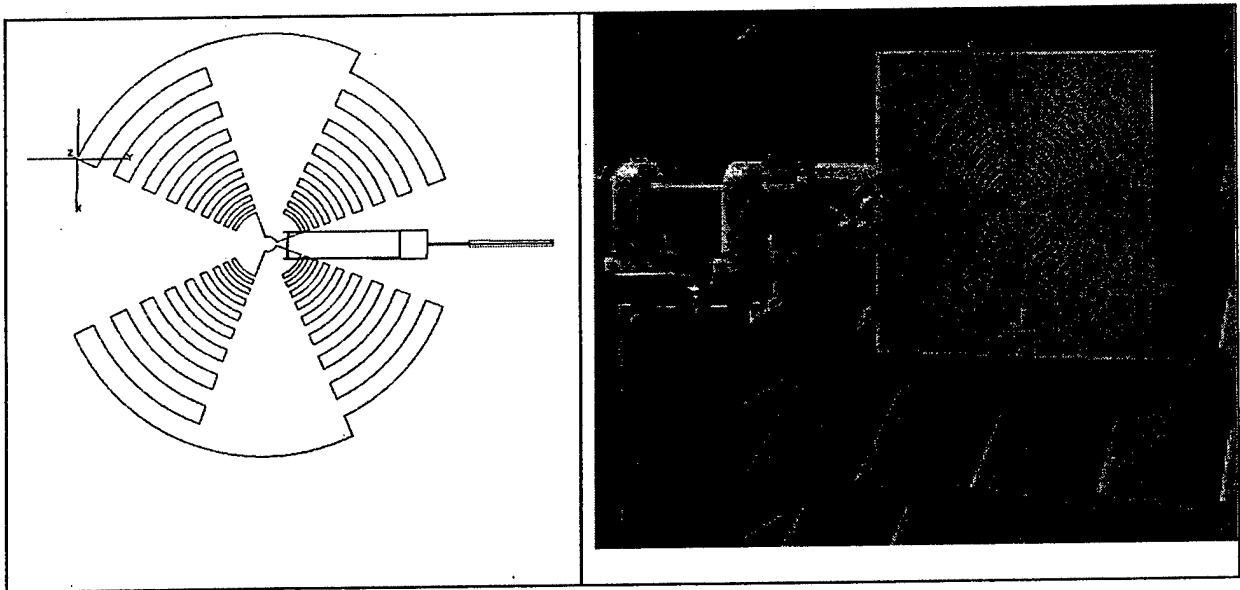
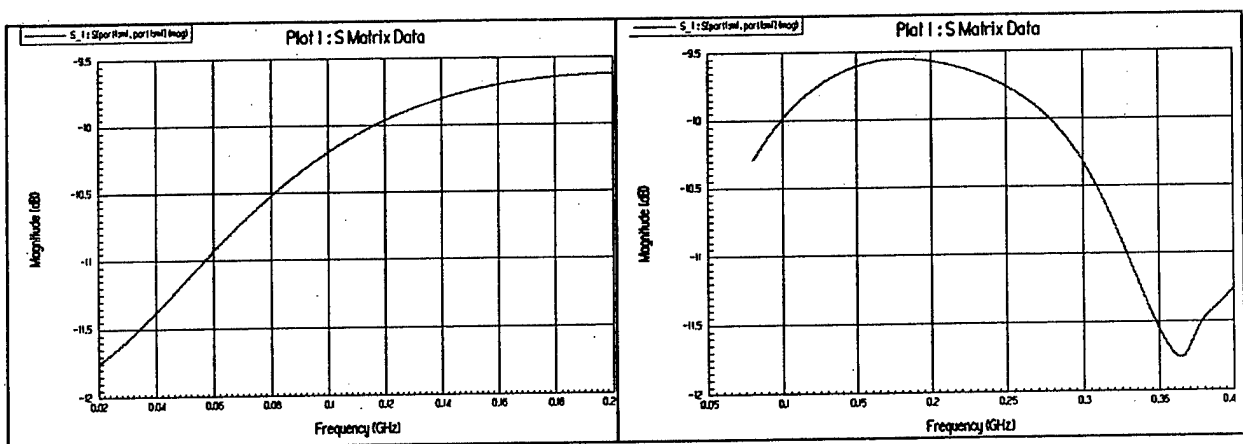


Fig. 1. a/ Sketch of the antenna fed by a coaxial cable; b/ Close-up view of planar antenna in Georgia Tech Research Institute (GTRI) indoor range.

Particular arrangement of the antenna elements at a feeding point and log-periodic shape of the radiating elements provide good antenna-cable impedance matching and results in extremely wideband antenna capability. In order to preserve high accuracy the return loss was simulated in separate frequency intervals. Predicted return loss is shown in Figs 2 to 4.



Figs.2. Predicted return loss in the 20–400 MHz range.

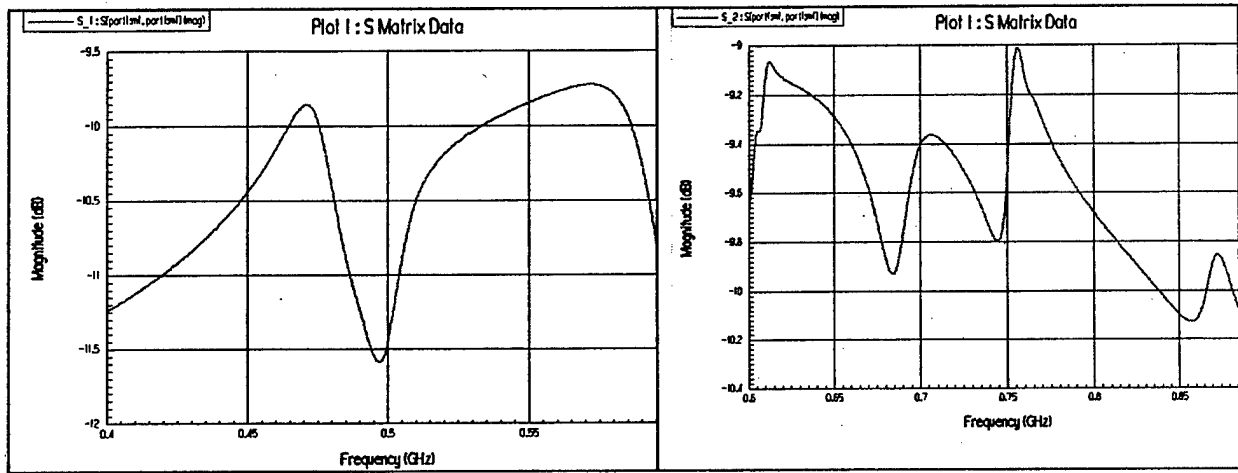


Fig. 3. Predicted return loss in the 400-900 MHz range.

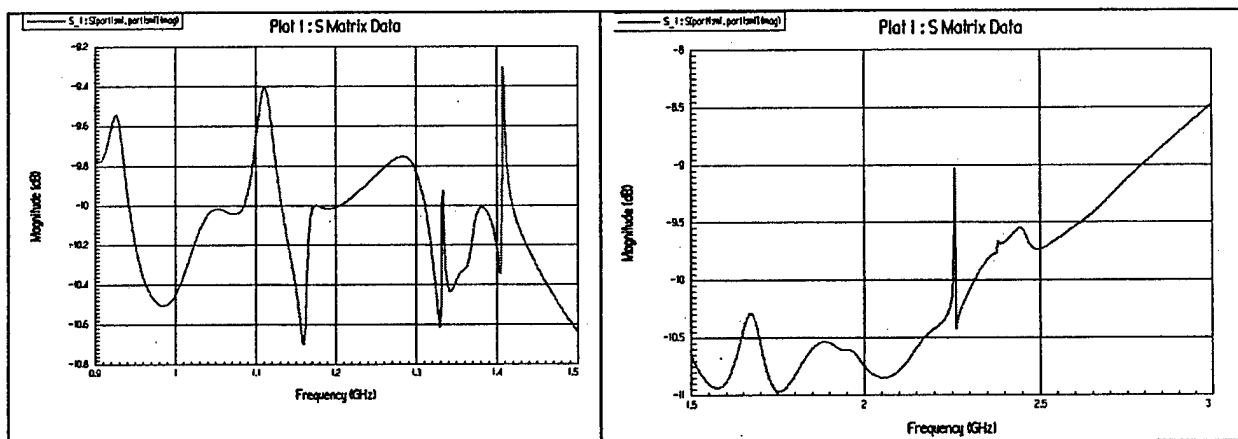


Fig. 4. Predicted return loss in the 900 MHz-2GHz range.

Test. Antenna impedance and far field characteristics were tested in the Georgia Tech Research Institute. The indoor antenna range allowed for the measurement of complex antenna impedance from 45 to 6000 MHz. In addition, far field antenna pattern was measured from 200 to 6000 MHz, for both vertical and horizontal polarizations, and for elevations of 0, 30, 60 and 90 degrees. We explored the feasibility of rigorous experimental characterization over the entire 30 to 6000 MHz frequency range.

Fig. 5 represents the magnitude of measured antenna return loss from 45 to 1000 MHz, while Fig. 6 shows that same parameter over the entire 45 to 6000 range of interest. Above 500 MHz the return loss is better than 3 dB, indicative that the design offers power transfer at one half the theoretical limit. Below 500 MHz the worst return loss is 1.9 dB (130 MHz), implying power transfer of 35 percent relative to the ideal case.

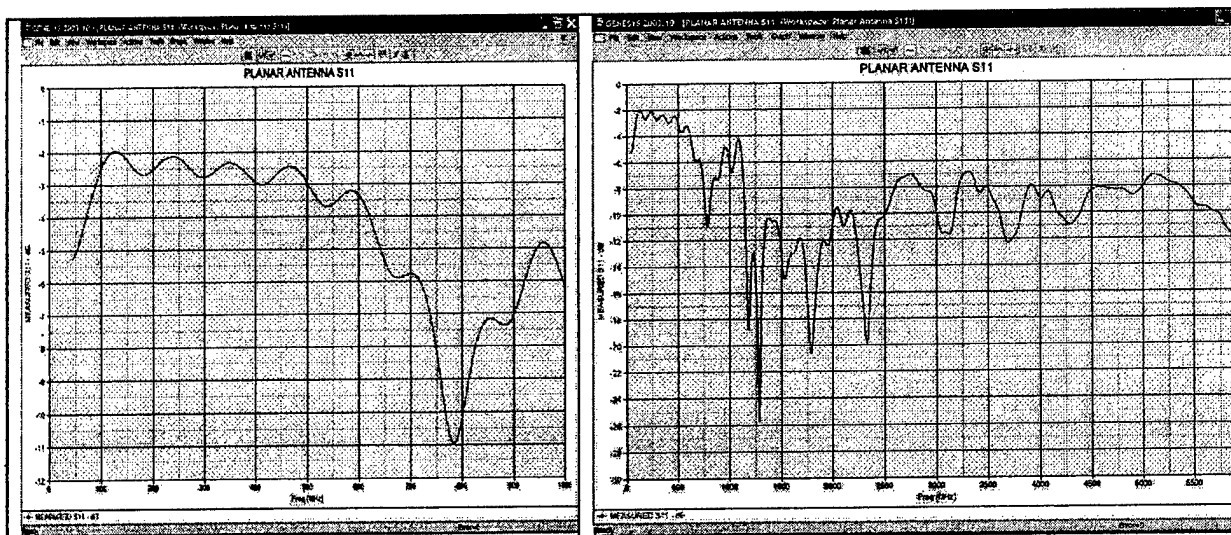


Fig. 5. Measured antenna return loss from 45 to 6000 MHz

Far field behavior of the antenna was recorded under 128 sets of conditions. Specifically, the device was measured at: 200, 300, 400, 500, 700, 1000, 1500, 2000, 2500, 3000, 3500, 4000, 4500, 5000, 5500 and 6000 MHz, vertical and horizontal polarizations, elevation angles of 0, 30, 60 and 90 degrees.

Because this design is most suited to source or load impedance of 75 to 100 ohms, measurements were done with a 75 ohm source at frequencies up to and including 1500 MHz - the practical limit for the best available 50-to-75 ohm transformer. Results at frequencies above 1500 MHz are with the antenna terminated in 50 ohms. Fig. 6 represents typical plots for vertical and horizontal polarization at 4000 MHz and 0 degrees elevation.

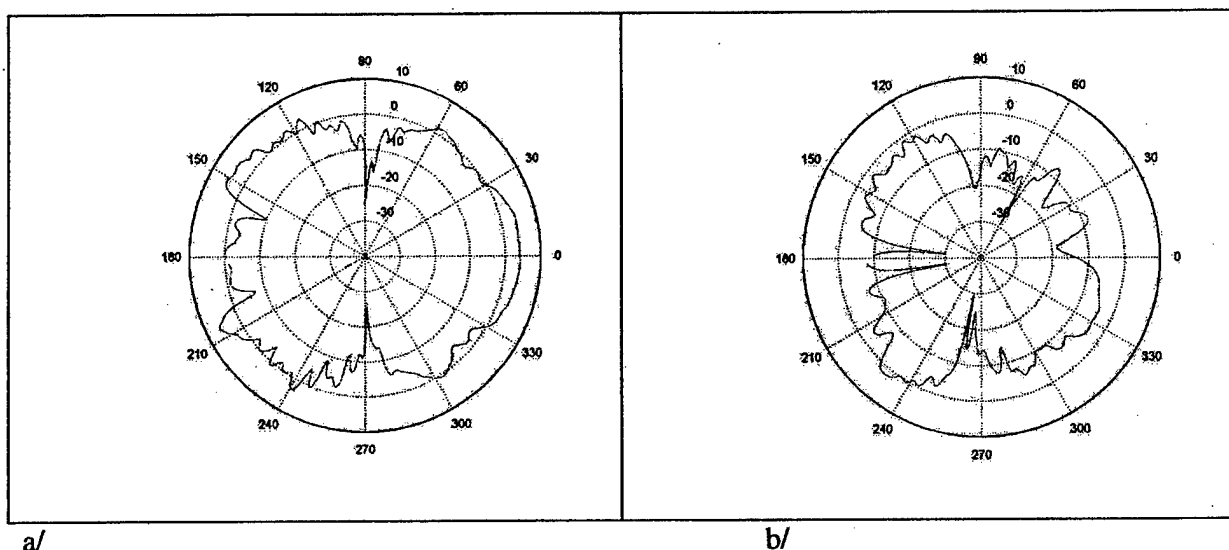


Fig. 6 Antenna gain at 4000 MHz: a/ 0 degree elevation, vertical polarization; b/ 0 degree elevation, horizontal polarization

The antenna demonstrated good impedance match and fairly acceptable gain performance over the 45 to 6000 MHz frequency range, with that performance achieved with only a small percentage of the overall antenna area requiring conductive metallization, an attribute that may lend itself to realization of a nearly transparent antenna. The minimal conductor area in the present configuration would allow the fabrication of a nearly optically clear structure with a conventional conductor. After weighing the relative merits of vacuum metallization of bare plastic and also chemical removal of metal from clad plastics, the clear choice employed silver applied to flexible polycarbonate sheeting by conventional silk-screening techniques. Fig. 7 represents the antenna fabricated by application of $\frac{1}{4}$ ounce silver (thickness $\sim .00035''$) to 0.010" thick polycarbonate. The antenna and associated cable and cable connector can be rolled and stored in a 2" diameter tube.

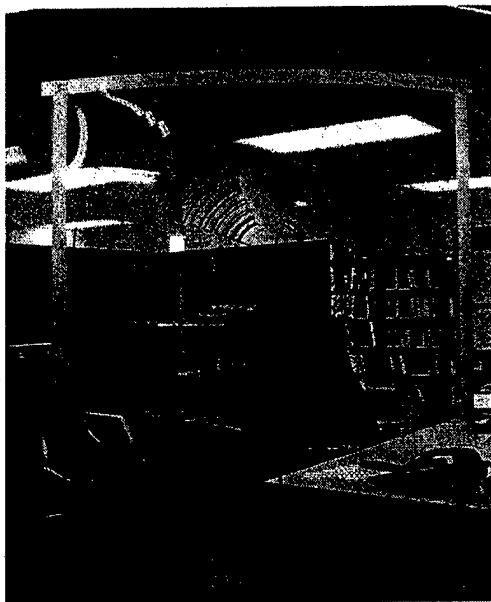


Fig. 7. Silver/polycarbonate antenna attached to curved office window

Further improvement of antenna impedance match and gain over the full 30 to 6000 frequency range is possible with the matching network. Fig. 8 illustrates the circuit, which employs a Mini-Circuits TCM4-19 4:1 impedance transformer along with two chip inductors and two chip capacitors, will fit within a 0.2" by 0.2" area on the antenna substrate.

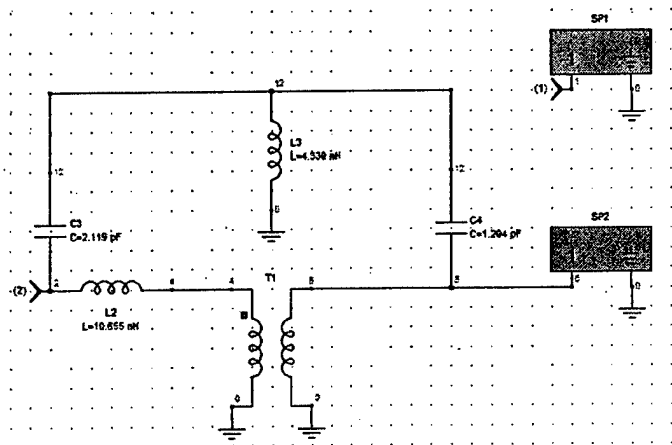


Fig. 8. Matching network for 30 to 6000 MHz antenna band

The matching network was designed based on the antenna impedance as measured at GTRI. Return loss is shown in Fig. 9a for the entire frequency range, and in Fig. 9b for 600 MHz and below. In both graphs the red plot depicts the antenna alone while the blue results represents the predicted overall performance with the matching network in place. The worst case return loss of

4 dB corresponds to the antennas ability to deliver not less than 60 percent of available power to a 50 ohm receiver.

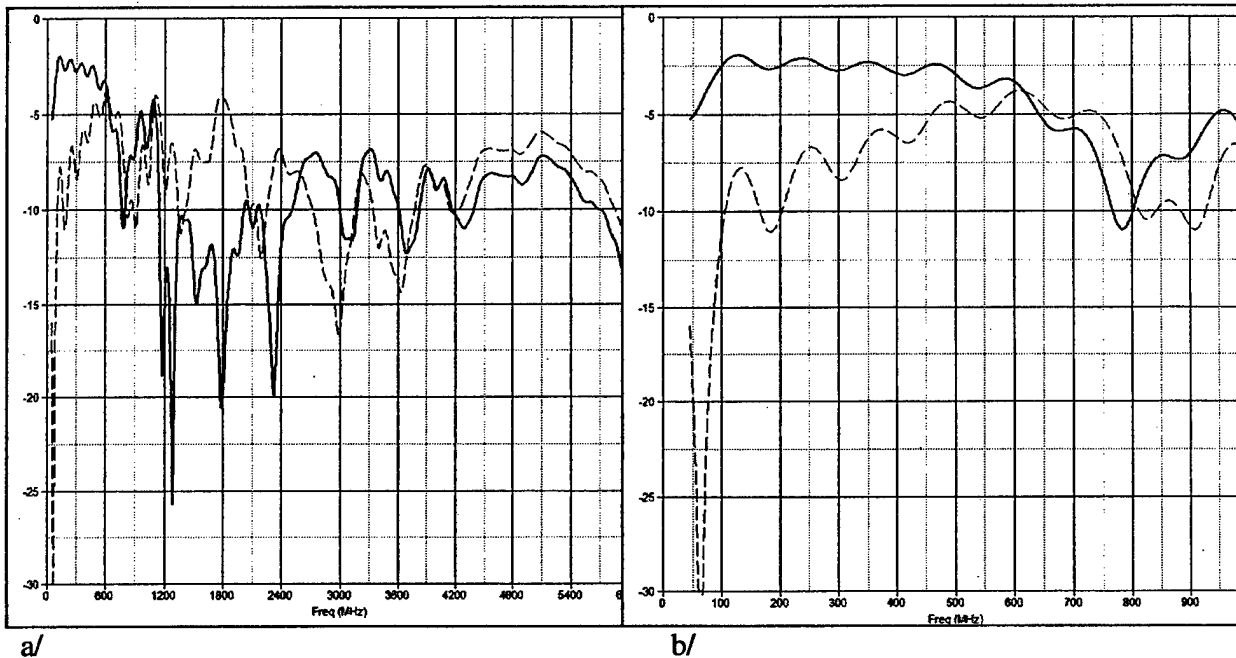


Fig. 9. a/ Return loss from 45 to 6000 MHz (a) and from 45 to 600 MHz (b). Predicted return loss for antenna with matching network-dashed line. Measured return loss of antenna alone-solid line.

3.0 CONCLUSIONS.

We have fabricated a nearly transparent version of the wideband antenna and have done so using inexpensive materials and techniques. We have also designed a miniature matching network for improved performance over the entire 30 to 6000 MHz band. Having log-periodic wings the antenna design differs from the original in that it actually presents quasi-log-periodic monopole and does not employ the balanced feed.

[1] R.H. DuHamel, "Frequency independent antennas", USA Patent, 2,985,879, 1961.

WIRELESS EMBEDDED RUST MONITORING SYSTEMS

K. Hietpas¹, B. Ervin², D.A. Kuchma³, H. Reis², and J. T. Bernhard¹

¹Electromagnetics Laboratory
Department of Electrical and Computer Engineering
University of Illinois at Urbana-Champaign
Urbana, IL 61801

²Non-destructive Testing and Evaluation Laboratory
Department of General Engineering
University of Illinois at Urbana-Champaign
Urbana, IL 61801

³Department of Civil Engineering
University of Illinois at Urbana-Champaign
Urbana, IL 61801

Abstract: This work describes ongoing development of an embedded sensor system for the early detection and prevention of deterioration of reinforcing steel tendons within concrete bridge girders. These devices will evaluate the condition of the steel tendon using ultrasonic techniques and then wirelessly transmit this data to the outside world without human intervention. The ultrasonic transducers and the interpretation of the sensed signals that allow detection and prognosis of tendon condition are detailed. Electrical characterization of concrete mixtures used in bridge construction is conducted and a wideband microstrip antenna is designed and fabricated to operate between 2.4 and 2.5 GHz when embedded in such a medium. Simulations and measurements of the embedded antenna element are presented. Transceiver selection and implementation are discussed as well as future work in operational protocols, sensor networking, and power sources. By implementing commercially available off-the-shelf components whenever possible, these devices have the potential to save millions of dollars a year in evaluation, repair and replacement of reinforced concrete girders.

1. Introduction

Highway systems are aging and slowly deteriorating, causing upkeep and replacement costs to continuously increase. This deterioration is caused primarily by corrosion occurring on the reinforcing steel tendons (rebar) used in these concrete structures. Assessment of the condition of these tendons is a difficult task, considering the steel is usually buried beneath 8 or more centimeters of concrete. There are no definitive empirical methods for detection of deterioration. Therefore repairs and replacements are based on mainly visual indications of failure. The cost of inspecting, rehabilitating and replacing degraded pieces of structures in the United States alone, using the current methodology, is estimated to be near \$210 billion dollars [1]. With proper testing methods that require fewer visual inspections and provide more accurate information about the condition of the steel reinforcement, this expense could be drastically reduced.

Current and proposed methods of evaluating the degree of steel tendon degradation can be imprecise and do not provide an accurate representation of what is occurring within the concrete. Visual tests are comprised of observing cracks in the girders and rust occurring on the outside of the concrete. The degradation has then progressed so far that a majority of the structure needs to be replaced. Other evaluation methods range from ground penetrating radar (GPR) to dragging a chain on bridge decks and listening for echo discrepancies in order to characterize the interior of these concrete structures [2-4]. Pinpointing positions of decay with ground penetrating radar is problematic due to several practical considerations, such as multi-level interference and the lack of a definitive method for interpretation of decay extent.

Some proposed methods involve embedding devices into concrete in order to perform tests within the structures and transmit information to the outside world [5-7]. The devices relay information about the corrosion factors (usually chloride ion concentration) within the concrete. These devices, however, are completely passive until a reading unit is placed near them, still requiring human interaction to obtain any data. Another method [8] involves embedding long sections of fiber optic cables into roadway and bridge structures to test for similar parameters. Fiber optics, however, must be placed within the entire structure and allowed an outlet from the concrete. These devices are designed to test for the proper conditions for corrosion to occur but do not actually test for corrosion damage. Therefore, they may report excessive levels of chloride ions or extreme temperatures whether or not the tendons are still healthy.

The purpose of the present project is to create a system of wireless embedded sensors that utilize ultrasonic techniques to test the condition of reinforcing tendons in concrete girders. Prestressed concrete bridge girders are constructed in dedicated factories that have stringent control over the process. The steel tendons are held under tension while the concrete is formed around them. The tendons are cut, causing the girders to bow; bowing counteracts the weight of the fully formed bridge that these girders support. A cross section of a bridge girder is shown in Fig. 1a. The devices will be mounted directly to the steel tendons as shown in Fig. 1b. These will interact in a large network to characterize and locate any corrosion damage in the reinforcing steel. The information gathered from the sensors will be relayed to an independent base station situated on the exterior of the bridge, which will upload that information via the commercial cellular network to the department of transportation.

Creation of these devices necessarily requires input from an interdisciplinary team. In the following two sections, we discuss two important aspects of this system: the active ultrasonic techniques used to sense the tendon condition and the electromagnetic design that enables wireless communication of this data from within the girder itself.

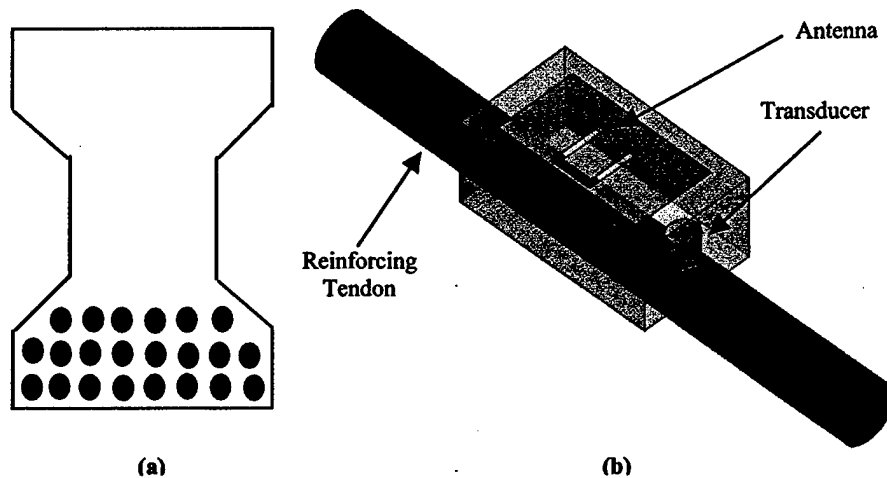


Fig. 1: Cross section of pre-stressed girder with approximate positions of reinforcing tendons shown (not to scale) (a) and proposed sensor implementation mounted to reinforcing tendon (b).

2. Ultrasonic Sensing and Data Interpretation

The mechanics of corrosion in reinforced concrete leads to an expansive product (rust at the cathode) and a loss of steel reinforcement diameter (at the anode) [9,10]. These reactions degrade the strength and aesthetics of the concrete structure due to disruption of the bond at the interface between the

steel and the surrounding concrete, loss of steel cross-sectional area, and longitudinal cracking in the concrete with rust stains. Fig. 2 illustrates the progressive general phases of degradation in reinforced concrete due to corrosion.

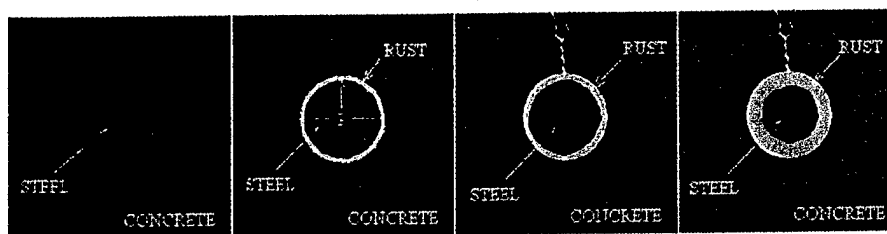


Fig. 2: Progressive phases of corrosion degradation in reinforced concrete

Currently, there are several techniques being developed to assess the degradation of concrete structures due to corrosion [10]. Among these, the use of guided ultrasonic waves has been proposed as a methodology for detecting and evaluating structural degradation caused by the corrosion process. Many sources provide a good analytical review of ultrasonic waves in cylindrical waveguides [11,12,13,14]. Guided ultrasonic waves have also been used to detect simulated corrosion degradation in reinforced concrete specimens including small notch defects [15] and debonding [16]. Rose et al. have also discussed the importance of using ultrasonic guided waves for inspection in industrial processes [17].

Guided waves are combinations of longitudinal and shear waves that continually interact with the boundaries to form a composite wave [17]. Energy flows mainly along the direction of the guiding configuration [18]. If the geometry of the waveguide affects the flow of energy, then the speed and attenuation of the waveform that has propagated through the waveguide should give a strong indication of its geometry. For example, Chung measured the change in the speed of a transmitted ultrasonic pulse for different diameters of concrete embedded reinforcement [19]. His findings confirmed that the geometry could be determined from the group velocity of guided ultrasonic waves. For the current investigation, guided ultrasonic waves will be used to assess simulated corrosion damage in the form of debonding between the embedded steel and the surrounding mortar.

Specimens were manufactured to simulate the entire range of possible delamination to estimate the feasibility of the technique in detecting corrosion damage. To simulate bond loss at the interface between the steel tendon and the surrounding concrete, a range of different lengths of tape were wrapped around the steel reinforcing bars (bar size #4) to inhibit bond during hydration of the surrounding mortar (0.45 water to cement ratio). The reinforcing steel

bars, with 106.68 cm (42") in length, were centered within the surrounding mortar specimens, which had the dimensions 10.16 cm x 10.16 cm x 91.44 cm (4" x 4" x 36"). Twelve specimens were manufactured, with the length of the tape starting at 7.62 cm (3") and ending at 91.44 cm (36") (completely debonded) in 7.62 cm (3") increments. The tape started on each specimen at the end where the sending transducer was mounted. Fig. 3 provides an illustration of the test specimens.

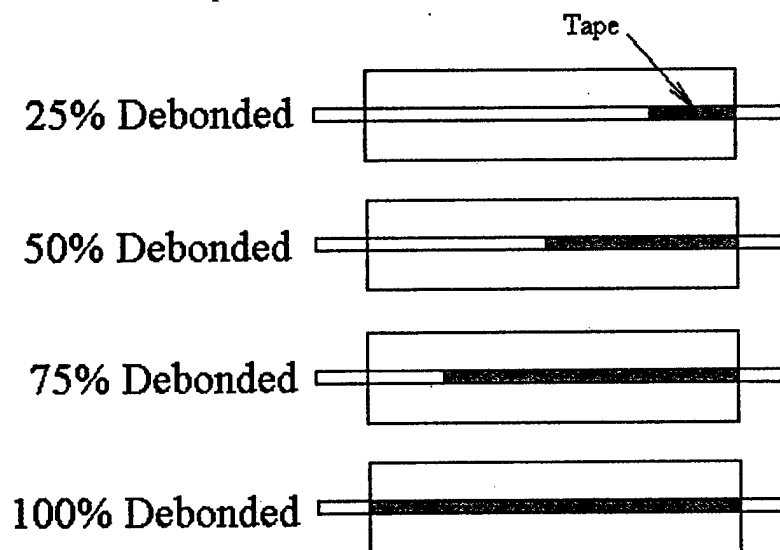


Fig. 3: Schematic diagram showing four test specimens with increasing amounts of tape-simulated debonding.

A broad range of frequencies was evaluated to test the specimens. A lower frequency range was used for final testing to avoid high attenuation of the waveform. However, Pavlakovic et al. found that higher frequency testing bands may attenuate less due to lower amounts of energy leakage to the surrounding concrete because of the wave structure of the generated higher guided wave mode [15]. In the first experiment, a single rectangular pulse with a pulse width of 6.25 μ s was used to excite the sending transducer. The pulse had a peak-to-peak voltage of 200 V. The filter was set with a high pass frequency of 75 kHz and a low pass frequency of 85 kHz, with a gain of 40 dB. The specimens were tested with direct (parallel to the tendon) and indirect (perpendicular to the tendon) transducer arrangements using the equipment setup shown in Fig. 4.

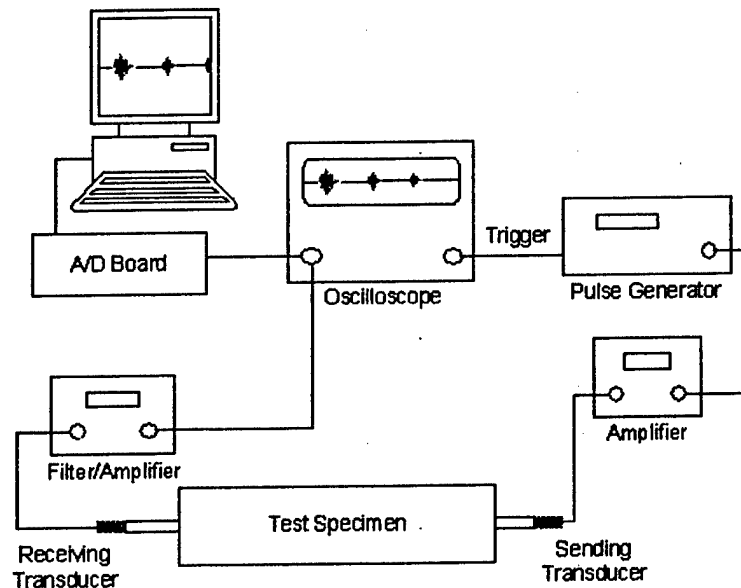


Fig. 4: Schematic diagram of laboratory testing setup showing the transducer mounted in direct transmission.

Fig. 5 shows the ultrasonic signal energy versus percent of debonding for the manufactured specimens where energy is defined as the integral of the square of voltage over the signal duration. In Fig. 5, four measurements were collected for each delamination length. The coefficient of determination is 0.89. Fig. 5 indicates that as the amount of debonding converges to 100%, more energy arrives at the receiving transducer. Leakage of ultrasonic energy to the surrounding mortar is thought to decrease as the bond between the steel and mortar decreases. Similar results were obtained using an indirect transducer arrangement, where the transducer is mounted perpendicular to the

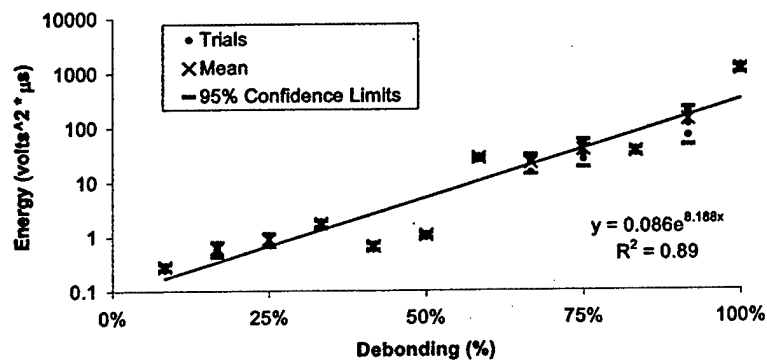


Fig. 5: Signal energy vs. percent of debonding using a direct transducer arrangement.

tendon [10]. Fig. 5 shows that as debonding increases incrementally in reinforced concrete, changes in energy allow for its detection and size estimation.

In a second experiment, a tone burst of 15 rectangular pulses with a pulse width of $3.33 \mu\text{s}$ was used to excite the sending transducer. The pulse had a peak-to-peak voltage of 200 V. The filter was set with a high pass frequency of 50 kHz and a low pass frequency of 300 kHz, with a gain of 40 dB. Fig. 6 shows the area under the power spectral density curve versus the percent of debonding, using a direct transducer arrangement for the frequency band of 100 kHz to 200 kHz.

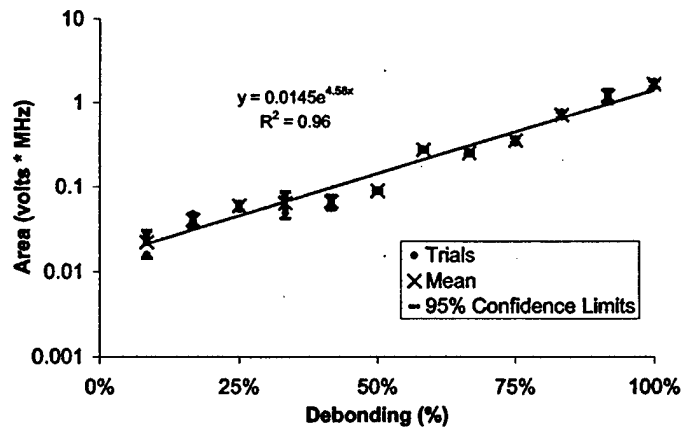


Fig. 6: Area under the power spectral density curve vs. percent of debonding using a direct transducer arrangement.

The coefficient of determination for the exponential trend line is 0.96. Fig. 6 indicates that less energy leaks into the surrounding mortar as more debonding occurs. Similar results were obtained for an indirect transducer arrangement. Fig. 6 shows that change in the area under the power spectral density curve can also be used to detect and estimate the amount of delamination between the steel tendon and surrounding mortar.

Active ultrasonic transducers will be integrated into the final package that will be embedded into concrete girders. The final package will also include the radio and antenna necessary for wireless communication of the sensed data. The design of these components is discussed in the next section.

3. Electromagnetic Design for Wireless Communication

3.1 Frequency selection

Two different frequency bands were considered for the operation of the wireless communication link for this system. The FCC allocates several different bands for the general use of Industry, Science and Medicine (ISM). These bands do not require special permits and only require that systems not interfere with each other. Two ISM bands, 2.4 to 2.5 GHz and 5.725 to 5.85 GHz, were considered due to the available bandwidth for data communication and the relatively small antenna size that would be required. The 2.4-2.5 GHz frequency band was chosen for this system due to the availability of off-the-shelf radio components.

3.2 Electrical Characteristics of Concrete

The electrical properties of the concrete used in girder construction were investigated to enable accurate modeling and design of the antenna that will be embedded in the structure. Two different mixtures of concrete were tested for their relative permittivity, permeability, and conductivity from 1 GHz to 3 GHz. These mixes, currently used in the construction of highway bridges, are detailed in Table 1.

Proposed Mix Design			
Constituent	Type	Mix #1 (lbs/ft ³)	Mix #2 (lbs/ft ³)
Cement	Type I Portland Cement	77.41	36.30
Fine Aggregate	River Sand	41.85	32.94
Coarse Aggregate	Trap Rock (3/4")	67.41	66.41
Water	Tap Water	9.85	11.59
Silica Fume	Force 10,000 (Grace)	10.25	7.26
Superplasticizer	ADVA Flow (Grace)	0.186	0.607
Accelerator	CaCl ₂	0.014	0.037

Table 1: Content of Concrete Mixtures

Others have characterized the electrical properties of various concrete mixtures over frequency [20]. Rhim et al. [20] tested various samples of concrete over a large frequency range including 1 to 20 GHz. Near 2.4 GHz,

he reports that the relative permittivity was approximately 4 while the conductivity was close to zero. To confirm this information for our particular mixes, samples of concrete were fabricated and measured. Samples were cast and allowed to air-dry for a minimum of seven days. All the samples were formed into cylinders with diameters of 7.62 (3"), 10.16 (4"), and 15.24 (6") cm. Each contained a slot to accommodate the dielectric probe that was used to measure the electrical properties of the concrete samples.

The Hewlett Packard 8507A Dielectric probe was used in conjunction with an Agilent 8510C Network Analyzer. Using this probe, the electrical properties of the various size and sand content samples were gathered. The findings of these tests are comparable to Rhim et al.'s findings [20]; the average relative permittivity of Mix #1 was approximately 4 while the conductivity varied between 0 and 0.04 Siemens/m. The permittivity and conductivity of Mix #2 were noticeably higher than the previous findings, having a relative permittivity of approximately 7 and conductivity near 0.1 Siemens/m. This result is most likely due to the higher proportions of cement and water in Mix #2.

The amount of expected signal loss within concrete at this frequency is found using Eq. (3). In Eq. (1), γ is the complex wave propagation coefficient; α the attenuation coefficient; β , the wave vector number; ω , the angular frequency (equal to $2\pi f$, where f is the operating frequency); μ , the permeability; ϵ , the permittivity; and σ , the conductivity. These calculations indicate that the attenuation of a signal within concrete will be very low. In 10 cm (approx. 4 inches) of concrete, a signal will only lose approximately 2.11 dB in Mix #1 concrete and 6.49 dB in Mix #2 at an operating frequency, f , of 2.448 GHz.

$$\gamma = \alpha + j\beta = \frac{\sigma}{2} \sqrt{\frac{\mu}{\epsilon}} + j\omega \sqrt{\mu\epsilon} \quad (1)$$

$$\alpha = \frac{\sigma}{2} \sqrt{\frac{\mu}{\epsilon}} \left[\frac{Np}{m} \right] \quad (2)$$

$$Loss[dB] = \alpha \left[\frac{Np}{m} \right] \times 0.1[m] \times 8.656 \left[\frac{dB}{Np} \right] \quad (3)$$

3.3 Antenna Selection, Design, and Simulation

A microstrip antenna design was chosen for this application, since the rugged planar design lends itself well to integration with the rest of the embedded

package and will not disturb the structural integrity of the concrete girder. Unfortunately, a standard microstrip patch has a very narrow bandwidth (~2%) [21], which makes it unsuitable for operation in the chosen frequency band. Thus, a microstrip U-slot antenna was selected because it expresses a far greater operational bandwidth (~10%) than a standard patch antenna [22]. Using the design methodology described by Weigand et al. [23], a U-slot microstrip antenna was specified to operate between 2.4 and 2.5 GHz when embedded in concrete. The U-slot antenna was designed on a substrate with permittivity of 2.2 and thickness of 3.175 mm. A diagram of the antenna with dimensions is provided in Fig. 7.

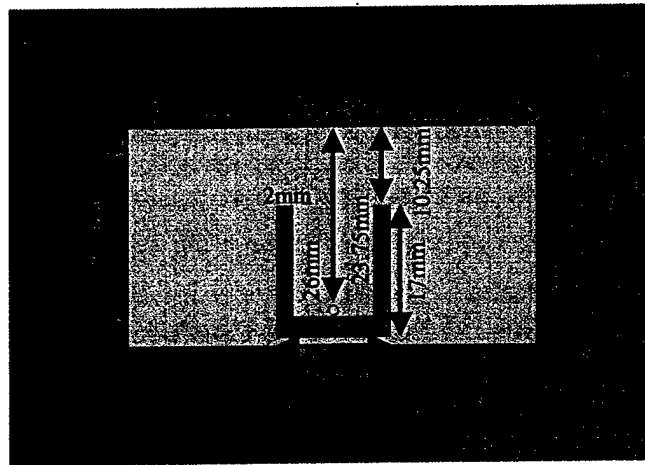


Fig. 7: Diagram of U-slot antenna with dimensions shown.

The Weigand method of designing a U-slot antenna allows for placement of the resonance points -- points where the imaginary component of the antenna's input impedance is zero. After designing the resonance points of the antenna using Weigand's method, the antenna design was further optimized using a commercial electromagnetic computational package [24] to be impedance matched at the appropriate frequencies when embedded. Another simulation package, Ansoft HFSS® [25], was also used to evaluate the design and compare results before the design was fabricated. Fig. 8 provides a comparison of the simulated return loss (S_{11}) obtained from the two simulation packages when the antenna is simulated below 5 cm of concrete. This data indicates that the antenna exhibits an acceptable impedance match (with $|S_{11}|$ less than -9.54 dB and VSWR (voltage standing wave ratio) below 2:1) in the 2.4-2.5 GHz frequency band when it is embedded in concrete. Radiation patterns of the embedded antenna are discussed in the next section.

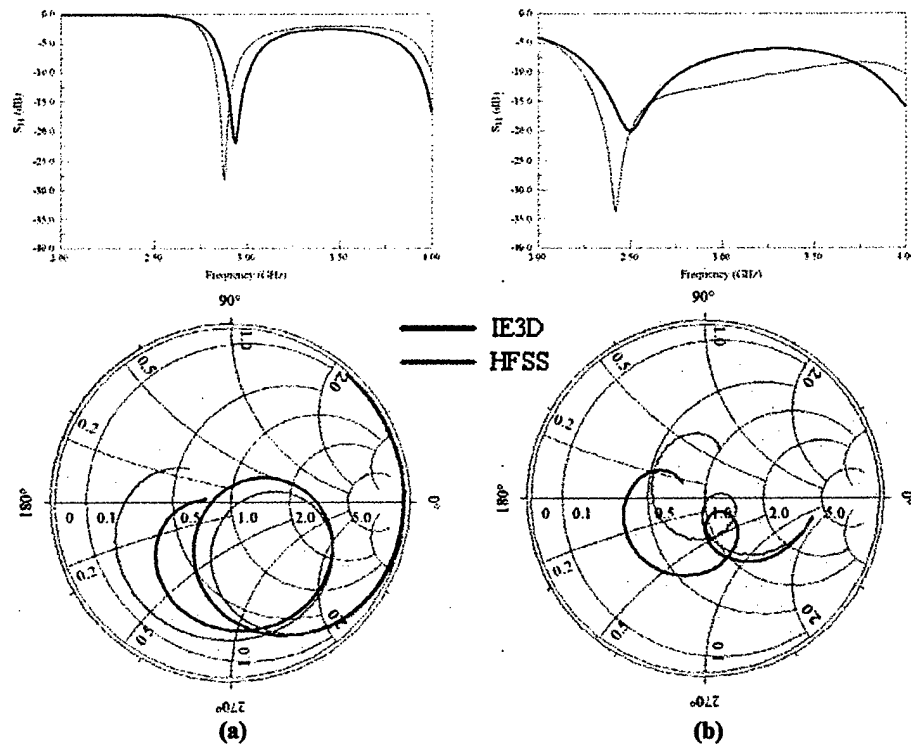


Fig. 8: Simulated return loss (S_{11}) and impedances in air (a) and concrete (b).

3.4 Antenna Fabrication, Testing and Results

After verifying that the antenna would present an impedance match within the required frequency band, a prototype was fabricated. Using Rogers Duroid® 5880 as the substrate material, the antenna shown in Fig. 9a was created along with a choke and cable long enough to extend out of a concrete block as shown in Fig. 9b. The choke ensures that the long metallic cable attached to the antenna does not radiate and distort the pattern of the antenna element. The return loss (S_{11}) and radiation patterns of this assembly were tested before being embedded into the concrete specimen. Measurements in air agreed very closely with the simulations and are not included here for brevity. In air, the antenna exhibits a uniform radiation pattern that is consistent with a microstrip patch antenna [21].

The antenna assembly was then coated with a spray-on plastic coating to electrically isolate it from the concrete. Next, the antenna was encased in a sample of Mix #1 concrete measuring 20.32 cm x 20.32 cm x 30.48 cm (8" x 8" x 12"). The antenna was embedded halfway into the block so that it was about 10 cm away from the concrete face. This distance was judged comparable to the space between the bottom tendons and the face of the

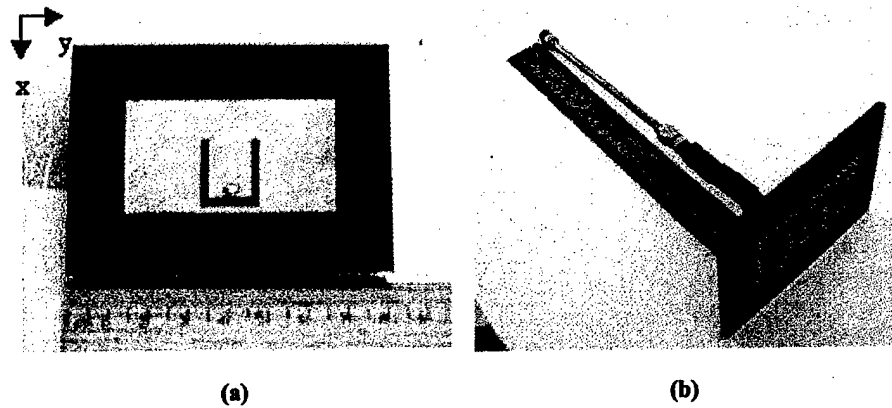
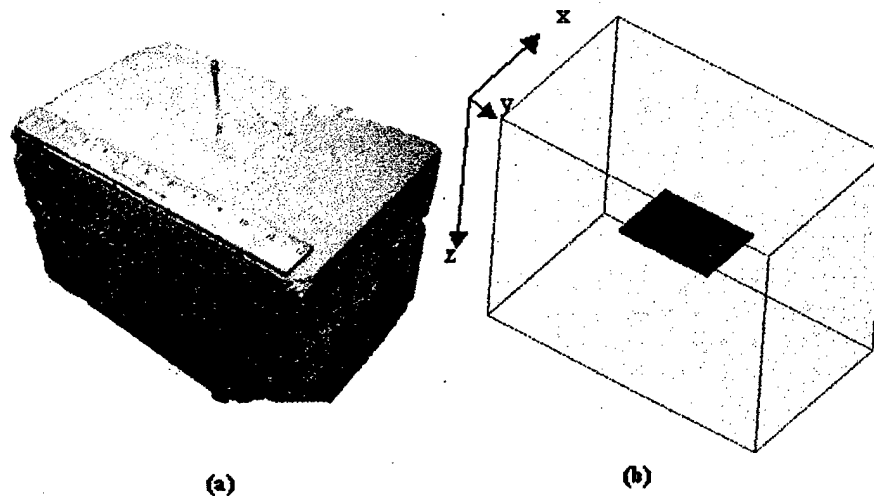


Fig. 9: U-slot (a) and assembly (b)

concrete girder. Care was taken to maintain proper alignment and placement within the concrete specimen. A picture of the completed embedded antenna for test as well as a graphic of the simulated version of the embedded antenna in HFSS[®] are provided in Fig. 10. The cable extends far enough out of the concrete block to be connected to test equipment without inducing any mechanical stress on the cable.



**Fig. 10: Antennas embedded in concrete specimens
(a) physical specimen (b) modeled in HFSS[®].**

The concrete block assembly was then tested with the network analyzer and the return loss and radiation patterns were measured and compared to the simulated data (Fig. 11). The operating band of the embedded assembly (defined by a return loss less than -9.54 dB) encompasses the range from 2

GHz to well above 4 GHz as shown. The measurements show a larger bandwidth than expected and the antenna operates well in the 2.4-2.5 GHz band. The increased bandwidth of the embedded prototype is most likely due to inhomogeneities (i.e., aggregate and small air pockets) in the concrete sample that were not included in the simulations. The far field radiation patterns of embedded concrete assembly were measured in an anechoic chamber. The test setup in the anechoic chamber, pictured in Fig. 12, was reinforced to support the weight and size of the concrete specimen. The far field patterns of the assembly are shown in Fig. 13 along with simulation results from HFSS[®] using a conductivity of 0.1 Siemens/m (which is slightly higher than expected for this mixture of concrete). Again, the presence of inhomogeneities in the concrete specimen can account for the difference in effective conductivities. The maximum gain from this assembly is approximately -7 dBi.

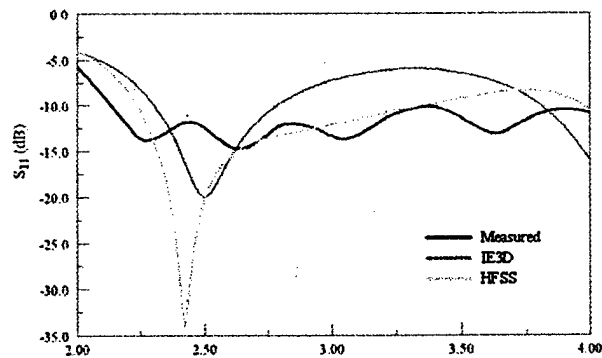


Fig. 11: Measured return loss (S_{11}) in concrete compared to simulated results.

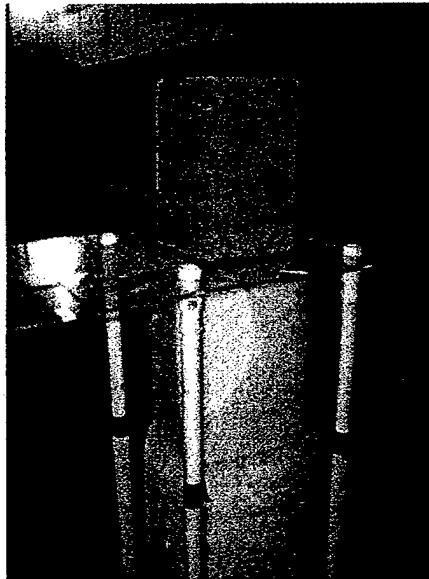


Fig. 12: Embedded assembly in concrete specimen in the anechoic chamber for radiation pattern tests.

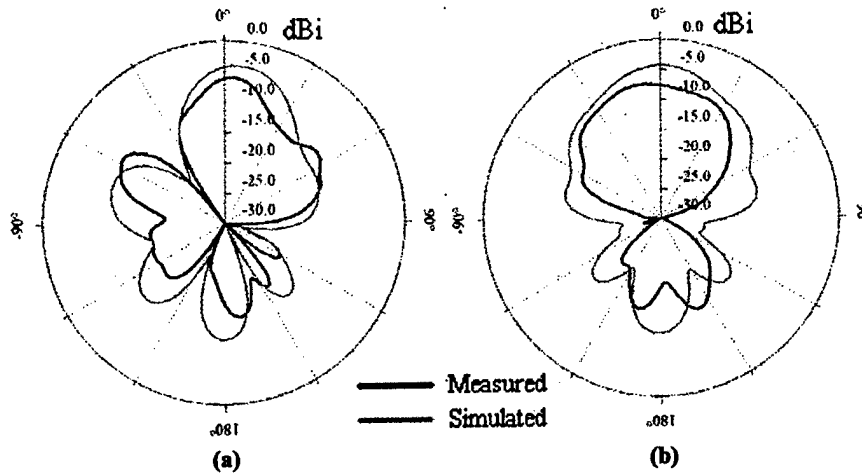


Fig. 13: Measured and simulated radiation patterns in the E-plane ($\phi=0^\circ$) (a) and H-plane ($\phi=90^\circ$) (b) of the embedded antenna assembly in concrete.

To determine the maximum possible range of the embedded assembly using an antenna with -7 dBi gain, the Friis Transmission Formula (Eq. (4)) was used [26]. This is the standard equation used for determining the received power in a typical line-of-sight wireless transmission. The following assumptions were made for these calculations:

- the embedded transceiver broadcasts (P_s) with 1 mW (0 dBm)
- receiver sensitivity (minimum P_L) is -80 dBm
- gain of the TX antenna (G_t) is -7 dBi
- gain of the RX antenna (G_r) is 6 dBi (typical patch antenna in air)
- mismatch factor (q_t) is 0.98 (found using the network analyzer)

$$P_L = \frac{\lambda^2}{(4\pi r)^2} e_t q_t D_t e_r q_r D_r |p_r \cdot p_t|^2 P_s \quad (4)$$

$$e_t D_t = G_t \quad e_r D_r = G_r \quad (5)$$

$$q_t = \frac{4R_A R_s}{|Z_A + Z_s|^2} \quad (6)$$

The maximum range found using Eq. (4) under these conditions would be 87 meters. For most bridge applications, this range will be perfectly adequate to send a signal between the embedded transmitter and the local base station.

3.5 Transceiver Selection

Based upon the previous choice to use the 2.4 to 2.5 GHz ISM band, a suitable transceiver was sought to allow proper control and up to 200 mW of output power. A transceiver from Aerocomm (AC5124C) was selected that offers a suitable package size with straightforward programming capabilities. It can transmit in 77 non-interfering channels using frequency hopping spread spectrum techniques. Each radio transceiver can be programmed to communicate with a specific module or modules using unique media access control (MAC) addresses. A development kit from the manufacturer enables transceiver programming as well as communication testing through a computer program. This program also contains a diagnostic tool that will repeatedly send prearranged packets back and forth between two radios to verify their operation. To verify that the embedded antenna transmits and receives data, one radio transceiver was connected to the embedded antenna inside the concrete block and a receiving antenna was attached to a simple monopole antenna in air. Placed 7 meters apart, the two devices exchanged data with a packet error rate of about 0.1%. This level of performance is more than adequate for this application based on the projected frequency of data collection and time between wireless transmissions.

4. Future Work

4.1 System-Level Design and Implementation

Completion of the project requires solutions to several system-level issues. We are currently designing wireless network configurations and system protocols that minimize the amount of time the modules must be fully powered. Additionally, we are implementing a suitable low-power microcontroller with adequate memory that will control both the sensing and communication aspects of module operation. Finally, we are investigating the inclusion of moldable gel battery packs and energy scavenging techniques to power the embedded sensors over the useful lifetime of the girder. We anticipate that local bridge base stations will be designed to blend in to the aesthetics of the structure and will be powered using rechargeable solar technology.

4.2 Accelerated Corrosion Tests and Transducer Configuration

To evaluate the ability of the proposed system to evaluate/characterize corrosion damage, accelerated corrosion tests are currently being conducted.

Prior to accelerated corrosion, each specimen has been cured for twenty-eight days and immersed in a 5% NaCl bath for an additional three days to ensure uniform moisture distribution. Then, a copper mesh is used as the cathode and the reinforcing tendon is used as the anode for the reaction. The voltage and current are continuously monitored to estimate the percentage of corrosion using Faraday's Law. The percentage of corrosion estimated in this way has been confirmed by actual measurements of the mass loss of the steel reinforcement after being removed from the surrounding concrete. To further develop the proposed sensing system, ultrasonic transducers will also be mounted orthogonal to the tendon (indirect transducer configuration) on a long continuous beam. Accelerated corrosion will again be induced at certain locations along the beam to confirm the effectiveness of the proposed system to remotely detect/characterize corrosion damage.

5. Conclusions

This work describes ongoing development of an embedded sensor system for the early detection and prevention of deterioration of the reinforcing steel tendons within concrete bridge girders. These devices will evaluate the condition of the steel tendon using ultrasonic techniques and then wirelessly transmit this data to the outside world without human intervention. These wireless embedded sensors are designed to present minimal volumes to maintain the structural integrity of the concrete girder. The work outlined here shows the feasibility of both the detection of tendon conditions as well as the wireless link that will enable communication of this data to the outside world. Using commercially available off-the-shelf components, implementation of these devices has the potential to save millions of dollars a year in evaluation, repair and replacement of reinforced concrete girders.

6. Acknowledgments

This material is based upon work supported by the National Science Foundation under grant number CMS-0201305.

7. References

- [1] T. P. Fuhr, T. P. Ambrose, D. R. Huston and A. J. McPadden, "Fiber Optic Corrosion Sensing for Bridges and Roadway Surfaces", Proceedings of the Smart Systems for Bridges, Structures, and Highways Conference, vol. 2446, San Diego, CA, 1995
- [2] C. W. Turner, M. Z. Arif and X. Xia, "Characterization of Concrete Structures by Acoustic Resonance Spectroscopy", IEEE Ultrasonics Symposium, pp. 1107-1110, 1994.

- [3] H. C. Rhim and O. Büyüköztürk, "Wideband Microwave Imaging of Concrete for Nondestructive Testing", *Journal of Structural Engineering*, vol. 126-12, pp. 1451-1457, 2000.
- [4] S. K. Sinha, A. J. Schokker and R. I. Shivprakash, "Non-contact Ultrasonic Imaging of Post-Tensioned Bridges to Investigate Corrosion and Void Status", *Proceedings of 2003 IEEE Sensors*, pp. 487-492, 2003.
- [5] R. Ross and M. Goldstein, "Monitor Warns of Bridge Corrosion", *Better Roads: Better Bridges*, August, 2003.
- [6] D. G. Watters, P. Jayaweera, A. J. Bahr and D. L. Huestis, "Design and Performance of Wireless Sensors for Structural Health Monitoring", *AIP Conference Proceedings*, May, 2002.
- [7] B. Carkhuff and R. Cain, "Corrosion Sensors for Concrete Bridges", *IEEE Instrumentation & Measurements Magazine*, June 2003, pp. 19-24, 2003.
- [8] P. L. Fuhr and D. Huston, "Corrosion Detection in Reinforced Concrete Roadways and Bridges Via Embedded Fiber Optic Sensors", *Smart Mater. Struct.*, vol. 7, pp. 217-228, 1998.
- [9] N. J. Carino, "Nondestructive Techniques to Investigate Corrosion Status in Concrete Structures", *Journal of Performance of Constructed Facilities*, vol. 13-3, pp. 96-106, 1999.
- [10] H. L. M. Reis and B. Ervin, "Detection of Corrosion in Reinforced Concrete Structures using an Ultrasonic Approach", *Technical Report UIUC ENG 03-3001*, University of Illinois at Urbana-Champaign, Urbana, Illinois, 2003.
- [11] M. Redwood, *Mechanical Waveguides*, New York: Pergamon Press Ltd., 1960.
- [12] H. Kolsky, *Stress Waves in Solids*, New York: Dover Publications, Inc., 1963.
- [13] J. L. Rose, *Ultrasonic Waves in Solid Media*, Cambridge: University Press, 1999.
- [14] B. Pavlakovic and M. J. S. Lowe, "Disperse User's Manual Version 2.0.11", Imperial College, University of London, 2001
- [15] B. Pavlakovic, M. J. S. Lowe and P. Cawley, "The Inspection of Tendons in Post-Tensioned Concrete Using Guided Ultrasonic Waves", *INSIGHT*, vol. 41-7, pp. 446-452, 1999.
- [16] W. Na, T. Kundu and M. R. Ehsani, "Ultrasonic Guided Waves for Steel Bar Concrete Interface Testing", *Materials Evaluation*, vol. 60-3, pp. 437-444, 2002.

- [17] J. L. Rose, "A Baseline and Vision of Ultrasonic Guided Wave Inspection Potential", *Journal of Pressure Vessel Technology*, vol. 124, pp. 273-282, 2002.
- [18] B. A. Auld, *Acoustic Fields and Waves in Solids: Volume II*, New York: John Wiley & Sons, 1973.
- [19] H. W. Chung, "Effects of Embedded Steel Bars upon Ultrasonic Testing of Concrete", *Magazine of Concrete Research*, vol. 30-102, pp. 19-25, 1978.
- [20] H. C. Rhim and O. Büyükoztürk, "Electromagnetic Properties of Concrete at Microwave Frequency Range", *ACI Materials Journal*, vol. 95-3, pp. 262-271, 1998.
- [21] J. Q. Howell, "Microstrip antennas", *IEEE Transactions on Antennas and Propagation*, vol. 23-1, pp. 90-93, 1975.
- [22] T. Huynh and K. F. Lee, "Single-layer single-patch wideband microstrip antenna", *Electronics Letters*, vol. 31-16, pp. 1310-1312, 1995.
- [23] S. Weigand, G. H. Huff, K. Pan and J. T. Bernhard, "Analysis and Design of Broadband Single-Layer Rectangular U-slot Microstrip Patch Antennas", *IEEE Transactions on Antennas and Propagation*, vol. 51-3, pp. 457-468, 2003.
- [24] Zeland Software, IE3D[®], Version 8.0, 1999.
- [25] Ansoft Corporation, HFSS[®], Version 9.1.
- [26] J. Griffiths, *Radio Wave Propagation and Antennas*, Englewood Cliffs, New Jersey: Prentice-Hall International, 1987.

Parameter Study of a Single Isolated Element and Infinite Arrays of Balanced Antipodal Vivaldi Antennas

M. W. Elsallal and D. H. Schaubert

Center for Advanced Sensor and Communications Antennas

Department of Electrical and Computer Engineering

University of Massachusetts, Amherst, MA 01003

w.elsallal@ieee.org and schaubert@ecs.umass.edu

Abstract: The Balanced Antipodal Vivaldi Antenna (BAVA) is studied to determine its characteristics and to develop design data. Single elements operate well as traveling-wave-like antennas, and they may be useful in small arrays. In large arrays, modeled here as infinite arrays, numerical simulations show that three operating bands may be possible, and that impedance anomalies bound the most useful operating band. The parameter studies indicate some control of the anomalies is possible. Predicted array bandwidths of 1.4:1 have been achieved concurrently with a second, low-frequency operating band.

1. Introduction

As electronic systems have gained the capability to operate over wider bandwidths and as military and civilian operations have become more dependent on RF and microwaves for communication and sensing, the demand for wideband and multiband antennas has increased. Furthermore, high performance antennas often require electronic beam steering, which necessitates a phased array. The Vivaldi antenna, first appearing in 1979 [1], has been the initiative for the research towards a wide bandwidth single element radiator. Several generations of this antenna has been developed such as the Linear Tapered Slot Antenna (LTSA), Constant Width Slot Antenna (CWSA), Broken Linear Tapered Slot Antenna (BLTSA) [2]. The Bunny Air Antenna has also shown appreciable bandwidth [3]. For multi-band, widescan and dual polarized phased array antenna systems, exponentially flared versions of the stripline-fed notch [4] have been developed and are the dominant solution for multioctave scanning arrays. The design of these antennas has been aided by modern computational tools, which have enabled parameter studies that elucidate performance and that lead to design curves [5].

The Antipodal Vivaldi Antenna (AVA) was introduced in 1988. The AVA utilizes a tapered transition from microstrip to antipodal slot line [6]. However, the antipodal conductors cause the electric field vector to skew, producing a cross-polarized field, even in the boresight direction, that is not constant over the operating bandwidth. The Balanced Antipodal Vivaldi Antenna (BAVA) eliminates the boresight cross-polarization by using a triplate structure [7]. The BAVA uses an exponential flare into a three conductor slotline to slowly rotate the opposing electric field vectors of the triplate (stripline) mode into substantially parallel vectors for which the cross-polarized portions cancel, in the boresight direction. Hall's work on the BAVA is limited to single elements and linear arrays. No published data has appeared for the BAVA in a planar array environment as would be used to achieve an ultra-wideband, widescan and dual polarized phased array system. Munro [8] has studied the BAVA in an infinite array, but those results were not published outside reference [8] because experimental results for small arrays seemed to be at odds with predictions from numerical simulations. Today, computational EM tools are available to replicate Munro's work and to extend it to more thoroughly study BAVA arrays. An error in Munro's work as reported in [8] has been discovered, eliminating the discrepancy with experiments. This paper reports the results of an initial study intended to better understand the performance of these antennas and to develop design guidelines. Although this goal is not yet fully met, several useful insights have been gained and are presented.

2. Design Parameters and Method of Analysis

The design parameters of the BAVA are defined in Figure 1. The configuration uses two arcs and an exponentially tapered curve. The arcs are elliptical transitions forming a balun that is compromised of two quarter ellipses with vertical axes, Cr2 and Cr3, and horizontal axes, Cr1 and Cr4. For all of the data presented here, $Cr2 = Cr3 = (Ha - Fw)/2$. The metallic BAVA fins, therefore, have a vertical edge of length $G = (B - Ha)/2$. The tapered curve is an exponential transition with an opening rate, R, so that the curve is defined by the equation:

$$y = c_1 e^{Rz} + c_2 \quad (1)$$

where

$$c_1 = \frac{y_2 - y_1}{e^{Rz_2} - e^{Rz_1}} \quad (2)$$

$$c_2 = \frac{y_1 e^{Rz_2} - y_2 e^{Rz_1}}{e^{Rz_2} - e^{Rz_1}} \quad (3)$$

where (y_1, z_1) and (y_2, z_2) are points at the start of the curve and the aperture, respectively.

The antenna has an aperture height, H_a , which can be smaller than the element height, B . In an array environment, the parameter $A = H$ -plane spacing and $B = E$ -plane spacing. Substrate parameters define the dielectric properties, namely the dielectric permittivity, ϵ_r , and substrate thickness, t .

Three different electromagnetic computational tools were employed to compute the input impedance and the radiation patterns. The primary computational tools for the simulations presented here are Ansoft HFSS [9] that uses Finite Element Method (FEM), and CST Microwave Studio that uses the Finite Integral Time domain (FIT) solver [10]. A code that was developed at the Antenna Lab of the University of Massachusetts [11, 12], which is a Frequency Domain-Method of Moments (FD-MoM), has been used to verify the infinite array results from HFSS and CST. All simulated designs were excited using a stripline port normalized to 50Ω .

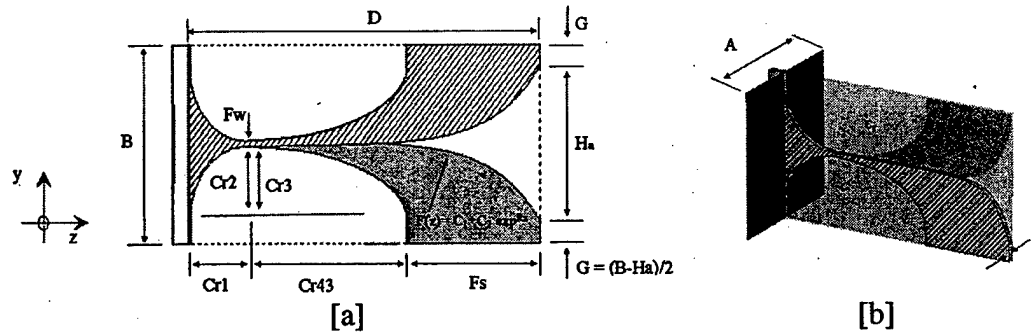


Figure 1: Structure of the Balanced Antipodal Vivaldi Antenna (BAVA). [a] Top view with all metal parameters. The hatched area is on the surface of the substrate and forms the ground plane of the stripline in the feed region. An identical conductor is located at the lower surface of the substrate. The lightly shaded area represents a conductor embedded in the middle of the substrate and forms a tapered stripline transmission line in the feed region. [b] Isometric view showing the substrate parameters.

3. Single Element Study

A common approach to the design of narrow bandwidth arrays begins with an examination of an isolated element. Although mutual coupling effects contribute

significantly to phased array performance, especially wide bandwidth arrays, the study of isolated elements, sometimes provide insights into array performance, as well as quantifying the element behavior. Munro and Schaubert have parameterized a number of isolated elements by tailoring the opening rate and studying the radiation pattern behavior with and without a ground plane [8]. Because of the relevance of that work to this study, some of their results have been reproduced and are shown here.

The fixed parameters used for the studies reported in this section are listed in the table below.

Table 1: Fixed Parameter Values for Isolated BAVA element

Cr1	1.39 cm
Cr2	1.39 cm
Cr3	1.39 cm
Cr4	4.01 cm
Fs	1.50 cm
D	6.90 cm
t	0.158 cm
ϵ_r	2.32
Fw	0.121 cm
Ha	2.90 cm
G	0.0 cm
B	2.90 cm

Three features of the single, isolated BAVA are:

- As the opening rate decreases, the lowest frequency at which the VSWR achieves useful values also decreases. However, there is a large hump in the VSWR plot that eliminates frequencies above the initial operating band, Fig. 2a. At frequencies above this hump, lower opening rates offer more usable bandwidth than higher rates.
- The beamwidth of the radiation pattern broadens and the gain decreases as the opening rate increases, Fig. 2b and Fig. 3.
- Adding a ground plane behind the BAVA eliminates the backward radiation, but introduces reflection nulls and impacts the beamwidth, Fig. 4.

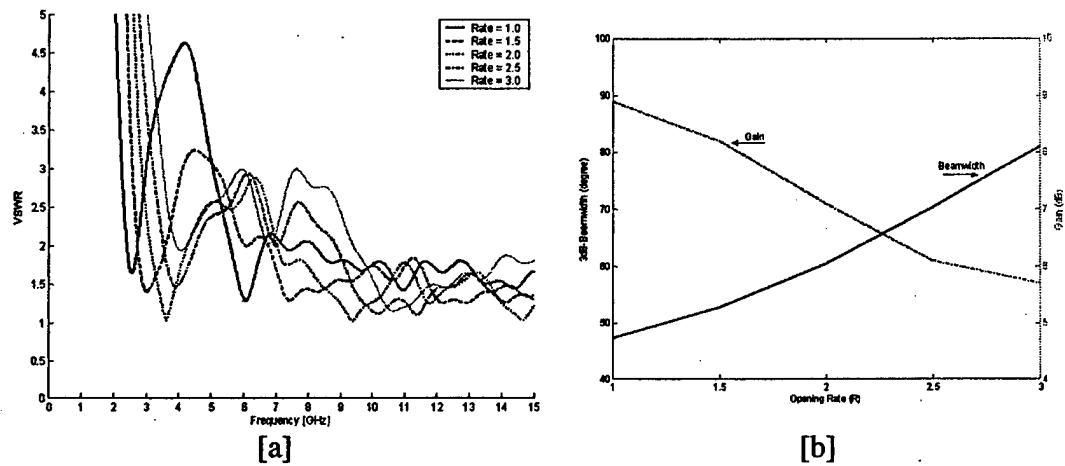


Figure 2: Effect of opening rate (R) on performance of an isolated BAVA. [a] VSWR. [b] Beamwidth and gain performance at 12 GHz. R=1.0, 1.5, 2.0, 2.5 and 3.0

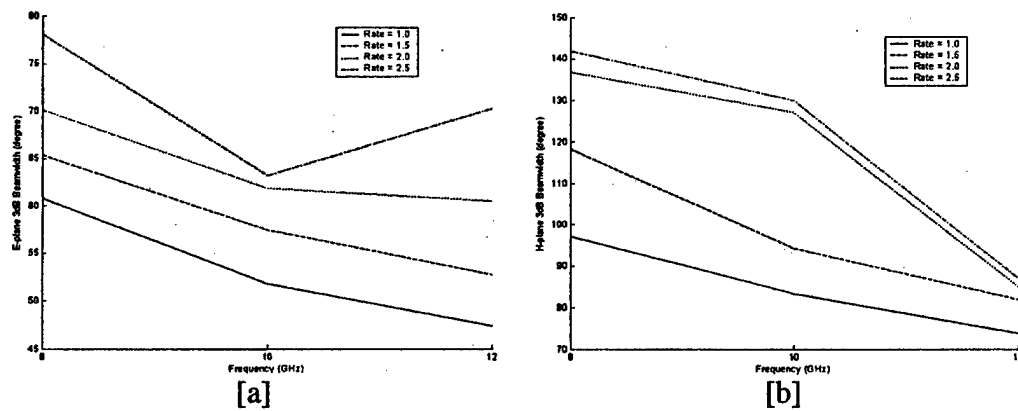
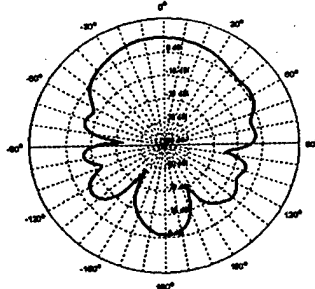
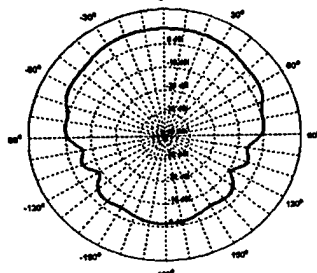


Figure 3: Radiation pattern beamwidths vs. operating frequency. [a] E-plane. [b] H-plane. R=1.0, 1.5, 2.0 and 2.5

Without a Ground Plane

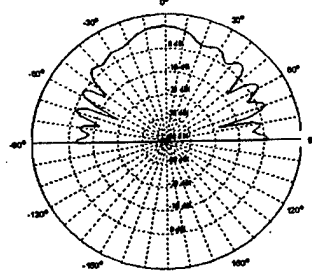


[a]

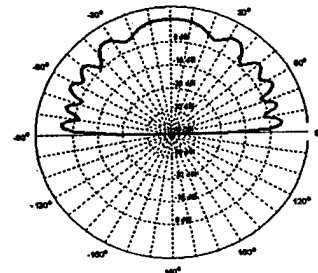


[c]

With a Ground plane



[b]



[d]

Figure 4: Effects of ground plane on radiation pattern. [a] and [b] E-plane. [c] and [d] H-plane. $R=2.0$.

The BAVA shown in Fig. 5 was built on RT/duriod 5870 substrate with a relative dielectric constant of 2.32 and total thickness of 62 mils. The input impedance of the fabricated element measured from 0.5 to 15GHz depicts periodic peaks of the resistance and oscillations of the reactance. This behavior is typical in wideband BAVAs. From 6 to 15GHz, the VSWR is less than 2.1, with a mean value of about 1.5. From 3 to 6 GHz, the VSWR is generally better than 2.5, and could be improved by another design iteration. The figure also demonstrates a good agreement between results from measurements and simulation using HFSS and CST.

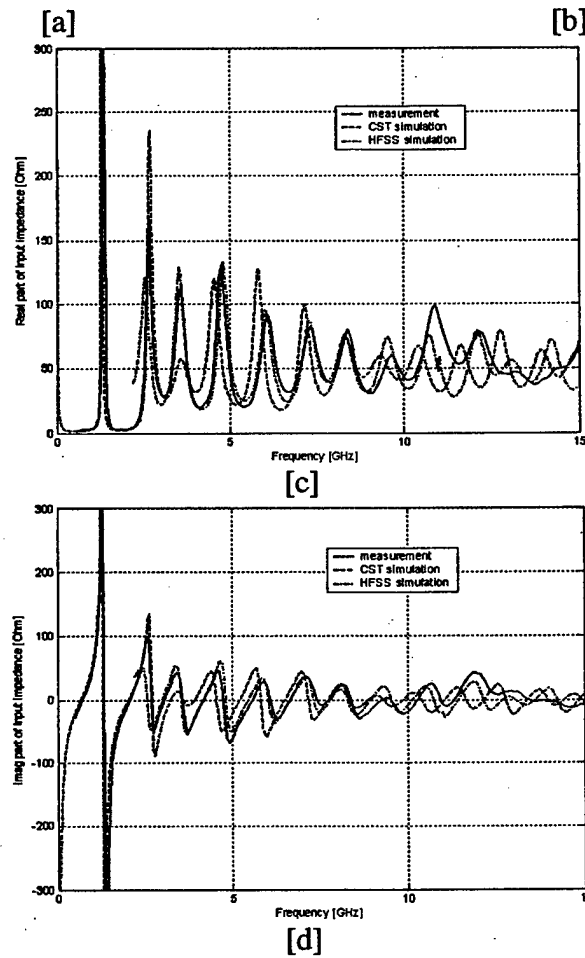
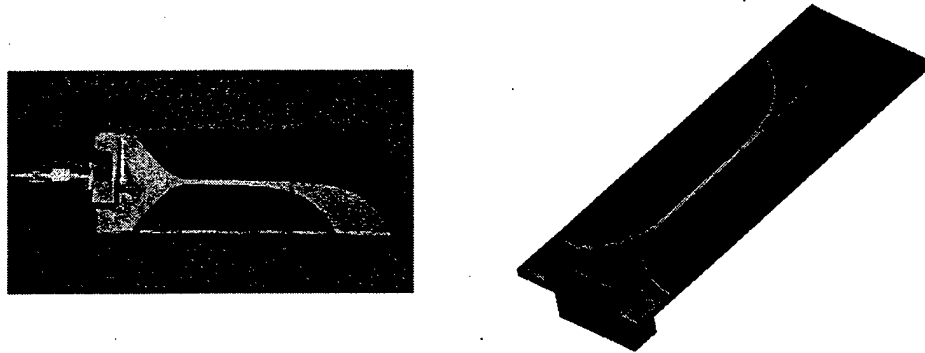


Figure 5: Measured and computed performance of an isolated BAVA. [a] Photo of the element. [b] Model used for simulation in CST and HFSS. [c] Resistance. [d] Reactance. $R=2.0$. Note: The reference plane for these impedances is at the end of the 1.5-cm stripline section visible in (a) and (b), i.e., at edge of substrate.

It is typical for single notch antennas to have a low frequency cut-off when the aperture height, H_a , equals to $\lambda_{\max}/2$ or when the antenna depth, D , is less than 1-2 times λ_{\max} , where λ_{\max} is the low frequency's wavelength. The optimized BAVA design whose calculated VSWR is depicted in Fig. 6 has $H_a = 4 \text{ cm} = 0.6$ wavelength at 4.5 GHz, where the antenna begins its continuous operating band. Except for a region near 16 GHz, the VSWR is less than 2 up to 20 GHz.

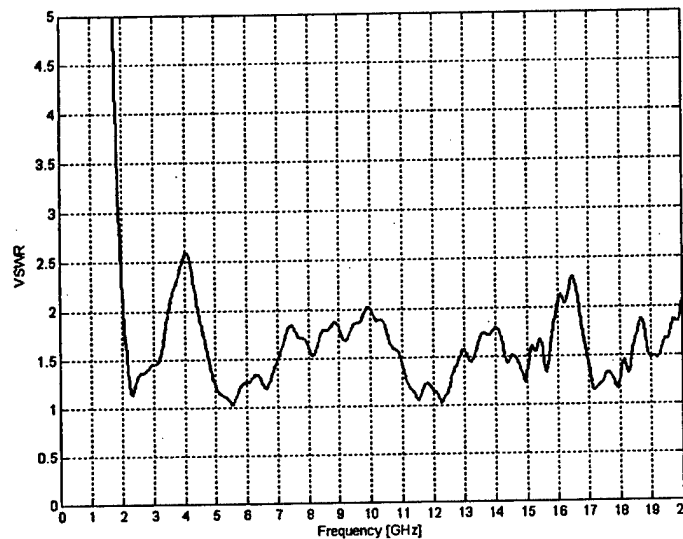


Figure 6: Calculated VSWR of an optimized design of balanced antipodal Vivaldi antenna (BAVA) isolated element. $t = 0.316 \text{ cm}$, $\epsilon_r = 6.15$, $F_w = 0.103 \text{ cm}$, $R = 1.75$, $B = H_a = 4.0 \text{ cm}$, $G = 0.0 \text{ cm}$, $Cr_1 = 6.1 \text{ cm}$, $Cr_2 = Cr_3 = 1.94 \text{ cm}$, $Cr_4 = 2.0 \text{ cm}$, $F_s = 3.0 \text{ cm}$, and $D = 11.1 \text{ cm}$.

4. Subarray of Balanced Antipodal Vivaldi Antennas

A five-element, E-plane linear array was fabricated using RT/duriod 5870 laminate. The 5-port scattering matrix was measured and used to compute the active reflection coefficient, Fig. 7. The radiation pattern of the fully driven array is almost symmetric in the E-plane and H-plane. The E-plane half-power beamwidth is approximately 45 degrees while it is about 140 degrees in the H-plane and the computed active gain of the linear array is about 7.0dB at 3.0GHz.

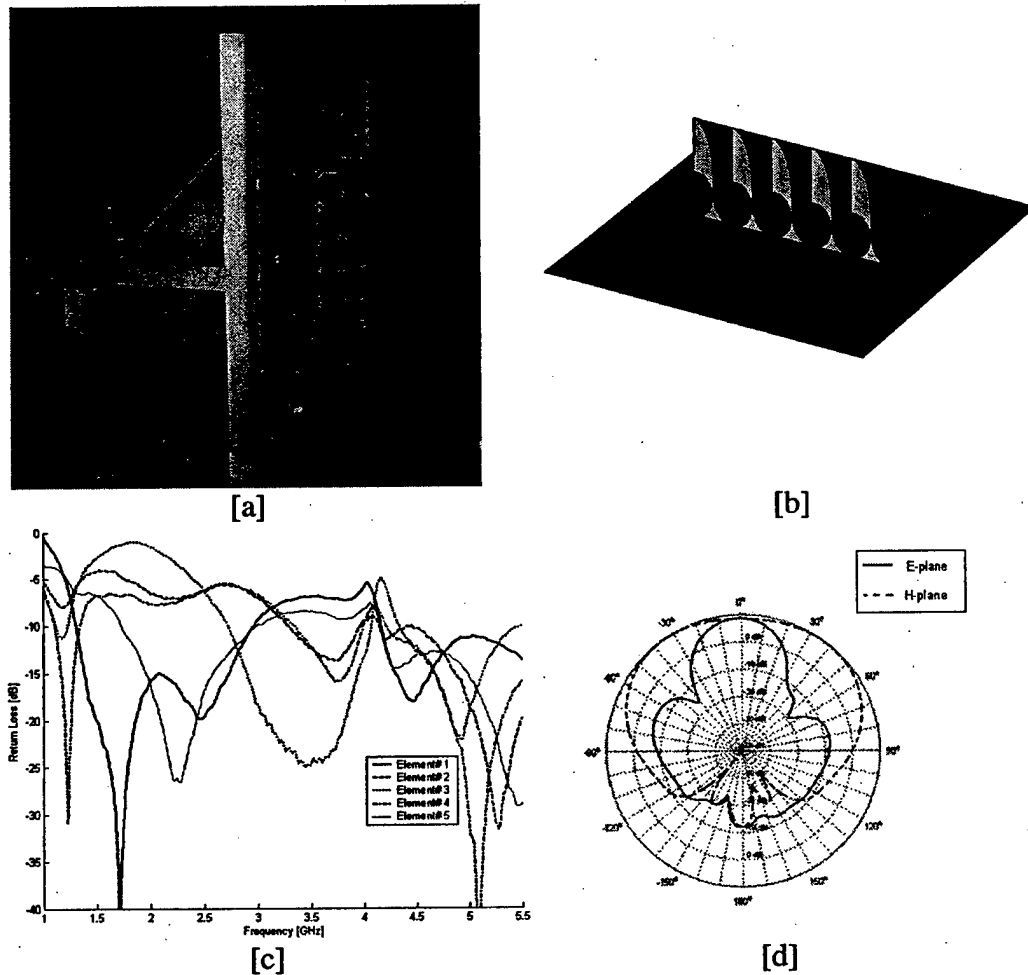


Figure 7: The performance of 5x1 linear BAVA subarray. [a] Photo of subarray. [b] Rendering of subarray model used in the CEM simulator. [c] Active return loss from measured [S] parameters (broadside beam). [d] Simulated E and H-plane radiation pattern of the array when all elements are excited at 3.0 GHz.

The design parameters for the elements are listed in the table below.

Table 2: Design Parameter Values for BAVA element in 5x1 Linear Array

Cr1	1.10 cm	Fs	2.70 cm	Fw	0.121 cm
Cr2	1.10 cm	D	4.90 cm	Ha	2.40 cm
Cr3	1.10 cm	R	1.20	G	2.40 cm
Cr4	1.10 cm	t	0.158 cm	B	3.00 cm
		ϵ_r	2.32		

Fig. 8, Fig 9 and Fig. 10 show that simulations with HFSS and CST agree reasonably well with measurements.

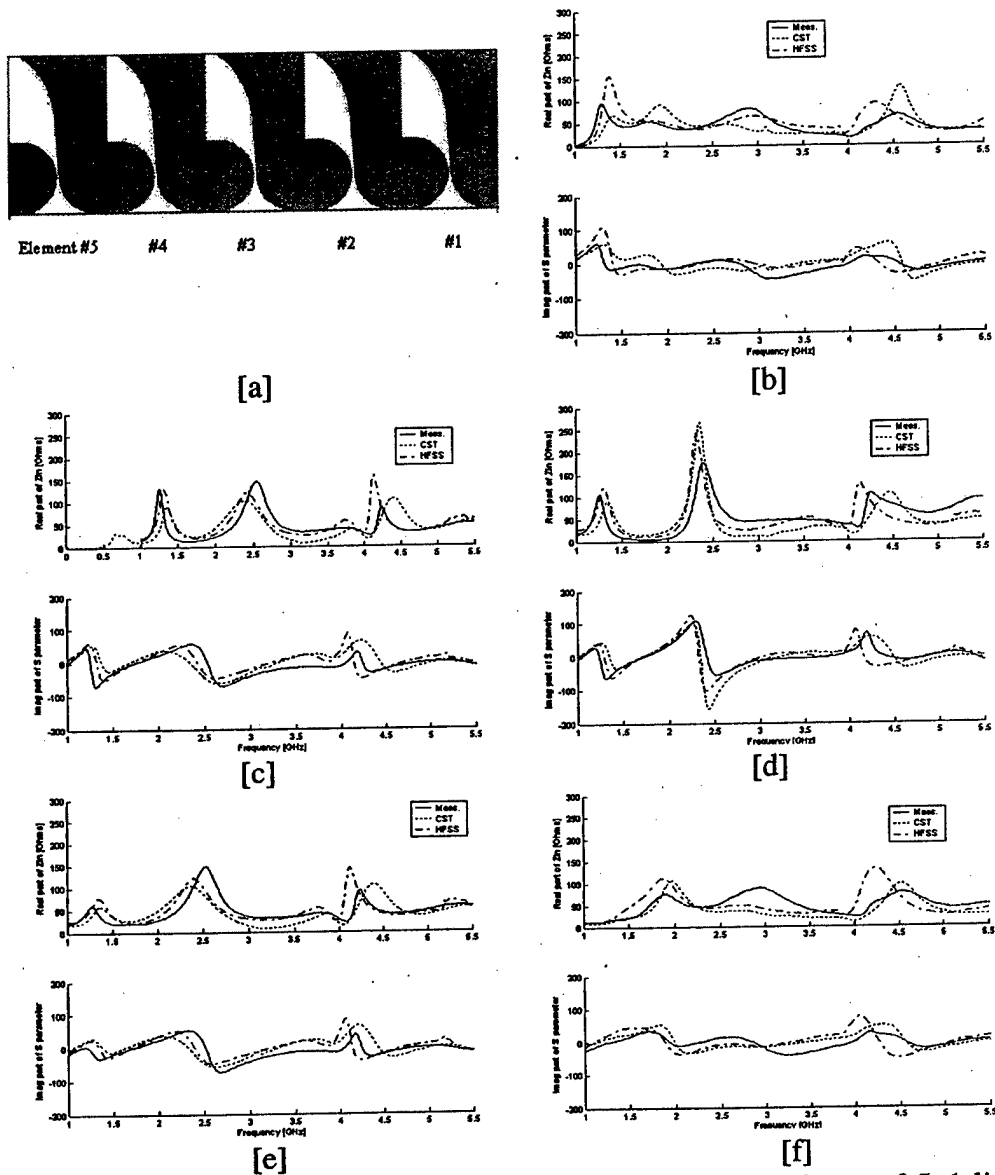


Figure 8: A comparison between broadside active input impedance of 5x1 linear subarray obtained from measured [S]-parameters and HFSS and CST simulations. [a] Element arrangement in subarray. [b] Element # 1. [c] Element #2. [d] Element #3. [e] Element #4. [f] Element #5.

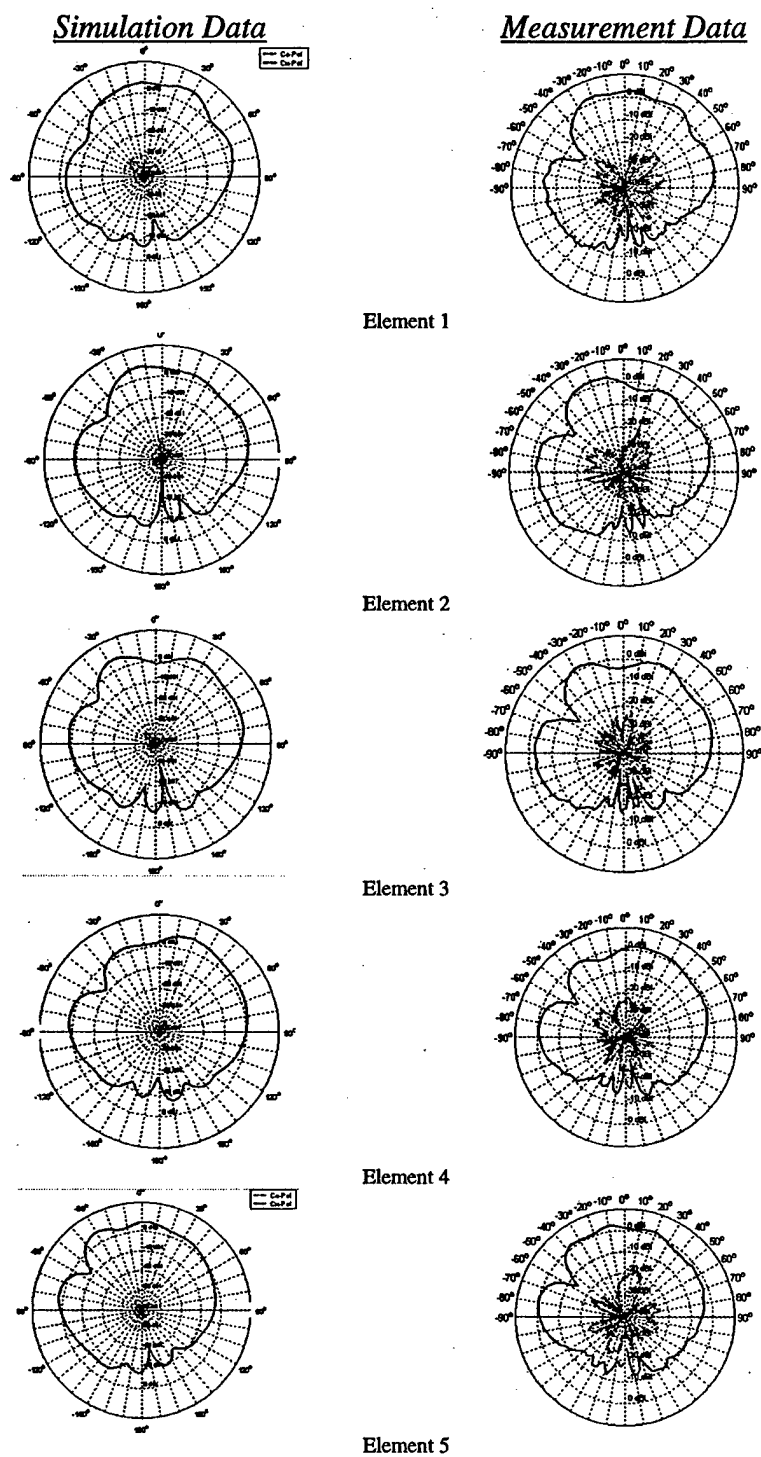


Figure 9: Comparison of E-plane embedded element patterns obtained from measured data and HFSS simulations at 2.8 GHz. Dashed is x-pol.

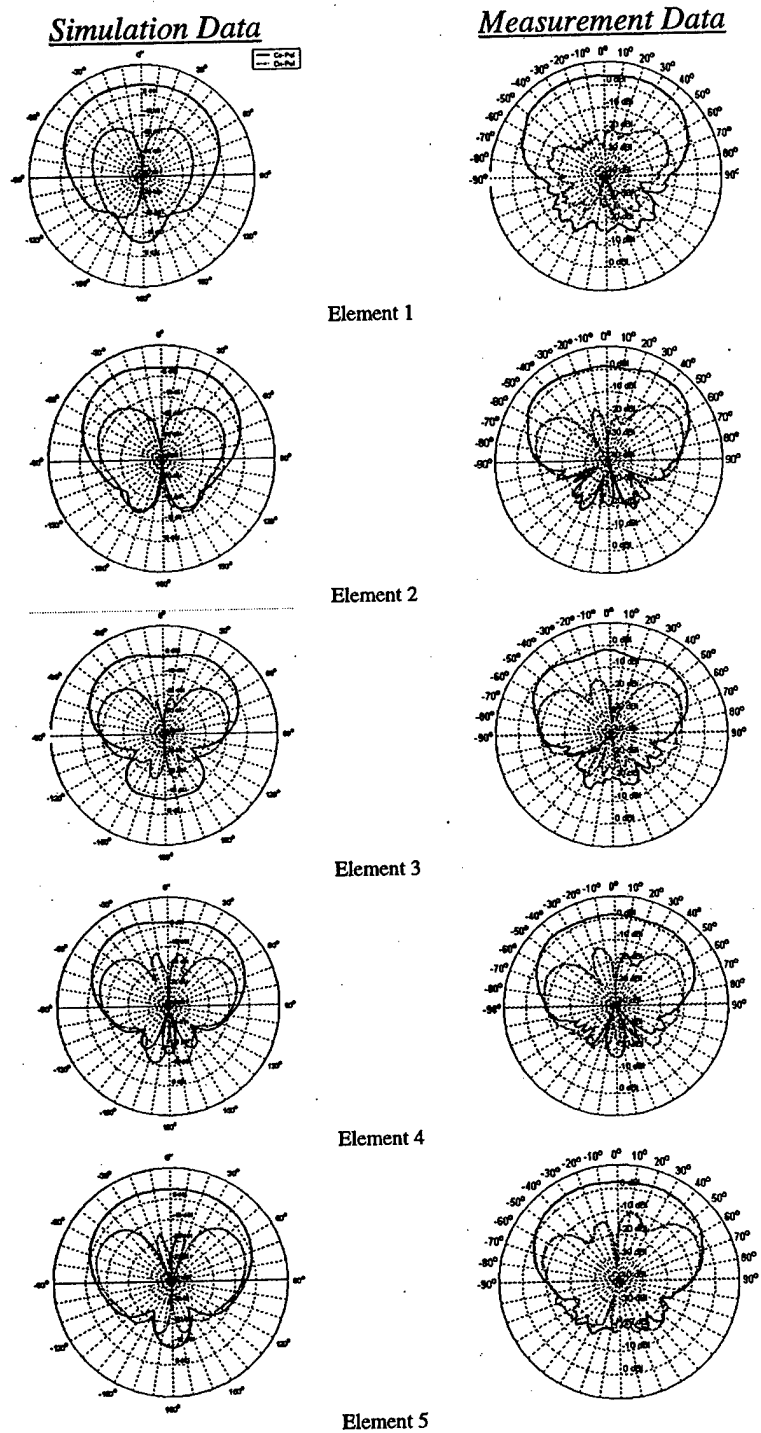


Figure 10: Comparison of H-plane embedded element patterns obtained from measured data and HFSS simulations at 2.8 GHz. Dashed is x-pol.

Referring to the data collected from the measurement and simulations:

- Results from the HFSS and CST computational models qualitatively agree with the measured data.
- The embedded E-plane pattern is slightly skewed. It has a dip at 55 degrees that disturbs the symmetry of the pattern, but it is better than AVA antennas where a pattern dip occurs at 40 degrees [6, 7, 13].
- The BAVA elements are not symmetric, i.e., the inner fin is completely embedded in dielectric whereas the outer fins lie on the surface of the substrate. Therefore, the return losses of elements #1 and #5 are not equal and the radiation patterns are not mirror-symmetric.
- The anomaly that occurs consistently in all of the 5 elements around 4.0 GHz may be a self-induced anomaly since it also shows up in the reflection coefficient of the isolated element as seen Fig 11.

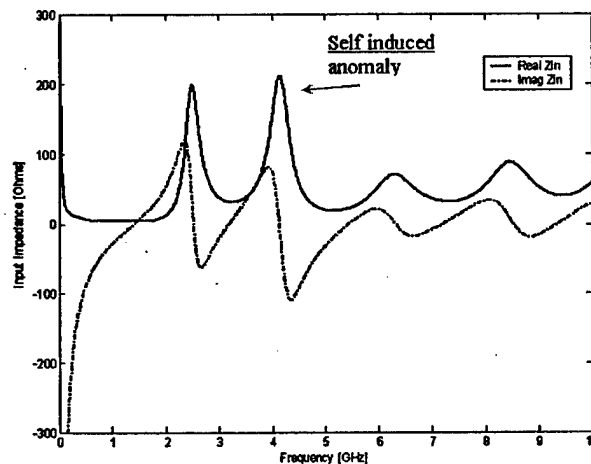


Figure 11: Input impedance of an isolated element taken from the 5x1 linear subarray.

5. BAVA in an Infinite Array Environment

The single, isolated BAVA has radiation and impedance characteristics that suggest it may be useful as an element in a wide bandwidth array. In this section, a computational study of the BAVA in an infinite array is described. The impact

of four key design parameters is illustrated by means of parameter studies. These studies recall that the desirable characteristics of single elements, as described in this paper and elsewhere [7, 14, and 15], may be overwhelmed by anomalies. In the early development of Vivaldi arrays, anomalies often were encountered [5], but eventually many of them were understood and can be avoided, for example [16].

It is worthy to note that the asymmetric nature of the BAVA antenna (center conductor inside the dielectric substrate and outer conductors exposed to air) makes this antenna unsuited for phased array simulation in a metallic waveguide [17]. The asymmetry of a BAVA array and the mirror symmetry of a waveguide simulator are depicted in Fig. 12. Because a BAVA array cannot be simulated in a waveguide, the only means to assess the performance of a large array, other than building the array, is by using computational models as is done in this paper.

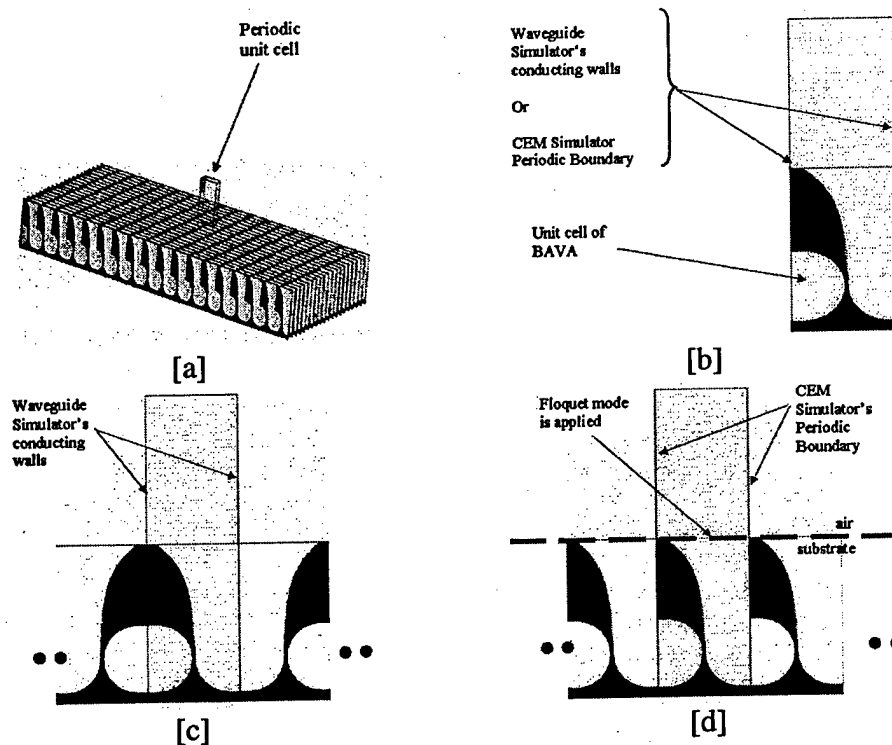


Figure 12: Infinite array evaluation in waveguide and CEM simulators. [a] Sketch of large array of BAVA with periodic unit cell around the central element. [b] Single BAVA element used in a periodic unit cell of a waveguide and CEM simulator. [c] Equivalent infinite array of BAVA represented by the waveguide simulator. [d] Equivalent infinite array of BAVA represented by CEM models.

Because it is not practical to experimentally validate computed results for large, finite BAVA arrays, the results presented here have been checked by comparison of results from two or more different CEM tools.

a. Wideband Balun's Design

In order to accurately evaluate the effect of the design parameters (F_s , B , H_a , and R) the transition from stripline to triline must be designed to have minimum effect on the behavior of the BAVA. A stripline-triline-stripline test circuit was modeled and the results shown in Fig. 13 demonstrate that the computed input impedance on low permittivity substrate ($\epsilon_r = 1.0$ and $\epsilon_r = 2.32$) is not significantly affected by the balun. In this paper, a fixed design of the balun section of the BAVA is used in all the simulations, $Cr1 = Cr2 = Cr3 = Cr4 = 1.7\text{cm}$. This results in a semicircular arc at the balun.

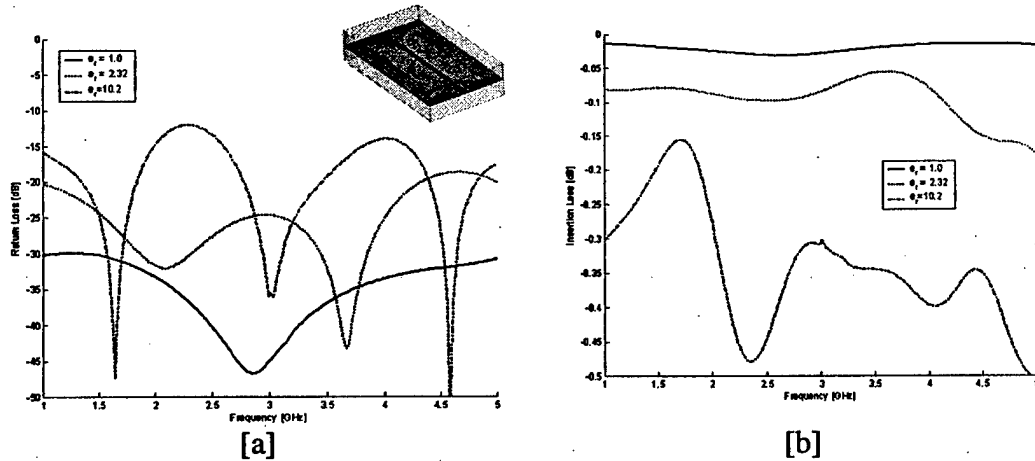


Figure 13: Stripline-triline-stripline transition test circuit. [a] Return loss. Insert is the HFSS model. [b] Insertion loss. $t = 0.158\text{cm}$, $\epsilon_r = \{1.00, 2.32 \text{ and } 10.2\}$ and $F_w = \{0.226, 0.121 \text{ and } 0.0286\}\text{cm}$ respectively, $B = 4.53\text{cm}$, $Cr1 = Cr2 = 1.7\text{cm}$. The length of the triline section is 3.00cm .

b. Discussion of the Results of Infinite Array Analysis

The design parameters can be classified into three categories, *substrate*, *array* and *element*, as illustrated in Fig. 14.

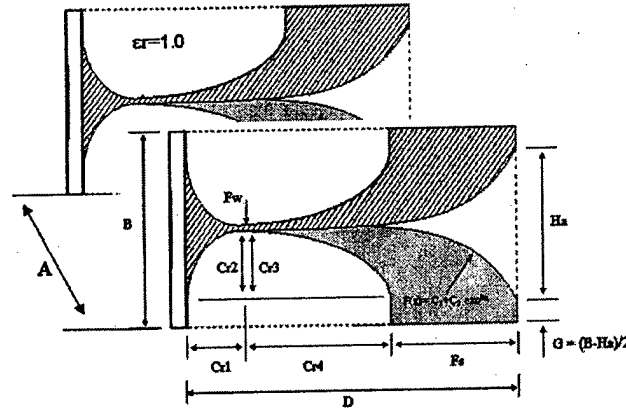


Figure 14: Element, Array and Substrate parameters.

Substrate parameters (ϵ_r and t): In order to minimize the number of parameters under study and to eliminate the uncertainty that is associated with guide wavelength of an inhomogeneous structure, the substrate was fixed to free space with a thickness $t = 0.158\text{cm}$. Based upon previous studies of Vivaldi antenna arrays, it is expected that the salient trends of dielectric-loaded BAVAs will be similar to those of the dielectric-free antennas. The impact of substrate permittivity can be evaluated in a future study.

Array parameters (A and B): The H-plane spacing, A , and E-Plane spacing, B , determine the frequencies at which grating lobes enter real space and also affect mutual coupling. Furthermore, note that the metallic fins are affected by the E-plane spacing because the straight section of length G must satisfy $G = B - H_a$.

Element parameters ($Cr1$, $Cr2$, $Cr3$, $Cr4$, Fw , Fs , H_a , B , R and D): These parameters have the greatest impact on the shape of the metallic fins. In this paper, only Fs , B , H_a and R are explicitly varied. Note that D varies with Fs , so there is an implicit variation of D in the parameter study of Fs . As noted earlier, $Cr1=Cr2=Cr3=Cr4=1.7\text{cm}$ for the studies here. Also, $Fw = 0.226\text{cm}$.

The fixed parameters used for the studies reported in this section are listed in the table below.

Table 3: Fixed Parameter Values for Infinite BAVA Array Studies

Cr1	1.7 cm	t	0.158 cm
Cr2	1.7 cm	ϵ_r	1.0
Cr3	1.7 cm	Fw	0.226 cm
Cr4	1.7 cm	A	4.53 cm

Since this study was motivated by the work of Munro [8], the BAVA design from that work is used as a starting point for the analyses presented here. Fig. 15 depicts the performance of this antenna, for which four anomalies are observed at 2.18 GHz, 3.26 GHz, 3.94 GHz, and 4.4 GHz. The antenna has two operational (VSWR < 2:1) bands at 0.5 GHz and 2.6 GHz. For each of these operating bands, the bandwidth is $F_H/F_L \sim 1.25$. The grating lobes enter visible space when the array operates at 3.31 GHz, above the frequency of Anomaly #2.

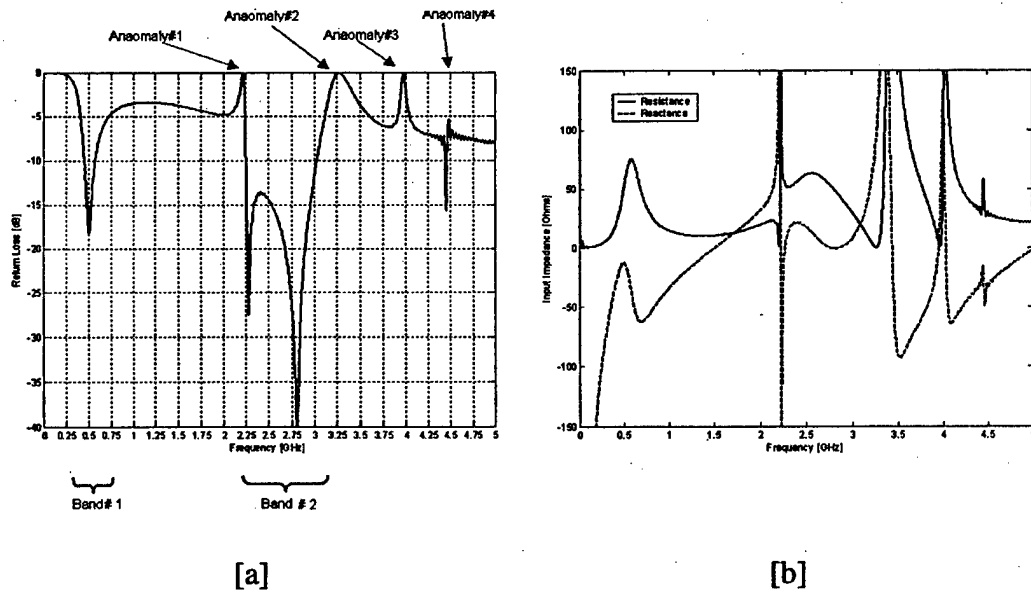


Figure 15: Performance of Munro's BAVA infinite array. [a] Return loss. [b] Input impedance. $R=0.7$, $B=4.53\text{cm}$, $H_a=3.525\text{cm}$, $G=0.5025\text{cm}$, $F_s=4.1\text{cm}$, and $D=7.5\text{cm}$.

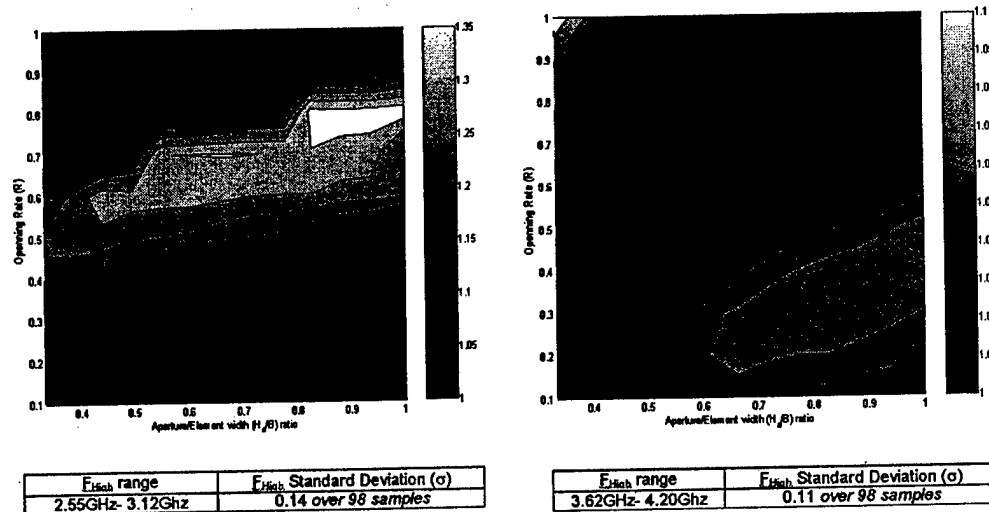
The studies that follow relate particularly to the two operating bands identifiable in Fig. 15. The lower operating band, near 0.5 GHz, is relatively independent of the parameters studied so far. The other operating band is limited by anomalies #1 and #2, and potentially by the onset of grating lobes, if Anomaly #2 can be moved above 3.31 GHz. For some parameter values, the return loss between anomalies #2 and #3 is greater than 10 dB, allowing a third operating band. Although this is above the frequency corresponding to 0.5-wavelength element spacing, it may be useful for applications that require only limited scanning.

In this paper, the parameter study of infinite arrays of BAVAs is conducted for several values of B , H_a , R , and F_s , so the entire test set consists of 108 test cases.

All input impedance data shown here are for the antenna operating in an infinite array with broadside beam and the array has a ground plane at the base of the elements.

- Opening Rate (R) and Aperture Height (Ha)

The design presented in figure 15 has been parameterized for a set of opening rates, R, and aperture heights, Ha. The positions of all four anomalies are approximately independent of those two parameters, but the shape and depth of the curve between the anomalies is affected. Therefore, the operational bandwidth of the array can be altered by proper choice of R and Ha. Fig. 16 shows contour plots of the bandwidth ratio F_H/F_L versus R and Ha. Lighter colors mean the array has more bandwidth. Fig. 16a relates to the operating band between anomalies #1 and #2, whereas Fig. 16b relates to the operating band between anomalies #2 and #3. Since the anomaly locations are not particularly sensitive to R and Ha, the highest frequency of each band does not change dramatically over the range of these parameters, as indicated in the tables with each plot.



[a]

[b]

Figure 16: Design guide to achieve maximum bandwidth from Ha and R parameter study. Contours define constant values of F_{High}/F_{Low} ratio for each operating band. [a] Band #2. [b] Band #3. $R=0.7$, $B=4.53\text{cm}$, $F_s=4.1\text{cm}$, $D=7.5\text{cm}$, $H_a=\{4.53, 4.25, 4.00, 3.75, 3.525, 3.25, 3.00, 2.75, 2.5, 2.25, 2.00, 1.75, 1.5\}$ and $R=\{0.1, 0.2, 0.3, 0.4, 0.5, 0.6, 0.7, 0.8, 0.9 \text{ and } 1.0\}$.

The results of the R and Ha study can be summarized as follows:

Band 1, near 0.5 GHz

Although the data for this operating band are not shown in Fig. 16, Band 1 has a relatively constant bandwidth $F_H/F_L \sim 1.2 - 1.3$.

Band 2, between Anomalies #1 and #2

The largest bandwidth is obtained when the element's aperture height, H_a , is at least 0.85 times the E-plane spacing in the array. That is, the section labeled G in Fig. 14 should be small. The associated opening rate is approximately 0.8. Good performance can be obtained for values of H_a that are as small as 0.5B if the opening rate is reduced to about 0.6. For all cases depicted in Fig. 16a, no grating lobe is present.

Band 3, between Anomalies #2 and #3

If operation above the frequency corresponding to 0.5-wavelength element spacing is allowed, bandwidth on the order of 5 per cent can be achieved in this band. However, these bandwidths are not achieved for the same set of R and H_a that yield good performance in Band 2. Hence this operating band may not be useful unless a different set of fixed parameters can be found to allow simultaneous operation in both Bands 2 and 3.

Within each of the operating bands, the radiated field is linearly polarized in the boresight direction, as expected.

- **Element height (B)**

The antenna height, B, defines the E-plane spacing of the elements in the array. Fig. 17 shows the return loss of a BAVA as the element height increases from 3.6 cm to 4.53 cm.

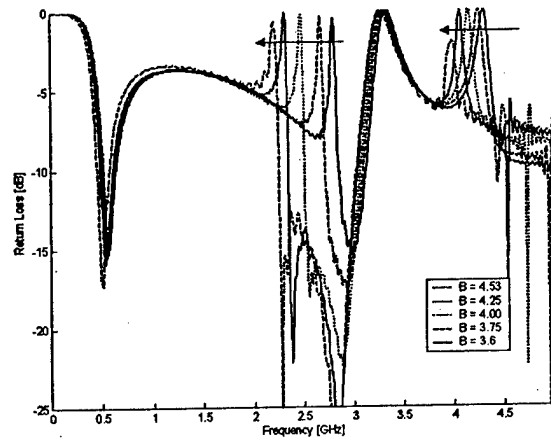


Figure 17: Variation of return loss with element height. $R=0.7$, $F_s=4.1$ cm, $D=7.5$ cm, $H_a=3.525$ cm, and $B=\{3.6, 3.75, 4.0, 4.25 \text{ and } 4.53\}$.

These results are summarized as follows:

Band 1, near 0.5 GHz

This operating band is affected only slightly by the element height.

Band 2, between Anomalies #1 and #2

Anomaly #1 moves lower in frequency as B increases and the impedance match is good throughout Band 2. Therefore, increasing B increases the usable bandwidth of Band 2. The maximum value of B shown in Fig. 17 is 4.53 cm, which is equal to A. This value of element spacing results in grating lobe onset at 3.31 GHz.

Band 3, between Anomalies #2 and #3

This band is not usable for the particular parameters chosen here.

Since anomaly #1 has a large impact in the bandwidth of Band 2, it would be useful to understand its cause and then to eliminate it. (Anomaly #2 occurs relatively near the frequency corresponding to the onset of grating lobes, so it is not so crucial to the bandwidth performance of the array.) So far, we have not

identified a single parameter or a useful relationship that controls the frequency of anomaly #1. For the particular parameters used in Fig. 17, anomaly #1 corresponds closely with the frequency at which the open circular region near the balun is one wavelength in circumference. The parameter variation in Fig. 17 is achieved by increasing the length G (see Fig. 14) while keeping all other parameters constant. Increasing G also increases the circumference of the loop.

At anomaly #1, there is a strong current flowing around this region and the currents on all three conductors of the triline section of the balun are approximately in phase instead of resembling the desired transmission line mode, Fig. 18. This suggests that a loop resonance of this region may contribute to anomaly #1. However, anomaly #1 has been found to be sensitive to H-plane spacing, A , of the array, so this loop resonance cannot be determined from only the physical size of the region.

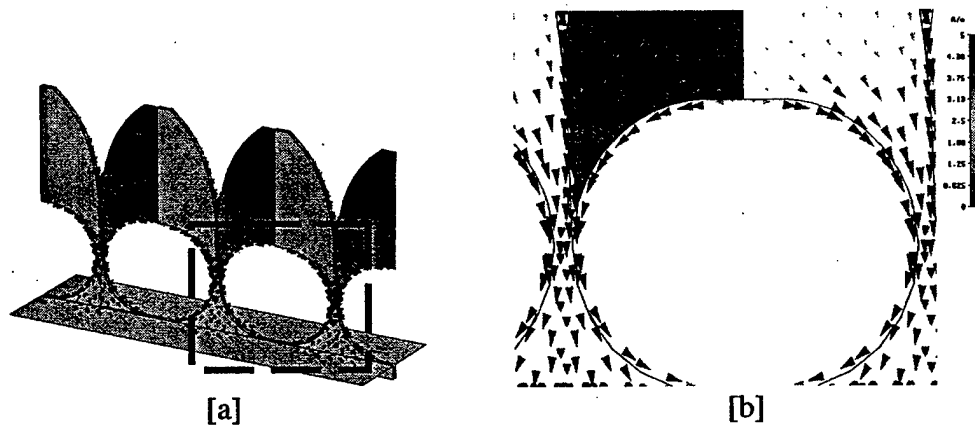


Figure 18: Surface current density of BAVA in an infinite array, 2.2GHz. The lightly shaded area is on the surface of the substrate. The dark area is the conductor embedded in the middle of the substrate. [a] A unit cell of 3-elements within an infinite array environment. [b] An enlarged window as marked in (a). $R=0.7$, $F_s=4.1\text{cm}$, $D=7.5\text{cm}$, $H_a=3.525\text{cm}$, $R=0.7$ and $B=4.53$.

- **Flare-side Depth (F_s)**

The effect of changing the flare-side depth, F_s , is shown for a few cases in Fig. 19. Since $D = Cr1 + Cr4 + F_s$, the antenna depth also varies in these plots.

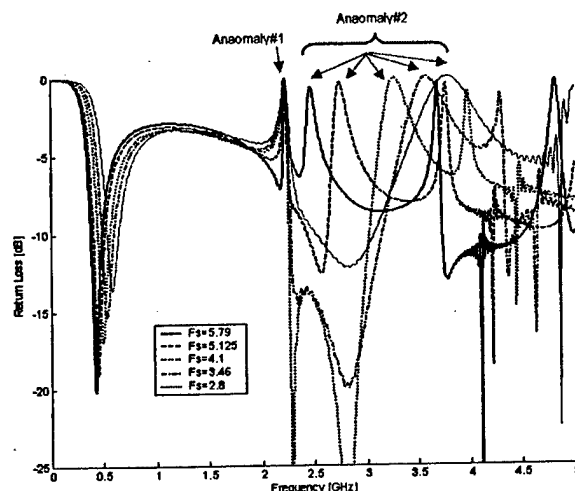


Figure 19: Variation of return loss with flare depth. $R=0.7$, $B=4.53$ cm, $D=7.5$ cm, $H_a=3.525$ cm, and $F_s=\{5.79, 5.125, 4.1, 3.46, 2.8\}$.

Observations from the flare-side, F_s , study:

Band 1, near 0.5 GHz

The center frequency of this operating band moves lower as F_s increases, while the bandwidth and impedance match at the center frequency remain relatively constant.

Band 2, between Anomalies #1 and #2

Anomaly #1 is not affected by the changes in F_s , but anomaly #2 is strongly affected, moving downward as F_s increases. However, the frequency of anomaly #2 is not uniquely related to F_s . In studies that are under way and not yet completed, anomaly #2 is found to be sensitive to Cr_4 and D , also. The impedance match and useful bandwidth of Band 2 is quite sensitive to F_s . For the shortest value, 2.8 cm, the return loss is no better than 13 dB, and the useful bandwidth ($VSWR < 2$) is less than one-half the frequency range between the two anomalies. For $F_s = 3.46$ and 4.1 cm, the antenna is well matched in Band 2 and the useful bandwidth is a large fraction of the frequency range between the anomalies. As F_s increases further, the useful bandwidth is pinched off as anomalies #1 and #2 approach each other.

Band 3, between Anomalies #2 and #3

This band is not useful for the particular parameter values used here. Although the plot suggests that the return loss is more than 10 dB for $F_s = 5.79$ cm, there appear to be additional anomalies in this band, making it of doubtful value.

6. Conclusion

Balanced Antipodal Vivaldi Antennas have been studied as single isolated elements, and in a 5x1 linear array and infinite arrays. The goal of these studies is to better understand the performance of these antennas and to develop design guidelines. As of this time, that goal is only partially fulfilled. However, some important characteristics of the antennas have been identified and the impact of certain design parameters has been quantified. With these understandings, it is possible to determine appropriate applications for BAVA antennas. As our understanding increases, it may be possible to extend the operating frequency range of these antennas so that they become even more useful.

The single elements operate well if they are large enough to support a traveling-wave-like mode of operation. Their resistance and reactance display peaks and oscillations somewhat like those observed in stripline-fed Vivaldi antennas. The 5x1 linear array was not optimized, so no conclusions can be drawn regarding applications. However, it is clear that this small array radiates a well-formed beam and that the interior elements have an acceptable impedance match.

Extensive computational studies of infinite arrays of BAVAs have revealed three potential operating bands and three troublesome impedance anomalies. The lower operating frequency band was relatively constant in the studies conducted here, and not much effort was devoted to determining how to control this band of operation. The primary band of interest here is referred to as Band 2 and it lies between anomalies #1 and #2. The highest frequency of this operating band is, for appropriate parameter choices, not too different from the frequency at which grating lobes begin to enter visible space, i.e., the element spacing is one-half wavelength. This makes Band 2 attractive for phased array applications. The lower frequency of Band 2 is limited by Anomaly #1. The dependence of antenna bandwidth and of anomalies #1 and #2 on four key design parameters is illustrated by the parameter studies, but definitive relationships between the parameters and antenna performance have not yet been determined.

7. Acknowledgment

The authors thank several individuals whose contributions have been valuable in this work. Jennifer Munro designed and built the isolated element and 5x1 linear

subarray. Eric Marklein assisted in measuring the passive [S] parameters and radiation patterns of the 5x1 linear subarray. Mr. James West and Rockwell Collins provided access to computational resources. The contributions of these individuals and organizations are greatly appreciated.

8. References

- [1] P. J. Gibson, "The Vivaldi Aerial," Proc. 9th European Microwave Conference, 1979, pp. 101-105.
- [2] K. S. Yngvesson et al, "Endfire Tapered Slot Antenna on Dielectric Substrates," IEEE Trans on Antennas and Propagation, Vol. 33, No. 12, Dec. 1985, pp.1392 – 1400.
- [3] J. J. Lee et al, "Wide band bunny-ear radiating element," IEEE Antenna and Propagation Society International Symposium, 1993, pp. 1604-1607.
- [4] L. R. Lewis, M. Fasset and J. Hunt, "A Broadband Stripline Array Element," Digest of 1974 IEEE Ant and Propagat. Symp., pp. 335-337. 1974.
- [5] T. H. Chio and D. h. Schaubert, "Parameter Study and Design of Wide-Band Widescan Dual-Polarized Tapered Slot Antenna Arrays," IEEE Trans on Antennas and Propagation, Vol. 48, No. 6, Jun. 2000, pp.879 – 886.
- [6] E. Gazit, "Improved Design of the Vivaldi Antenna," IEE Proceedings, Vol. 135, No. 2 Apr 1998. pp. 89 – 92.
- [7] J. D. Langely et al, "Balanced Antipodal Vivaldi Antenna for Wide Bandwidth Phased Arrays," IEE Proceeding of Microwave and Antenna Propagations, Vol. 143, No. 2 Apr 1996, pp. 97-102.
- [8] J. A. Munro, "Analysis of Balanced Antipodal Vivaldi Antennas," Master of Science Thesis, Dept. Of Electrical and Computer Engineering, University of Massachusetts, Amherst, May 1997.
- [9] Ansoft Corporation; www.ansoft.com
- [10] CST, Inc.; www.cst.de
- [11] D. H. Schaubert et al, "Moment Method Analysis of Infinite Stripline Fed Tapered Slot Antenna Arrays with a Ground Plane", IEEE Trans. Antenna and Propagation. Vol. AP-42, No. 8, pp1161-1166, Aug. 1994.
- [12] J. Shin, "Improved Method of Moments Computations Applied to Tapered Slot Antenna Arrays," Master of Science Thesis, Dept. Of Electrical and Computer Engineering, University of Massachusetts, Amherst, Sept. 1994.

- [13] J. Noronha et al, "Designing Antennas for UWB Systems," Microwave and RF Magazine, June 2003, pp. 53 -61.
- [14] C. Wu et al, "A Design of 120-Degree Vertical Polarized Sector Antenna Using Very Short Balanced Antipodal Vivaldi Antenna," Antennas and Propagation Society International Symposium, 2002, IEEE, Vol. 2, pp 16-21, Jun. 2002
- [15] L. C. Kuo et al, "3-D FDTD Design Simulation and Experimental Measurement of a Ka-Band Planar Antipodal Linearly-Tapered Slot Antenna (ALTSA)," IEEE Microwave and Wireless Components Letters, Vol. 11, No. 9, pp 382 – 384, Sept. 2001
- [16] H. Holter et al, "Elimination of Impedance Anomalies in Single- and Dual-Polarized Endfire Tapered Slot Phased Arrays," IEEE Trans. Antennas and Propagation, Vol AP-48, No. 1, pp. 122-124, Jan. 2000
- [17] P. W. Hannan et al, "Simulation of a phased-array antenna in a waveguide," IEEE Trans. Antenna and Propagation, Vol. AP-13, pp 475-476, May 1965.

Log-Periodic Networks of Resonant Circuits: Models for Wideband, Electrically Small Antennas

P. E. Mayes and P. W. Klock
Electromagnetics Laboratory
Electrical and Computer Engineering Department
University of Illinois at Urbana-Champaign

Abstract:

A parallel resonant (tank) circuit can be specified by the three element parameters, G , L and C . An alternative way of specifying the circuit is to use the natural (resonant) radian frequency, ω_0 , the conductance at resonance, G , and the "characteristic admittance", Y_c . The premise of this paper is that another resonant system, with geometry far removed from that of the tank, will have (near resonance) approximately the same impedance as the tank when the latter three parameters are used to determine the parameters of the tank. An electrically small conical radiating resonator (CRR) is used as an example of this relationship. Results of both modeling and measurements are used to demonstrate the equivalence. Since the radiating system converts more of the input power into radiation as the frequency increases, the agreement away from resonance is improved when the value of G increases with frequency in the appropriate way.

The impedance bandwidth of the system is increased when several tanks are connected in series. Choosing the resonant frequencies of the tanks to form a log-periodic progression provides, in some sense, optimum performance. The wide band impedance of the network of series-connected tanks can be reproduced by a set of nested CRR's. Once a specific realization, such as the CRR, is chosen, it may be possible to introduce an alternative model that is more specific to the physical system. In the case of the CRR, a section of transmission line can be used to represent the TEM guide formed by the region between two concentric cones. Once again, results of both modeling and measurements are used to demonstrate the degree of equivalence.

1. Introduction

A nested set of conical radiating resonators (CRR) has previously been introduced as a type of wideband, electrically small antenna [1]. The similarity between such

antennas and a log-periodic (LP) network of resonant circuits provides considerable insight into the operation of the antenna. Although computer solution of discretized integral equations will often produce a greater degree of accuracy [2], computer-aided analysis of approximate models is usually much faster and requires a smaller amount of computer resources. Furthermore, consideration of a circuit model may suggest several alternative ways to achieve a desired operation [3]. This work is not intended to replace computer modeling, but was carried out in parallel with efforts to improve the subsectional representation of nested sets of CRR.

2. The Tank Model

First, we seek to establish that the impedance of a parallel resonant ("tank") circuit is similar to that of a single conical radiating resonator. The notation used herein to describe the parameters of the tank circuit is given in Figure 1. L and C denote the inductance and capacitance, respectively; the reactive elements that are responsible for the resonant behavior. The unavoidable loss in the inductance is accounted for by the resistance, R , in series with L . Practically, the loss in the capacitor, C , may be negligible, but the parallel conductance, G , is nevertheless a useful parameter when adjusting the impedance of the tank to mimic that of an antenna, wherein G would account for the effect of the radiation.

The radiating structure to be the object of attention here is a rotationally symmetric, low-profile device constructed from two concentric, conducting cones as shown in cross section in Figure 2. The radial distance from the (virtual) apices of the cones and their rims is a . The lower cone has a hole of radius, a_{min} , that is also the inner radius of the shield of a coaxial cable that is connected to the lower cone at the periphery of the aforementioned hole. The center conductor of the coaxial cable is connected to the tip of the upper cone. The coaxial cable is thus connected to the concentric cones in a manner that provides a path for the rf power supplied to the cones from a source at the far end of the cable. The power transmitted from the source to the cones, by means of the cable, is confined between the cones from the cable-cone junction to the aperture formed at the outer radius of the cones, where a portion of the power is radiated. The system thereby performs the function of an antenna, converting guided to radiated power. The power that is not radiated at the aperture is reflected back toward the source. In the absence of reflections at the coax-antenna junction, the reflected power will travel back along the cable to the source where, cable and source being matched, it will be absorbed.

A basic premise of this paper is that the impedance behaviors of a tank and a single CRR, as functions of frequency, are similar. In support of this contention, we first develop expressions for the input admittance of the circuit of Figure 1.

$$Y = G + (j\omega C + \frac{1}{R + j\omega L}) \quad (1.1)$$

For an ideal inductor ($R = 0$), the resonant (radian) frequency, ω_0 , is given by the condition, $B = 0$:

$$\omega_0 = \frac{1}{\sqrt{LC}}$$

By defining a "characteristic impedance"

$$Z_c = \sqrt{\frac{L}{C}}$$

Equation (1.1) with $R = 0$ can be recast as

$$Y = G - j \frac{1 - \left(\frac{\omega}{\omega_0}\right)^2}{\frac{\omega}{\omega_0} Z_c} \quad (1.2)$$

Once the desired performance, in terms of Z_c and ω_0 , has been obtained, the circuit parameters can be obtained from

$$L = \frac{Z_c}{\omega_0} \text{ and } C = \frac{1}{\omega_0 Z_c}. \quad (1.3)$$

When R is not zero, Equation (1.1), when written in terms of ω_0 and Z_c , becomes

$$Y = \frac{1 - \left[\frac{\omega}{\omega_0}\right]^2 + RG + j \frac{\omega}{\omega_0} [RY_c + GZ_c]}{R \left[1 + j \frac{\omega}{\omega_0} \frac{Z_c}{R}\right]} \quad (1.4)$$

Figure 3 shows how the input impedance varies with the choice of $Z_c = 1/Y_c$. As Z_c becomes larger, so does the value of the resistance at resonance. Choosing Z_c properly, therefore, will produce a match between the tank and any reasonable desired value of resistance, i.e. the characteristic impedance of a feeder.

The resistance at resonance is also affected by the other parameters of the tank. This dependence must also be considered even though the variation of the other parameters is likely to be limited. For example, Figure 4 shows how the impedance locus is affected by the value of R , the resistance in series with the inductance. The minimum value of this resistance is established by the quality factor of the inductor. Increasing the resistance is most likely limited by the desire to maintain the efficiency of power transfer, e.g. from the input to the conductance, G .

3. The (radiation) conductance

When using the tank as a circuit that has behavior approximately equivalent to that of an antenna, loss must be added to account for radiation. For the radiating conical resonator shown in Figure 2, the conductance element, G , is used for this purpose. Figure 5 shows how, for certain fixed values of R and Z_c , the input impedance depends upon several values of G .

It is apparent from the above results that, although the general shape of the impedance locus remains the same for a wide variety of parameters, the size and location of the locus upon the Smith Chart is significantly different for the different values of R , L , G and C . So it is now in order to show that the impedance of a conical radiating resonator has the same general shape and that there are values of R , L , G and C that make the performance of the tank roughly equivalent to that of the CRR, at least over some band near resonance.

To provide experimental data a single CRR was constructed with the following parameters: $\theta_1 = 90$ degrees, $\theta_2 = 80$ degrees, $a = 7.3$ cm, $a_{\min} = 0.0635$ cm. The antenna was resonated at sizes that were electrically small by placing wires across the aperture. Four 22-gauge wires produced resonance at 521 MHz where the radius is 0.127λ ($ka=0.8$). A photograph of a physical model of the CRR is shown in Figure 6. Figure 7 is a Smith Chart showing the input impedance measured for the antenna of Figure 6. The general shape of this locus is certainly of the same form as those of Figures 3, 4 and 5. The task at hand is to find the values of R , L , G and C that produce the best correspondence between the computed and measured results. To this end we first, for the sake of simplicity, assume that the value of R is negligibly small. From Equation (1.2) we see that $G = Y$ at the frequency where $B = 0$. This equation also links Z_c with B . By setting $K = \omega/\omega_0$, and taking the derivative of B with respect to K , we find that

$$Z_c = \frac{2}{\left[\frac{dB}{dK} \right]_{K=1}} \quad (1.5)$$

Figure 8 recasts the measured impedance data into conductance and susceptance versus frequency. From these data, we find that the frequency of zero susceptance ($K=1$) is 521.4 MHz and that the normalized (to 0.02 S) conductance, g , is 0.0765 there. Evaluating the slope of b (B normalized to 0.02 S)

$$\left[\frac{db}{dK} \right]_{K=1} \approx 7.55 \quad (1.6)$$

so that $z_c = Z_0/50 = 0.265$, $\omega_0 = 3.276 \times 10^9$ rad/sec, $L = 4.85$ nH, and $C = 19.18$ pF. Figure 9 is a repeat of the measured data of Figure 7 plus the impedance of the approximately equivalent tank circuit. Although only three numbers (z_c , ω_0 and g) were used as parameters of the tank, the agreement between the measured and computed data is good over a wide frequency band. The main discrepancy is apparently caused by using a constant value of g over the entire band. Since the antenna radiation will increase with frequency, a better model would replace the constant g with one that varies with frequency.

The aperture of a CRR most closely corresponds to a source in the form of a closed loop. The radiation resistance of a small loop of electric current increases as the fourth power of the frequency [4]. The radiation conductance of a small loop of magnetic current would behave in a similar way. We would expect that such a model would most accurately represent the radiation from the CRR. Having selected the constant value of g to match the data measured at resonance, the frequency-dependent values would be given by

$$g(f) = g(f_0) \left(\frac{f}{f_0} \right)^4 \quad (1.7)$$

Figure 10 presents once again the comparison between the measured and computed data. However, this time the conductance is allowed to vary with frequency as indicated above. Also, the frequency band covered by the computations for the tank has been adjusted to correspond more closely to that of the measured data. The discrepancy between the two data sets has almost disappeared, although there remains some difference between the reactances at the upper end of the band.

4. Effect of loss in the inductor

A further refinement of the tank circuit can be made by including the loss in the inductor (value of R). Actually, the measured input impedance for the antenna includes this effect and it can only be separated from the radiation loss by evaluating the efficiency of the antenna. An equivalent tank circuit with only parallel elements would have the form shown in Figure 11.

For equivalence, G' and B' must be given by

$$G' + jB' = Y' = \frac{1}{Z} = \frac{1}{R + j\omega L} = \frac{R - j\omega L}{R^2 + \omega^2 L^2} \quad (1.8)$$

The condition of zero susceptance now occurs at $\omega = \omega_1$, where

$$B + B' = \omega_1 C - \frac{\omega_1 L}{R^2 + \omega_1^2 L^2} = 0$$

or

$$\omega_1 = \sqrt{\frac{L - CR^2}{L^2 C}} \quad (1.9)$$

Note that, when

$$R \ll \sqrt{\frac{L}{C}}, \quad \omega_1 \approx \sqrt{\frac{1}{LC}} = \omega_0$$

The zero susceptance condition occurs in the measured data at $\omega = \omega_1$. If the efficiency is used to evaluate the ratio of power dissipated in G (power radiated in the antenna case) to the power input (power radiated plus the power dissipated in G'), i.e.

$$e|_{\omega=\omega_1} = \frac{G}{G + G'} \quad (1.10)$$

then the measured value of $G + G'$ is known, and

$$G = e|_{\omega=\omega_1} (G + G')$$

From this, we can determine G' as

$$G' = (G + G') - G$$

This is the basis of the "Wheeler cap" method of determining experimentally the efficiency of a resonant antenna[5]. The value of $G + G'$ is determined from a measurement of the input admittance with the antenna in free space. The value of G' is found by measuring the admittance when $G = 0$, i. e. when radiation is blocked by placing the antenna inside a cavity with conducting walls. The cavity

should be large enough that near fields of the antenna do not induce currents in the cavity walls and yet small enough that cavity resonances do not unduly affect the measured admittance. For the antenna of Fig. 6 with four equally spaced 22-gauge wires, the efficiency was determined by the Wheeler cap method to be approximately 80%.

5. A broadband network of tank circuits

To this point the effort has been confined to the relationship between a single tank and a conical radiating resonator. A well-known disadvantage of electrically small antennas is narrow impedance bandwidth. However, it is also well known that the impedance bandwidth of a resonant circuit can be readily extended by adding more resonances to the network. We are thereby led to propose that several tanks be connected in series as an example application of this principal. Figure 12 shows a network of n tanks so connected. The goal of producing increased bandwidth with series-connected tanks leads to consideration of scaling the resonant frequencies of the tanks in a log-periodic fashion. That is, the ratio of adjacent resonances should be held constant. In order for the input impedance to return to the same value, the conductances of tanks with lossless inductors must be held constant. These principles have been employed in the computation of the input impedance versus frequency for several sets of series-connected tanks.

Figure 13 shows the results for a set of two tanks. The parallel (high-impedance) resonances of the circuit are separated in frequency by the ratio $\tau = 0.95$. At these frequencies the impedance locus crosses the real axis on the Smith chart. At frequencies between the two resonances the impedance traverses a loop. The size of the loop is dependent upon the value of τ . If the impedance at the center of the loop is not suitable for matching to external circuitry, it can be moved to some other value by simply adding a transformer at the input. In the example shown in Figure 13, adding a 1:7 transformer has moved the center of the loop so that it very nearly coincides with the center of the chart. Doing so produces a substantially constant SWR approximately equal to 2 over the band (1.05:1) determined by the value of τ . It has been historical practice to use the half-power points to define the band limits. We continue using that method here, although acknowledging that many applications will require a better match, to facilitate the comparison with previous work. The centered circle in Figure 13 denotes the points of half-power match. The half-power match bandwidth is then determined by the intersection of the impedance plot with this curve. In Figure 13 the (half-power) match band extends from a relative frequency of 0.979 to 1.075, a bandwidth of about 1.1. Figures 14 and 15 show the computed input impedance loci for the cases where more resonators are added to the network. In Figure 14, for three resonators, the match band extends from 0.98 to 1.13, a bandwidth of 1.15. Note that, although the loops have about the same size, they are not

centered on the chart. Thus, even though the value of τ remains constant, the SWR increases in parts of the band. This is a result of the lack of symmetry in the circuit because each tank is resonant at a different frequency. When the number of resonators is increased to four, the input impedance shown in Figure 15 forms three loops and the match band extends from 0.984 to 1.186, a bandwidth of 1.21. Of course, since each resonator occupies a finite volume, there is a limitation in the number of resonators that can be used to extend the match bandwidth.

6. A transmission line model

When considering the conical radiating resonator, the equivalent circuit can take a more specific form. The fields established in the region between the two cones by an on-axis feed are predominantly TEM, satisfying a field equivalent of transmission line equations. A characteristic impedance can be defined for this mode and equivalence can be established between the fields and the voltage and current of a standard TEM line. An approximate equivalent circuit then takes the form of a uniform section of line terminated in a conductance, G , that absorbs the same amount of power that is radiated in the physical antenna. The resonant length of this line can be varied by terminating the line with a reactive element. To make the line shorter than one-quarter wavelength, the reactive termination should be an inductance. The resulting equivalent circuit for a conical radiating resonator takes the form shown schematically in Figure 16. A section of lossless transmission line of length, l , and characteristic resistance, R_0 , is terminated at one end by an inductance, L , and conductance, G , in parallel.

When the equivalent circuit contains explicit representation of some of the known geometric features of the physical antenna, as is the case in the line model of the CRR, fewer parameters remain to be determined by measurement. For example, in the CRR the characteristic impedance of the TEM mode guided by the two adjacent cones is known to be given by

$$R_0 = 60 \ln \left(\frac{\tan\left(\frac{\theta_2}{2}\right)}{\tan\left(\frac{\theta_1}{2}\right)} \right) \quad (1.11)$$

Table 1 lists some values of R_0 for angles that are used in the models to follow.

Table 1
Characteristic impedances of lines in equivalent circuit for CRR.

$\theta_1(\text{deg})$	$\theta_2(\text{deg})$	$R_0(\text{ohms})$
90	80	10.526
80	70	10.875
70	60	11.576
60	50	12.816

Of course, the length of the line in the equivalent circuit is the same as the radius of the corresponding resonator in the CRR. The values of G and L cannot be directly determined from the geometry of the CRR. However, G and L can be adjusted so that the impedance computed for the approximate equivalent line circuit agrees with the measurements of the CRR at a single frequency, say, at resonance. For the antenna of Figure 6, $R_0 = 10.526$ (from Table 1) and the line section length, ℓ , is 7.3 cm.

The data that follows were computed using MathCAD to implement calculations of the input impedance, Z_{in} , of the terminated line section.

$$Z_{in} = R_0 \frac{Z_r \cos(\beta\ell) + jR_0 \sin(\beta\ell)}{R_0 \cos(\beta\ell) + jZ_r \sin(\beta\ell)} \quad (1.12)$$

where Z_r is the terminating impedance and β is the free-space phase constant for the line. The computed values of Z_{in} have been renormalized with respect to 50 ohms to facilitate comparison with measurements made in a 50-ohm system. Figure 17 shows the input impedance computed for the equivalent circuit after the values of G and L have been adjusted to provide resonance at approximately 521 MHz and normalized impedance (in agreement with the measured value) of 6.3.. The inductance so found was 3.135 nH. For comparison, Figure 17 also repeats the measured values from Figure 7. The discrepancy away from resonance suggests that, as before, the radiation conductance is changing with frequency, but also that the reactance is inadequately represented by a single fixed inductor.

The equivalent circuit for a set of nested CRR's is a set of uniform line sections connected in series as shown in Figure 18. Figure 19 displays on a Smith chart

the computed input impedance of a system of only two lines with ratio of lengths equal to $\tau = 0.975$. This behavior is quite analogous to that of a series connection of two tanks of slightly different resonant frequencies. The normalized input impedance is denoted by circular data points. The center of the loop is moved numerically to the center of the chart by an ideal 1:12 transformer, as shown by the square data points. The half-power locus is, once again, marked by triangular data points. The increased bandwidth of this more complex structure is readily apparent.

In Figures 20 and 21, more resonators have been added to form two and three loops, respectively. Table 2 summarizes and compares the results by listing the half-power band limits, the frequency spans, the frequency ratios of the band limits and the half-power bandwidths for each case.

Table 2

Band limits, frequency spans, band ratios and half-power bandwidths of several systems of n conical radiating resonators. These numbers are based upon half-power match points only.

n	f_u(MHz)	f_l(MHz)	Span(MHz)	Ratio	HPBW
2	553	518	35	1.068	0.065
3	571	518	53	1.102	0.097
4	592	518	74	1.143	0.134

7. Conclusions and Future Work

Although the line model for a single CRR needs further development to make performance predictions that are as accurate as those of the tank model, the line model for a nested set of CRR's contains the essential information to illustrate the concept of bandwidth enhancement using multiple resonances. One physical antenna with two resonators has been constructed and some measurements have been made. In this antenna the resonant frequencies are controlled by selecting different wire sizes for the edge elements, but the radial dimensions of the radiating apertures are the same. A second antenna, which employs approximate log-periodic scaling of the dimensions of the resonators, is currently under construction.

8. Acknowledgements

The work reported here was supported, in part, by grants from NASA (NAG 3-2840) and the Communities Foundation of Texas, Inc.

9. References

[1] P. E. Mayes and W. Gee, "Using Multiple Resonant Radiators for Increasing the Impedance Bandwidth of Electrically Small Antennas," Proc. 24th Annual Antenna Applications Symp., Allerton Park, Illinois, Sept. 2000.

[2] J.-S. Zhao, W. C. Chew and P. E. Mayes, "Accurate Analysis of Electrically Small Conical Antennas by Using the Low-Frequency Method," Proc. 24th Annual Antenna Applications Symp., Allerton Park, Illinois, Sept. 2000.

[3] P. E. Mayes, "Inductively Loaded, Stacked Sector Antennas," Proc. 25th Annual Antenna Applications Symp., Allerton Park, Illinois, pp. 152-170, Sept. 2001.

[4] W. L. Stutzmann and G. A. Thiele, Antenna Theory and Design, p. 101, New York, Wiley, 1983.

[5] H. A. Wheeler, "The Radiansphere Around a Small Antenna," Proc. IRE, vol. 47, pp. 1325-1331, Aug. 1959.

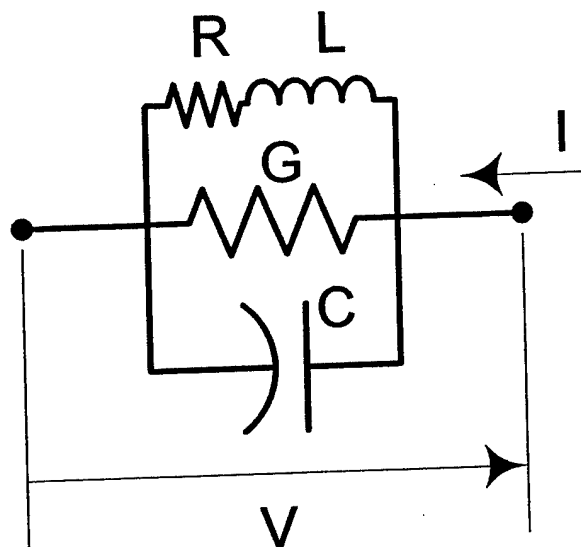


Figure 1. Schematic diagram of a parallel resonant (“tank”) circuit and its defining elements.

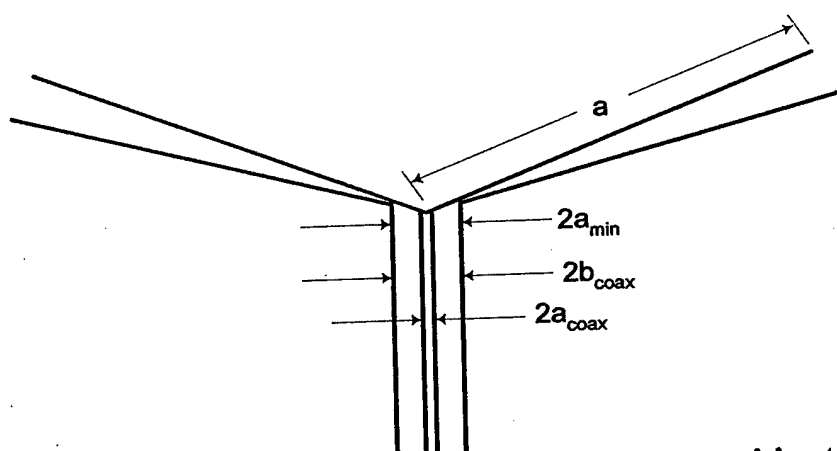


Figure 2. Cross-sectional view of a radiating resonator comprising two cones and a coaxial feed cable.

Impedance of a Single Tank Circuit
 $G=0.001\text{ S}$, $R=0.5\text{ ohms}$, $Z_c\text{ in ohms}$

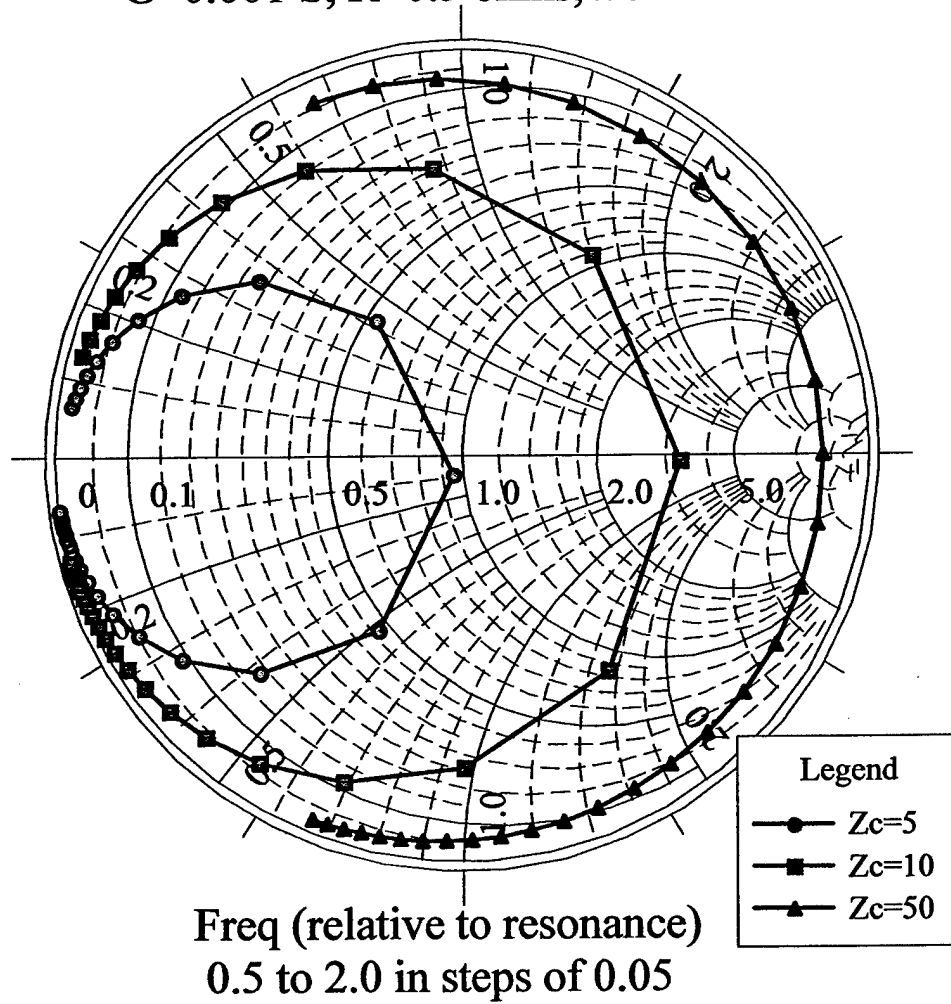
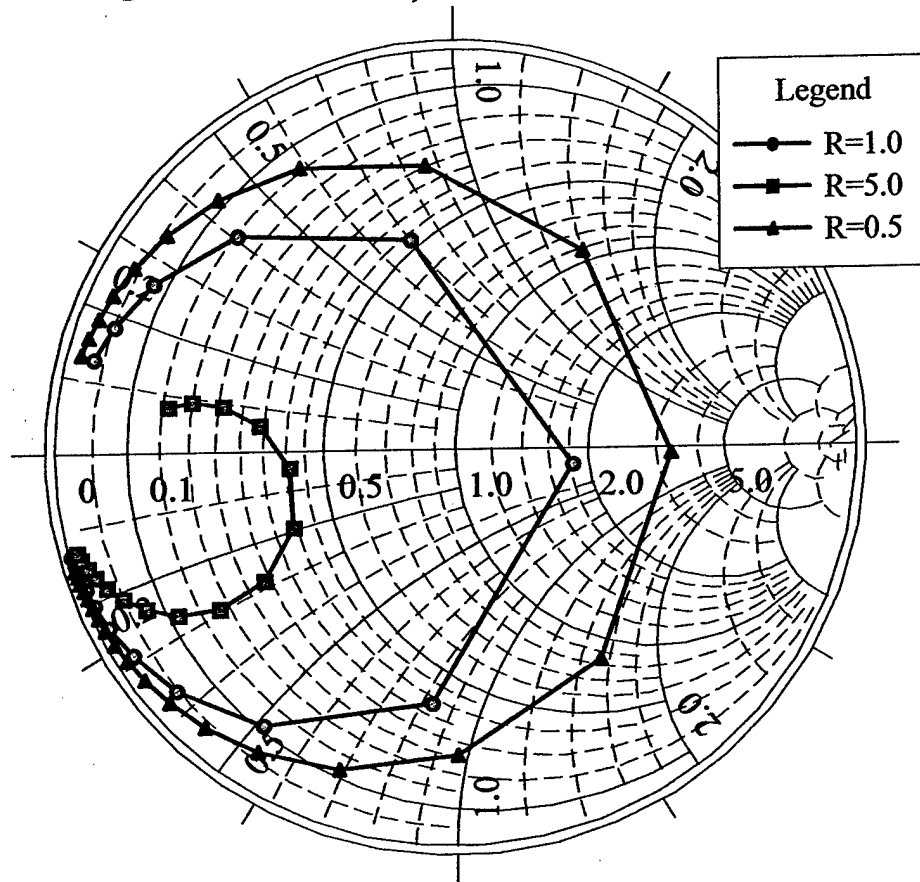


Figure 3. Smith Chart plot of impedance of tank circuit of Figure 1 showing the dependence upon Z_c .

Impedance of a Single Tank Circuit
 $G=0.001$ siemen, R in ohms, $Z_c=10.0$



Relative Frequency: 0.5 to 2.0, $f_0=1.0$

Figure 4. . Smith Chart plot of impedance of tank circuit of Figure 1 showing the dependence upon R .

R=0.5, Zc=50.0 ohms

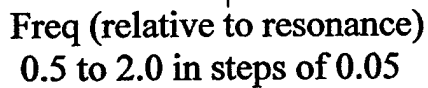


Figure 5. Smith Chart plot of impedance of tank circuit of Figure 1 showing the dependence upon G .

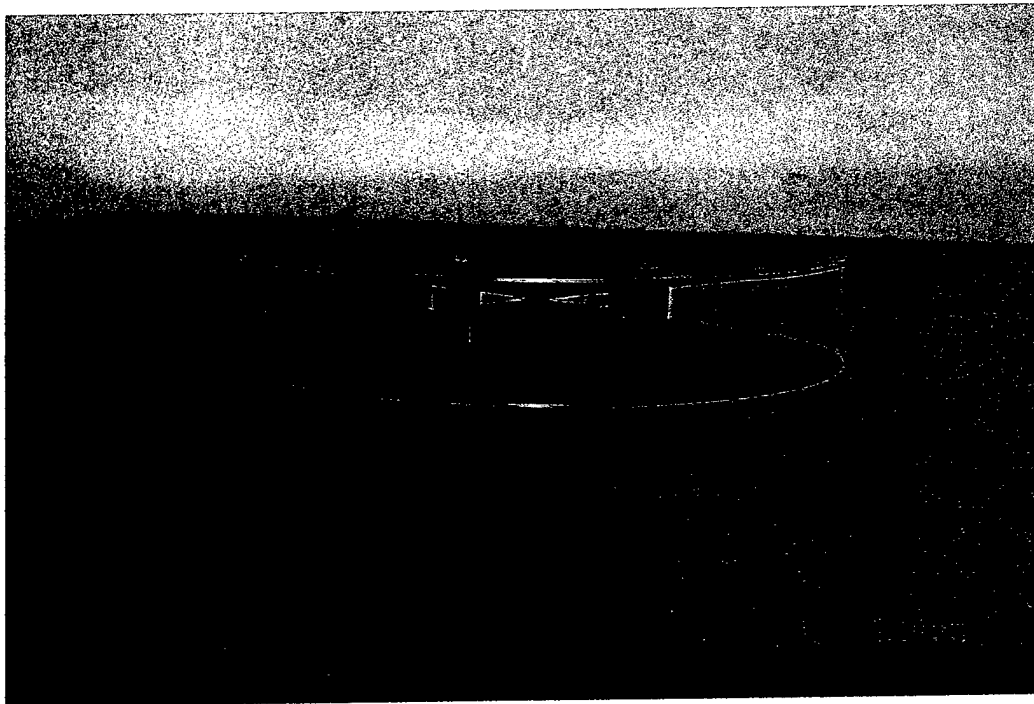
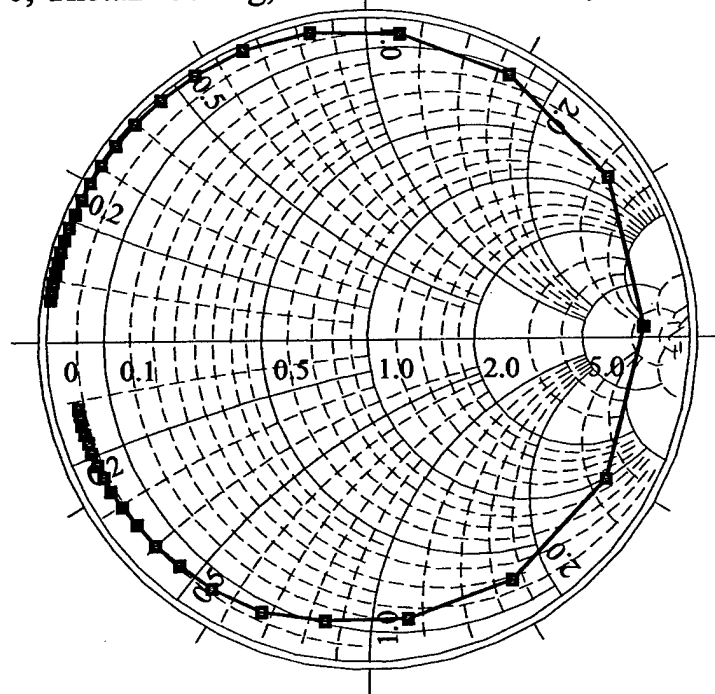


Figure 6. Physical model of a conical radiating resonator mounted on a 14-inch square ground plane. This model is terminated with four 26-gauge wires (inductors). The second cone and set of wires are actually the optical images produced by the ground plane.

Measured Impedance of Single Conical Resonator
Terminated with Four Equally Spaced No. 22 Wires
Theta1=90, Theta2=80 deg, Radii: Outer=7.3 cm, Inner=0.0635 cm



Frequency from 100 to 900 MHz
at 20 MHz spacing

Figure 7. Input impedance measured for single conical radiating resonator loaded at aperture with four equally spaced No. 22 wires.

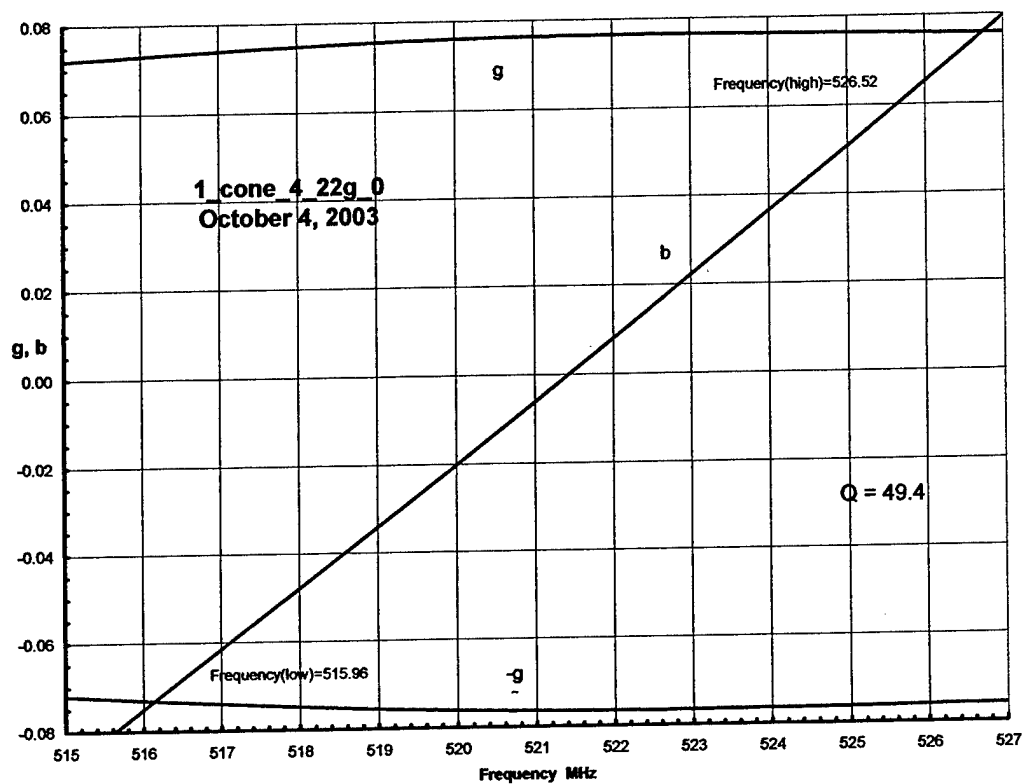


Figure 8. Plot of measured g and b versus frequency for conical radiating resonator with four 22 AWG wire terminations.

Comparison of Measured Impedance of a Single CRR
with Computed Impedance of a Single Tank Circuit
with $R=0$, $Z_{c\text{nor}}=0.265$, $G_{l\text{nor}}=0.0765$, $Z_0=50$ ohms

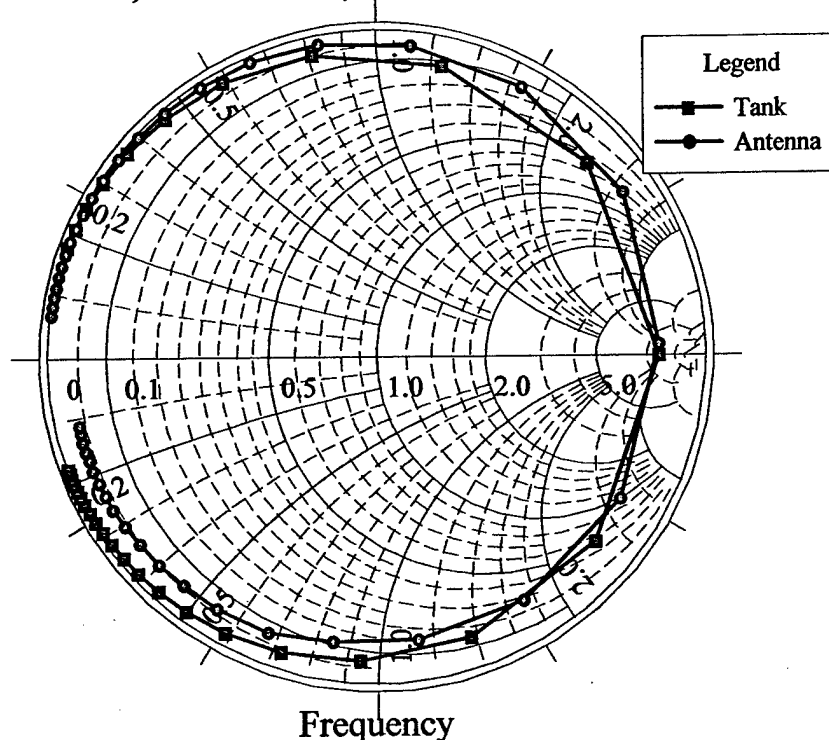


Figure 9. Comparison of measured impedance of single conical radiating resonator with that of an approximate equivalent tank circuit with constant conductance to account for radiation loss.

Comparison of Measured Impedance of a Single CRR
 with Computed Impedance of a Single Tank Circuit
 with $R=0$, $Z_{cnor}=0.265$, $G_{nor}=0.0765f^4$, $Z_0=50$ ohms

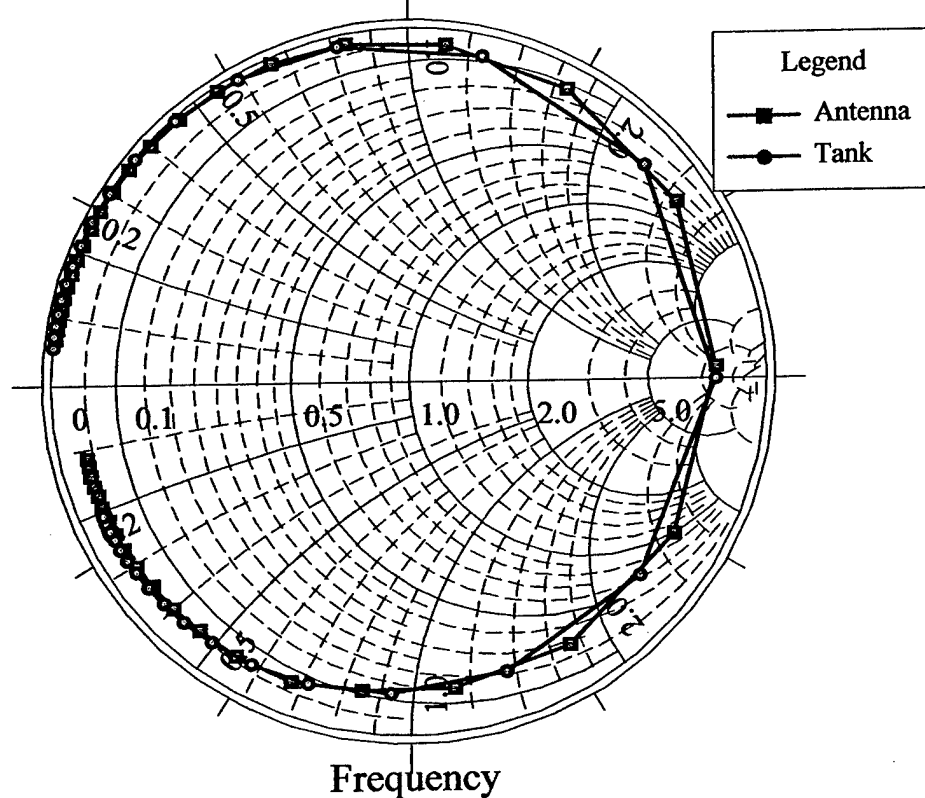


Figure 10. Comparison of measured impedance of single conical radiating resonator with that of an approximate equivalent tank circuit with frequency-dependent conductance to account for radiation loss.

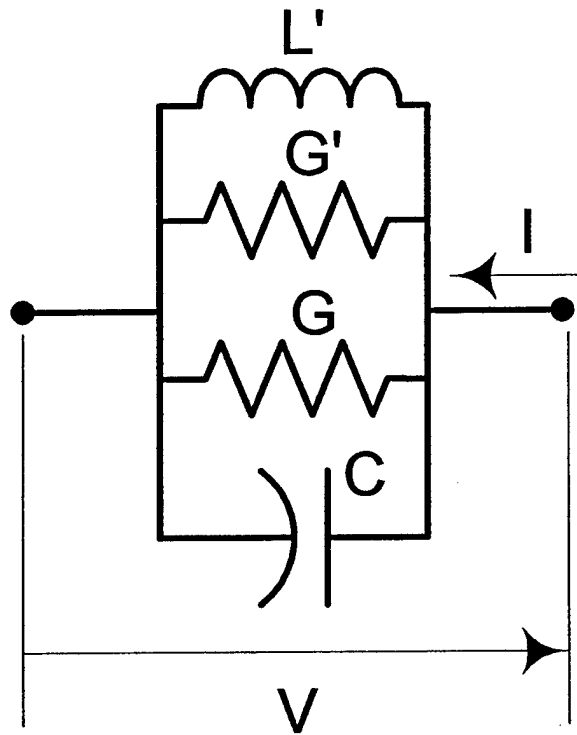


Figure 11. Equivalent tank circuit having only parallel elements.

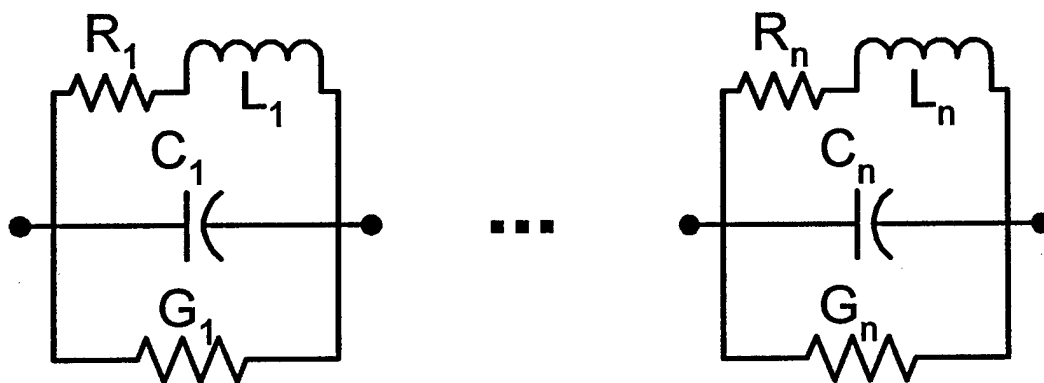


Figure 12. Schematic diagram of arbitrary number of tanks connected in series.

Impedance of Two Series-Connected Tank Circuits
 $\tau=0.95$, $G_1=G_2=0.075$ S, $R_1=R_2=0$ ohm, $Z_c=0.25$

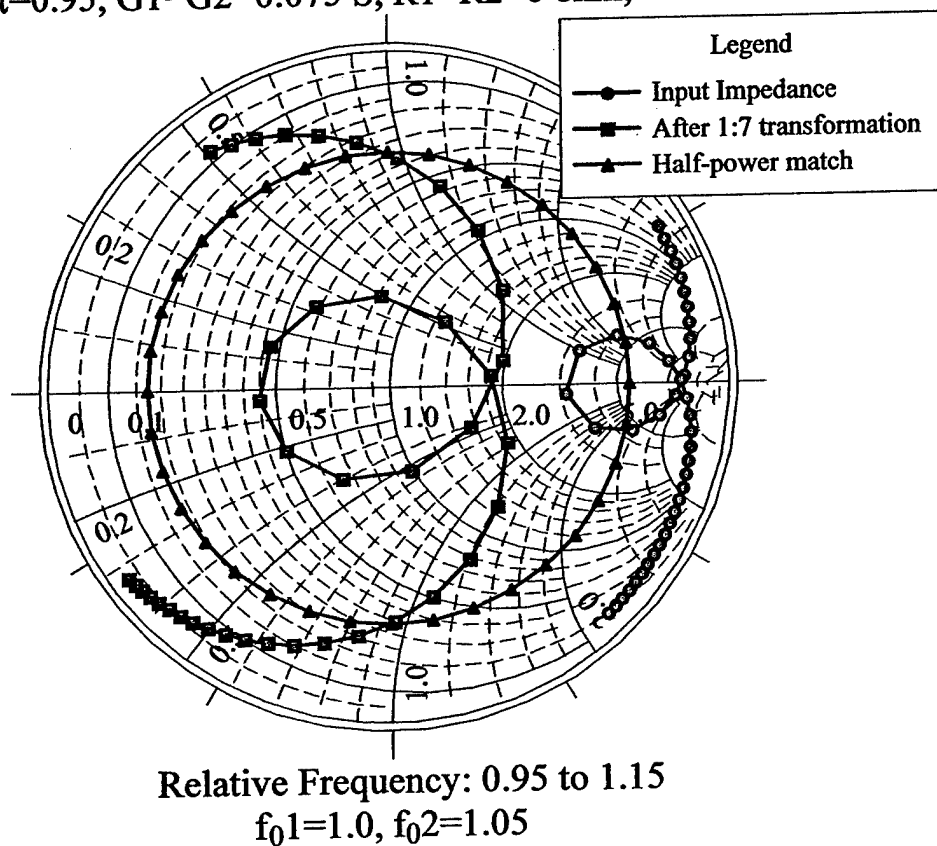


Figure 13. Computed impedance for two series-connected tank circuits, impedance after transforming, and half-power match locus.

Impedance of Three Series-Connected Tank Circuits
 $\tau=0.95, R_1=R_2=R_3=0, Z_{01}=Z_{02}=Z_{03}=0.25$
 $G_1=G_2=G_3=0.0765 \text{ S}$

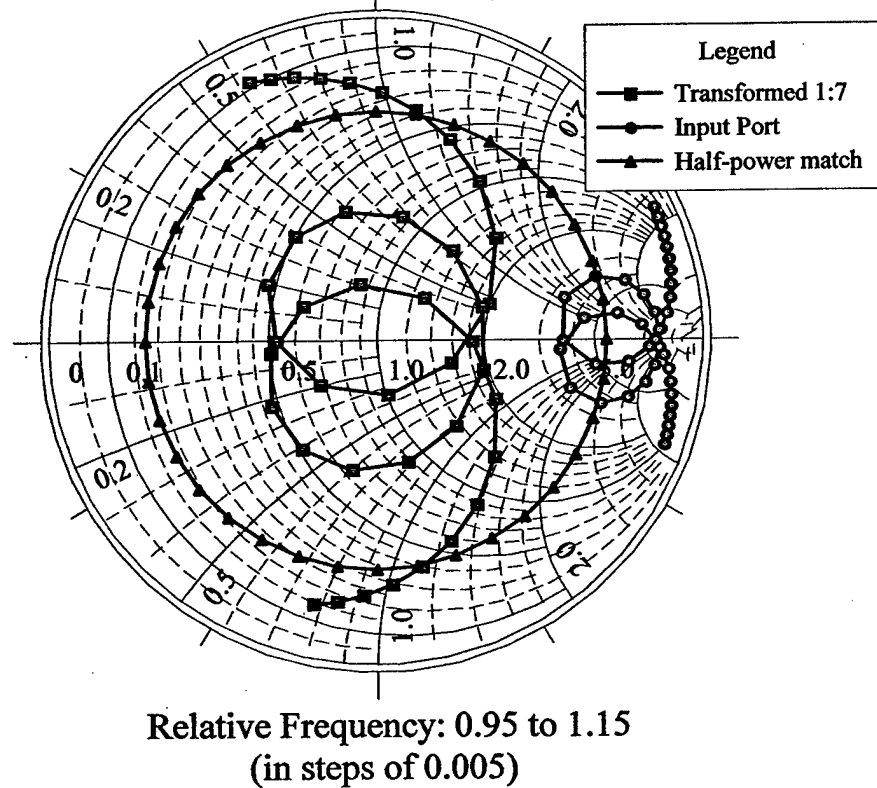
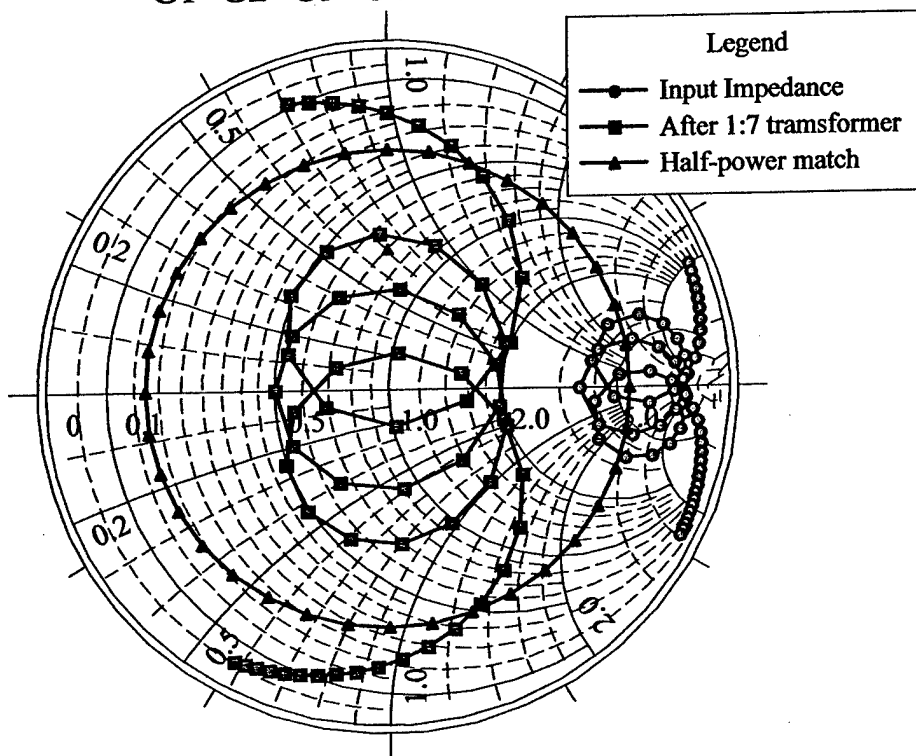


Figure 14. Computed impedance for three series-connected tank circuits, impedance after transforming, and half-power match locus.

Impedance of Four Series-Connected Tank Circuits
 $\tau=0.95, R_1=R_2=R_3=R_4=0, Z_{c1}=Z_{c2}=Z_{c3}=Z_{c4}=0.25$
 $G_1=G_2=G_3=G_4=0.0765 \text{ S}$



Relative Frequency: 0.95 to 1.25
 (in steps of 0.005)

Figure 15. Computed impedance for four series-connected tank circuits, impedance after transforming, and half-power match locus.

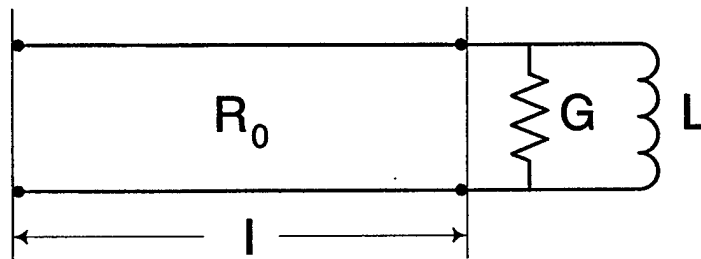
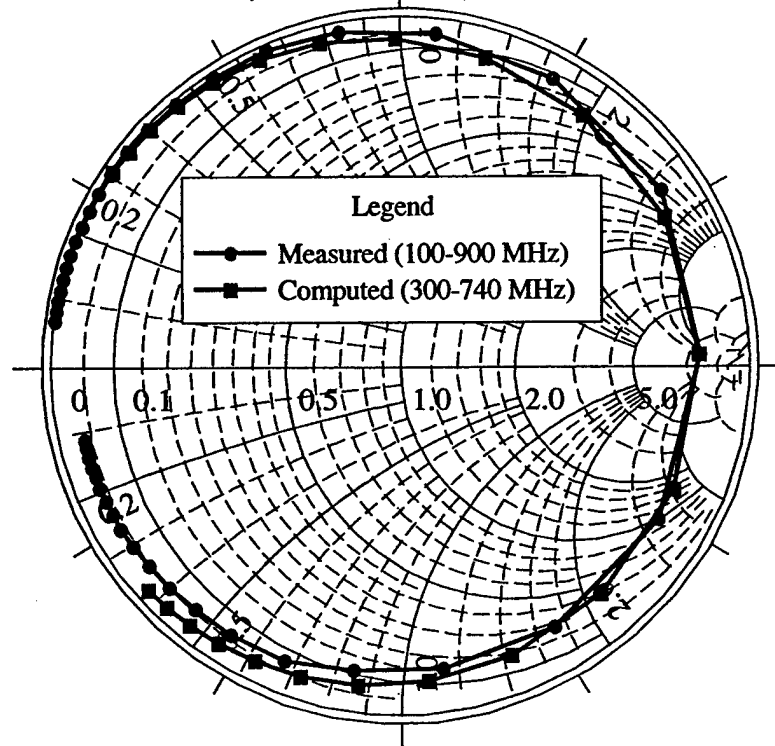


Figure 16. An approximate equivalent circuit for a single conical radiating resonator.

Comparison of Measured Impedance of a Single CRR
with Computed Impedance of an Approximate Equivalent
Single Terminated Line Section, $R_0=10.526$ ohms,
 $len=7.3$ cm, $L=3.135$ nH, $R=315$ ohms



Frequency increment=20 MHz

Figure 17. Comparison of measured impedance of single conical radiating resonator with that of an approximate equivalent line circuit with constant conductance to account for radiation loss.

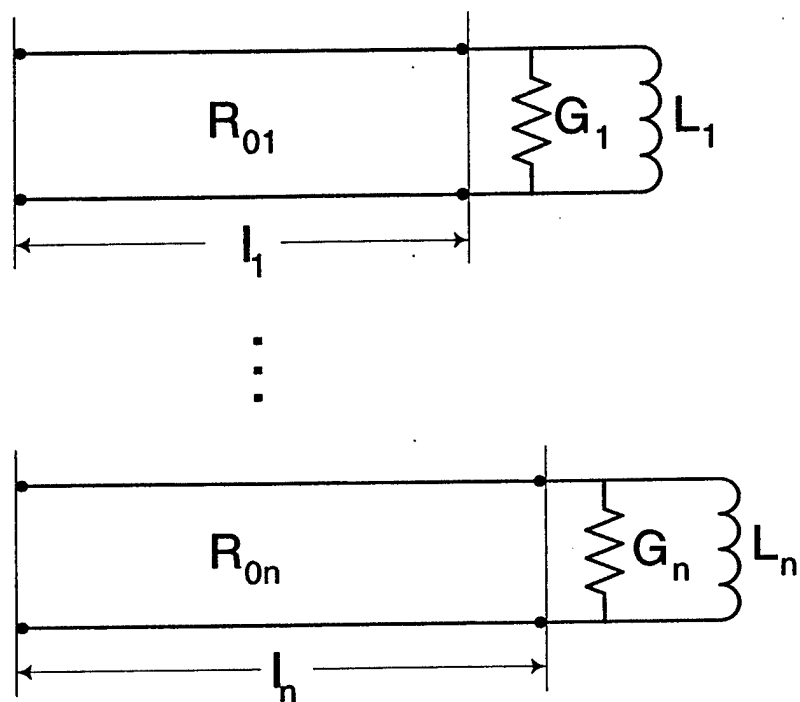
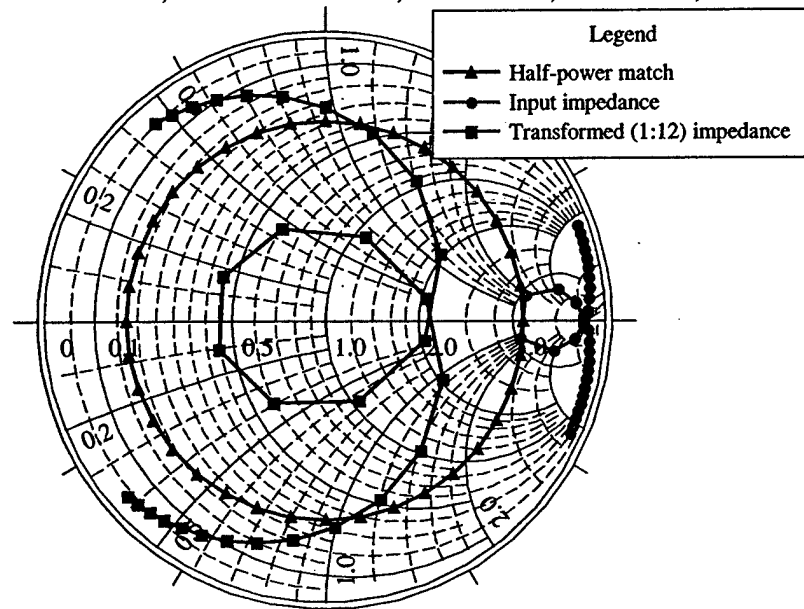


Figure 18. . An approximate equivalent line circuit for a stack of conical radiating resonators.

Impedance of Two Terminated Lines in Series

$G_{nor}=0.0765$, $R01=10.526$, $R02=10.86$ ohms, $L1=3.1$ nH, $l1=7.3$ cm, $\tau=0.975$



Frequency: 500 to 575 MHz
(in 2.5 MHz steps)

Figure 19. Computed impedance for two series-connected, terminated, uniform line sections, impedance after transforming, and half-power match locus.

Impedance of Three Terminated Lines in Series, $\tau=k, G_{nor}=0.0765$
 $R_{01}=10.526, R_{02}=10.86$ ohms, $L_1=3.1$ nH, $l_1=7.3$ cm, $k=0.975, k_3=(k+\epsilon)^2$

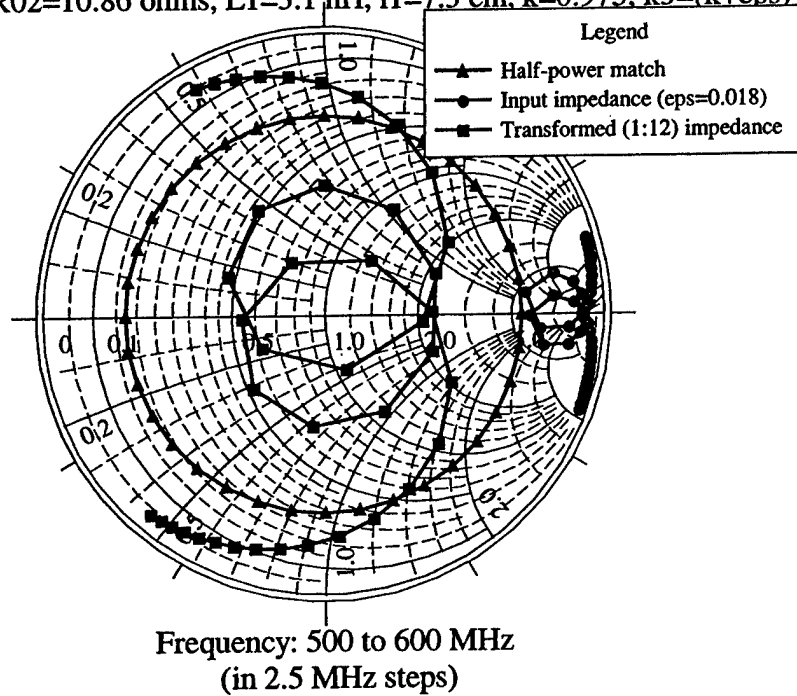


Figure 20. Computed impedance for three series-connected, terminated, uniform line sections, impedance after transforming, and half-power match locus.

Impedance of Three Terminated Lines in Series, $G_{nor}=0.0765$
 $R_{01}=10.526$, $R_{02}=10.86$, $R_{03}=11.58$, $R_{04}=12.82$ ohms, $L_1=3.1$ nH,
 $L_n=k_n*L_1$, $k_2=k$, $k_3=(k+0.018)^2$, $k_4=(k+0.035)^3$, $\tau=0.975$

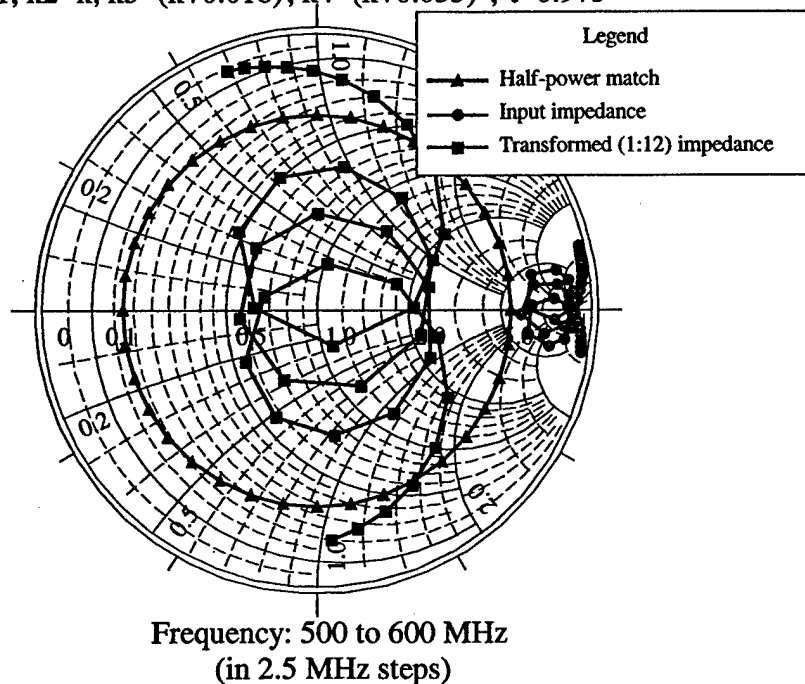


Figure 21. Computed impedance for four series-connected, terminated, uniform line sections, impedance after transforming, and half-power match locus.

EFFICIENT PATTERN AND IMPEDANCE BANDWIDTH ANALYSIS OF REACTIVELY STEERED ARRAYS

David F. Kelley and Samuel D. Reier
Department of Electrical Engineering
Bucknell University
Lewisburg, PA 17837
dkelley@bucknell.edu, reier@bucknell.edu

Abstract

Reactively steered array antennas consist of a circular arrangement of parasitic elements that surround a central element. The central element is excited directly by a source, and the parasitic elements are connected to reactive loads (capacitors and/or inductors) that can be adjusted to steer the main beam and one or more nulls to any desired direction. The selection of appropriate reactive loads is complicated by the requirement for the radiation pattern and input impedance to vary by only a small amount over the operating bandwidth of the system. Some kind of optimization procedure must therefore be used to determine the load configuration. Such procedures require the calculation of the array characteristics for each candidate set of reactive loads. This "forward" problem usually comprises the most time-consuming part of the procedure. This paper describes a straightforward and efficient method to evaluate candidate array configurations that combines superposition of embedded element patterns and interpolation of pattern and mutual impedance data over frequency. The method eliminates the need to execute a full analysis procedure for every candidate configuration. It should be appropriate for use with any type of optimization procedure.

1 Introduction

Reactively steered phased arrays consist of one or more active elements driven by an RF signal source and several parasitic elements. The parasitic elements are loaded by reactive components (capacitors, inductors, or transmission line stubs) that can be varied to adjust the relative phases of the element currents. By controlling the reactance values, the main beam of the array can be scanned to any

desired direction. Pattern nulls can be created in other directions as well. These arrays have the advantage of electronic pattern control without the complicated, expensive, and relatively heavy feed network associated with traditional phased arrays. Thus, there is considerable interest in their use in wireless and consumer electronics applications.

A typical design is shown in Figure 1, in which a central active monopole element is surrounded by six reactively loaded parasitic elements. All elements are mounted on a finite metallic ground plane. This structure is widely used (for example, see [1] and [2]), since it represents a good compromise between full azimuthal coverage and compact size. The parasitic elements are typically spaced approximately 0.25λ from the central element in order to achieve good coupling between elements. A structure similar to that shown in Figure 1 will be investigated in the examples presented here, but the methods described are applicable to any array geometry.

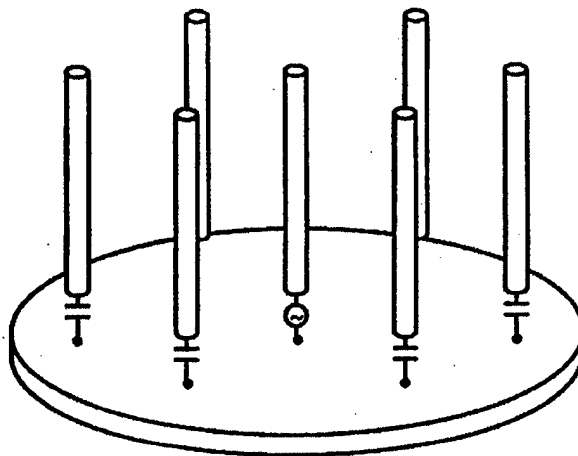


Figure 1. Physical structure of a hexagonal reactively steered array.

It is not usually possible to determine directly the reactive load values required to satisfy a given set of main beam and null-steering specifications; therefore, an optimization procedure of some kind must be employed. Such procedures usually generate a set of one or more candidate solutions to the problem in an iterative process, in which the fitness of each candidate must be evaluated. Generally, this means that the radiation pattern must be calculated for each solution, a task that is often accomplished using a full-wave analysis approach such as the method of moments, the finite element method, or the finite difference time domain method.

Depending on the complexity and size of the array and the presence of any surrounding scatterers, the burden on computational resources can be severe. It will be shown in Section 2 that in many situations the radiation pattern can be calculated quickly using the embedded element patterns of the array elements, thus avoiding time-consuming full-wave analysis. Specifically, once the major physical features of the array (e.g., overall size, element lengths, and element diameters) have been determined the radiation pattern can be found quickly and efficiently for each new set of reactive loads.

A practical array must be capable of operating over a specified range of frequencies without a significant change in its performance characteristics. Consequently, in addition to gain and null-steering properties, an optimization procedure must consider bandwidth properties as well. That is, the gain, null depths and locations, and input impedance must remain within specified limits over the operational bandwidth of the system. However, if frequency domain methods are used to analyze the array, element pattern and impedance data are valid only at single frequencies. Data could be generated for a large number of frequencies that span the operating bandwidth, but this represents an inefficient approach. A simple interpolation procedure based on the method of undetermined coefficients is described in Section 3 that calculates pattern and impedance data at any desired frequency. The method requires that full-wave analysis be applied at only a handful of frequencies.

The primary motivation for this work was to investigate the application of particle swarm optimization to the design of reactively steered arrays. This approach is a member of the new class of "evolutionary" or "biologically based" procedures and is briefly described in Section 4. Particle swarm optimization typically requires thousands of radiation pattern calculations per program execution; therefore, the techniques for improving efficiency described here greatly reduce the time required to obtain a solution. A few representative examples are described in Section 5, and conclusions are presented in Section 6.

2 Efficient Pattern Calculation

The essential components of the pattern calculation method described in this section were first presented in [3] and [4]; however, the manner in which the method is used here is substantially different. Consequently, several important implementation details are introduced. As shown in [5], the total radiated field $E(\theta, \phi)$ of a phased array is given by

$$\mathbf{E}(\theta, \phi) = \sum_{n=1}^N V_n \mathbf{g}_{scn}(\theta, \phi), \quad (1)$$

where N is the total number of elements in the array, V_n is the voltage measured at the terminals of the n^{th} element (as shown in Figure 2), and $\mathbf{g}_{scn}(\theta, \phi)$ is the *short-circuit embedded element pattern* of the n^{th} element. The last quantity is the electric field radiated by the entire array when the terminal voltage of the n^{th} element is forced to have a value of unity at zero phase and the terminals of all of the other elements are shorted. Quantities in boldface type are vectors. Note that embedded element patterns contain both magnitude and phase data. An expansion of the radiation pattern similar to that in (1) is given in [3]. The latter is in terms of *open-circuit embedded element patterns*, which are obtained when the terminal current of a given element is forced to have a value of unity at zero phase and the terminals of all of the other elements are opened. Both expansions are based on the principle of superposition.

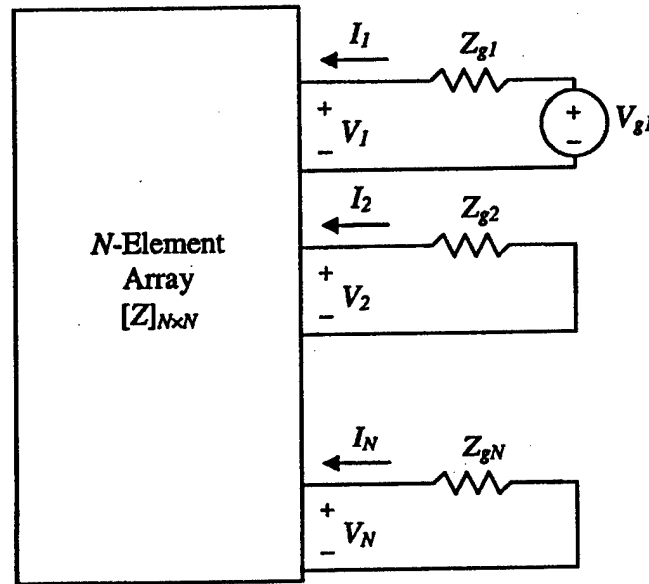


Figure 2. Network representation of an N -element array.

If there are only M discrete spatial directions in which pattern data are of interest, then this relationship can be expressed in matrix form as

$$[E] = [g_{sc}] [V], \quad (2)$$

where $[E]$ is an $M \times 1$ vector containing the total field data, $[g_{sc}]$ is an $M \times N$ matrix containing embedded element pattern data, and $[V]$ is an $N \times 1$ vector containing the terminal voltages. The element pattern matrix $[g_{sc}]$ is formed by filling the n^{th} column with the embedded element pattern data for the n^{th} element. Both vectors and the matrix in (2) are in general complex-valued. The pattern data can include one or both polarizations of the far field. For example, the upper half of $[E]$ could contain the θ -components, and the lower half could contain the ϕ -components. The vector would consist of only one component type if the other component type were of no interest. The data in the embedded element pattern matrices can be decomposed in a similar manner.

As shown in Figure 2, the array can be considered to be an N -port network with $N-1$ loads connected to the parasitic elements and with the RF signal source represented by the Thévenin equivalent circuit formed by V_{g1} and Z_{g1} . The parasitic elements are loaded with either capacitive or inductive reactances at their feed points. Although the generator voltage is applied only to the central element, non-zero voltages appear across the reactive loads because of mutual coupling. The terminal voltages are related to the generator voltage by the relationship

$$[V] = [Z][Z] + [Z_g]^{-1}[V_g], \quad (3)$$

where $[V_g]$ is an $N \times 1$ vector containing the generator voltages, $[Z]$ is the $N \times N$ mutual impedance matrix relating the terminal voltages to the terminal currents, and $[Z_g]$ is an $N \times N$ diagonal matrix containing the values of the reactive loads connected to the parasitic elements and the generator impedance connected to the central element. More specifically, $[Z_g]$ has the structure

$$[Z_g] = \begin{bmatrix} R_{g1} + jX_{g1} & \cdots & 0 \\ & jX_{g2} & \\ \vdots & & jX_{g3} \\ & & \ddots \\ 0 & \cdots & jX_{gN} \end{bmatrix}, \quad (4)$$

where element 1 corresponds to the driven element. Although (4) assumes that pure reactances load the parasitic elements, non-zero resistances could be added either to account for component losses or to represent intentionally introduced resistances whose purpose is to enhance the bandwidth of the system. In the vector $[V_g]$ only the entry corresponding to the central element is non-zero.

Substituting (3) into (2) yields

$$[E] = [g_{sc}]Z\{[Z] + [Z_g]\}^{-1}[V_g]. \quad (5)$$

A similar result is presented in [3] and is given by

$$[E] = [g_{oc}]\{[Z] + [Z_g]\}^{-1}[V_g], \quad (6)$$

where $[g_{oc}]$ is an $M \times N$ matrix containing the open-circuit embedded element pattern data for the array. The latter result can also be found from (5) using the relationship

$$[g_{oc}] = [g_{sc}]Z, \quad (7)$$

which is derived in [5].

The expressions given in (5) and (6) provide a computationally efficient means for determining the radiation pattern of a reactively steered array. This speed becomes especially important if nonlinear optimization is used to find the reactive loads required to achieve specified radiation characteristics. In a typical optimization procedure radiation patterns are calculated for a large number of candidate load configurations. In the past (for example, see [1], [6] and [7]), this "forward" calculation task has been accomplished using a full-wave analysis approach. To be fair, some of this past work has involved varying the array geometry as well as the load configuration, in which case the approach described here would not be applicable. Nevertheless, there have been few examples presented in the literature of array design procedures that take advantage of the time savings possible when only the loads are varied.

Using (5) or (6), the radiation pattern of the fully loaded and excited array can be found with only a few matrix multiplications and one matrix inversion. All of the matrices and vectors except $[g_{sc}]$ (or $[g_{oc}]$) are small, so the inversion is not computationally expensive. The embedded element pattern data and the mutual impedance matrix are calculated or measured only once and are stored before executing the optimization procedure. As long as the physical structure of the array does not change, these quantities remain unchanged as well; the values of the reactive loads do not affect either $[g_{sc}]$ (or $[g_{oc}]$) or $[Z]$. For a given set of reactive loads it is only necessary to compute the inverse of $\{[Z] + [Z_g]\}$, multiply it by $[V_g]$, and then multiply $[g_{sc}][Z]$ (or $[g_{oc}]$) by the result. Even greater efficiency can be achieved by recognizing that $[V_g]$ has only one non-zero element. Thus, for example, (6) can be further reduced to

$$[E] = [g_{oc}] \{([Z] + [Z_g])^{-1}\}^{<1>} V_{g1}, \quad (8)$$

where the superscript $<1>$ indicates the first column of the matrix $\{([Z] + [Z_g])^{-1}\}$, and where V_{g1} is the voltage applied to the driven element (a scalar quantity). The radiated field in a given direction is found simply by evaluating the dot product of the vector $V_{g1} \{([Z] + [Z_g])^{-1}\}^{<1>}$ with the appropriate row of $[g_{oc}]$. In many cases, the entire pattern need not be found, but only the field radiated in a few directions.

The accuracy of (5) and (6) depends in turn on the accuracy with which the embedded element patterns and mutual impedance matrix are calculated or measured. If any nearby scatterers are included in the full-wave analysis model or measurements used to determine $[g_{sc}]$ and $[Z]$, then the effects of those scatterers on the radiation pattern of the fully-excited array will be included. For example, if a metallic structural element in close proximity to the array causes asymmetry in the element patterns and has an impact on the mutual impedances, those effects will be included to the extent that the structure is modeled accurately. The full power of this approach was perhaps not fully expounded in [3].

The input impedance Z_{in} of the array is given by

$$Z_{in} = \frac{V_1}{I_1}, \quad (9)$$

where I_1 , the current flowing into the terminals of the central element, and V_1 , the voltage across those terminals, are the first entries, respectively, of the terminal current and voltage vectors, which can be found using

$$[I] = ([Z] + [Z_g])^{-1} [V_g] = ([Z] + [Z_g])^{-1} V_{g1} \quad (10)$$

and

$$[V] = [Z]([Z] + [Z_g])^{-1} [V_g] = ([Z]([Z] + [Z_g])^{-1}) V_{g1}. \quad (11)$$

3 Matrix Interpolation

The embedded element pattern and mutual impedance matrices used to calculate the radiation pattern of the array are frequency-dependent quantities and must be determined either by measurement or by full-wave analysis. It is impractical to obtain these matrices for a large number of frequencies spanning the bandwidth of

interest. Alternatively, an interpolation approach has been developed that uses pattern and mutual impedance data calculated via full-wave analysis at only a few frequencies to determine the same quantities at other frequencies within the operating bandwidth. The reactively steered arrays considered here are not wideband devices, because the elements must operate near resonance in order to have currents induced in them of sufficiently large magnitude. Typical bandwidths are only a few percent. Consequently, the method of undermined coefficients [8], a form of polynomial data-fitting, provides very good interpolation results.

It was found that the variation over frequency of each entry in the embedded element pattern and mutual impedance matrices can be represented to good accuracy by a 4th-order polynomial. For example, the real part of the mutual impedance Z_{11} can be interpolated over the operating bandwidth as

$$R_{11}(f) \approx a_{0,11} + a_{1,11}f + a_{2,11}f^2 + a_{3,11}f^3 + a_{4,11}f^4, \quad (12)$$

where f is the frequency of interest, and $a_{0,11}$ through $a_{4,11}$ are coefficients that must be determined. If (12) is evaluated at five distinct frequencies covering the bandwidth of interest, then a system of five independent equations can be constructed in order to obtain the five unknown coefficients. Expressed in matrix form, the system of equations is

$$\begin{bmatrix} 1 & f_0 & f_0^2 & f_0^3 & f_0^4 \\ 1 & f_1 & f_1^2 & f_1^3 & f_1^4 \\ 1 & f_2 & f_2^2 & f_2^3 & f_2^4 \\ 1 & f_3 & f_3^2 & f_3^3 & f_3^4 \\ 1 & f_4 & f_4^2 & f_4^3 & f_4^4 \end{bmatrix} \begin{bmatrix} a_{0,11} \\ a_{1,11} \\ a_{2,11} \\ a_{3,11} \\ a_{4,11} \end{bmatrix} = \begin{bmatrix} R_{11}(f_0) \\ R_{11}(f_1) \\ R_{11}(f_2) \\ R_{11}(f_3) \\ R_{11}(f_4) \end{bmatrix}. \quad (13)$$

Similar matrix equations can be constructed for the remaining entries in the mutual impedance matrix and for the entries in the various embedded element pattern matrices. Thus, each entry has associated with it five unique coefficients that permit a polynomial approximation of that quantity at any desired frequency. For example, the mutual impedance matrix evaluated at an arbitrary frequency f is approximated using

$$[Z(f)] \approx [a_0] + [a_1]f + [a_2]f^2 + [a_3]f^3 + [a_4]f^4, \quad (14)$$

where $[a_0]$ through $[a_4]$ are the matrices containing the complex coefficients required to perform the interpolation.

4 Particle Swarm Optimization

Particle swarm optimization is a relatively new approach that is conceptually easy to understand and use [9, 10]. Like genetic algorithms and other evolutionary methods, particle swarm optimization generates a population of possible solutions that advance toward the best solution. The method is especially useful when a particular problem is nonlinear in many variables. Each variable can be thought of as a unique dimension within the solution space; thus, the set of variables defines the particle's location in that space. In the case of a reactively steered array there are six variables, which store the values of the six reactive loads connected to the parasitic elements. While genetic algorithms use recombination and mutations to evolve to an optimal solution, the particles that constitute the swarm "fly" through the solution space in search of the optimal solution.

The particle swarm algorithm is depicted graphically in the flow chart shown in Figure 3. The particles initially have randomly assigned positions and velocities. Each particle is also assigned a subset of neighbors from within the swarm. The use of neighborhoods allows for convergence to multiple solutions and increases the chance of finding the globally best solution. A fitness function is used to determine how closely each particle satisfies the goals of the problem, and the fitness scores are stored. The velocity of each particle is then modified according to the particle's best position (best solution) so far as well as the best position among its neighbors, with the weight between the two randomly assigned. Each particle then moves to its next position based on its new velocity. In order to prevent the particles from straying outside the region of allowable solutions, limits are imposed on position and velocity. The new positions are scored again using the fitness function, and the cycle continues until a particle finds a satisfactory solution. Experience has shown that for most problems with relatively wide regions of convergence, best results are obtained with approximately 50 particles [9]. The use of fewer particles provides insufficient coverage of the solution space, but the use of a greater number of particles leads to time-wasting redundancy.

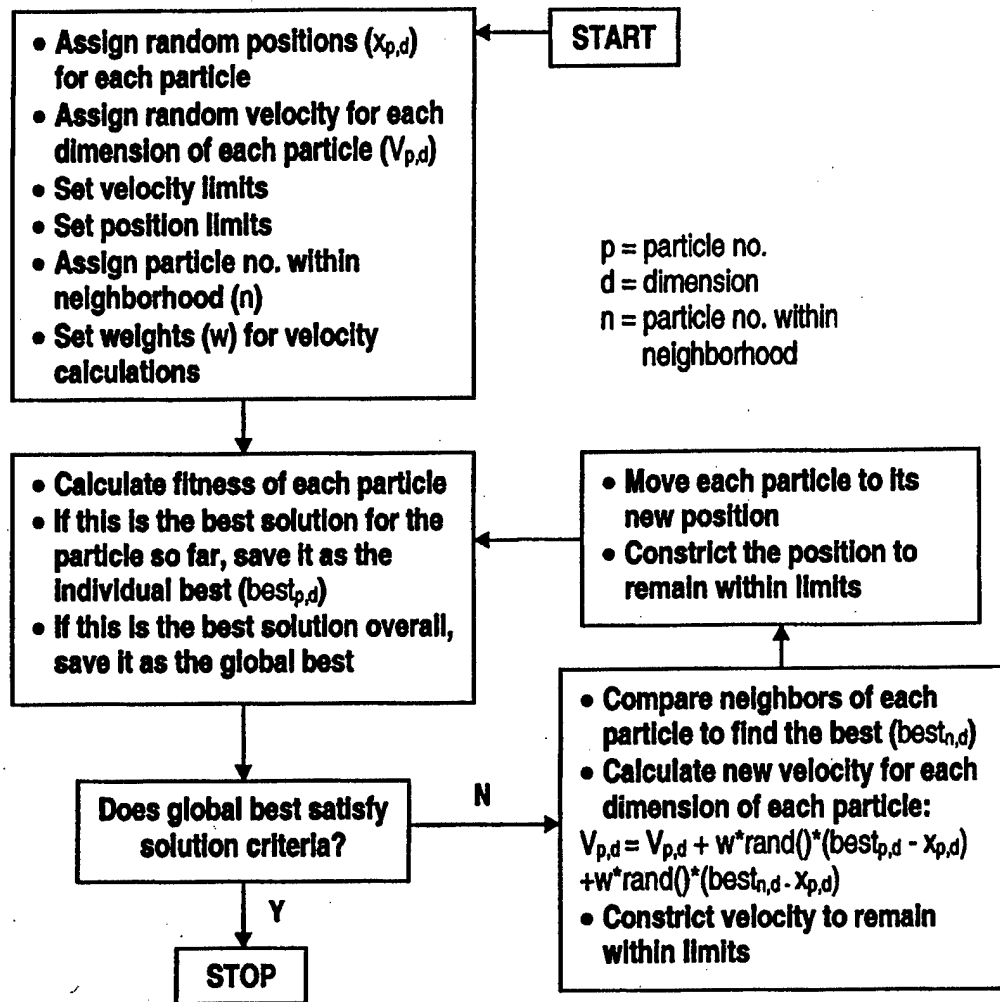


Figure 3. General structure of the particle swarm algorithm (adapted from [10]).

5 Examples and Results

To illustrate the application of the radiation pattern calculation method, several array designs for the WiFi band (2.4-2.497 GHz, a 4% bandwidth) are investigated using particle swarm optimization. A seven-element hexagonal array like the one shown in Figure 1 is the baseline configuration. Each array element is a monopole with a length of 2.76 cm and a diameter of 2.38 mm. With these

dimensions the elements are resonant within the WiFi band, a condition that allows strong currents to be excited along the elements. The parasitic elements are spaced 3.06 cm (approximately 0.25λ) from the central element at 60° intervals. The array is located over an infinite, perfectly conducting ground plane for demonstration purposes; a more realistic finite ground plane could be modeled, if desired. The mutual impedance matrices and embedded element patterns were calculated using *EZNEC*, a commercial version of the method of moments implementation NEC-2 [11]. Data were computed at the center frequency of the WiFi band (2.4485 GHz), at the band edges (2.4 and 2.497 GHz), and at the one-third (2.43233 GHz) and two-thirds (2.46467 GHz) bandwidth frequencies.

Simple combinations of inductors and capacitors were considered for use as the reactive loads for the antenna; however, it was found that the change in reactance with frequency of such combinations resulted in a serious degradation of performance over the operating bandwidth. Shorted transmission line stubs with variable lengths were chosen instead, since stubs can provide both positive and negative values of reactance and, if the characteristic impedance Z_o is low enough, relatively small changes in reactance with frequency. The reactance X_{stub} of a shorted stub of length l is given by

$$X_{stub} = Z_o \tan(\beta l), \quad (15)$$

where $\beta = 2\pi/\lambda$. Note that the wavelength along the stub can be substantially shorter than the free-space wavelength. Stub lengths from zero to $\lambda/4$ produce inductive reactances, and lengths from $\lambda/4$ to $\lambda/2$ produce capacitive reactances. The six stub lengths are therefore allowed to vary from 0 to $\lambda/2$, and they serve as the six variables that are adjusted by the particle swarm optimization procedure. In a practical implementation the stub lengths might be controlled via MEMS switches.

Particle swarm optimization was employed to meet three different sets of specifications, which are outlined in Table 1 below. In Case 1, the main beam is steered to an azimuth angle of 0° , which is the angular position of one of the parasitic elements, and a null is steered toward 90° . This is a moderately challenging task, since the main beam and null are relatively close together, and the null depth is 25 dB below the main beam. Case 2 is essentially the same as Case 1, except that the main beam is steered to a direction between two elements, a situation in which it might be a bit more difficult to achieve the desired gain. Case 3 represents the most challenging task, since a second relatively deep null is specified only 40° away from the main beam. After a few initial test runs, it was

found that a swarm of 50 particles produced good results after a reasonable number of iterations. This agrees with the guidelines presented in [9, p. 314].

Table 1. Summary of particle swarm optimization results.

	Case 1	Case 2	Case 3
Desired Gain	10 dBi @ 0°	10 dBi @ 30°	8 dBi @ 0°
Desired Nulls	-15 dBi @ 90°	-15 dBi @ 90°	-10 dBi @ 40° -10 dBi @ 90°
Achieved Gain	10.3 dBi @ 0°	10.3 dBi @ 30°	7.9 dBi @ 0°
Achieved Nulls	-36.2 dBi @ 90°	-27.6 dBi @ 90°	-10.4 dBi @ 40° -32.1 dBi @ 90°
No. of Iterations	1066	2365	2048
Elapsed Time (sec)	75.1	169.0	137.1
Input Impedance	$24.8 + j77.1 \Omega$	$22.8 - j43.6 \Omega$	$24.4 + j0.1 \Omega$

Before the optimization procedure begins the desired main lobe gain and direction are specified. The level and direction of one or more nulls can be specified as well. Each time the particles move to a new position, the new lengths of the transmission line stubs are used to calculate the reactances loading the parasitic elements. Those loads, along with the embedded element patterns and the mutual impedance matrices, are used to calculate the far-field patterns at the center frequency of 2.4485 GHz and at the two band edges at 2.4 and 2.497 GHz using (5). It is assumed that the results at intervening frequencies vary smoothly between those obtained at the center and edge frequencies. The computed patterns are compared to the specifications; an appropriate fitness score is assigned to each particle; the particles' velocities are updated; and the particles are allowed move again. The process is repeated until the specifications are met or most nearly achieved.

It is possible for the optimization algorithm to run indefinitely without finding a solution if the initial array performance specifications are too difficult or impossible to meet. This could happen if, for example, an unrealistically high gain is specified or if the desired main beam and null directions are too close together. In these instances the user must rely on knowledge of basic principles of array theory and experience with the optimization procedure to decide when a solution is good enough. This became evident in each of the three cases summarized in Table 1. In all cases the gain requirements were met or very nearly met, but the main beams and nulls were not always in the specified directions. To prevent the program from running indefinitely, two stop conditions

were defined. The first terminates the program if there is no improvement in the globally best solution after 1000 iterations, and the second simply limits the program to a total of 5000 iterations. The latter condition was never reached in the three cases considered here.

Once an appropriate set of reactive loads is found, a simple single-stub impedance matching network is designed to transform the input impedance of the driven element to $50\ \Omega$ at the center frequency. The return loss is then calculated at ten frequencies spanning the WiFi band using the mutual impedance matrix interpolation method outlined in Section 3. For the cases considered here, a good match is defined as a return loss of -10 dB or better over the operating bandwidth. Occasionally it was not possible to obtain a good match at all frequencies, in which case the solution was rejected, and the optimization process was repeated. The input impedances listed in Table 1 represent those optimization results that produced the best radiation patterns and broadband matches. No case required more than a few runs of the optimizer to achieve the presented results.

The radiation patterns obtained for Case 1 at the center frequency (2.4485 GHz) and at the two edge frequencies (2.4 and 2.497 GHz) are shown in Figure 4. The return loss for the same case is shown in Figure 5. The design achieves the main beam and null specifications listed in Table 1, but the null minimum is not located exactly at 90° at all three frequencies. This occurs primarily because the optimizer was instructed to keep the radiated field at or below -15 dBi at 90° , not to place the minimum at 90° . Although the distinction is subtle, the former specification is more realistic in practice. Similarly, the main beam direction also varies slightly among the three frequencies, but the gain at 0° is maintained at or above 10 dBi across the band. The return loss is below -10 dB at all frequencies as well.

As was mentioned earlier, it is sometimes necessary to run the optimizer several times for a given case in order to obtain a solution that both satisfies the pattern constraints and results in a good broadband match. This can be a problem if full-wave analysis is required to evaluate each potential solution. However, by using the stored embedded element patterns and mutual impedance matrices to calculate the far-field patterns for each new load configuration, the average elapsed time for 100 iterations of the optimizer is reduced to about 7 sec when implemented in MATLAB on a late model laptop computer with a 1.5 GHz Intel processor. It is important to note that, had (5) not been used, each run of the optimizer would have required 50,000 to 100,000 executions of *EZNEC* in order to achieve a satisfactory solution.

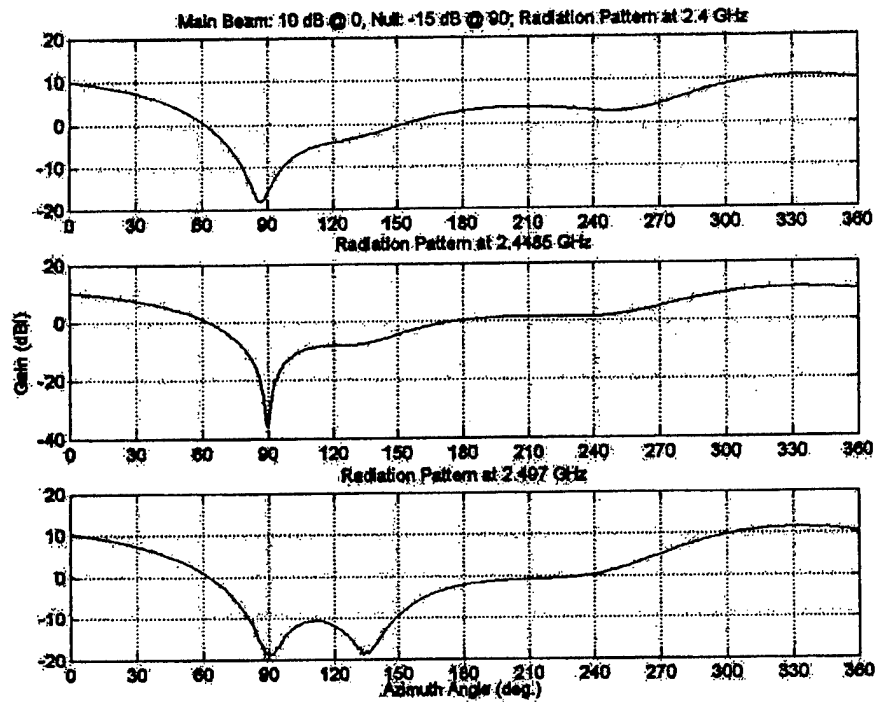


Figure 4. Radiation patterns for Case 1.

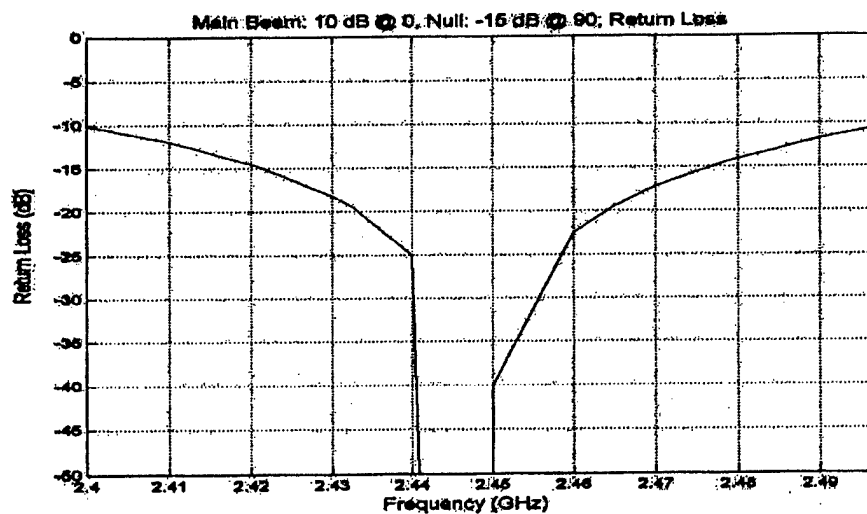


Figure 5. Return loss results for Case 1.

The results obtained for Case 2 are shown in Figure 6 and Figure 7. In this case the gain at 30° (the angular direction between two elements) is specified to be 10 dBi or greater with a null at 90° maintained below -15 dBi. In spite of these more challenging specifications, the optimizer is able to find a solution with low return loss over the entire band. As in Case 1, the null minima are displaced slightly as frequency changes.

Finally, the pattern and return loss results for Case 3 are shown in Figure 8 and Figure 9, respectively. The specifications call for a gain of 8 dBi at 0° and nulls with depths of -10 dBi each at 40° and 90° . Once again, the optimizer is able to satisfy the null constraints, even if the minima are not located at 40° and 90° . The gain at 0° is almost 8 dBi across the band, and the return loss performance is very good. The gain and null steering specifications are more modest for this case because of the close proximity of the nulls to the main beam. Still, the optimizer did not quite meet them. This illustrates the need to be aware of realistic performance expectations before applying an optimization procedure. As shown in Table 1, the optimizer requires only 1-2 minutes per run to achieve these results.

6 Conclusion

Reactively steered arrays achieve good performance with low weight and complexity. They should become a cost-effective solution in many applications, if efficient optimization procedures can be developed to determine the reactive load values required to satisfy a given set of specifications. The radiation pattern analysis method presented here greatly increases the speed of optimization procedures by eliminating the need to use full-wave analysis methods to check candidate solutions. A further increase in efficiency can be achieved by employing the interpolation method described here to generate frequency-dependent results over a fairly wide bandwidth. There is no significant difference in optimization speed between simple and complicated array and support structure geometries, since the embedded element pattern and mutual impedance matrices incorporate all of the effects of nearby scatterers; the matrices are the same size regardless of the complexity of the problem geometry. The accuracy of the method is determined primarily by the degree to which the array is accurately modeled.

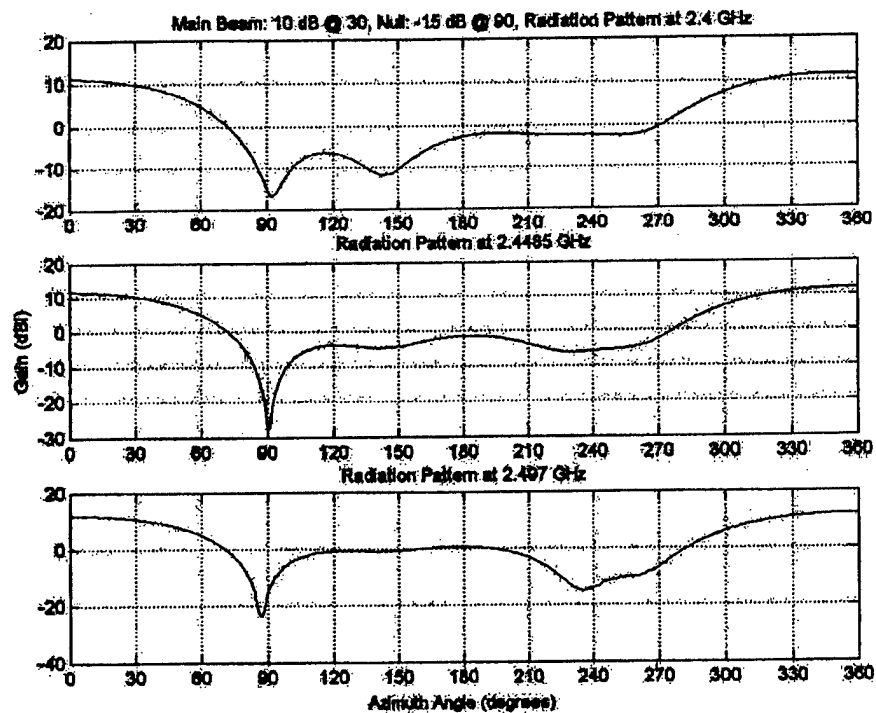


Figure 6. Radiation patterns for Case 2.

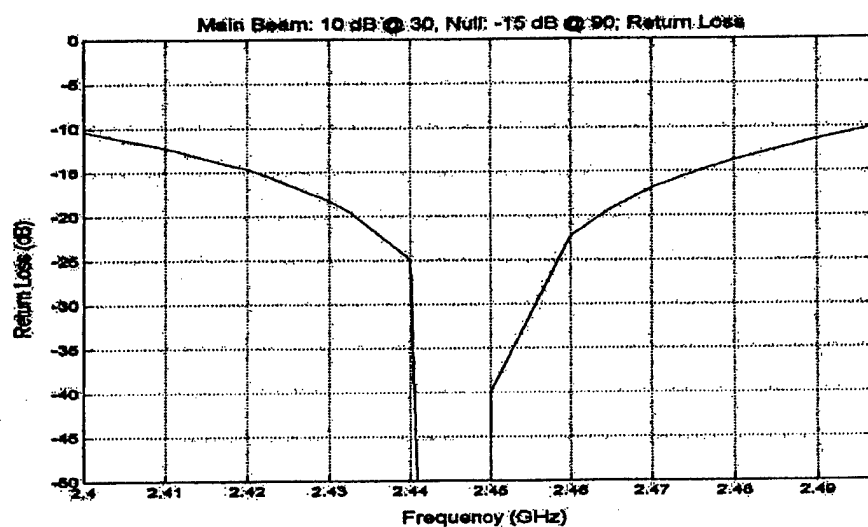


Figure 7. Return loss results for Case 2.

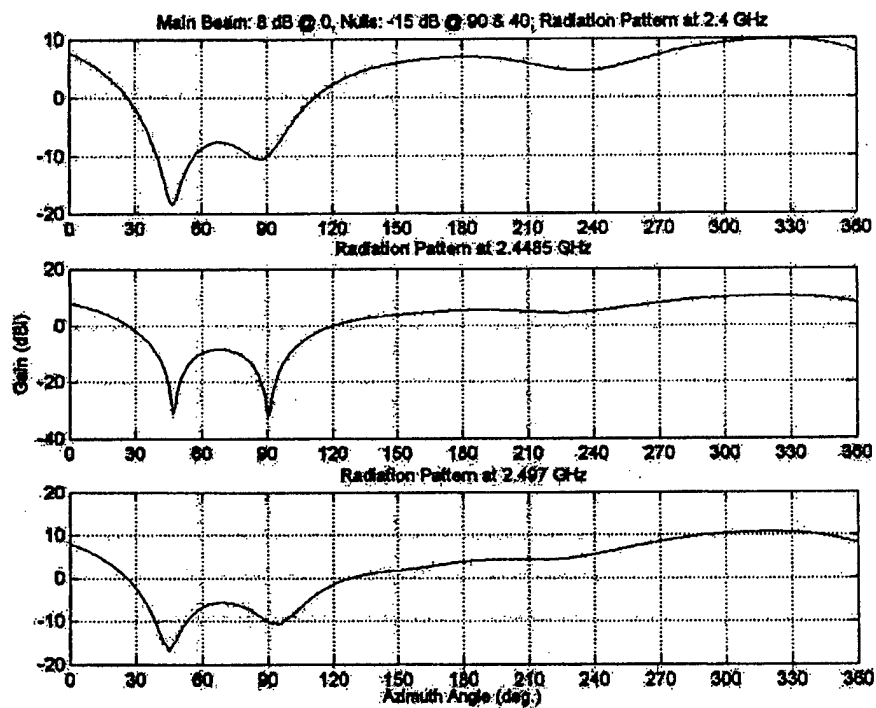


Figure 8. Radiation patterns for Case 3.

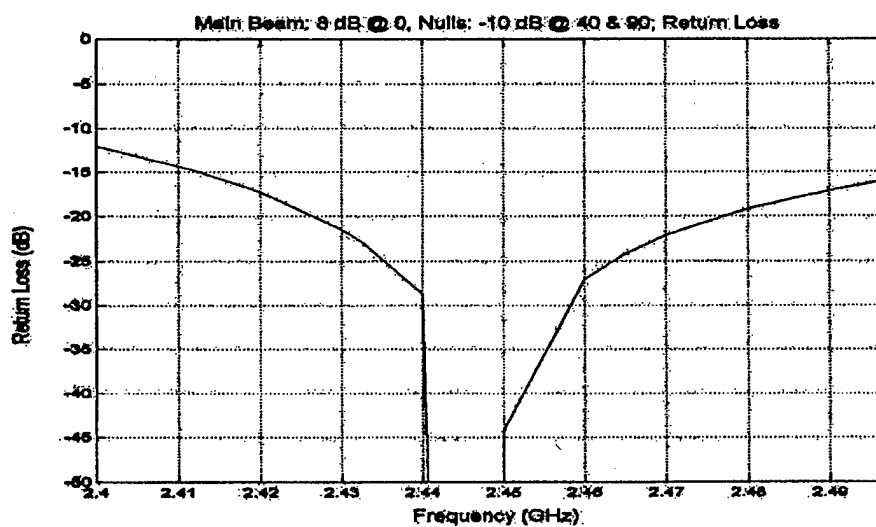


Figure 9. Return loss results for Case 3.

7 References

- [1] D. Thiel and S. Smith, *Switched Parasitic Antennas for Cellular Communications*, Norwood, MA: Artech House, 2002.
- [2] K. Gyoda and T. Ohira, "Design of Electronically Steerable Passive Array Radiator (ESPAR) Antennas," *Proc. IEEE Antennas Propagat. Soc. Int. Symp.*, vol. II, pp. 922-925, July 2000.
- [3] R. Harrington, "Reactively Controlled Directive Arrays," *IEEE Trans. Antennas Propagat.*, vol. AP-26, no. 3, pp. 390-395, May 1978.
- [4] J. Mautz and R. Harrington, "Modal Analysis of Loaded N -Port Scatterers," *IEEE Trans. Antennas Propagat.*, vol. AP-21, no. 2, pp. 188-199, March 1973.
- [5] D. Kelley, "Relationships Between Active Element Patterns and Mutual Impedance Matrices in Phased Array Antennas," *Proc. IEEE Antennas Propagat. Soc. Int. Symp.*, vol. I, pp. 524-527, June 2002.
- [6] T. Ohira and K. Gyoda, "Electronically Steerable Passive Array Radiator Antennas for Low-Cost Analog Adaptive Beamforming," *Proc. IEEE Int. Conf. Phased Array Syst. Technol.*, May 2000, pp. 101-104.
- [7] R. Schlub, J. Lu, and T. Ohira, "Seven-Element Ground Skirt Monopole ESPAR Antenna Design from a Genetic Algorithm and the Finite Element Method," *IEEE Trans. Antennas Propagat.*, vol. 51, no. 11, pp. 3033-3039, November 2003.
- [8] L. Johnson and R. Riess, *Numerical Analysis*, 2nd ed., Reading, MA: Addison-Wesley Publishing Company, Inc., 1982, Section 5.2.
- [9] J. Kennedy and R. Eberhart, *Swarm Intelligence*, San Francisco, CA: Morgan Kaufmann Publishers, 2001.
- [10] D. Boeringer and D. Werner, "Particle Swarm Optimization Versus Genetic Algorithms for Phased Array Synthesis," *IEEE Trans. Antennas Propagat.*, vol. 52, no. 3, pp. 771-779, March 2004.
- [11] R. Lewallen, *EZNEC Pro 3.0*, Beaverton, OR, <http://www.eznec.com>.

A Performance Comparison of Various Ultra Wideband Antennas Using the 3-Antenna Method

Akihide Maeda and Takehiko Kobayashi

Wireless Systems Laboratory, Tokyo Denki University

2-2 Kanda-nishiki-cho, Chiyoda-ku, Tokyo 101-8457, Japan

Phone/Fax: +81-3-5280-3839 E-mail: a.maeda@grace.c.dendai.ac.jp

Abstract

Ultra wideband (UWB) technologies have been developed to exploit a substantially new spectrum resource and to realize ultra-high-speed communication, high precision radar, and other sensing systems. Distortionless signal transmission is desirable for UWB wireless systems to accommodate such applications. The antennas used in these systems should meet several requirements: directivity (either directional or omnidirectional), low voltage-standing-wave-ratio (VSWR), low dependence of gain and group delay on frequency, and small delay spread. However, so far there was not been a full performance comparison of UWB antennas. In this study the 3-antenna method was used to achieve high accuracy, and measured and compared the performances of four representative families of UWB antennas: the monopole antenna, the double-ridged-waveguide horn (DRH) antenna, the meander line antenna, and the log-periodic dipole array (LPDA) antenna (and the narrowband half-wavelength dipole antenna for comparison) in the frequency range of 2 to 18 GHz. In terms of VSWR and dependence of gain and group delay on frequency, the volcano-smoke monopole was the best and the DRH was the second best. The LPDA antenna, designed to operate between 2 to 6 GHz yielded the largest group delay, because its electric center moved forward with increasing frequency; it also gave the largest delay spread.

1. Introduction

Antennas are an essential part of ultra wideband wireless systems. Whereas signal transmission with a minimal distortion is needed to accommodate high-rate communication or high-precision radar applications, the antenna significantly affect the UWB transmission characteristics. The antennas used in these systems, therefore, should meet several requirements [1], [2]:

Constant directivity over the UWB bandwidth: Either a directional or omnidirectional radiation pattern independent of the frequency is needed, because the variation in directivity results in the ripples in the frequency transfer function in certain directions.

Low return loss (low VSWR): The mismatches at the antenna and the circuitry degrade the overall dispersion characteristics because of multipath within the feeding cable.

Low dependence of gain and group delay: If the gain, group delay, or both depend on frequency, the pulse waveform is distorted. Constant group delay implies that the phase linearly increases with frequency.

Low delay spread: All the above affect the resulting delay spread, which should be minimal to suppress the signal distortion.

This paper describes the measured results and compares the performances (VSWR, gain, group delay, and impulse responses) of four representative UWB antennas together with a narrowband half-wavelength dipole antenna. We used the 3-antenna method [3] which does not require a standard antenna, to achieve high precision in gain measurements.

2. Measurement Description

All the measurements were carried out in a radio anechoic chamber. For VSWR measurements, the reflecting coefficients S_{11} at antenna inputs were measured with a vector network analyzer (VNA). For the other measurements, the transmitting and receiving antennas were placed 3-m apart, which fulfills the far-field condition for all the antennas under test; and the transmission coefficients S_{21} from the transmitting antenna inputs to the receiving antenna outputs were measured with the VNA. Calibration was performed with a coaxial calibration kit between the transmitting antenna input and the receiving antenna output (namely, the ends of the antenna feeding cables). Coaxial connectors were all SMA type.

2.1 Gain Measurement by the 3-Antenna Method

The 3-antenna method [3] eliminates the need for a standard antenna, which is difficult to obtain within an ultra wide bandwidth in general. Three sets of measurements are carried out using the three possible combinations of antenna A , B , and C . The result is a set of equations given by

$$\begin{aligned} G_A + G_B &= |S_{21}|_{AB} + 20 \log \left(\frac{4\pi R}{\lambda} \right) \\ G_B + G_C &= |S_{21}|_{BC} + 20 \log \left(\frac{4\pi R}{\lambda} \right) \\ G_C + G_A &= |S_{21}|_{CA} + 20 \log \left(\frac{4\pi R}{\lambda} \right), \end{aligned} \quad (1)$$

where the G_A , G_B , and G_C are the absolute gain in decibels of the antennas A , B , and C at a frequency and a direction under consideration; R is the antenna separation; λ is the wavelength; and the subscripts to $|S_{21}|$ indicate the specific combinations of two antennas. The simultaneous solution of these equations gives the gains of all three antennas as follows:

$$\begin{aligned} G_A &= \frac{1}{2} \left\{ |S_{21}|_{AB} - |S_{21}|_{BC} + |S_{21}|_{CA} + 20 \log \left(\frac{4\pi R}{\lambda} \right) \right\} \\ G_B &= \frac{1}{2} \left\{ |S_{21}|_{AB} + |S_{21}|_{BC} - |S_{21}|_{CA} + 20 \log \left(\frac{4\pi R}{\lambda} \right) \right\} \\ G_C &= \frac{1}{2} \left\{ -|S_{21}|_{AB} + |S_{21}|_{BC} + |S_{21}|_{CA} + 20 \log \left(\frac{4\pi R}{\lambda} \right) \right\} \end{aligned} \quad (2)$$

2.2 Antennas under Test

Our investigation focused on the following four UWB antenna families, shown in Fig. 1 (a) to (d):

- (a) *Monopole antenna*: Taniguchi *et al.* [4] developed this antenna, simplifying the volcano smoke antenna referred to by Kraus [5]. This consisted of a circular ground plane with a diameter of 100 mm and a teardrop-shaped monopole with a height of 25 mm. This antenna radiates omnidirectionally in the H plane and achieved low VSWR (< 1.3) from 3 to 20 GHz by optimizing its shape and size (see Appendix A).
- (b) *Double-ridged waveguide horn (DRH) antenna*: This is a most commonly used UWB directional antenna. The antenna under test was WBH2-18S, designed to operate from 2 to 18 GHz, made by Q-par Angus® [6]. The aperture size was 119×86 mm.
- (c) *Meander line antenna*: This is a commercially available miniature UWB antenna, SMT-3TO10M, made by SkyCross® [7]. Its size was 18.5 × 21.5 × 4.2 mm, excluding a coaxial connector.
- (d) *Log-periodic dipole array (LPDA) antenna*: This is another conventional, directional UWB antenna [5]. The antenna under test was designed to operate from 2 to 6 GHz and fabricated on a trapezoidal printed circuit board. The size of the board was 49-mm long × 51-mm wide.

A narrowband (5.0 GHz) half-wavelength dipole antenna equipped with a balun to accommodate a coaxial feed, shown in Fig. 1 (e), was also measured for comparison with the above UWB antennas. Two antennas of each family and one of the DRH antennas were used in the 3-antenna measurements, because the DRH antenna had the highest gain among the antennas under test. The measured radiation directions were as follows: the monopole antennas were measured at the direction included in the ground plane (horizontal), which was not necessarily the antenna main beam direction (Appendix A), but some applications such as array processing for UWB propagation studies [8] requested a use of omnidirectional antennas at and near the horizontal direction; the other antennas were measured at the main beam boresight (for the meander line antenna, the direction perpendicular to both the element surface and the coaxial connector axis and facing the radiating element), as shown in Fig. 2.

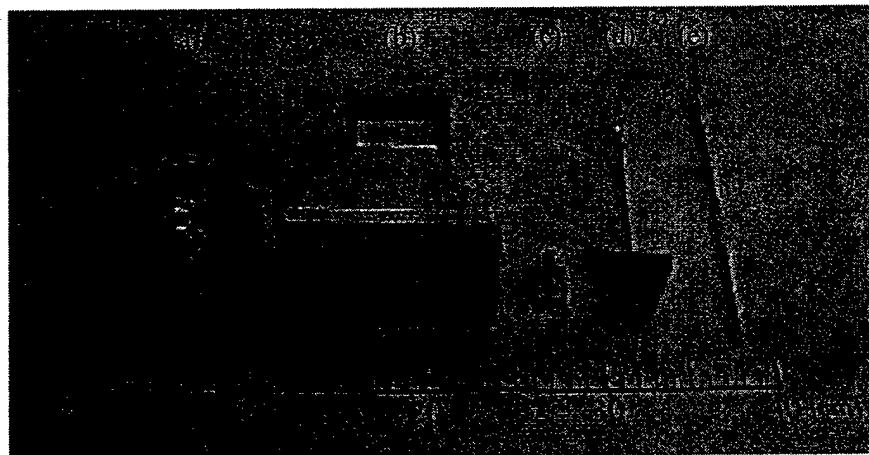


Fig. 1. The antennas under test: (a) monopole antenna, (b) DRH antenna, (c) meander line antenna, (d) LPDA antenna, and (e) 5-GHz half-wavelength dipole antenna.

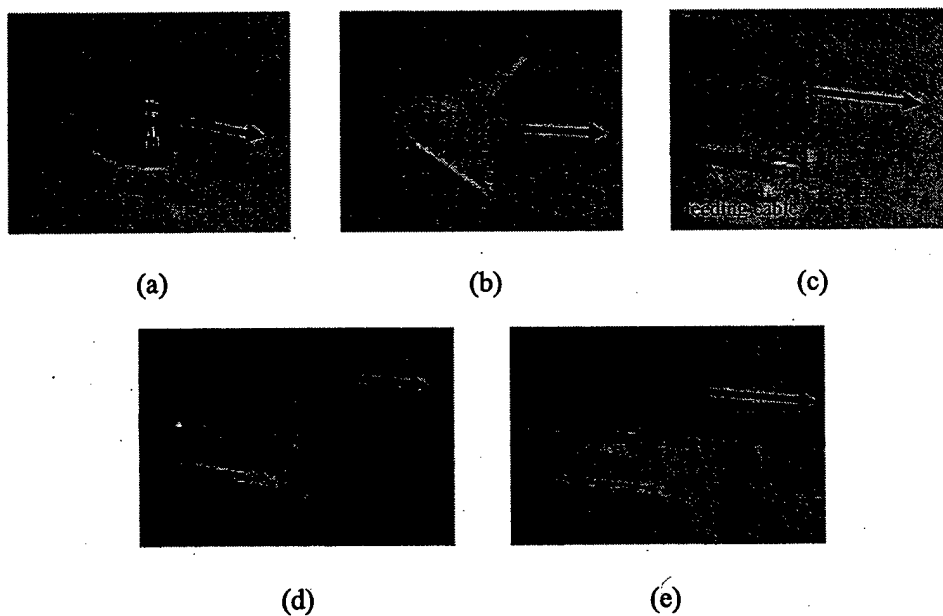


Fig. 2. The directions of measurements of the antennas: (a) monopole antenna, (b) DRH antenna, (c) meander line antenna, (d) LPDA antenna, and (e) 5-GHz half-wavelength dipole antenna.

3. Measurement Results and Discussion

3.1 VSWR

The VSWR measurement results of the five antennas are shown in Fig. 3. The monopole antenna yielded $VSWR < 1.3$ —the lowest among the five antennas—from 3 to 18 GHz (Fig. 3(a)). The variation of VSWR within the bandwidth was also the smallest. The DRH antenna exhibited $VSWR < 2.2$ —the second lowest—from 2.1 to 18 GHz (Fig. 3(b)), but the VSWR oscillatorily fluctuated. The notches in VSWR were observed in roughly 1.2 GHz intervals, caused by interference between the forwarded wave and the reflected wave from the horn aperture with 125-mm difference in path length. The VSWR of meander line antenna (Fig. 3(c)) was less than 2.5—the third lowest—from 3 to 9 GHz. The VSWR of LPDA antenna (Fig. 3(d)) exceeded 3—the worst—even in its designed bandwidth of 2 to 6 GHz, and greatly fluctuated. The half-wavelength dipole antenna (Fig. 3(e)) gave $VSWR = 1.1$ at its operating frequency of 5 GHz and $VSWR = 1.5$ near the third harmonic frequency of 14 GHz. The limited operating bandwidth is regarded as being due to the frequency characteristics of its balun. The variations in VSWR among the two antennas of the same family were less than 0.2.

3.2 Absolute Gain

The absolute gains of the five antennas measured and calculated with the 3-antenna method are shown in Fig. 4. The gain of the monopole antenna (Fig. 4(a)) was from -3 to 0 dBi with the measured bandwidth. The fluctuation in gain was the smallest among the five antennas. The DRH antenna yielded the gain from 6 to 12 dBi (Fig. 4(b)), since this antenna directionally radiates with a typical half-power beamwidth of 60° . The 6-dB fluctuation in the gain was attributable to a disturbed aperture distribution, whereas the 6 dB was much larger than that expected from the reflection ($VSWR = 2$ corresponds to a transmission loss of 0.5 dB). The gain of meander line antenna (Fig. 4(c)) ranged from -10 to 0 dBi with an average of approximately -3 dBi from 3.1 to 10 GHz. The LPDA antenna gave a relatively flat gain varying from 2.5 to 5 dBi from 2.5 to 6 GHz (but -5 dBi at 2 GHz—the lowest frequency of its designed bandwidth). The gain of the half-wavelength dipole antenna resulted in 3.0 dBi at 5 GHz, while the theoretical gain was 2.15 dBi. This 0.85-dB difference exhibited a typical measurement accuracy, which was within a reasonable range when considering the uncertainty in S_{21} measurement (typically 0.5 dB) and its accumulation in the 3-antenna method calculation (Eq. (2)). Figure 4 (e) revealed that even the half-wavelength dipole antenna brought about a certain wideband gain of

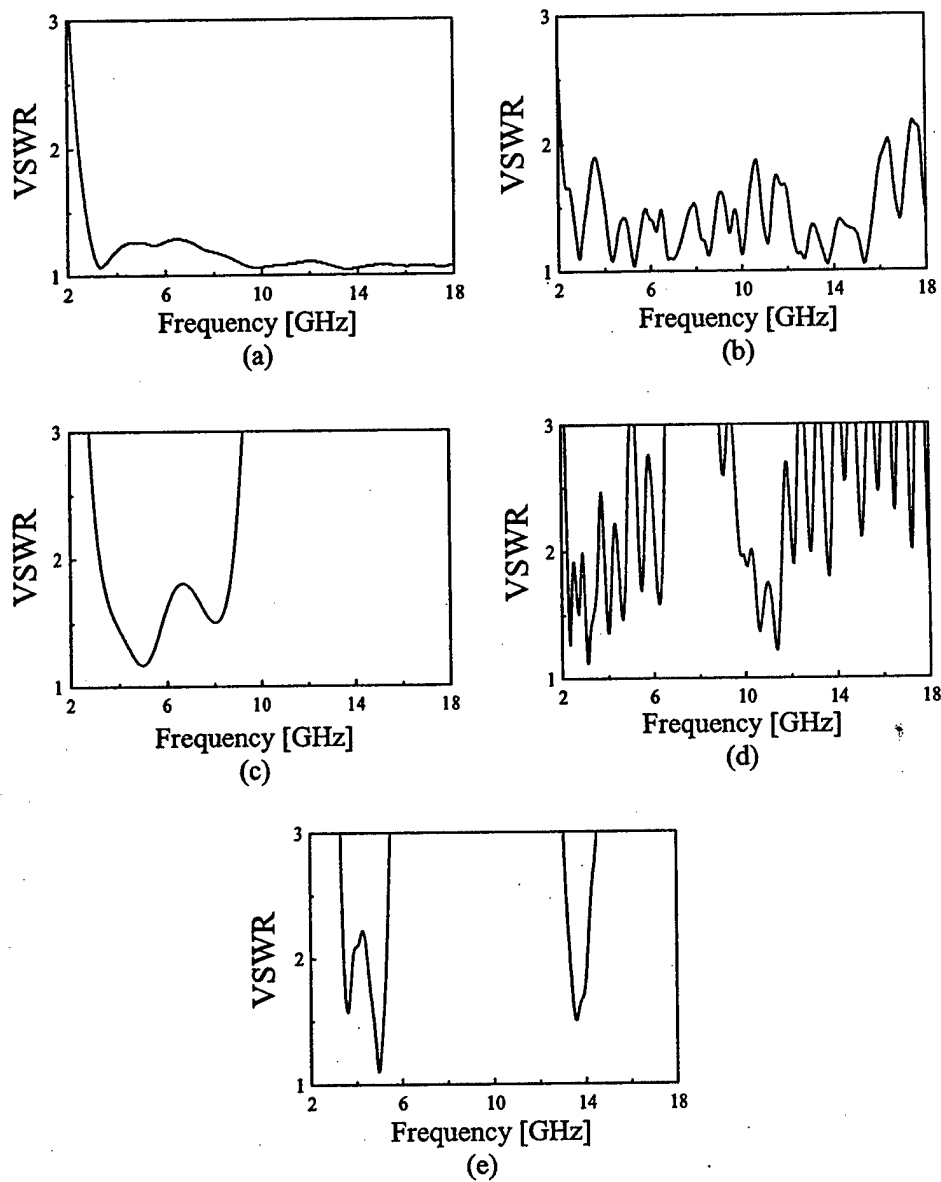


Fig. 3. The measured voltage standing wave ratio of the five families of antennas: (a) monopole antenna, (b) DRH antenna, (c) meander line antenna, (d) LPDA antenna, and (e) 5-GHz half-wavelength dipole antenna.

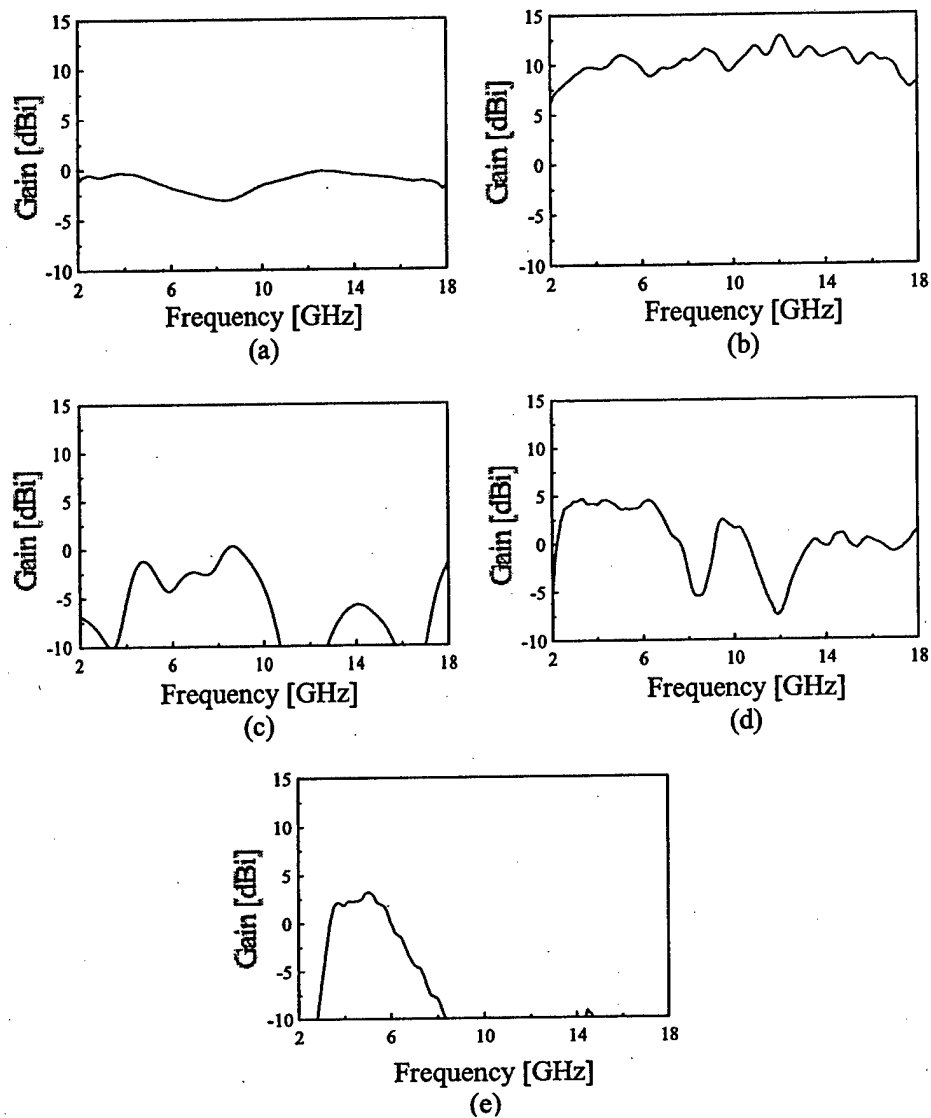


Fig. 4. The measured absolute gain of the five families of antennas measured with the 3-antenna method: (a) monopole antenna, (b) DRH antenna, (c) meander line antenna, (d) LPDA antenna, and (e) 5-GHz half-wavelength dipole antenna.

more than 2.0 dBi from 3.5 to 5.5 GHz. The variations in gain of the same family were within 0.3 dB.

3.2 Group Delay

The group delay of each antenna was measured with the VNA by directing a pair of the same antennas face-to-face and 3-m apart and by halving the group delay (of two antennas) to result in that of one antenna. The results are shown in Fig. 5. The maximum and average group delays within the designed bandwidth were as follows:

- (a) *the monopole antenna:*
0.25 and 0.08 ns from 3 to 18 GHz
- (b) *the DRH antenna:*
0.74 and 0.24 ns from 2 to 18 GHz
- (c) *the meander line antenna:*
1.30 and 0.27 ns from 3.1 to 10.6 GHz
- (d) *the LPDA antenna:*
2.00 and 1.35 ns from 2 to 6 GHz
- (e) *the half-wavelength dipole antenna:*
0.80 and 0.68 ns from 3.3 to 5.5 GHz

Since even the narrowband dipole antenna had a substantial wideband gain from 3.5 to 5.5 GHz as mentioned in the previous section, its group delay is shown Fig. 5 (e). The group delay of the LPDA antennas decreased almost linearly from 2.0 to 0.8 ns from 2 to 6 GHz, because the electric center moved forward with increasing frequency. Although the LPDA antennas have been widely used for wideband applications, the large group delay makes this antenna unsuitable for UWB waveform transmission. In terms of the group delay, the monopole antenna was the best, followed by the DRH antenna.

3.3 Impulse Response

The impulse response of a pair of the same antennas was measured with VNA by sweeping the frequency from 2 to 18 GHz and by Fourier-transforming the frequency responses into the time domain. The results are shown in Fig. 6, where the abscissas of the graphs start at 10 ns, which corresponds to the propagation path length of 3 m. To compare the impulse responses of the five antennas, we derived the delay spreads, though the delay spreads have conventionally used for making statistical evaluation of the multipath propagation environments. The derived delay spreads were as follows:

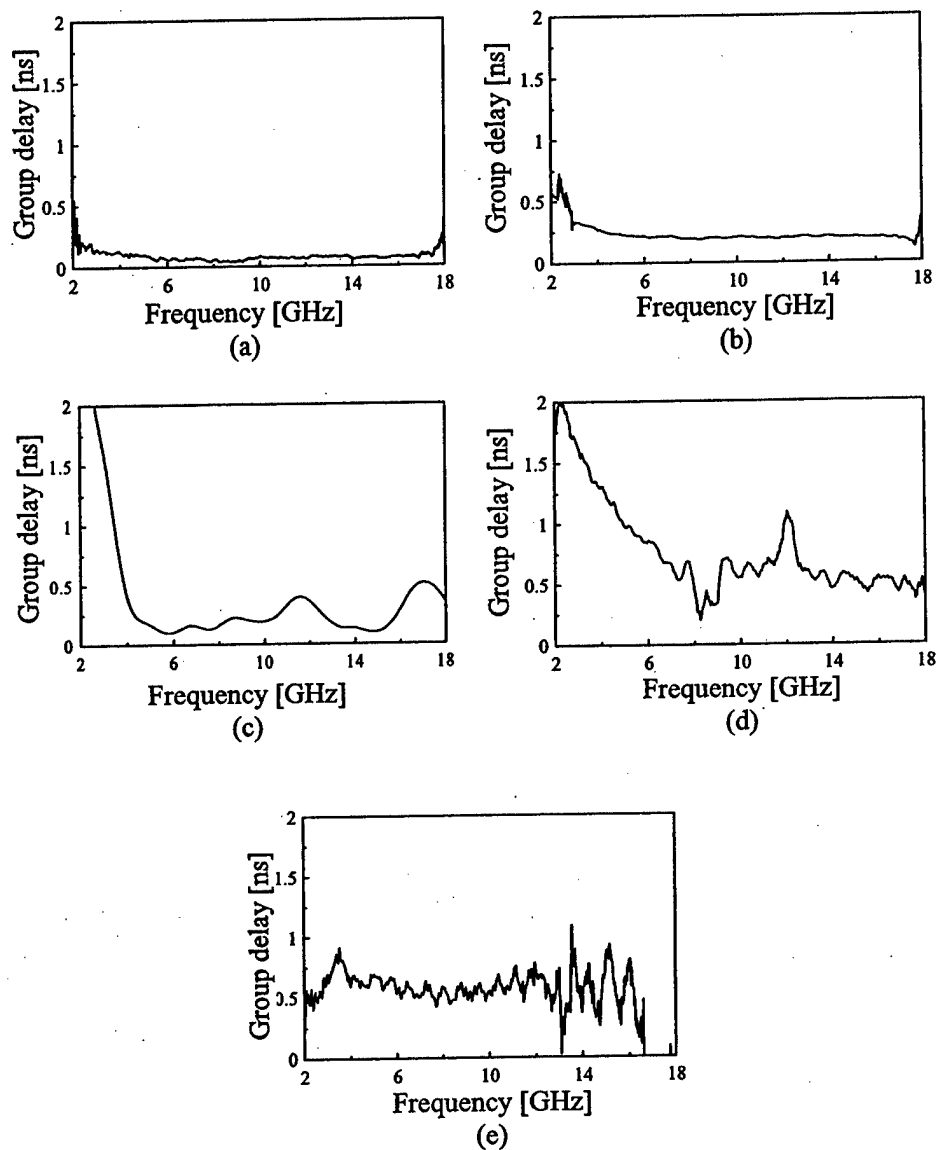


Fig. 5. The measured group delay of the five families of antennas: (a) monopole antenna, (b) DRH antenna, (c) meander line antenna, (d) LPDA antenna, and (e) 5-GHz half-wavelength dipole antenna.

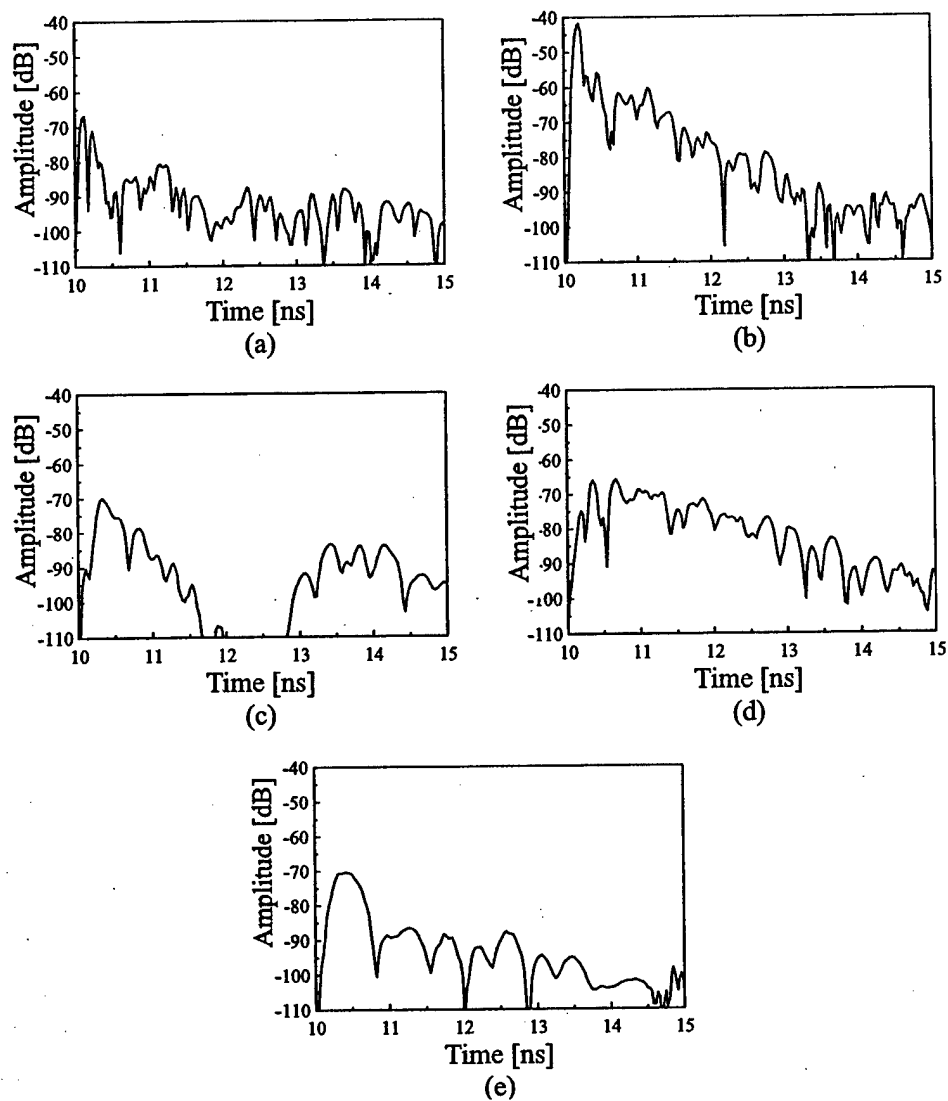


Fig. 6. The measured impulse responses of a pair of antenna families under test: (a) monopole antenna, (b) DRH antenna, (c) meander line antenna, (d) LPDA antenna, and (e) 5-GHz half-wavelength dipole antenna. The abscissas start at 10 ns, which corresponds to the propagation length of 3 m.

(a) <i>the monopole antenna:</i>	0.28 ns
(b) <i>the DRH antenna:</i>	0.12 ns
(c) <i>the meander line antenna:</i>	0.10 ns
(d) <i>the LPDA antenna:</i>	0.65 ns
(e) <i>the half-wavelength dipole antenna:</i>	0.29 ns

As expected from the frequency dependence of gain and group delay, the monopole, the DRH, and the meander line antennas yielded shorter delay spreads than the LPDA antenna.

4. Conclusion

The UWB performances—VSWR, absolute gain, group delay, and impulse responses—of the four UWB antennas and one narrowband one were measured and evaluated. The absolute gains were measured with the 3-antenna method, which resulted in a typical accuracy of less than 1 dB. The omnidirectional monopole antenna, simplified from the volcano-smoke antenna, and the directional DRH antenna were the best among all antennas under test, considering the UWB waveform transmission. The LPDA antenna yielded the largest group delay and delay spread, because its electric center moved forward with increasing frequency. The LPDA antenna is probably not suitable for UWB waveform transmission without appropriate compensation.

5. Acknowledgment

This work has been supported in part by a grant for Top Priority Research and Development to be Focused (Frequency Resources Development) from the Ministry of Public Management, Home Affairs, Posts and Telecommunications of Japan within its R & D Support Scheme for Funding Selected IT Proposals, and in part by the Research Institute for Science and Technology, Tokyo Denki University, under the grant Q02J-08.

Appendix A

The monopole antenna [4] was developed to meet omnidirectional in azimuth and low VSWR requirements [8] by simplifying and optimizing the shape and size of volcano-smoke antenna [5]. The evolution process from an infinite biconical antenna via the volcano-smoke antenna to the monopole antenna is summarized as follows: Infinite biconical antennas (Fig. A1(a)) have a self-similar structure and are, therefore, frequency-independent, and

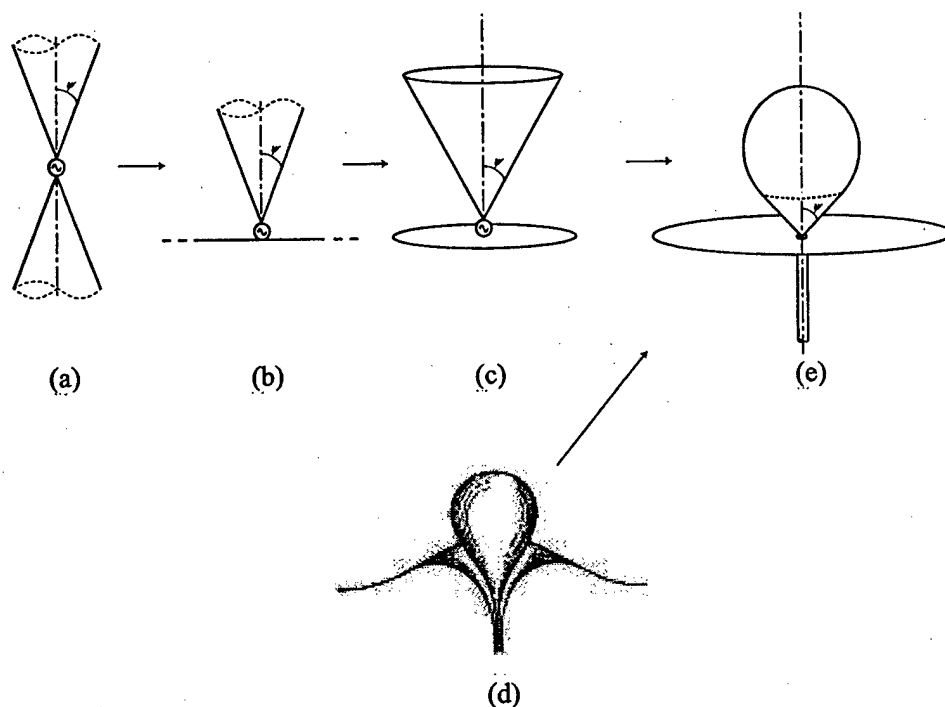


Fig. A1. Evolution of broadband omnidirectional antennas: (a) infinite biconical, (b) infinite monocone (c) finite monocone (discone), (d) volcano smoke (in cutaway view) , and (e) proposed antenna.

omnidirectional in azimuth. By replacing one of the cones with the infinite ground plane, the infinite biconicals are extended to infinite monocones (Fig. A1(b)), which are also frequency-independent and omnidirectional. By truncating the ideal infinite monocone, a real finite monocone (Fig. A1(c)), widely known as a discone, can be obtained. This structure is omnidirectional in azimuth, but not frequency-independent anymore since the truncation causes reflected current from the base of the cone. The volcano smoke antenna (Fig. A1(d)) substantially fulfills the above two requirements simultaneously, but its shape is not well-defined.

The proposed monopole antenna consists of a circular ground plane and a teardrop that is defined as a combination of a finite cone and a sphere to be inscribed inside the cone at the cone's base, as shown in Fig. A1(e). The teardrop is excited with a coaxial cable penetrating the ground plane. This antenna is considered either as a rounded finite monocone antenna (Fig. A1(c)) or

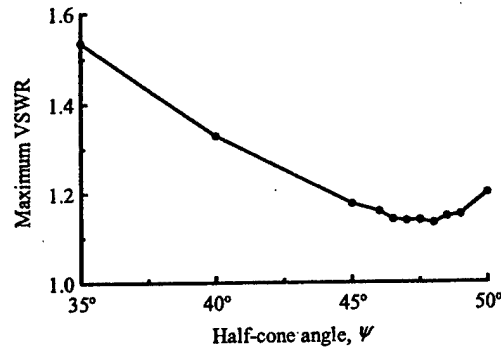


Fig. A2. Computed maximum VSWR of the proposed antenna between 3.1 and 10.6 GHz.

as a simplified form of the volcano smoke (Fig. A1(d)). Input impedances of the infinite biconical and infinite monocone antennas are governed by the half-cone angle ψ (Fig. A1(a) and (b)). It is also thought that the input impedance of the proposed antenna is determined by the half-cone angle ψ . The input impedance was calculated with the finite integration method [9]. Assuming 50- Ω excitation, the maximum VSWR between 2 and 10 GHz is shown in Fig. A2, from which the optimum half-cone angle ψ is found 48°. This formation was found to outperform the finite monocone in the VSWR through calculation and the first prototype experiment [10]. The minimum height of the teardrop was calculated to be around a quarter wavelength at the lowest operation frequency. The monopole antenna being tested in this paper was constructed as shown in Figs. A3 and A4. The teardrop was 25 mm high and the ground plane was 100 mm in diameter. The calculated (finite integration method) and measured VSWR are shown in Fig. A5. This antenna demonstrated VSWR < 1.3 between 3 and 20 GHz. The calculated (with the finite integration method) and measured E-plane radiation patterns of this antenna at 3, 6, 9, and 12 GHz are depicted in Figs. A5 and A6, where 0° corresponds to the zenith and 90° and 270° correspond to the horizontal plane. This antenna was utilized for an array antenna formation in spatio-temporal UWB channel sounding to achieve 10° and 0.67-ns resolution in spatial and temporal domains [8]. The channel sounding system was also successfully deployed in various propagation environments [11].

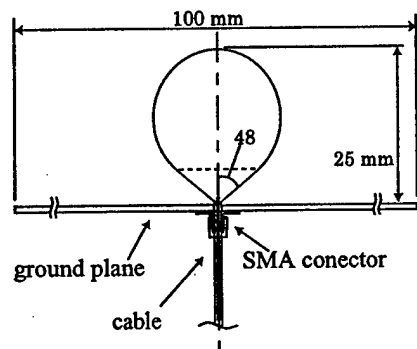


Fig. A3. Cross section of the prototype antenna.

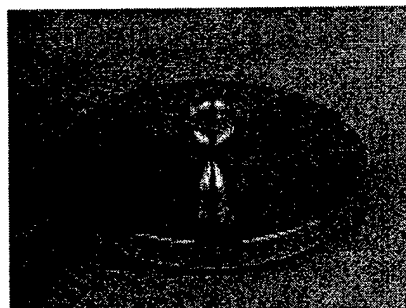


Fig. A4. The prototype antenna.

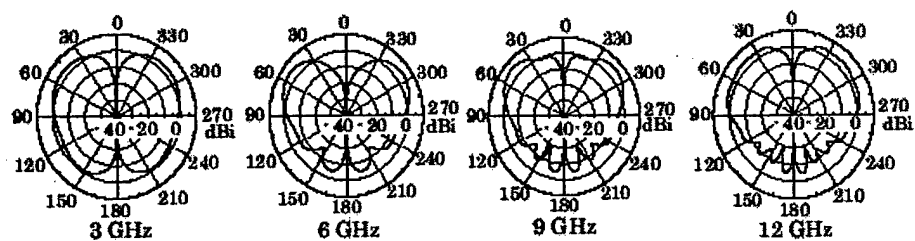


Fig. A5. Calculated E-plane radiation patterns of the prototype antenna.

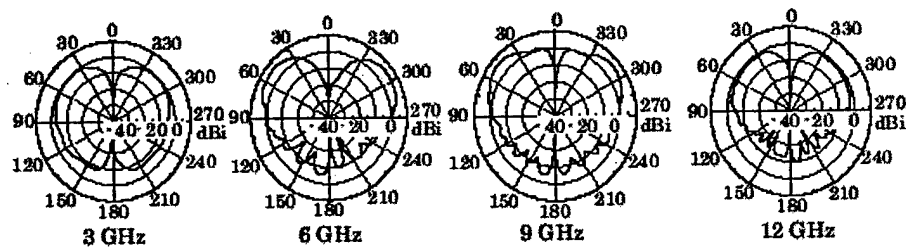


Fig. A6. Measured E-plane radiation patterns of the prototype antenna.

6. References

- [1] J. Takada, "Review on antenna design and channel characterization of ultra-wideband technologies," in *The 1st Electrical Engineering/Electronics, Computer, Telecommunications and Information Technology Annual Conference (ECTI-CON 2004)*, Pattaya, Thailand, May 13-14, 2004.
- [2] W. Sorgel, C. Waldschmidt and W. Wiesbeck, "Antenna characterization for ultra wideband communications," in *2003 Int. Workshop on Ultra Wideband Systems (IWUWBS 2003)*, cr1030, Oulu, Finland, June 2-5, 2003.
- [3] A. C. Newell, C. F. Stubenrauch, and R. C. Baird, "Calibration of microwave antenna gain standards," *Proc. IEEE*, vol. 74, pp. 129-132, Jan 1986.
- [4] T. Taniguchi and T. Kobayashi, "An omnidirectional and low-VSWR antenna for the FCC-approved UWB frequency band," in *IEEE Antennas and Propag. Society Int'l Symp.*, vol. 3, pp. 460-463, Columbus, OH, June 22-27, 2003.
- [5] J. D. Kraus, "Antennas, 2nd ed.," McGraw-Hill, New York, NY, 1988, pp. 692-694.
- [6] <http://www.skycross.com/pdf/SMT3TO10MA.pdf>
- [7] http://www.q-par.com/pages/1.5_to_18_GHz_Wide_band_horn.pdf
- [8] K. Haneda, J. Takada, and T. Kobayashi, "Experimental evaluation of a SAGE algorithm for ultra wideband channel sounding in an anechoic chamber," in *2004 Int. Workshop on Ultra Wideband Systems Joint with Conference on Ultra Wideband Systems and Technologies (Joint UWBST & IWUWBS 2004)*, WA3-2, Kyoto, Japan, May 18-24, 2004.
- [9] T. Barts, *et al.*, "Maxwell's grid equations," *Frequenz*, vol. 44, no. 1, pp. 9-16, 1990.
- [10] T. Taniguchi and T. Kobayashi, "An Omnidirectional and low-VSWR antenna for ultra-wideband wireless systems," *2002 IEEE Radio and Wireless Conf. (RAWCON 2002)*, pp. 145-148, Aug. 11-14, 2002.
- [11] K. Haneda, J. Takada and T. Kobayashi, "Double directional ultra wideband channel characterization in a line-of-sight home environment," in *COST 273 11 th Management Committee Meeting*, Duisburg, Germany, Sept. 20-22, 2004, to be presented.

2ND-MODE FOUR-ARM SLOT SPIRAL ANTENNAS

Nathan Stutzke, Neill Kefauver, Dejan Filipovic
Department of Electrical and Computer Engineering
University of Colorado at Boulder
425 UCB, Boulder, CO 80309-0425

Abstract: The design and performance of a 4-arm equiangular slot spiral antenna operating in the 2nd-mode is discussed. Three feeding methods are proposed including a dual infinite or Dyson balun, a dual microstrip feed, and a vertical coaxial probe feed. The Dyson balun provides a broadband feed with little far-field contamination. However, it is difficult to fabricate identically on multiple antennas and imposes limits on the antenna design parameters. The dual microstrip feed is planar and easily fabricated but far-field contamination can result from radiation of the microstrip lines and coupling of the microstrip and slot traveling waves. The vertical probe feed can be reliably fabricated and duplicated on multiple antennas, has a single port, and requires no underlying mode forming network. It also allows design flexibility with respect to slot-to-metal ratio and growth rate. Numerical tools including an in-house Finite-Element Boundary-Integral (FE-BI) code and Ansoft HFSS are used in designing the antennas. Antenna performance is verified with measurements.

1. Introduction

Spiral antennas are attractive for mobile communications, early warning, direction finding, and other applications due to their low profile, broadband pattern and impedance characteristics, circularly polarized radiation, and multi-mode capabilities. They can be fabricated in wire, printed strip or printed slot form, the latter of which will be investigated in this paper. Two spiral geometries that have received much attention in the past are the equiangular and Archimedean type. Equiangular spirals belong to a class of antennas termed frequency independent antennas [1,2]. Although Archimedean spirals do not fall into this category if a strict definition given by Rumsey is imposed, they exhibit nearly frequency independent performance over wide bandwidths and have been more widely investigated than equiangular spirals [2,3]. True frequency independence requires an infinitely large antenna with infinitely small feed transition in the center. Thus, frequency limits are imposed in practice by the finite dimensions of the antenna.

According to the band theory, radiation at a particular frequency occurs in rings where the circumference of the spiral is $M\lambda$, where M is the mode being excited [2,3]. Thus, the maximum diameter of the antenna determines the lowest frequency of operation, while the size of the center feed region limits the high frequency performance. At low frequencies where the $M\lambda$ ring approaches the outer edges of the antenna, unradiated power can be reflected from the ends of the spiral arms and reradiated with the opposite polarization sense. Reflections from the arm ends can be minimized by carefully designing their terminations to absorb the unradiated energy. Arm terminations are often implemented with absorber paint or impedance tapers realized with multiple chip resistors. For the antennas in this paper a circular open end and single chip resistor are utilized as an arm termination. At high frequencies radiation of residual in-phase currents can occur where the circumference is $K\lambda$, where $K > M$. Typically radiation from higher order modes is undesired and results in pattern deformation and deteriorated symmetry of the conical cut patterns or omnidirectionality. The radiating region of the antenna can be designed so as to maximize radiation efficiency of the desired mode and reduce the amount of contamination from higher order modes. In general, self-complementary spirals (50% slot, 50% metal) provide the best compromise between radiation efficiency and other antenna parameters of interest such as impedance, omnidirectionality, and axial ratio.

In order to excite the M^{th} -mode of a spiral antenna a total phase progression of $M \cdot 360^\circ$ is required at the feed region. If properly excited the same phase progression will be present along a conical cut in the antennas far field. It is generally accepted that an N -arm spiral can radiate $N-1$ broadband modes. While the 1st mode has one broad beam in the boresight direction, all other spiral modes have a conical beam with a broadside null. The phasing necessary to excite the second mode on a four arm spiral (180° between arms) and a typical radiation pattern are shown in Figure 1. Unidirectional patterns of this type were first obtained with a 4-arm non-planar conical spiral operating in the 2nd mode [4]. Similar spirals utilizing complex mode forming networks are used in surveillance applications [2].

In this paper 4-arm printed slot spirals excited in the second mode are investigated. Three feeding methods for 2nd-mode operation are proposed. These are the dual-Dyson balun, a dual microstrip feed, and a single vertical coaxial probe feed. Advantages and limitations of each will be discussed while numerical simulations and measurements are presented to verify the performance of the feeds and the antenna itself. Antenna operation is simulated with Ansoft HFSS and an in-house FE-BI code. Ansoft HFSS is used mainly to model the complicated microstrip fed antenna while the FE-BI code is used for the vertical probe feed and ideal

planar feed (Dyson balun). Simulations utilize an infinite waveguide backing realized with a perfect absorber [5]. Measured antennas have metallic cavities loaded with absorber. All data are presented in terms of normalized frequency f/f_0 , where f_0 is the frequency at which $2\lambda_0=\pi d$ and d is the spiral diameter.

2. Dual-Dyson Balun Feed

The first reported method of feeding a two-arm slot spiral antenna was the infinite coaxial balun proposed by Dyson [6]. Recently dual mode operation of a 4-arm Archimedean slot spiral with a dual-Dyson balun was demonstrated [7]. The infinite or Dyson balun is fabricated by soldering a semi-rigid coaxial cable between slot arms and forming a coax to slotline transition at the center. Figure 2 indicates how the phasing conditions for 2nd-mode operation (180° per arm, 720° total) are achieved for the 4-arm slot spiral with a dual-Dyson balun. Notice that adjacent arms are connected resulting in a CPW-like structure in the center and wound into a spiral. As denoted in the figure, both ports are fed in phase for 2nd-mode operation. The infinite balun can provide broadband impedance characteristics with little contamination of the antennas far-field. Drawbacks of this feeding method include tedious fabrication, difficulty in duplicating the feed identically on multiple antennas, changes in cable properties due to extensive heating during fabrication, and feed cable losses at higher frequencies. Also, a sufficient amount of metal must be left between the slot arms in order to allow soldering of the coaxial cable to the ground plane and to match the input impedance to 50Ω. Thus, for a given aperture size the spatial requirements for feed fabrication, losses, and impedance requirements will limit the arm length (determined by growth rate) and or slot to metal ratio of the antenna.

2.1 Design Considerations

Several parameters affect the impedance and radiation properties of the spiral antenna. Slot-to-metal ratio, arm length (determined by growth rate for a given aperture size), and arm termination are a few. Slot-to-metal ratio affects both the input impedance and radiation properties of the spiral. Equiangular spirals are often designed to be self-complementary (50% slot-to-metal ratio) because they typically have more symmetric patterns than high or low slot-to-metal ratio spirals. For example, Figure 3 shows the simulated (with FE-BI code) omnidirectionality of three 5cm diameter 4-arm spirals with 25, 50 and 75% slot-to-metal ratios. All three are fed with an ideal planar feed and the arms are terminated in a perfect absorber. The self-complementary geometry shows the best omnidirectionality over the frequency range investigated. Other parameters not shown such as gain, input reactance, and axial ratio also exhibit the best values for self-complementary structures. In general, the longer the spiral arms the better the far-field performance. However, it has been shown that the arm length needs only to be on

the order of a wavelength at the lowest frequency of operation to achieve symmetric 1st-mode radiation patterns [6].

Proper arm termination is critical at the low end of the frequency band where un-radiated traveling wave energy can reflect from the ends and reradiate with opposite polarization. One previously employed technique with Archimedean spirals is the use of a lossy impedance taper implemented with multiple lumped resistors [8]. This technique is not well suited for equiangular spirals as the slot width quickly increases as you move away from the arm end. Instead, a circular open end and a single resistor at the junction with the slot line are utilized (see antenna in Figure 3.4). Omnidirectionality at an elevation of 45° is shown in Figure 4 for a dual-Dyson equiangular spiral with various resistor values at the arm terminations. Chosen values correspond to chip resistors that were available. Notice that the impact on performance is more evident at low frequencies where the radiating ring approaches the outside of the antenna. At the low frequency end 182Ω resistors provide nearly a 2dB improvement in omnidirectionality as compared to 10Ω resistors. According to the simulated data it appears that the resistor value is not extremely critical as long as it falls within a somewhat broad range. The appropriate value will differ depending on the antenna geometry and utilized substrate.

2.2 Realized Antenna

The dual-Dyson balun antenna shown in Figure 5 is fabricated on a 0.0508cm (0.020") thick Rogers Ultralam substrate with $\epsilon_r = 2.5$ and has a maximum diameter of 5cm. The dual-Dyson balun is constructed from two 1.19mm (0.047") diameter semi-rigid coaxial cables. For 2nd mode excitation, radiation will occur where the circumference is 2λ so the lowest theoretical frequency of operation is $f_0 \approx 4\text{GHz}$. In the central region, from a radius of 4mm to 8mm, the spiral is Archimedean with a slot width of 0.5mm and a metal width of 2mm. Outside a radius of 8mm, the spiral is equiangular with a slot-to-metal ratio of 30%. The combination of Archimedean and equiangular spirals leaves sufficient metal area for embedding the infinite coaxial balun. The cable length necessary for constructing the Dyson balun is short relative to that required if the Archimedean center region was continued throughout the geometry. This somewhat simplifies the balun fabrication and reduces the losses due to the feed cables. Additionally, the only hardware required for mode formation is a simple power divider since the two ports are fed in phase.

The theoretical free space input impedance of a self-complementary (50% slot-to-metal ratio) 4-arm equiangular spiral operated in the 2nd mode using the Dyson balun type feed is 94Ω. However, the input impedance varies with slot-to-metal

ratio, and is dependent on the thickness and permittivity of the substrate used for fabrication. For example, Figure 6 shows the simulated input impedance with three different substrate thicknesses corresponding to those on hand at the time of fabrication. For thicker substrates the input impedance is reduced. However, thicker substrates result in less efficient operation and adversely affect the far-field performance. The 0.0508cm (0.020") thick substrate was found to be the best compromise for lowering input impedance without compromising far-field performance. This substrate also provides mechanical rigidity and thermal stability to prevent warping during fabrication of the infinite balun. With a 30% slot-to-metal ratio and utilized substrate the average input impedance is around 75Ω , resulting in a nominal return loss of -14dB without any impedance matching circuitry.

2.3 Results

Simulated and measured results for the above described antenna are plotted versus normalized frequency f/f_0 , where $f_0=4\text{GHz}$ for this antenna. Simulated results are obtained with the antenna embedded in an infinite ground plane using an FE-BI code. A circular waveguide filled by a perfectly matched absorber is used to suppress backward radiation. Measured results are obtained with the antenna embedded in a circular ground plane with diameter of approximately $6\lambda_0$. An absorber filled cavity is used to suppress backward radiation during measurements and could be removed if bidirectional radiation is desired.

It should be noted that the antenna was fabricated with the feed points slightly offset from the center. Simulated data are obtained with feeds in approximately the same location, as well as with the feeds perfectly centered. This fabrication error degrades some far-field parameters, particularly the omnidirectionality at higher frequencies. However, there is good agreement between simulated and measured results with the offset feeds. Thus, it is safe to assume that if the antenna were fabricated more precisely, the measured data would correlate with the simulated data for perfectly centered feeds. Also, measured data are presented here with the complex far-field response of a single channel/port rotated by 180° and added to the original response.

Simulated and measured return loss with offset feeding points is shown in Figure 7. Simulated return loss is obtained directly at the actual feed points in the center of the antenna while the measured return loss includes the infinite balun feed cables. Numerical simulations predict return loss better than 10dB for the frequency range investigated. For $f/f_0 < 1.5$ there is reasonable agreement of the measured and simulated values. At higher frequencies, however, the return loss of the realized antenna deviates from the predicted behavior and is worse than

expected. This change in return loss may be due to thermal and mechanical stresses presented to the cables during assembly. Note that the overall oscillation in the measured return loss is due to the ringing effect in the feed cables.

Maximum gain versus normalized frequency is shown in Figure 8. The nominal measured gain of the antenna is around 3dBic for $f/f_0 > 1.5$. More gain variation with frequency is observed experimentally than is predicted numerically. This may be due to the finite size ground plane used in measurements or some fabrication issues that are difficult to control such as solder residue, effects from feed cables, and temperature effects on cable losses due to soldering. Overall, there is reasonable agreement between measured and simulated data. It is apparent that the offsetting of the feeds is not detrimental to the antenna gain. In fact, gain is somewhat higher over the middle of the frequency range of interest.

Axial ratio is an important parameter for spiral antennas, indicating the purity of the circular polarization. Measured and simulated axial ratio at the point of maximum gain (ϕ_{\max} , θ_{\max}) for the proposed antenna is shown in Figure 9. Axial ratio is high at low frequencies where the antenna is not electrically large enough to support radiation from the 2λ ring. At higher frequencies the axial ratio decreases. The simulated results with offset feeding points predict axial ratio below 3dB for $1.3 < f/f_0 < 3.2$. The measured axial ratio is slightly higher, but is below 5dB for $f/f_0 > 1.2$. Comparing the two simulated results with offset and centered feeds shows that offsetting of the feed points does not significantly affect the antenna performance with respect to its ability to produce circularly polarized radiation at the angle of maximum gain.

Spirals are well known for their omnidirectional radiation patterns [2,3]. Measured and simulated omnidirectionality at the elevation (θ_{\max}) of maximum gain for the proposed antenna are shown in Figure 10. With the offset feed points there is good agreement between simulated and measured omnidirectionality. However, the omnidirectionality is significantly deteriorated. With centered feeding points simulations predict omnidirectionality below 3dB from $f/f_0 \approx 0.9$ to $f/f_0 \approx 3$. If the infinite balun feed structure were better fabricated it is expected that the measured performance would be much improved. Additionally, the offset feeding causes radiation from the 4th mode to be higher than expected, as indicated by the increasing pattern asymmetry starting near $f/f_0 = 2$. For the properly fed antenna, simulations show pattern contamination from higher modes beginning with the 6th mode near $f/f_0 = 3$, as theory predicts.

Measured and simulated co- and cross-polar radiation patterns at $1.5f_0$ are shown in Figure 11. Notice that some small pattern ripple due diffraction from the finite

size ground plane is evident. At this frequency the effects of the offset feed points are not yet apparent. Decomposition of the modal content of the measured antenna pattern [3] is shown in Figure 11. Theoretically the radiation from the 4th mode should be significantly less efficient than what was measured. However, as discussed earlier, the realized antenna has offset feed points and is thus plagued by more efficient 4th mode radiation. It is important to note that the exponential/equiangular spiral growth is more sensitive to the accuracy of the feed phasing than corresponding (small) Archimedean growth. At $f/f_0=3.75$ radiation from the 4th mode is as large as that from the desired 2nd mode. It is expected that the 4th mode content would significantly decrease if the feed points were centered, as indicated in Figure 9 by the low omnidirectionality with the centered feed for $f/f_0>1.6$.

3. Vertical Coaxial Probe Feed

Another method for feeding a 4-arm slot spiral antenna demonstrated for the first time in this work is a single vertical coaxial probe. Cross-section and top views of the feed structure are shown in Figure 13. The vertical probe feed consists of an absorber filled cavity through which a small semi-rigid coaxial cable passes. The inner conductor of the coax makes contact to the top metal in the center between the slot spiral arms which in this case is similar to the signal line of a conductor backed coplanar waveguide with finite size ground planes. The outer conductor of the coax is connected to a small metallic disk on the bottom side of the substrate providing a proper grounding path for the currents. Two metallic pins connect the metal between adjacent spiral arms (grounding conductor of the CPW) to the metallic disk on the bottom side of the substrate to give the desired phase progression for 2nd mode operation. To the best of our knowledge this feed has never before been used in conjunction with 4-arm slot spiral antennas. The vertical probe feed method can be reliably fabricated and does not pose lower limits on the metal width between slots. This allows a wider range of slot-to-metal ratios and arm lengths to be explored. Also, an antenna fed in this manner has a single port and requires no mode forming network. However, if the feed region is not designed carefully the far-field performance can be somewhat degraded as compared to the properly built infinite dual-Dyson balun.

3.1 Design Considerations

With the vertical probe feed there are few limitations on the spiral dimensions. However, in addition to the parameters discussed in section 2.1, the design of the vertical probe feed can significantly affect the input impedance and the far-field performance of the antenna as well. Of particular importance is the size of the ground disk which connects the outer conductor of the coaxial feed to the spiral arms on the top side of the substrate. Whereas the theoretical input impedance of

each port of the dual-Dyson feed is $\sim 95\Omega$, the vertical probe feed is essentially feeding the two ports in parallel and the input impedance is cut in half. This would seem to provide a very close match to the 50Ω feed cable, however, the added capacitance from the grounding disk tends to further reduce the input impedance. For example, the simulated input impedance of three identical 5cm diameter equiangular spirals with different size ground disks is shown in Figure 14. As expected the input impedance decreases as the ground disk size increases due to the increased capacitance at the feed region. The feed region design can affect the far field performance as well. Figure 15 shows the omnidirectionality at the elevation angle of maximum gain for the same three cases of ground disk size. Clearly the far-field performance is significantly degraded if the ground disk is taken too large. Note that the minimum size of the disk is determined by the distance between the two grounding pins, or the physical fabrication limits. The metal width between slots needs only to be just somewhat larger than the diameter of center conductor of the coax probe. Thus, if the ground disk is kept small it can be designed solely to give a desired input impedance. For 2nd mode operation it is apparent that to maximize far field performance and minimize return loss the ground disk should be kept as small as possible.

3.2 Realized Antenna

The vertical probe fed equiangular spiral antenna shown in Figure 16 is realized on a 0.031" thick Roger's RT/duroid 5880 substrate with relative permittivity of 2.2. The feed cable is a 0.085" semi-rigid coax. The spiral is equiangular, self-complementary, and each arm is $1\frac{1}{2}$ turns. The diameter is 10cm which gives a theoretical minimum operation frequency of $f_0 \approx 2\text{GHz}$. The equiangular geometry begins at a radius of 0.5cm giving a theoretical maximum frequency of approximately 20GHz which is well above the frequency range of interest for this antenna. The ground disk has been optimized for minimum return loss and has the shape shown in Figure 13. This shape provides sufficient area to solder the outer coax conductor and grounding pins to without significantly degrading the return loss.

3.3 Results

Measured and simulated results are again shown versus normalized frequency. For this particular antenna the low frequency cutoff is approximately 2GHz. Measured results are obtained with the antenna embedded in a 4 foot diameter circular ground plane and with an absorber filled metallic cavity backing. Numerical results are from the FE-BI code unless stated otherwise and are for the case of an infinite ground plane with infinite waveguide backing.

Measured return loss is compared to that obtained numerically with both HFSS and the in-house FE-BI code in Figure 17. Measured return loss is better than 15dB for the majority of the 5:1 bandwidth displayed. Note that effects due to the feed cable connector have been gated out of the measured data. Losses due to the cable have not been compensated for, however. This is evident at the high frequency end where the measured return loss drops below the predicted value. Both codes predict the return loss reasonably well.

Maximum gain is displayed in Figure 18. A nominal gain of approximately 3.5dBic for $f/f_0 > 1.5$ is achieved with good agreement between measurement and numerical simulation with the FE-BI code. Figure 19 shows excellent agreement between the measured and predicted elevation of maximum gain (θ_{max}). Maximum gain angle is relatively constant near 40° over a 5:1 bandwidth. The axial ratio taken at the azimuth and elevation of maximum gain is presented in Figure 20. Axial ratio is below 3dB for nearly all of the frequency range investigated indicating a high degree of circular polarization. There is good agreement between measured and numerical results below $f/f_0 = 3$. At higher frequencies there is some disagreement, however, the measured axial ratio is lower than the predicted value. Note that the axial ratio is dependent on the point at which it is taken. Typically axial ratio increases when moving further away from the boresight direction will vary somewhat along a conical cut.

The conical beam symmetry characterized again with omnidirectionality (taken at an elevation angle of 45°) is shown in Figure 21. Numerical results predict omnidirectionality better than 3dB over more than a 3:1 bandwidth while measurements show omnidirectionality below 3dB for only a 2:1 bandwidth. For normalized frequency from 2 to 4 the omnidirectionality is approximately 2dB higher than expected. Above $f/f_0 = 4.5$ there is good agreement between measurements and simulation. If the 2nd mode of a 4-arm spiral is ideally excited the first contamination from higher order modes should be from mode 6 near $f/f_0 = 3$. Above that, mode 10 at $f/f_0 = 5$ should be the next unwanted mode that radiates efficiently. However, it is evident that pattern symmetry begins to degrade at $f/f_0 = 2$ indicating that the 4th mode is radiated more efficiently than expected. This may be due to feed point asymmetry on the fabricated antenna resulting in slight differences in the magnitude and/or phase of the excitation of the two sets of arms.

Several measured radiation patterns for the vertical feed equiangular spiral are shown in Figure 22. Both co-polar and cross-polar gains are plotted for 10° increments in the azimuth direction. From a normalized frequency of 1.5 to 6 the patterns are reasonably symmetric and show a high degree of circular polarization.

Notice that at low frequencies some pattern deformation due to diffraction effects of the finite size ground plane are observed.

4. Dual Microstrip Feed

The microstrip feed consists of a microstrip line printed on the bottom side of the substrate, as shown in Figure 23. The metal between slot arms serves as the ground plane of the microstrip. At the central feed region the microstrip lines cross the slot lines perpendicularly are terminated in a short circuit. Mastering the design of the microstrip feed would significantly simplify fabrication as the antenna would be entirely planar. Particularly, the repeatability for large quantities would be improved and the overall cost would be reduced as well. Also, the microstrip width can be tapered to provide a broadband impedance transition from the feed port (typically 50Ω) to a given antenna input impedance.

4.1 Design Considerations

Several research groups in the past have attempted to implement a microstrip feed with two arm spirals [9,10]. Major difficulties typically encountered include radiation from the feed line in the opposite polarization sense, coupling between microstrip and slot line traveling waves, and asymmetry in the feeding structure (no dummy microstrip line). This feed technique imposes size limitations similar to the Dyson balun. While the Dyson balun does not radiate and does not interfere with the slot line mode, the microstrip feed certainly does. Intuitively it is clear that the smaller the microstrip line is compared the metal between slots, the less it will interfere with antenna performance. This can be accomplished by modifying the spiral itself and/or by reducing the microstrip width (which increases its characteristic impedance). As for the antenna, growth rate can be increased and slot-to-metal ratio can be decreased. However, if the growth rate is taken too large or the slot width too narrow the antenna performance can be significantly degraded even with an ideal feed. Also, if the slot width is decreased the antenna input impedance will decrease which will require a wider microstrip to match it. Reducing the microstrip width while preserving its characteristic impedance can be accomplished by reducing the substrate thickness and/or increasing its permittivity. Thinner substrates have the disadvantage of poor mechanical rigidity. High permittivity substrates, on the other hand, significantly degrade spiral antenna performance. Further investigation of how each of these parameters affects antenna performance is necessary in order to design antennas that operate well over wide bandwidths.

4.2 Realized Antenna

As a first attempt to show the ability of this type of feed to produce 2nd-mode radiation patterns the same geometry as was used for the dual-Dyson balun is

taken as the starting point. Similar to the previous antenna, a 0.02" thick Roger's Ultralam substrate with relative permittivity of 2.5 is used for fabrication. Rather than soldering coaxial feed cables to the metal between slot arms, two microstrip lines are fabricated on the opposite side of the substrate. At the outer edge the microstrip lines are designed to have a characteristic impedance of 50Ω . The microstrip lines are then wound at the same rate as the antenna and linearly tapered to an impedance of 75Ω to match the input impedance of the equiangular spiral. Two coaxial probe feeds are integrated vertically into the absorbing cavity to feed the microstrip lines from their outer edge.

4.3 Results

Since the microstrip feed structure is difficult to setup up in the FE-BI code Ansoft's HFSS is used to model the antenna performance. Preliminary simulations and measurements show that this feeding method is indeed capable of producing 2nd-mode radiation patterns. For example, Figure 24 shows measured and simulated radiation patterns at 1.5 ϕ_0 . Both co- and cross-polar gains are plotted. Note that the measured data consists of only two principle plane cuts. Although not explicitly shown here, as frequency increases the higher order spiral modes, as well as radiation from the microstrip (with maximum at the broadside direction) quickly become more influential and both omnidirectionality and broadside null depth deteriorate.

5. Conclusion

Three 2nd-mode feeding methods for 4-arm slot spirals have been proposed, two of which have not previously been employed in the same manner. The dual-Dyson balun is sensitive to fabrication errors and imposes limits on design parameters such as slot-to-metal ratio and growth rate. The vertical probe feed is not planar, but is relatively easy to fabricate and replicate on multiple antennas, allows the input impedance to be tailored, and requires no mode forming network. It too is somewhat susceptible to higher than expected 4th mode radiation due to asymmetry at the feed point. The dual microstrip feed imposes similar size limits, the microstrip line itself can radiate, and coupling of the microstrip and slotline modes can occur. Further investigation of the dual microstrip feed is in progress. Of the three realized antennas, the vertical probe feed spiral has the best performance. The proposed methods show promise for use as broadband feeds in a wide variety of applications.

6. References

- [1] V. H. Rumsey, "Frequency Independent Antennas", IRE International Convention Record, vol. 5, pp. 114-118, 1957.
- [2] R. Duhamel & J. Scherer, "Frequency Independent Antennas", in *Antenna Engineering Handbook*, R. Johnson & H. Jasik, ed., ch. 14, McGraw-Hill, 1993.
- [3] J. Corzine & J. Mosko, *Four-arm spiral antennas*, Artech House, 1990.
- [4] J. D. Dyson and P. E. Mayes, "New Circularly-Polarized Frequency-Independent Antennas with Conical Beam or Omnidirectional Patterns", *IRE Trans. Antennas and Propagation*, vol. , pp. 334-342, 1961.
- [5] T. Ozdemir & J. Volakis, "A comparative study of an absorbing boundary condition and an artificial absorber for truncating finite element meshes", *Radio Science*, vol. 29, no. 5, pp. 1255-1263, 1994.
- [6] J. D. Dyson, "The Equiangular Spiral Antenna", *IEEE Trans. Antennas and Propagation*, vol. 7, no. 2, pp. 181-187, 1959.
- [7] A. Bhobe, T. Cencich, J. Burford, & D. Filipovic, "Broadband dual-mode slot antenna", *Proc. 2003 Antenna Applications Symposium*, Monticello, IL, pp. 231-242, 2003.
- [8] M. Nurnberger & J. Volakis, "New Termination and Shallow Reflecting Cavity for Ultra Wide-Band Slot Spirals", *IEEE Antennas and Propagation Society International Symposium*, vol. 3, pp. 1528-1531, 2000.
- [9] D. L. Saul, "Cavity-Backed Spiral Has Microstrip Feed", *Microwaves*, pp. 88-89, 1981.
- [10] M. W. Nurnberger & J. L. Volakis, "A New Planar Feed for Slot Spiral Antennas", *IEEE Trans. Antennas and Propagation*, vol. 44, no. 1, pp. 130-131, 1996.

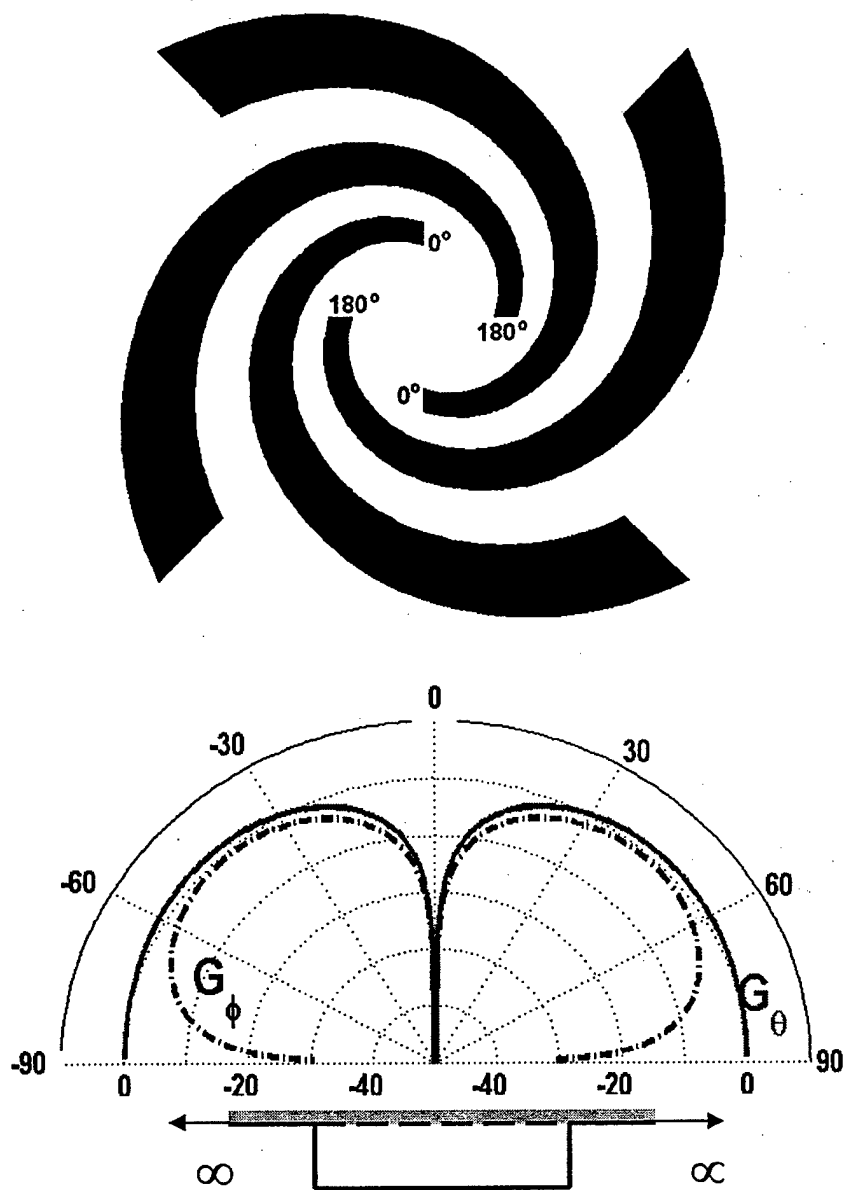


Figure 1. Phasing requirements for 2nd-mode excitation of a 4-arm spiral (top) and a typical 2nd-mode radiation pattern (bottom).

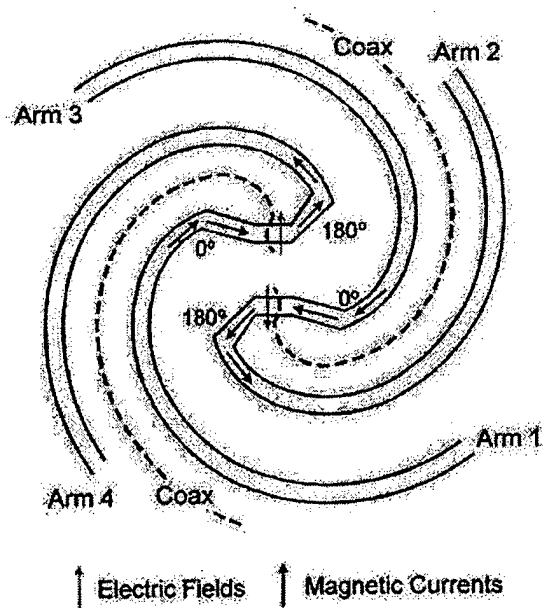


Figure 2. Dual-Dyson or infinite balun feeding method for 2nd-mode 4-arm slot spiral with two coaxial cables embedded in the ground plane between arms.

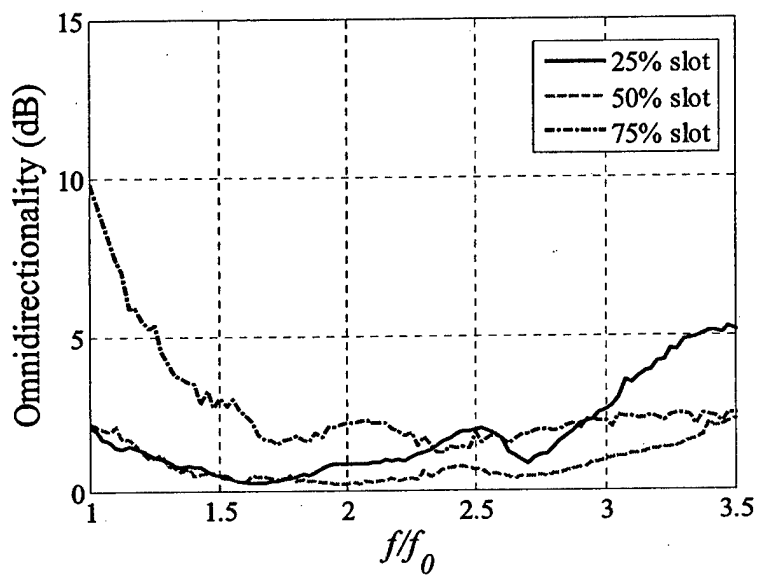


Figure 3. Omnidirectionality at an elevation of 45° for equiangular spirals with varying ratios of slot to metal.

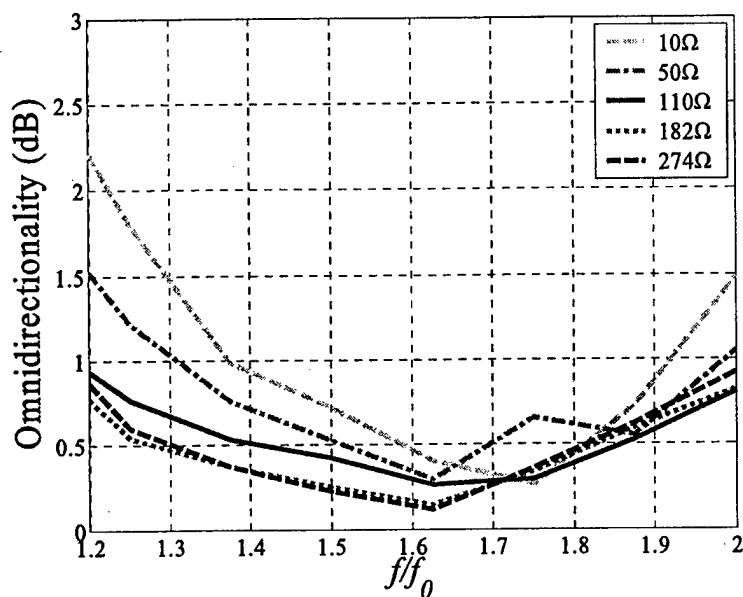


Figure 4. Simulated omnidirectionality at an elevation of 45° for a dual-Dyson equiangular spiral with various termination resistor values.

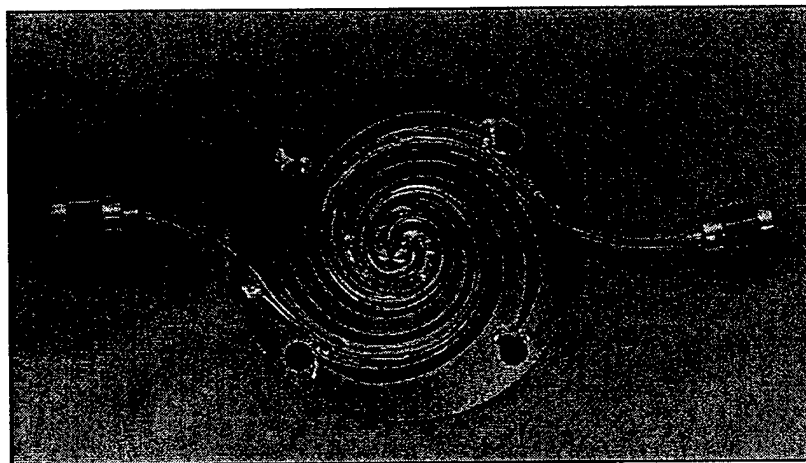


Figure 5. Realized dual-Dyson equiangular spiral with 30% slot-to-metal ratio and Archimedean center section.

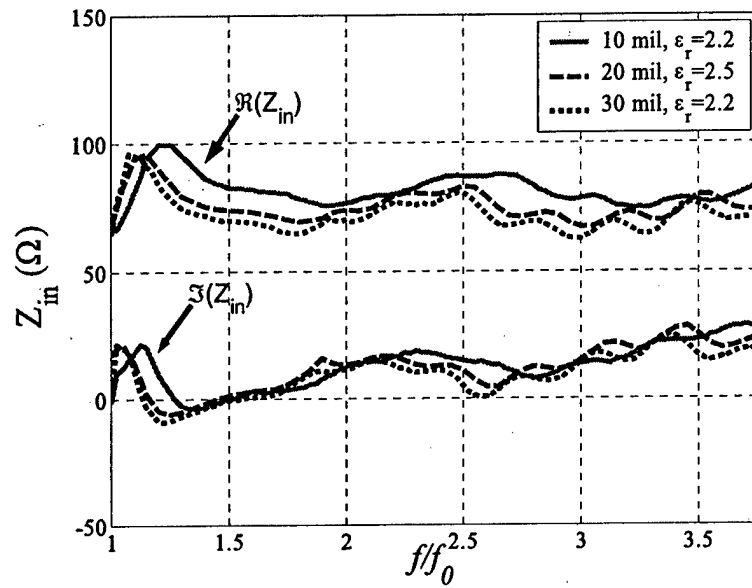


Figure 6. Simulated input impedance of dual-Dyson balun spiral for various substrates.

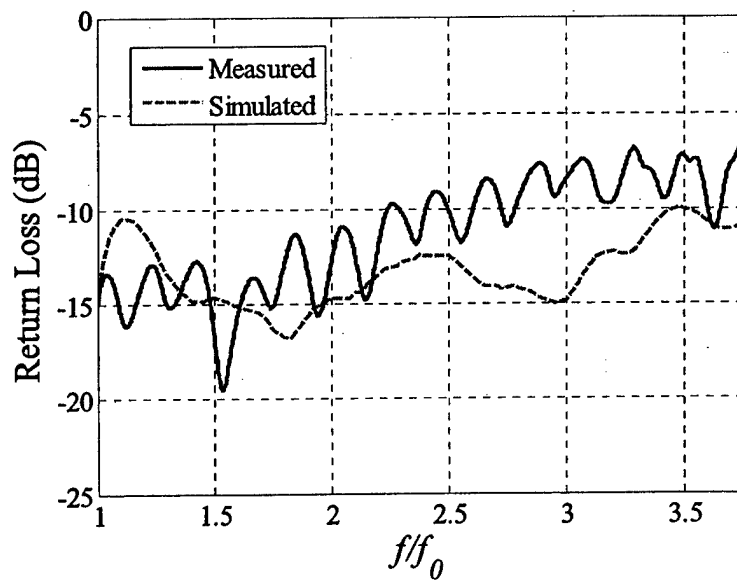


Figure 7. Measured and simulated return loss of spiral with dual-Dyson balun feed.

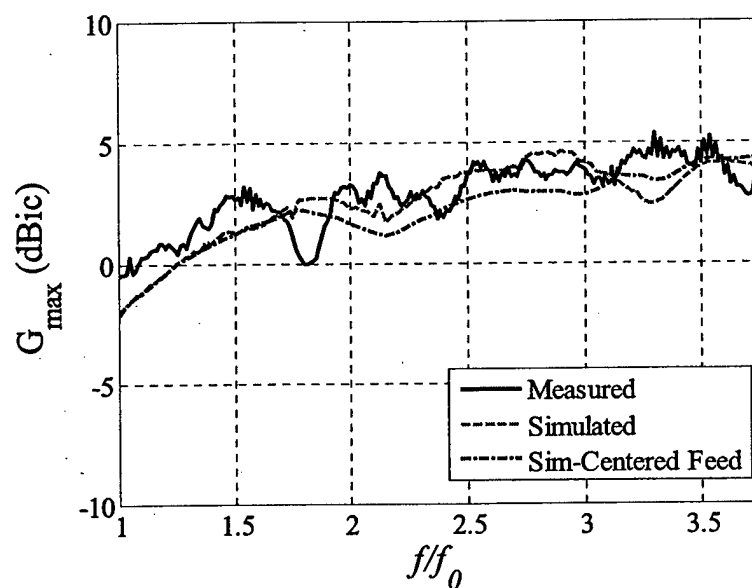


Figure 8. Measured and simulated maximum gain fo dual-Dyson balun spiral antenna.

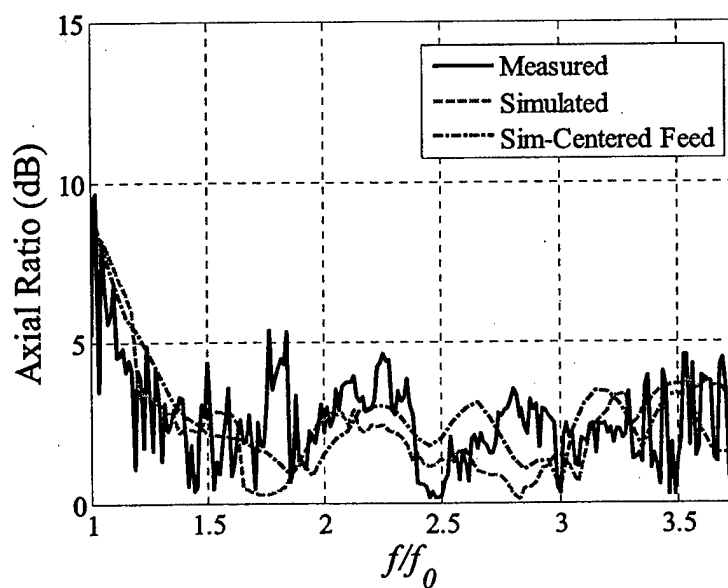


Figure 9. Measured and simulated axial ratio of dual-Dyson spiral at the azimuth and elevation of maximum gain.

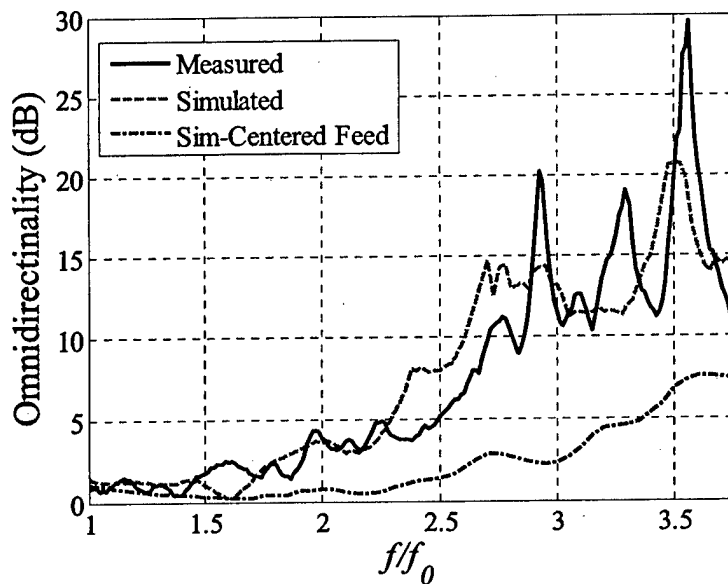


Figure 10. Measured and simulated omnidirectivity of the dual-Dyson spiral taken at an elevation of 45° .

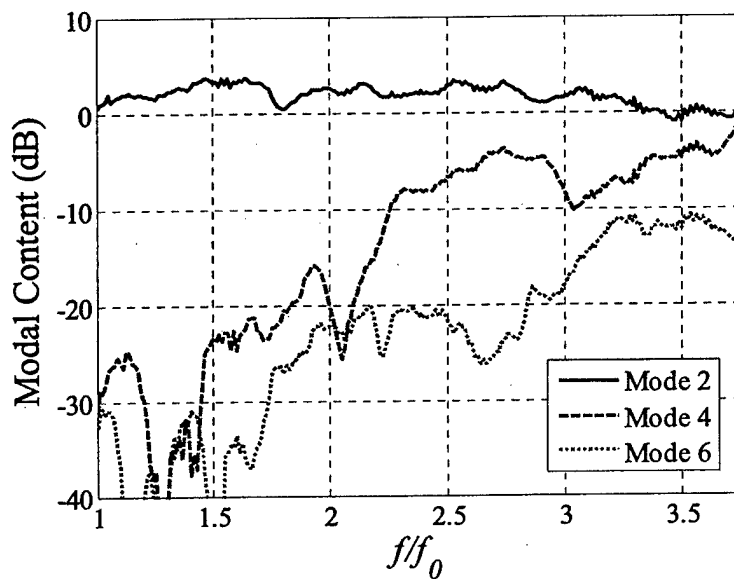


Figure 11. Modal pattern decomposition of the dual-Dyson spiral performed on a conical cut at the elevation of maximum gain.

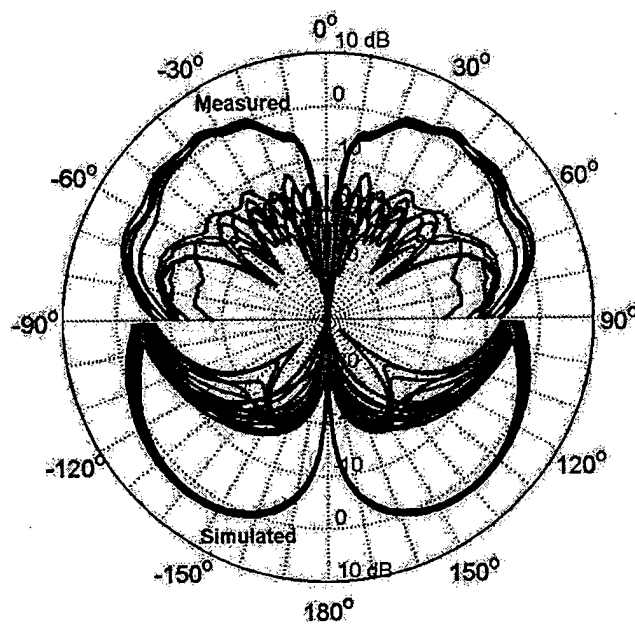


Figure 12. Measured and simulated radiation pattern of the dual-Dyson spiral antenna at $1.5f_0$.

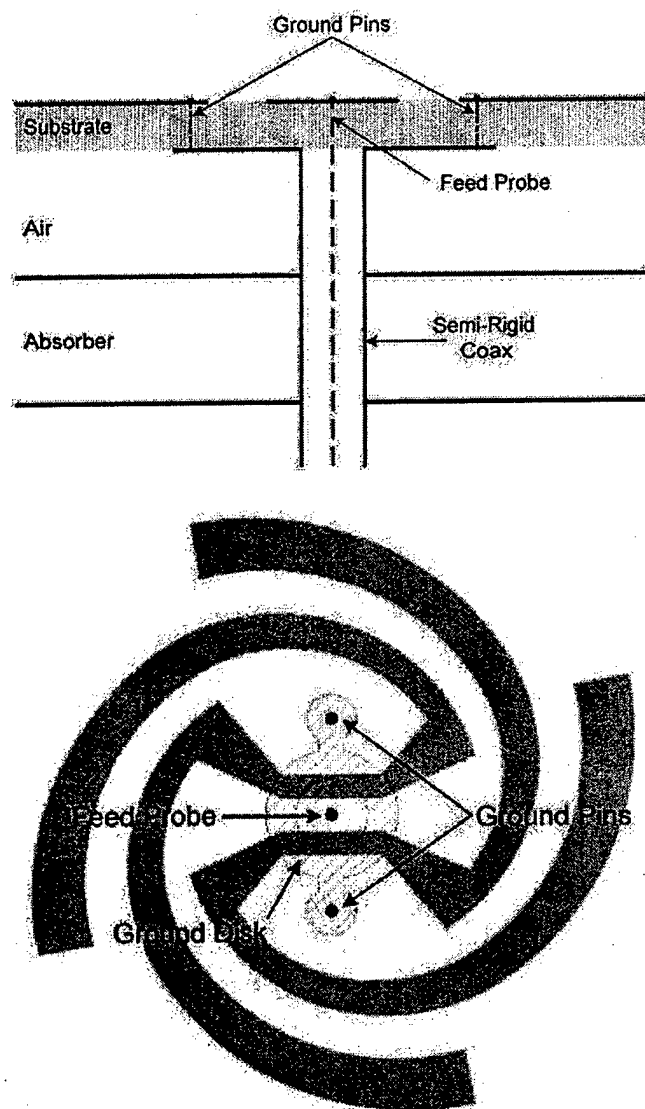


Figure 13. Side (top) and top (bottom) views of the single vertical probe feed for a 2nd-mode 4-arm slot spiral.

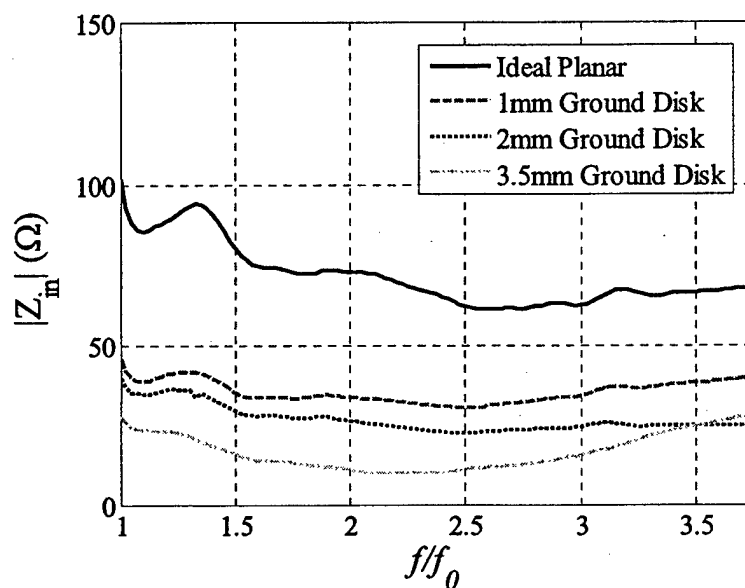


Figure 14. Magnitude of the input impedance of vertical probe feed antenna with various size ground disks as well as for the ideal planar feed.

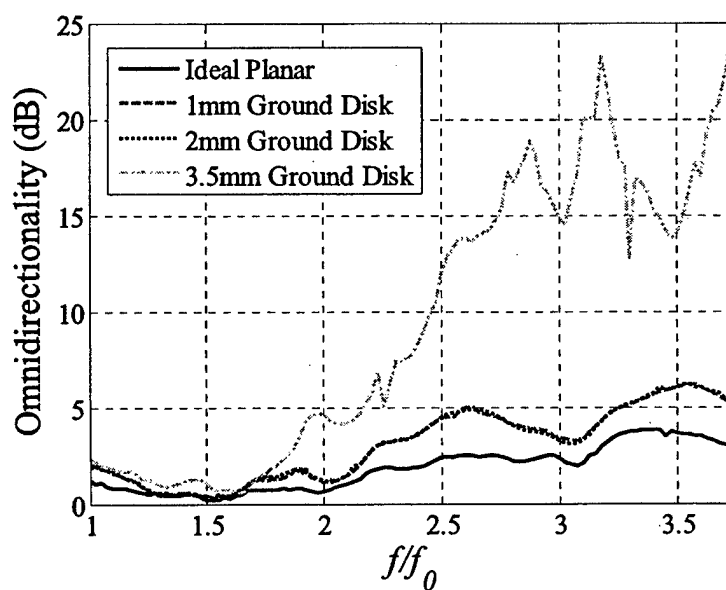


Figure 15. Omnidirectionality at the elevation of maximum gain for the vertical probe fed antenna with three sizes of grounding disk.

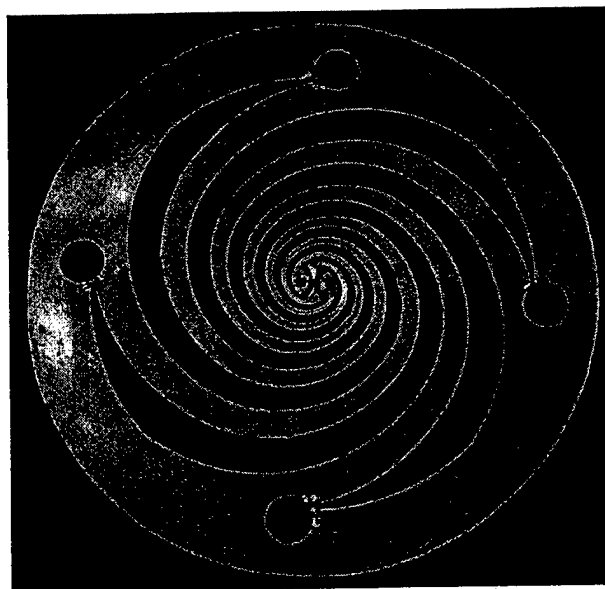


Figure 16. 10cm diameter 4-arm slot spiral antenna with vertical probe feed and open end/chip resistor arm terminations.

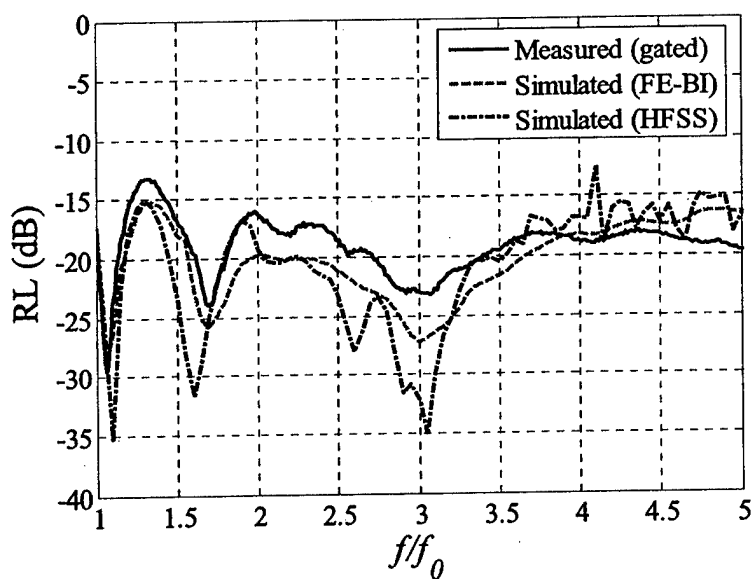


Figure 17. Measured and simulated (with both FE-BI and HFSS) return loss of the equiangular spiral with vertical probe feed.

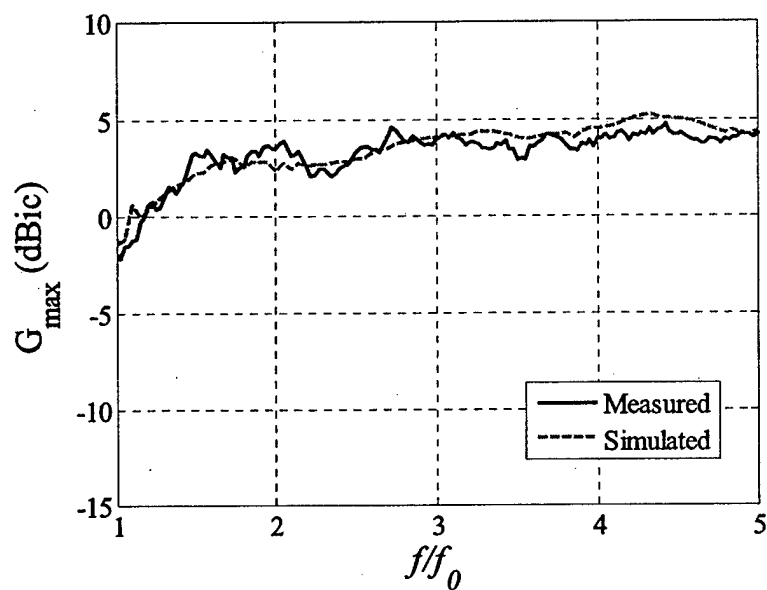


Figure 18. Measured and simulated maximum gain of equiangular spiral with vertical probe feed.

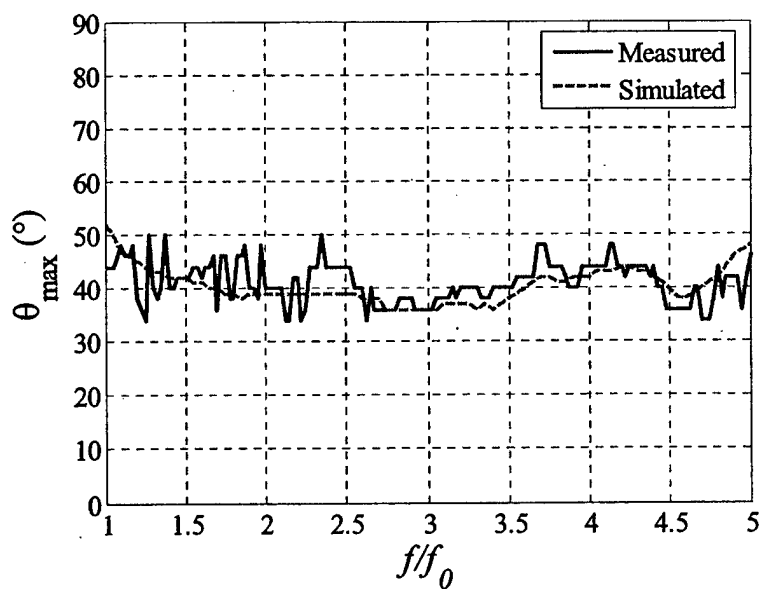


Figure 19. Measured and simulated elevation angle of maximum gain.

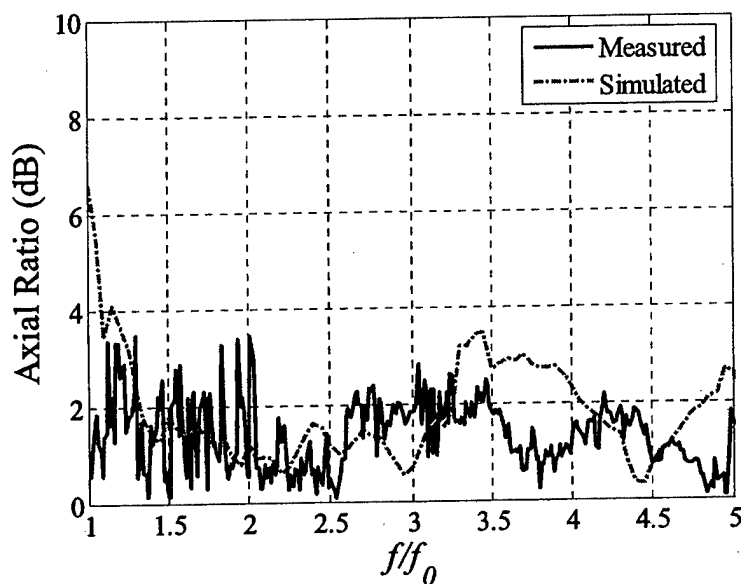


Figure 20. Measured and simulated axial ratio at the point of maximum gain for equiangular spiral with vertical probe feed.

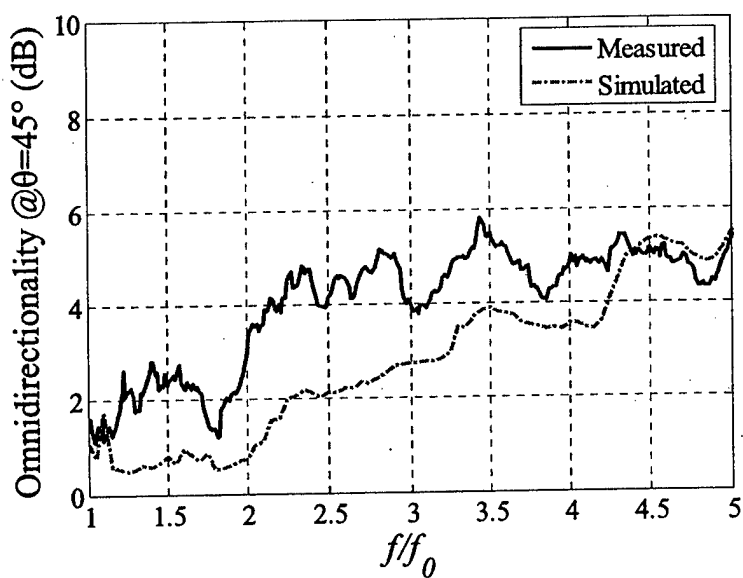


Figure 21. Measured and simulated omnidirectionality taken at of equiangular spiral with vertical probe feed.

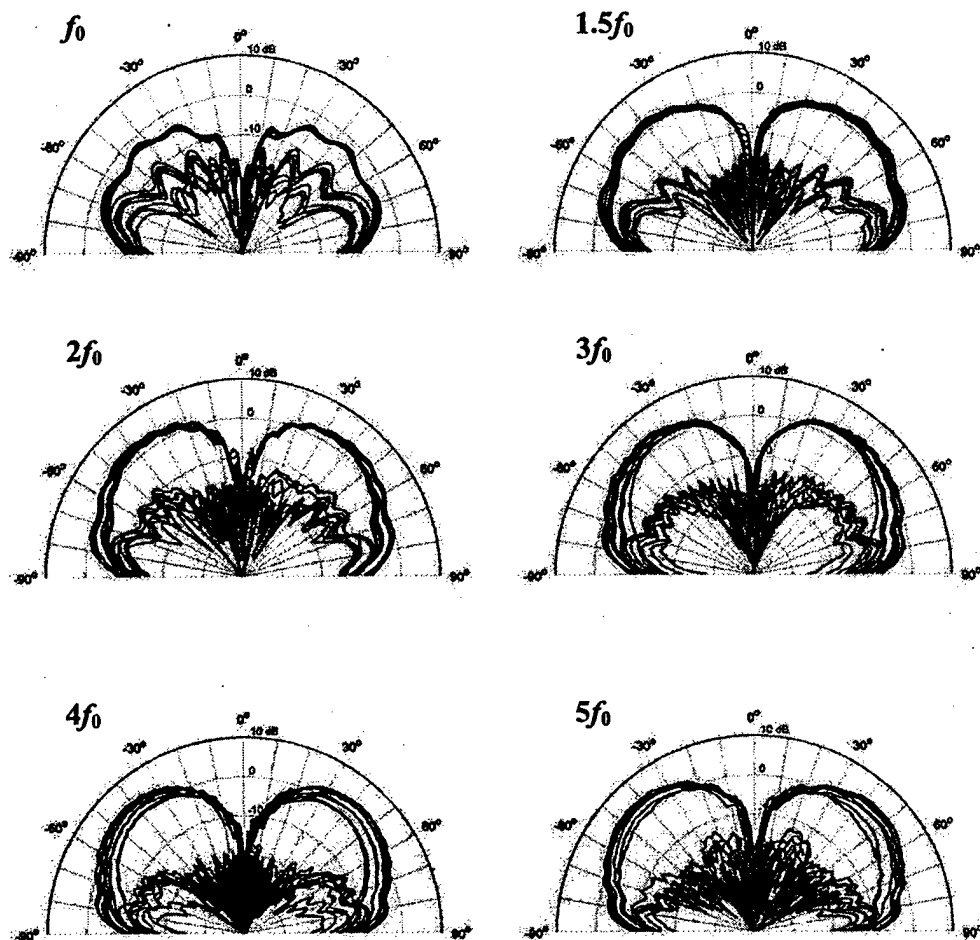


Figure 22. Measured radiation patterns of the vertical feed equiangular spiral.

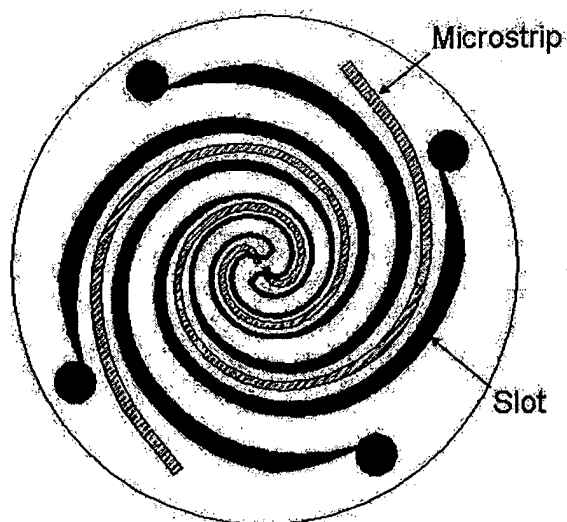


Figure 23. Dual-microstrip feeding method for 2nd-mode 4-arm slot spiral. Microstrip and slot are on opposite sides of the substrate.

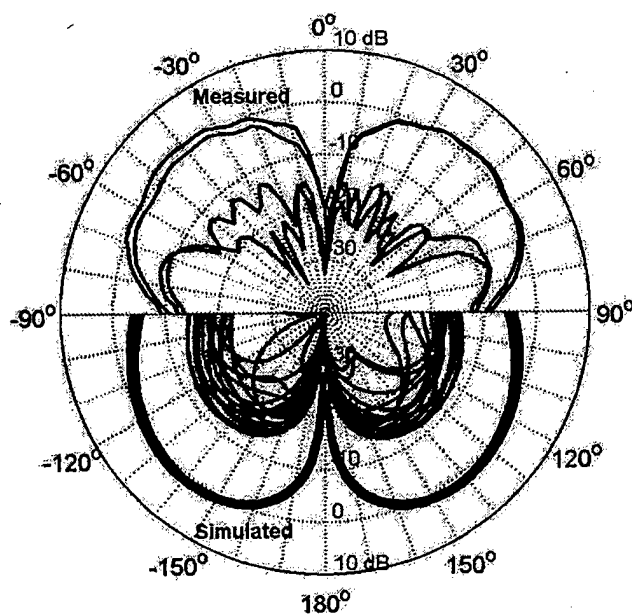


Figure 24. Measured and simulated radiation patterns of dual-microstrip feed equiangular spiral at $1.5f_0$.

COUPLED SECTORIAL LOOP ANTENNA (CSLA) FOR ULTRA-WIDEBAND APPLICATIONS*

Nader Behdad, and Kamal Sarabandi

Department of Electrical Engineering and Computer Science
University of Michigan, Ann Arbor, MI, 48109-2122
behdad@eecs.umich.edu, saraband@eecs.umich.edu

Abstract: A novel ultra-wideband antenna is proposed, which achieves ultra-wideband operation through proper magnetic coupling of two adjacent sectorial loop antennas in a symmetrical arrangement. A large number of CSLA antennas with different geometrical parameters are fabricated and their measured responses are used to experimentally optimize the geometrical parameters of the antenna to achieve ultra wideband operation. It is shown that, after optimizing the geometrical parameters of this antenna, it shows a VSWR of lower than 2 across an 8.5:1 frequency range while maintaining excellent polarization purity. Furthermore, the antenna has consistent radiation patterns in the first two octaves of its impedance bandwidth. Modified versions of the CSLA are also designed to reduce the overall metallic surface of the antenna while maintaining its wideband characteristics.

1. INTRODUCTION

A few decades after the early investigations on ultra-wideband (UWB) wireless systems, they have found various applications in a number of different wireless systems. Ground penetrating radars, frequency hopping communication systems for military applications, and UWB short pulse radars can be named as few examples. Such systems require antennas that are able to operate across a very large bandwidth with consistent radiation parameters. A number of different techniques have been used to design such wideband antennas. Traveling wave antennas and antennas with topologies that are entirely defined by angles are inherently wideband and have been extensively used [1]-[4]. Self complementary antennas provide a constant input impedance irrespective of frequency and have been extensively studied in [5]. Another technique for designing wideband antennas is to use multi-resonant radiating structures. Log-periodic antennas, microstrip patches with parasitic elements, and slotted microstrip antennas for broadband and dual-band applications are examples of this category [2], [6]-[8].

The electric dipole and monopole above a ground plane are perhaps the most basic type of antenna. These antennas are usually narrow-band antennas. However, in recent years, a number of different plate monopole antennas were introduced that have considerably large bandwidths [9]-[11]. Impedance bandwidth characteristics of circular and elliptical monopole plate antennas are examined in [9]. Wideband characteristics of rectangular and square monopole antennas are studied in [10] and a dielectric loaded wideband monopole is investigated in [11]. In this paper, a new type of single-element wideband antenna is proposed. The antenna is composed of two parallel coupled sectorial loop

* Patent pending

antennas (CSLA) that are connected along an axis of symmetry. The geometrical parameters of this antenna are experimentally optimized and it is shown that it can easily provide a wideband impedance match over an 8.5:1 frequency range with consistent radiation patterns across the first two octaves of its impedance bandwidth (a 4:1 frequency ratio). The antenna is then modified such that its overall metallic surface is substantially reduced. This considerably reduces its weight and wind resistance when it is designed to operate at lower frequencies for applications such as ground penetrating radars or TV broadcast where the antenna dimensions become large.

In what follows, first the design and experimental optimization of the geometrical parameters of the CSLA is presented. Then the geometry of this optimized CSLA is modified to reduce the overall metallic surface of the antenna and two modified CSLAs are introduced. Finally, the radiation parameters of these three antennas across their entire bands of operation are presented and discussed.

2. COUPLED SECTORIAL LOOP ANTENNA

a. Antenna Design

The topology of the proposed antenna is shown in Figure 1(b). The antenna is composed of two sectorial loops connected in parallel along the axis of symmetry (z-axis) as shown in Figure 1(a). The three parameters that affect the antenna response are the inner and outer radii of the loop R_{in} and R_{out} and the angle α as shown in Figure 1. In this paper, we pursue an experimental approach to optimize these geometrical parameters to achieve UWB operation. For the antenna shown in Figure 1(a), the lowest frequency of operation is determined by the overall effective circumference of the loop as expressed by the following approximate formula:

$$f_l = \frac{2c}{(\pi - \alpha + 2)\sqrt{\epsilon_{eff}}(R_{in} + R_{out})} \quad (1)$$

Where ϵ_{eff} is the effective dielectric constant of the antenna's surrounding medium, c is the speed of light, and R_{in} , R_{out} , and α are the geometrical parameters of the antenna as shown in Figure 1. The average radius of the loop, $R_{av} = (R_{in} + R_{out})/2$, is determined using (1). Therefore the parameters that remain to be optimized are α and $t = (R_{out} - R_{in})$.

In order to obtain the optimum value of α , nine different antennas with α values from 5° up to 80° with $R_{in} = 13\text{mm}$ and $R_{out} = 14\text{mm}$ were fabricated and their responses were measured. Since the antenna topology shown in Figure 1 needs a balanced feed, the topology in Figure 2 was used, where half of the CSLA over a ground plane is used and a simple coaxial probe feeds the antenna. For simplicity in the fabrication process, the antenna is printed on a thin dielectric substrate with dielectric constant of $\epsilon_R = 3.4$ and thickness of $500\mu\text{m}$ and is mounted on a $10\text{cm} \times 10\text{cm}$ ground plane. For brevity, only measured S_{11} values for $\alpha = 5^\circ, 20^\circ, 40^\circ, 60^\circ, 80^\circ$ are presented in Figure 3(a). It is seen that as α increases from 5° to 90° the impedance bandwidth increases and reaches its maximum at $\alpha = 60^\circ$ with an impedance bandwidth from 3.7 GHz to 10 GHz. The next step in the experimental optimization is to find the optimum t value. For doing so, three different antennas with $\alpha = 60^\circ$, $R_{av} = 13.5\text{mm}$, and $t = 0.4, 1.0$, and 1.6mm are fabricated and the measured S_{11} of these antennas are shown in Figure 3(b). As can be seen,

decreasing t results in achieving a wider bandwidth. This trend can be continued and wider bandwidths can be obtained by further decreasing t as is shown in the next subsection.

b. Radiation Parameters

In the previous section, the optimum geometrical parameters of the antenna were experimentally obtained. Based on this process, a CSLA with $R_{in}=27.8\text{mm}$, $R_{out}=28\text{mm}$, and $\alpha=60^\circ$ is fabricated and mounted on a $20\text{cm}\times 20\text{cm}$ ground plane. The dimensions are increased to lower the lowest and highest frequencies of operation and simplify the radiation pattern measurements. The antenna has a VSWR of lower than 2.2 from 1.7GHz to 14.5GHz (see Figure 9), which is equivalent to an 8.5:1 impedance bandwidth. The radiation patterns of the antenna are measured across the entire frequency band and are presented in Figures 4, 5, and 6. Figure 4 shows the far-field co- and cross polarized (E_θ , E_ϕ) radiation patterns in the azimuth plane (x-y plane). It is seen that the patterns are consistent up to $f=8$ GHz. As the frequency increases beyond 8 GHz, the radiation patterns start to change; however, they are similar to each other for $10\text{ GHz} \leq f \leq 16\text{ GHz}$. The radiation patterns in the elevation planes are also measured for two different planes at $\phi=0^\circ, 180^\circ, 0^\circ \leq \theta \leq 180^\circ$ (x-z plane) and $\phi=90^\circ, 270^\circ, 0^\circ \leq \theta \leq 180^\circ$ (y-z plane) and are presented in Figures 5 and 6 respectively. As frequency increases, the electrical dimensions of the antenna increase and as a result, the number of lobes increases. Also, the number of minor side lobes in the back of the ground plane ($90^\circ \leq \theta \leq 180^\circ$) increases significantly. This is caused by diffractions from the edges of the ground plane, which has larger electrical dimensions at higher frequencies. At lower frequencies, the radiation patterns are symmetric; however, as frequency increases, the symmetry is not observed very well. This is caused by the presence of the coaxial cable that feeds the antenna and disturbs the symmetry of the measurement setup. Since the cable is electrically large at higher frequencies, it has a larger effect on the radiation patterns of the antenna at these frequencies. In all the measured radiation patterns, the cross polarization level (E_ϕ) is seen to be negligible. This is an indication of good polarization purity across the entire frequency band.

3. MODIFIED CSLAs

a. Antenna Design

It is possible to scale the dimensions of the CSLA such that it operates at lower frequencies for applications such as TV broadcasting or ground-penetrating radars. For these applications the wavelength is large, therefore the antenna dimensions become very large. This increases the antenna weight and its wind resistance; therefore, it is desirable to reduce the metallic surface of the antenna as much as possible, while maintaining its characteristics. In order to do this, the electric current on the antenna surface is examined using numerical simulations based on the method of moments. The magnitude of the electric current on the surface of the antenna is shown in Figure 7 at four different frequencies. It is observed that the electric current density is very small in the sector confined in the range of $-30^\circ \leq \theta \leq 30^\circ$. This suggests that this sector of the antenna can be removed without significantly disturbing the current distribution on its surface. This results in a design that is shown in Figure 8(a) and, because of its similarity to the letter

"M", is called the "M1 CSLA". Applying the same approach to the "M1" antenna and examining its current distribution reveals that the electric current density is large around $\theta=30^\circ$, 60° , 120° , and 150° edges and has lower values in between ($30^\circ<\theta<60^\circ$). Therefore, another pie-slice section of the antenna, which is confined in the ranges $40^\circ<\theta<50^\circ$ and $130^\circ<\theta<140^\circ$ can be removed to obtain the antenna shown in Figure 8(b). This antenna is called the "M2" CSLA. Two "M1" and "M2" antennas with $\alpha=60^\circ$, $R_{in}=27.8\text{mm}$ and $R_{out}=28\text{mm}$ are fabricated on a thin substrate with thickness of 0.5mm and dielectric constant of 3.4 and mounted on a 20cm \times 20cm square ground plane. The measured return losses of these two antennas are given in Figure 9 along with the S_{11} of the original CSLA antenna with the same dimension. It is seen that all of the antennas have VSWRs lower than 2.2 in the frequency range of 2-14-GHz as shown in Table I. The best input match is, however, observed for the "M2" CSLA with the VSWR lower than 2 across its entire band of operation.

Antenna Type	Frequency Range	BW	MAX VSWR
Original CSLA	1.7- 14.5 GHz	8.5:1	2.2
"M1" CSLA	2-14.7 GHz	7.35:1	2.2
"M2" CSLA	2.05-15.3 GHz	7.46:1	2.2

Table I. Comparison between the bandwidth of the original, "M1", and "M2" CSLAs.

b. Radiation Parameters

The radiation patterns of the "M2" CSLA are measured at three different planes across its entire frequency band and are presented in Figures 10, 11, and 12. The co-pol, E_θ , and cross-pol, E_ϕ , far-field radiation patterns in the azimuth plane are shown in Figure 10 and are observed to be similar to those of the original CSLA. Similar to the previous section, the elevation patterns at x-z ($\phi=0^\circ$, 180° , $0^\circ \leq \theta \leq 180^\circ$) and y-z ($\phi=90^\circ$, 270° , $0^\circ \leq \theta \leq 180^\circ$) planes are measured and reported in Figures 11 and 12. Similar to the original CSLA, the patterns change as the frequency increases and the minor side lobe levels increase with frequency. The gains of the three CSLA antennas are measured in the anechoic chamber of the University of Michigan in the frequency range of $f=2\text{-}16$ GHz using a double-ridge standard horn reference antenna and are presented in Figure 13. The gain of the antennas are measured at $\theta=90^\circ$, $\phi=90^\circ$. As frequency increases from 2 to 6 GHz, the electrical size of the antenna increases and so does its gain. However, as is observed from Figure 13, the antenna gain decreases as frequency increases from 6 GHz up to 10 GHz. This is a consequence of the change in the direction of maximum radiation in the azimuth plane as is seen from Figure 10.

4. CONCLUSIONS

A novel ultra-wideband coupled sectorial loop antenna is designed that has an 8.5:1 impedance bandwidth. The antenna has consistent radiation parameters over a 4:1 frequency range with excellent polarization purity over the entire 8.5:1 frequency range. Modified versions of this UWB antenna, with reduced metallic surfaces and similar radiation parameters, were also designed, fabricated, and measured. Measurement results indicate that these modifications do not adversely affect the UWB behavior of the antenna.

ACKNOWLEDGMENT

Support for this project was provided by EMAG Technologies Inc.

5. REFERENCES

- [1] G.F. Ross, "The transient analysis of multiple beam feed networks for array systems", Ph.D. dissertation, Polytechnic Institute of Brooklyn, Brooklyn, NY, 1963.
- [2] C. A. Balanis, "Antenna Theory: Analysis and Design, Chap. 12", Wiley, 2nd Edition, 1996.
- [3] C. H. Walter, "Traveling Wave Antennas", Peninsula Pub., 1990.
- [4] R. G. Corzine and J. A. Mosko, "Four Armed Spiral Antennas", Artech House, 1990, Norwood, MA.
- [5] Y. Mushiake, "Self-Complementary Antennas: Principle of Self-Complementarity for Constant Impedance", Springer, 1996.
- [6] G. Kumar and K. Ray, "Broadband Microstrip Antennas", Artech House, 2003, Norwood, MA.
- [7] K. L. Wong, "Compact and Broadband Microstrip Antennas", Wiley, 2002, NY.
- [8] N. Behdad and K. Sarabandi, "A Multiresonant Single-Element Wideband Slot Antenna", IEEE Antennas and Wireless Propagation Letters, Vol. 3, 2004, pp. 5-8.
- [9] N. P. Agrawal, G. Kumar, and K. P. Ray, "New Wideband Monopole Antennas", IEEE Antennas and Propagation Society International Symposium, 13-18 Jul. 1997, Vol. 1, pp. 248-251.
- [10] M. J. Ammann, and Z. J. Chen, "Wideband Monopole Antennas for Multi-Band Wireless Systems", IEEE Antennas and Propagation Magazine, Vol. 45, 2003, pp. 146-150.
- [11] M. Lapierre, Y.M.M. Antar, A. Ittipiboon, A. Petosa, "A wideband monopole antenna using dielectric resonator loading", IEEE Antennas and Propagation Society International Symposium, 22-27 Jun. 2003, Vol. 3, pp. 16-19.
- [12] "IE3D Electromagnetic Simulation and Optimization Software", Zeland Software, Inc.

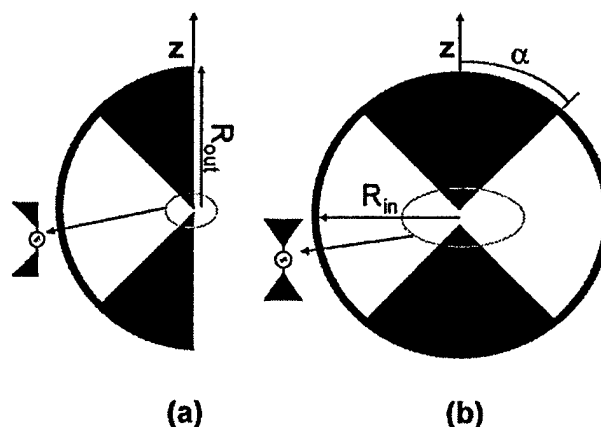


Figure 1. Topology of a sectorial loop antenna (a) and a coupled sectorial loop antenna (b)

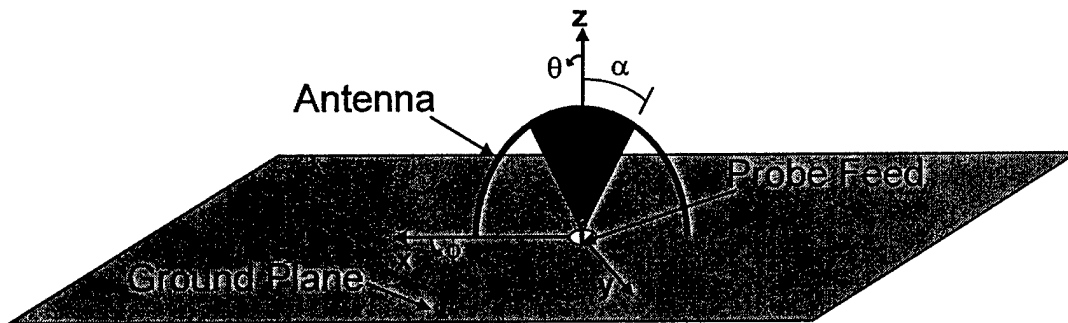


Figure 2. Three dimensional topology of the CSLA above a ground plane.

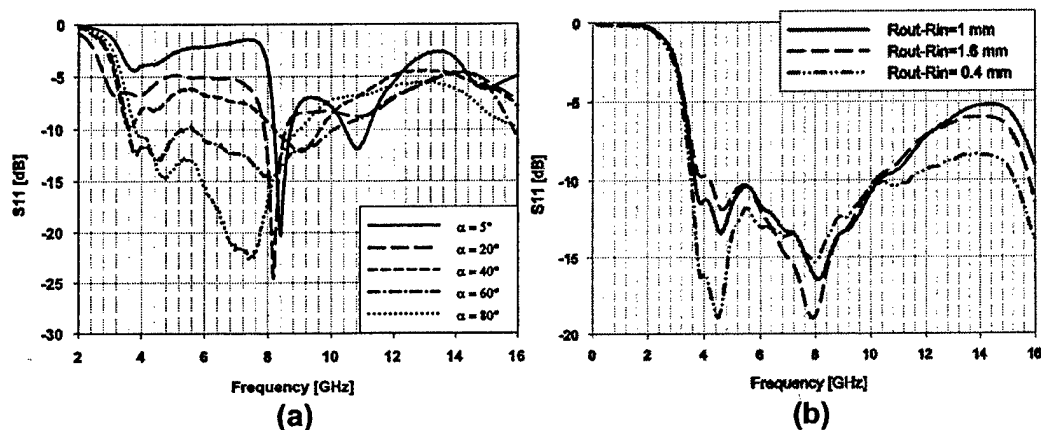


Figure 3. Measured S_{11} values of a number of CSLAs used in the experimental optimization process. (a) $R_{in}=13\text{mm}$, $R_{out}=14\text{mm}$, and different α values. (b) $(R_{in}+R_{out})/2=13.5\text{mm}$, $\alpha=60^\circ$, and different $R_{out}-R_{in}$ values.

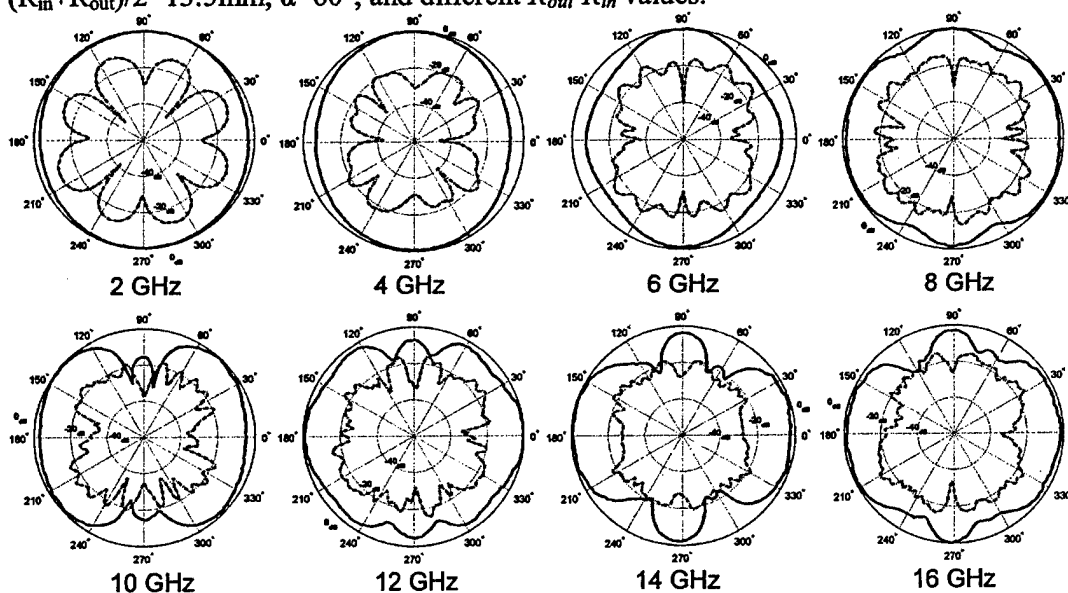


Figure 4. Measured radiation patterns of the CSLA in section 2 in the azimuth plane. The solid line is co-pol (E_θ) and the dash-dotted line is the cross-pol (E_ϕ) components

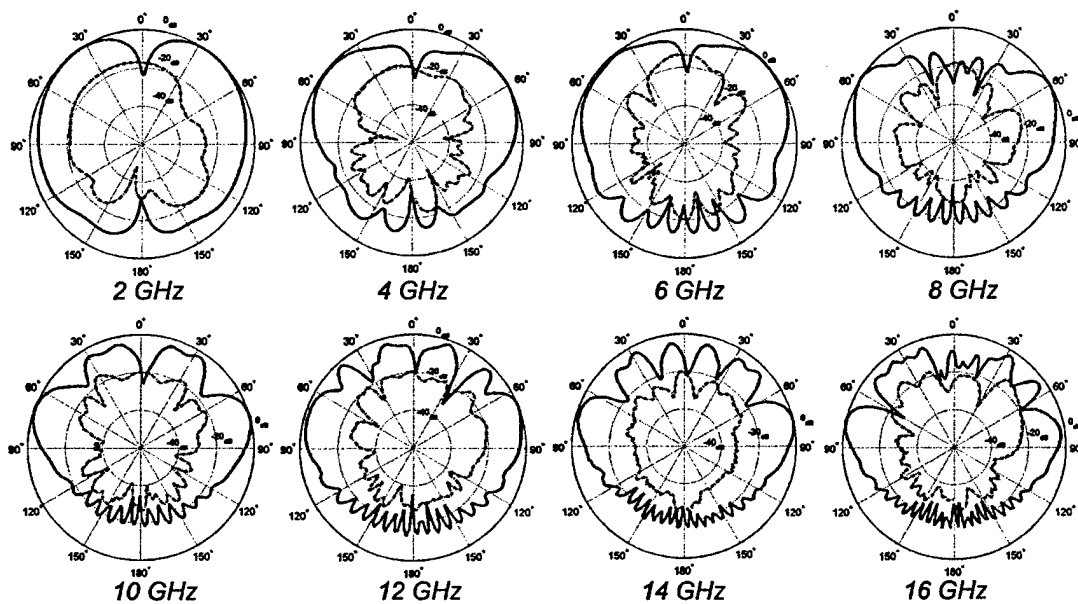


Figure 5. Measured radiation patterns of the CSLA of section 2 in the elevation plane ($\varphi=0^\circ, 180^\circ, 0^\circ \leq \theta \leq 180^\circ$). The solid line is co-pol (E_θ) and the dash-dotted line is the cross-pol (E_φ) components.

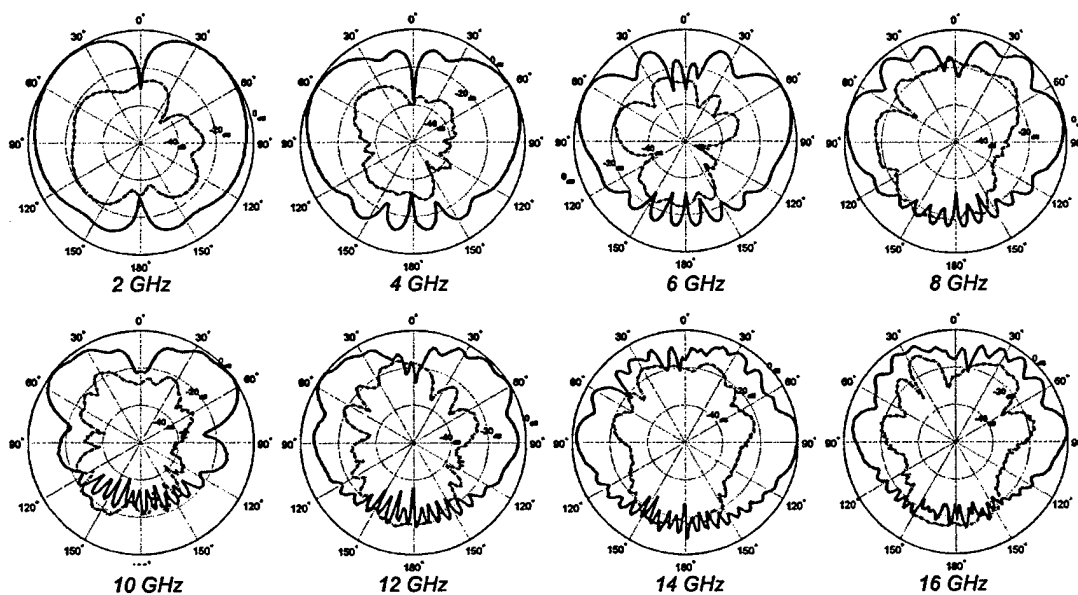


Figure 6. Measured radiation patterns of the CSLA of section 2 in the elevation plane ($\varphi=90^\circ, 270^\circ, 0^\circ \leq \theta \leq 180^\circ$). The solid line is co-pol (E_θ) and the dash-dotted line is the cross-pol (E_φ) components.

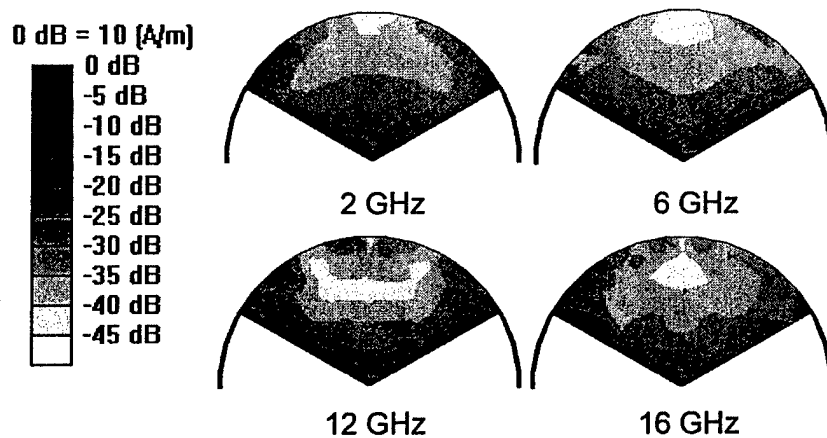


Figure 7. Electric current distribution across the surface of the CSLA of section 2 at four different frequencies.

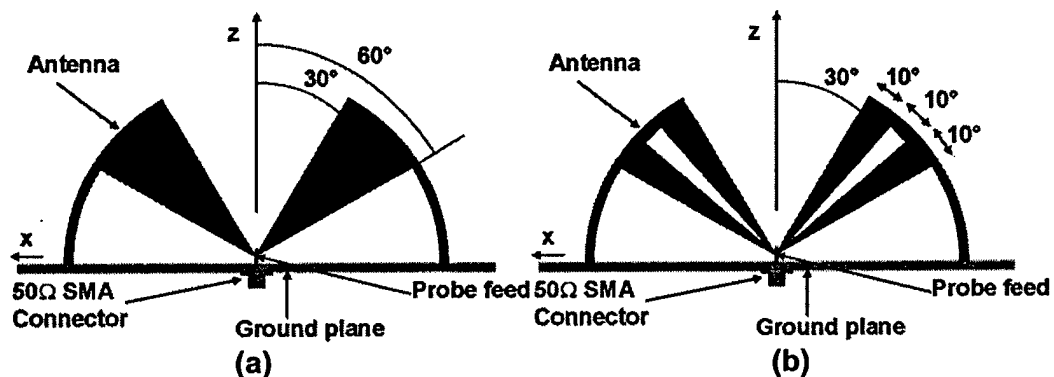


Figure 8. Topology of the modified CSLAs of section 3. (a) "M1" CSLA. (b) "M2" CSLA

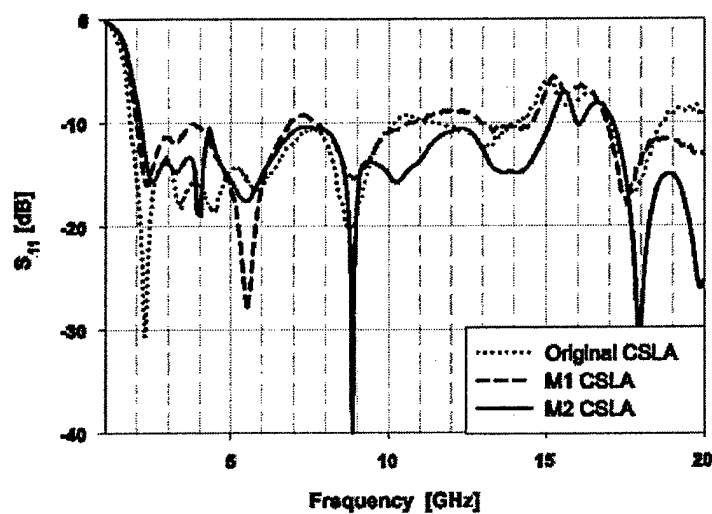


Figure 9. Measured S_{11} values of the original CSLA of section 2 and the "M1" and "M2" CSLAs of section 3.

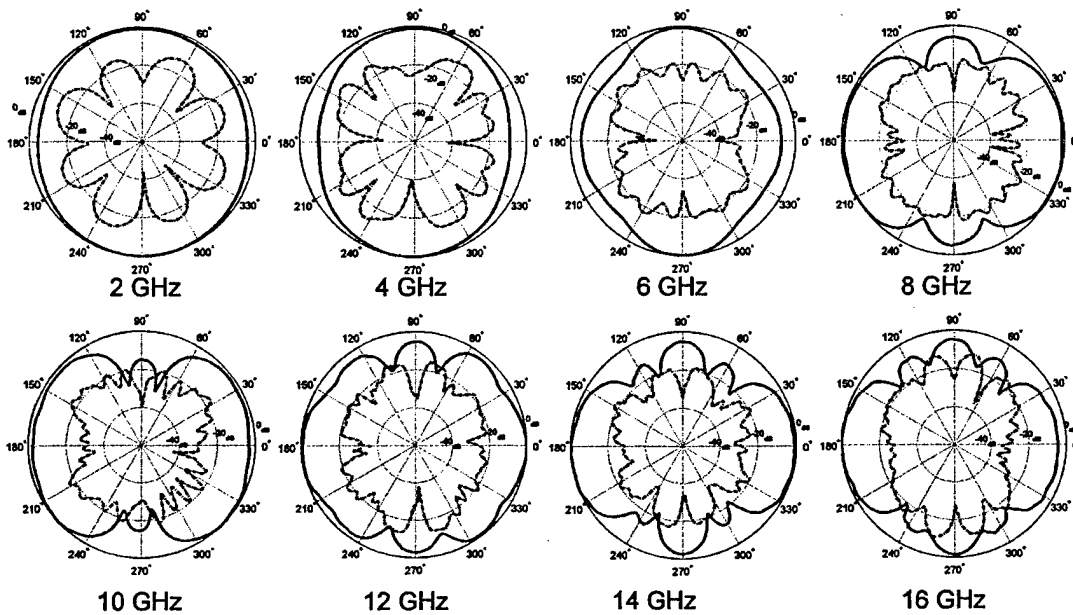


Figure 10. Measured radiation patterns of the "M2" CSLA in section 3 in the azimuth plane. The solid line is co-pol (E_θ) and the dash-dotted line is the cross-pol (E_ϕ) components.

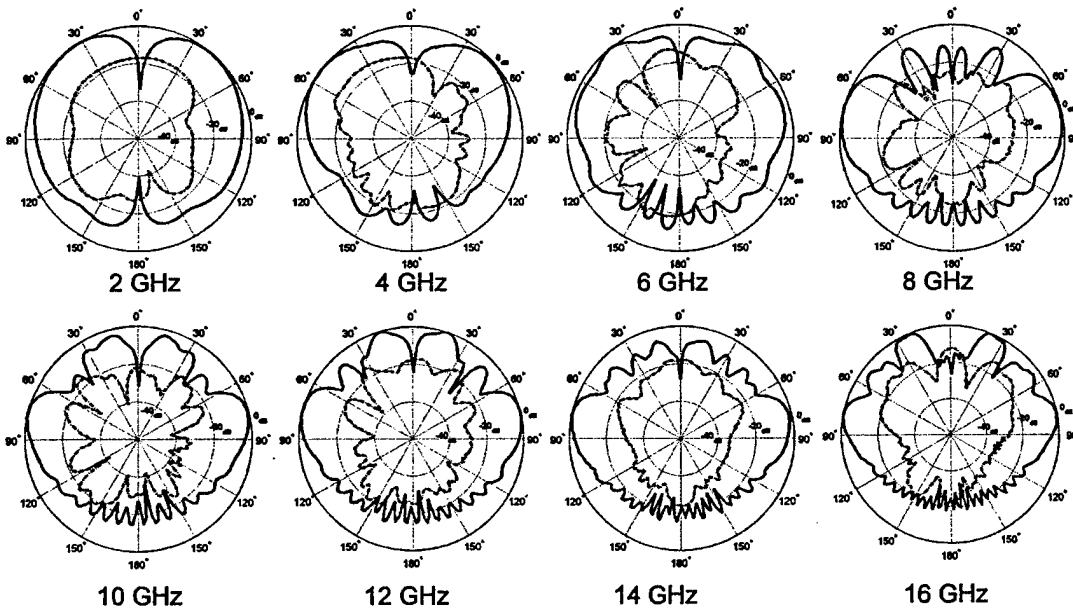


Figure 11. Measured radiation patterns of the "M2" CSLA of section 3 in the elevation plane ($\phi=0^\circ, 180^\circ, 0^\circ \leq \theta \leq 180^\circ$). The solid line is co-pol (E_θ) and the dash-dotted line is the cross-pol (E_ϕ) components.

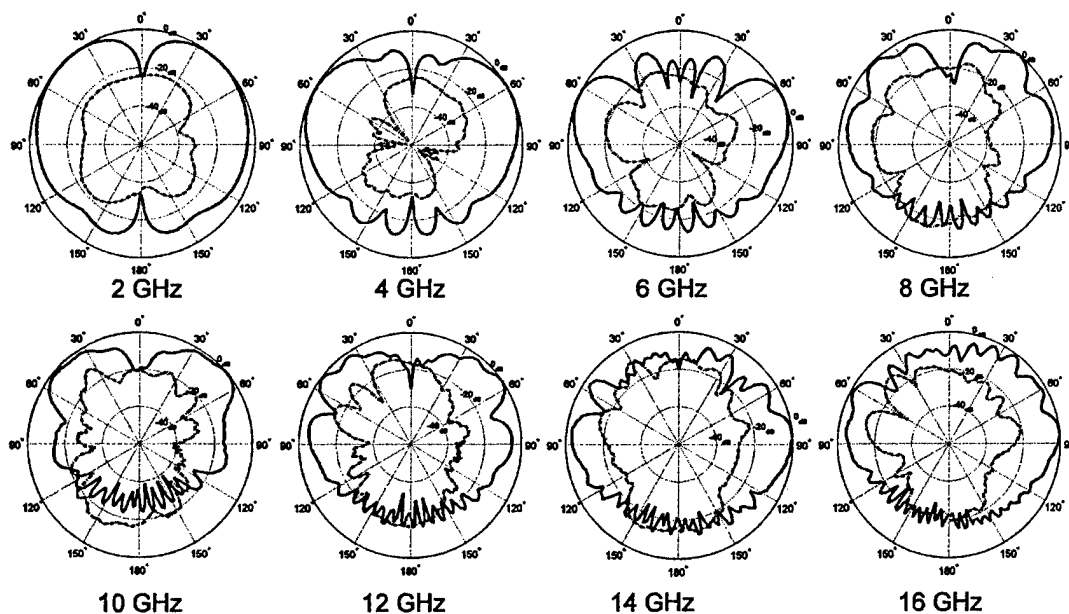


Figure 12. Measured radiation patterns of the "M2" CSLA of section 2 in the elevation plane ($\varphi=90^\circ$, 270° , $0^\circ \leq \theta \leq 180^\circ$). The solid line is co-pol (E_θ) and the dash-dotted line is the cross-pol (E_φ) components.

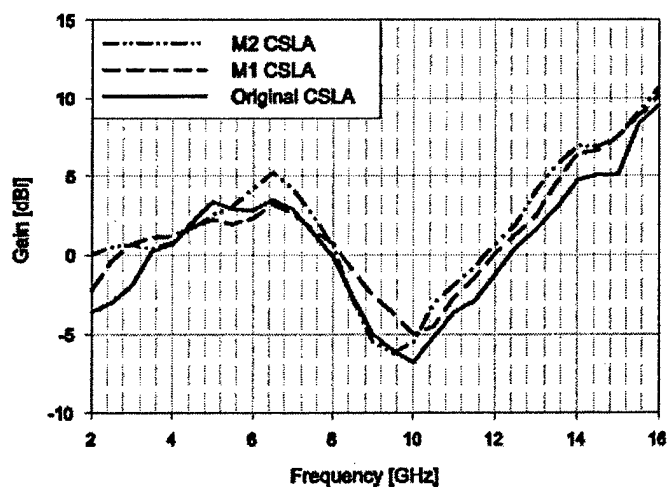


Figure 13. Measured gain of the original CSLA of section 2 and the "M1" and "M2" CSLAs of section 3. The gains are measured in the azimuth plane at $\varphi=90^\circ$, $\theta=90^\circ$.

A Circularly Polarized Metamaterial and Dielectric Resonator Antenna with Enhanced Bandwidth

Amelia Buerkle and Kamal Sarabandi

Electrical Engineering and Computer Science, The University of Michigan

Abstract

This work extends a previously developed method to improve the bandwidth of a dielectric resonator antenna (DRA) [1]. The prior technique combines a slot antenna and a DRA to effectively double the available bandwidth. With proper design it is observed that the resonance of the slot and that of the dielectric structure itself may be merged to achieve extremely wide bandwidth over which the antenna polarization and radiation pattern are preserved. In addition, using the dielectric resonator antenna, a volumetric source, improves the radiation power factor of the radiating slot. Bandwidths on the order of 25% at 2.4 GHz are achieved.

The current work extends this idea. Probe feeds are used to reduce back radiation and a parasitic probe is introduced to further increase bandwidth. Metamaterials are also used to provide size and additional bandwidth improvements. These changes are then incorporated into a circularly polarized (CP) design. A description of the design and simulation results are given. Results indicate 40% bandwidth at 277MHz. Measurements are to be carried out following fabrication.

A. Probe feed

One drawback of using a slot to feed the DRA is back radiation; the slot dimensions necessary to merge the resonances may be large enough to allow non-negligible radiation below the ground plane. Even though the DRA tends to direct the radiation upwards the amount of back radiation may not be acceptable for some applications. In order to reduce the back radiation a probe-feed is used in the present study. Although more difficult to fabricate, the probes also allow for easier implementation of a CP design. It is noted that using the probe feed leads to higher cross-pol levels in the H-plane (the $x - z$ plane in Fig. 3). Loop feeds could instead be used to mitigate cross-pol radiation and allow for lower axial ratios.

B. Parasitic Probe

The concept of merging resonances to augment bandwidth can also be extended to include additional resonances from parasitic elements. If properly designed the parasitic element yields a third resonance at the proper frequency.

For example, in the original design, an additional aperture can be added next to the fed aperture. The two apertures are coupled through the electric field in the DRA, each producing a resonance; all three resonances would share the same linear polarization. The presence of the second aperture exacerbates the back radiation problem. Alternatively, a parasitic probe can be added on the other side of the DRA, as shown in Figure 3(a). In this design a parasitic probe is short circuited to the ground plane opposite from the fed probe.

C. Metamaterials

Metamaterials are used to provide enhanced miniaturization while simultaneously increasing the bandwidth of the DRA resonance. Antenna size is generally determined by the wavelength in the antenna material:

$$\lambda_d = \frac{\lambda_o}{\sqrt{\mu_r \epsilon_r}} \quad (1)$$

where λ_o is the freespace wavelength and ϵ_r and μ_r are the relative permittivity and permeability, respectively. In the past, only high permittivity materials were available to decrease antenna size; however, the use of such materials leads to increased energy storage in the antenna near field and narrow bandwidth. Incorporating artificial metamaterials with both μ_r and ϵ_r greater than one can result in the same size antenna without the adverse effects of using high permittivity materials [2]. Since the energy storage effects are reduced, the ability of the structure to radiate power into free space is improved and the resonance bandwidth increases.

The simulation results of a study on a 2.4 GHz slot-fed DRA are given to provide qualitative evidence of the bandwidth enhancing capability of these materials. In each case, the intrinsic impedance ($\sqrt{\mu/\epsilon}$) is varied while the product $\mu_r \epsilon_r = 25$ and the DRA size, 2.67 cm square by 1.67 cm tall, are held constant. The degree of matching varied as the permittivity and permeability were adjusted; modifications such as changing the slot length and position of the DRA over the slot were made to achieve a -10dB match. The percent bandwidth of the DRA resonance is plotted versus the log of the intrinsic impedance of the DRA ($\log_{10} \sqrt{\mu_r/\epsilon_r}$) in Figure 1. It is observed that $\log_{10} \sqrt{\mu_r/\epsilon_r} = 0.24$, corresponding to $\mu_r = 8.62$ and $\epsilon_r = 2.9$, is an optimal configuration in terms of maximizing the bandwidth of this design. This demonstrates that, in general, using a combination of both μ_r and ϵ_r in design can improve the bandwidth.

In this design the metamaterial is a ceramic hexaferrite made by TransTech [4]. The material has relative permittivity and permeability of approximately 16 and 8.5, respectively. The magnetic loss tangent ($\tan \delta_m$) is approximately 0.04; $\tan \delta_e$ is estimated to be five to ten times smaller than $\tan \delta_m$. The current fabrication procedure limits the material thickness to roughly 0.5 cm. For this reason, a layered design using regular dielectric layers alternated with

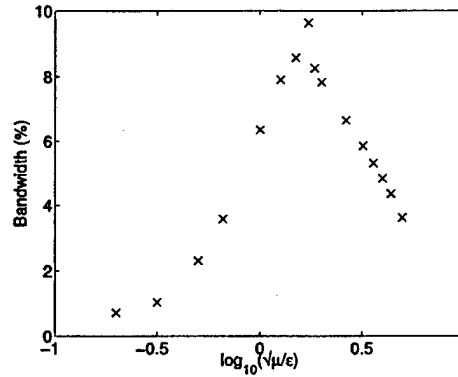


Fig. 1. Percent bandwidth versus the log of the DRA intrinsic impedance.

hexaferrite layers of the same thickness is used. The dielectric layers used in the fabricated design are Roger's TMM4 and have relative permittivity of 4.5 with $\tan \delta_e < 0.002$ [5].

It is difficult to accurately predict the resonance frequency of the layered DRA. The conventional dielectric waveguide model (CDWM) which is applied in [1] cannot be used with the dominant TE_x^{111} mode in the layered case because of the boundary conditions on the resonator ends. However, since the layer thickness is small compared to the wavelength inside the DRA an effective permittivity and permeability may be used to estimate the resonance frequency. Effective parameters are obtained by modeling the DRA layers as series capacitors and inductors with values corresponding to their respective permittivity and permeability. These expressions should only apply to the z component of the parameters (ϵ_z, μ_z) as the transverse components ($\epsilon_{x,y}, \mu_{x,y}$) are not affected by the layered design. However, the resulting anisotropy is neglected in this approximation. In the case of fourteen equal thickness, alternating hexaferrite and dielectric layers:

$$\mu_{r,eff} \approx \frac{\mu_{r1} + \mu_{r2}}{2} \approx 4.75 \quad \epsilon_{r,eff} \approx 2 \left(\frac{1}{\epsilon_{r1}} + \frac{1}{\epsilon_{r2}} \right)^{-1} \approx 7 \quad (2)$$

where 1 refers to the hexaferrite ($\epsilon_{r1} = 16, \mu_{r1} = 8.5$) and 2, the dielectric ($\epsilon_{r2} = 4.5, \mu_{r2} = 1$). Using these approximate values $\sqrt{\mu_{r,eff}\epsilon_{r,eff}} \approx 5.8$ which is near an average value of 6.5 obtained by considering the probe lengths and their respective resonance frequencies. The resonance frequency of TE_z modes may be found using

$$f = \frac{c}{2\pi\sqrt{\mu_{r,eff}\epsilon_{r,eff}}} \sqrt{k_x^2 + k_y^2 + k_z^2} \quad (3)$$

where c is the speed of light and μ_r and ϵ_r are the effective permeability and permittivity. The wavenumbers in the x, y , and z directions, k_x, k_y , and k_z ,

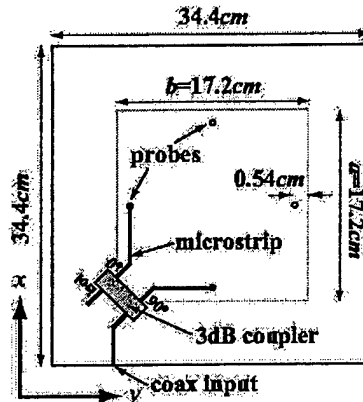


Fig. 2. Diagram of planned feed network using microstrip and a hybrid coupler.

are given by

$$k_x = \frac{n\pi}{a} \quad k_y = \frac{m\pi}{b} \quad k_z \tan(k_z h) = \mu_{r,eff} \sqrt{k_x^2 + k_y^2 - k_0^2} \quad (4)$$

where a , b , and h are the x , y , and z dimensions of the resonator. After solving equation 4 for the wavenumbers, the resonance frequency found from equation 3 is 264 MHz. This agrees with the simulated resonance at 260 MHz. Based on the radiation patterns the other simulated resonances at 319 and 370 MHz are believed to come from the probes; the lower of these being from the longer, fed probe, and the upper from the shorter, parasitic probe.

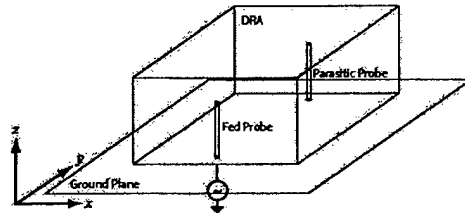
D. Circular Polarization

The application for which the antenna is designed requires circular polarization. A square DRA is ideal for CP implementation because two orthogonal modes can be excited using two probes along adjacent walls, as shown in Figure 3(b). At the DRA resonance E_z has a null at the midpoint of the DRA length in the y direction so the presence of the second probe should not affect the return loss at this frequency. At the probe resonance the effect of the second probe may be non-negligible. However, based on the return loss simulated with and without the second CP probe the effect is not substantial.

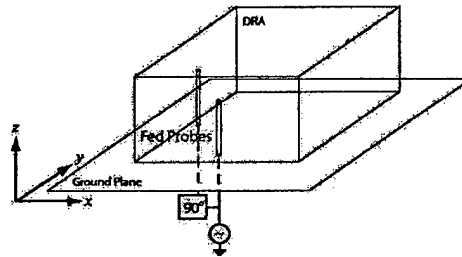
In the fabricated design a 90° hybrid coupler will be used to divide the input power to feed the two probes via microstrip as shown in Figure 2. Coaxial feeds could also be used rather than microstrip.

E. Simulation Results

A diagram of the final layered CP design with four probes, two fed and two parasitic, is shown in Figure 4. The DRA dimensions are 17.2 cm square by 7.5 cm tall; there are 14 layers each of which is 0.54 cm thick. The probes are located at the midpoint of each side, 0.54 cm in from the DRA edge.



(a) Probe fed DRA with parasitic probe.



(b) Circularly polarized probe fed DRA.

Fig. 3. Diagrams of probe fed DRA with (a) parasitic probe and (b) CP feed.

Simulations are carried out using the finite-difference time-domain (FDTD) method [3]. In order to simplify the FDTD model, the first probe is fed while the other fed probe is matched with a $50\ \Omega$ termination as it would be with the coupler. Therefore, the return loss reference plane is at the base of the fed probe rather than at the input to the coupler. Results for the return loss are shown in Figure 5. Since the design is symmetric an identical result is obtained when the other input probe is fed. The first resonance at 260 MHz is associated with the DRA, the second at 317 MHz with the fed probe, and the third at 370 MHz with the shorter, parasitic probe. The 10 dB bandwidth is 40% at 277 MHz. Copolarized radiation patterns in the $\phi = 90^\circ$ and $\phi = 0^\circ$ planes are shown in Figure 6. Again, the first probe is fed while the second CP probe is terminated in a matched load. Measurements will be carried out when antenna fabrication is completed.

REFERENCES

- [1] A. Buerkle, K. Sarabandi, and H. Mosallaei, Compact Slot and Dielectric Resonator Antenna with Dual-resonance, Broadband Characteristics. Submitted Nov. 2003 to *IEEE Trans. on Antennas and Propagation*.
- [2] H. Mosallaei, K. Sarabandi, Magneto-Dielectrics in Electromagnetics: Concepts and Applications, *IEEE Trans. on Antennas and Propagation*, vol. 52, Issue 6, June, 2004.
- [3] H. Mosallaei, *PhD dissertation*, University of CA., Los Angeles, 2001.
- [4] TransTech, Inc., Adamstown, MD. <http://www.trans-techinc.com/>.
- [5] Rogers Corporation, Rogers, CT. <http://www.rogers-corp.com/>.

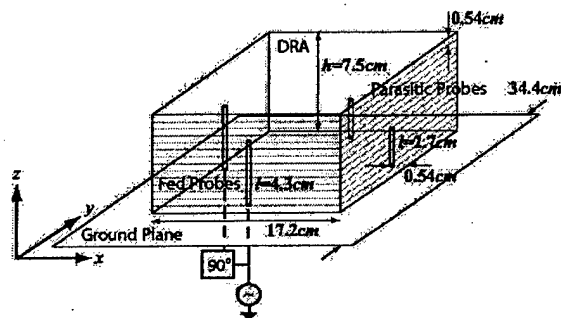


Fig. 4. Layered DRA design with circular polarization and two parasitic probes.

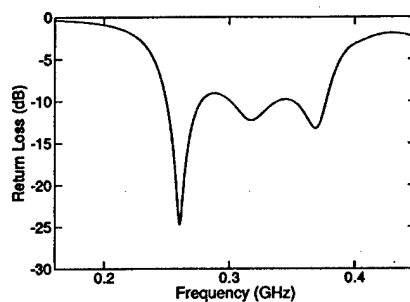


Fig. 5. Simulated return loss for the triple resonant metamaterial DRA. The first resonance at 260 MHz is associated with the DRA, the second at 317 MHz with the fed probe, and the third at 370 MHz with the shorter, parasitic probe.

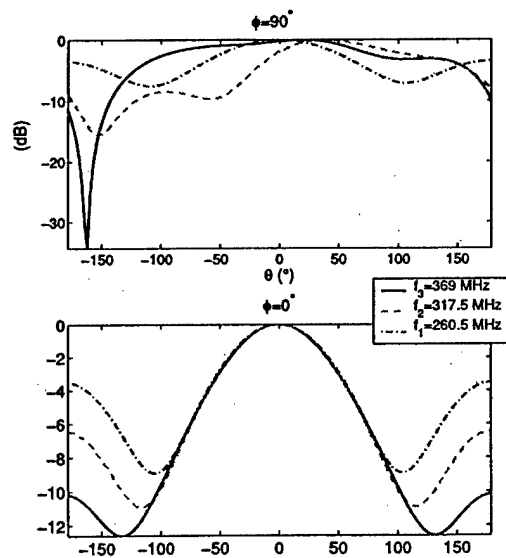


Fig. 6. Co-polarized radiation patterns at each resonance.

Analysis of a Radiation and Frequency Reconfigurable Microstrip Antenna

G. H. Huff and J. T. Bernhard

Electromagnetics Laboratory
Department of Electrical and Computer Engineering
University of Illinois at Urbana-Champaign
Urbana, IL 61801
<http://antennas.ece.uiuc.edu>

Abstract

In this work, a cavity model [1] of a radiation and frequency reconfigurable microstrip square spiral antenna [2] has been developed. This provides physical insight into the operation of the antenna and also serves as a foundation for the development of a generalized design methodology. To verify the cavity model of the reconfigured radiation antenna, commercially available full wave electromagnetic solvers have been used to examine the behavior of the radiating slots provided by the cavity model. Measured and simulated results are provided for a rectangular patch using this software approach to demonstrate the accuracy of modeling the radiation behavior of the radiating slots from the microstrip patch-mode. Measured and simulated results are then provided for the reconfigurable antenna, verifying the resonant operation and cavity model analysis used to characterize the antenna.

1. Introduction

The radiation and frequency reconfigurable single turn square spiral microstrip antenna [2, 3] has successfully demonstrated its versatility for several applications. Related work involving this reconfigurable antenna has illustrated its flexibility in array applications [2], as well as its behavior after integration onto generic laptop chassis [4]. To better serve both current and future applications, this paper focuses on the interpretation of the physical mechanisms which are responsible for the reconfigured radiation (which occurs over a common impedance bandwidth) and frequency behavior of the antenna.

For this particular microstrip geometry, which operates as a standing wave device, the cavity model [1, 5] is adopted to accurately capture the antenna's performance. In general, the versatility of the cavity model makes it very suitable for numerous antennas. It has proven to be a powerful analysis tool, and has demonstrated this outside the realm of traditional microstrip patch antennas [e.g., 6 and 7] with good success. Overall, this method provides straightforward results and an excellent physical interpretation of the radiating mechanisms associated with the antenna, along with a solid foundation for understanding the operation with respect to frequency. The model can then be used as the basis for a design methodology that can be used for new substrates, frequencies, and radiation requirements.

This paper begins with a brief description of the antenna's geometry and operation. The cavity model is presented next and discussed in the framework of the reconfigurable antenna. Following this, the appropriate cavities are then identified for each radiation reconfigurable configuration. With the cavities and local boundary conditions resulting from short and open circuits, the geometries of the radiating slots for the two antenna configurations (broadside and endfire) are then determined. The radiation characteristics for the equivalent set of cavities are examined next using commercially available software. To validate the method, the radiation behavior of a rectangular patch antenna on a finite ground plane is simulated and compared to measured data. Following this, the radiation properties of the reconfigurable antenna are simulated, and compared to measured values. The paper concludes with a short summary and discussion of future work.

2. Reconfigurable Antenna

2.1 Geometry and Behavior

The reconfigurable antenna geometry discussed in [2] is capable of switching between broadside and endfire radiation characteristics, maintained over a common impedance bandwidth centered around 6.9 GHz. The total linear dimension of the antenna is 81 mm ($\sim 2.5 \lambda_{\text{eff}}$), and it is fabricated on Duroid 5880 substrate with $\epsilon_r = 2.2$ and $h = 3.175$ mm (approximately 0.07λ at 6.9 GHz). The antenna geometry can be seen in Figure 1, and all relevant dimensions of the antenna are given in Table 1. The total footprint (area) of the antenna is approximately $0.5\lambda_0 \times 0.5\lambda_0$ at 6.9 GHz. To excite the antenna, a vertical SMA probe (diameter = 1.23 mm) is connected to the interior end of the spiral. The outer end of the spiral is shorted to ground with a copper via (diameter = 1.23 mm).

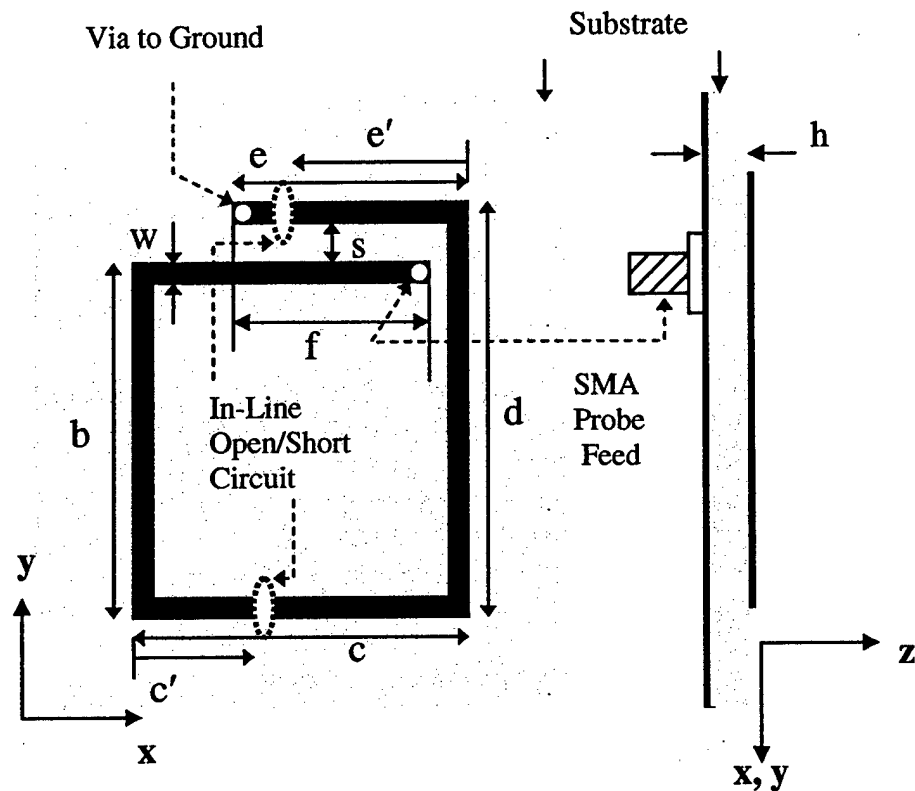


Figure 1. Antenna geometry and orientation for reconfigured radiation configurations. In the endfire configuration, the switch at e' is open and the switch at c' is closed, forming the square spiral geometry. For the broadside configuration the switch at c' is open and the switch at e' is closed, separating the spiral into the probe fed section and shorted parasitic section.

Table 1. Dimensions (mm) for the antenna geometry in Figure 1.

a	b	c	c'	d	e	e'	f	w	s	h
16.0	18.0	18.0	7.0	22.25	12.0	8.5	12	1.0	1.25	3.175

2.2 Operation

To alter the standing electric field distribution on the structure and reconfigure the radiation patterns, two surface mountable switching elements of dimension 1.0 mm x 1.0 mm (currently hard-wired for proof of concept) are incorporated into the design. For impedance tuning purposes, the local position of these switching elements may be properly adjusted to achieve the desired impedance match. In

the endfire configuration, the switch location at c' is closed and the switch location at e' is open. With this combination, the single turn square spiral geometry is recovered. In the broadside configuration, the switch location at c' is open and the switch location at e' is closed. In this configuration the antenna is composed of two separate sections: the probe-fed section and the grounded parasitic section which is excited via coupling across the contiguous section of length f , separated by the distance s .

3. Cavity Model

As previously stated, the antenna discussed in this work can be modeled by an equivalent set of cavities. However, the antenna does not directly follow the operation of a rectangular patch (or other canonical shape [1]), so the resulting cavity model and radiating slots must be reconsidered accordingly for the geometry and use of higher order modes in the cavity. In [1, 5] it can be found that for low impedance lines (e.g., rectangular patches), the slot configuration for a linearly polarized radiator is straightforward and is constructed as two slots (separated by the resonant length L). For each of these slots, there is a uniform electric field distribution with the appropriate polarization (based on the fringing field distribution of the patch along the resonant length). The present analysis continues by representing the equivalent slots with magnetic current elements [1, 5]. For brevity, this work deals primarily with the electric field representation of the radiating slots, so the magnetic currents will not be dealt with explicitly (although the analysis will be extended to this in the future).

3.1 Microstrip Patches and Radiators

To model the reconfigurable antenna as a resonant device, aspects of the cavity model are examined and discussed to justify the necessary assumptions associated with this analysis. For example, when modeling the rectangular microstrip geometry to higher degrees and/or for higher order modes, the low impedance line presented by the rectangular geometry can be thought of having four individual slots residing around the outer perimeter. Upon further investigation into the fundamental TM_{01} mode, it can be seen that the magnitude of the *secondary slots* (representing the fringing fields which support the modal - or sinusoidal - behavior along the sides of length L) is significantly smaller than the *primary slots* (along the width which support a uniform electric field distribution W). Along with the significantly smaller magnitude, the field distributions along these edges will experience destructive superposition in the far field at broadside due to the field polarization and spacing along these dimensions. For the reconfigurable antenna, the contributions from the slots associated with both of the characteristic

dimensions (L and W) will differ from that of rectangular patch geometry. This is attributed to the reconfigurable antenna geometry which is: (1) wrapped into the square spiral geometry along the resonant length L and (2) a high impedance line of dimensions such that $W \ll L$.

3.1.1 Long Microstrip Radiators

Although different from the reconfigurable antenna in many aspects, the long microstrip radiator in [6] has interesting parallels in its geometry. It consists of a conducting strip wrapped around the axis of a cylinder (resonant along the width W), which is fed by several microstrip lines along the circumference length L (parallel to the cylinder axis L) similar to several rectangular patches connected in parallel). In the case of the long microstrip radiator, the number of feeds needed to excite the TEM mode transverse to L that will effectively excite only the TM_{0m} mode (transverse to W in free space) requires several feeds per wavelength along the length L . This feeding technique is necessary to avoid exciting higher-order TM_{nm} modes. In a cavity model analysis of this antenna, the primary radiating slots would reside along the perimeter length L (polarized perpendicular to L), similar to a rectangular patch antenna. For the reconfigurable antenna, the TEM mode is again excited on the line as in the long microstrip radiator; however, the probe feed and narrow line require that the previous assumptions be reconsidered.

3.1.2 High Impedance Long Microstrip Radiators

In cases of a high impedance long microstrip radiator, where the width of the line is very narrow and there exists only a single edge feed (probe dimensions are comparable to the width W), the propagation along the line length L remains TEM. When considered as a cavity, this will resemble a TM_{0m} mode. In this configuration, the narrow line will experience the same phenomena as the patch (e.g. length extensions, etc.), seen in Figure 2. However, the field structure will be modified as previously stated to the extent that the slots experiencing the modal distribution (transverse to L) become the primary radiating mechanism due their greater effective slot width, and the secondary slots are now ignored in a first order analysis, opposite to the case of a rectangular patch.

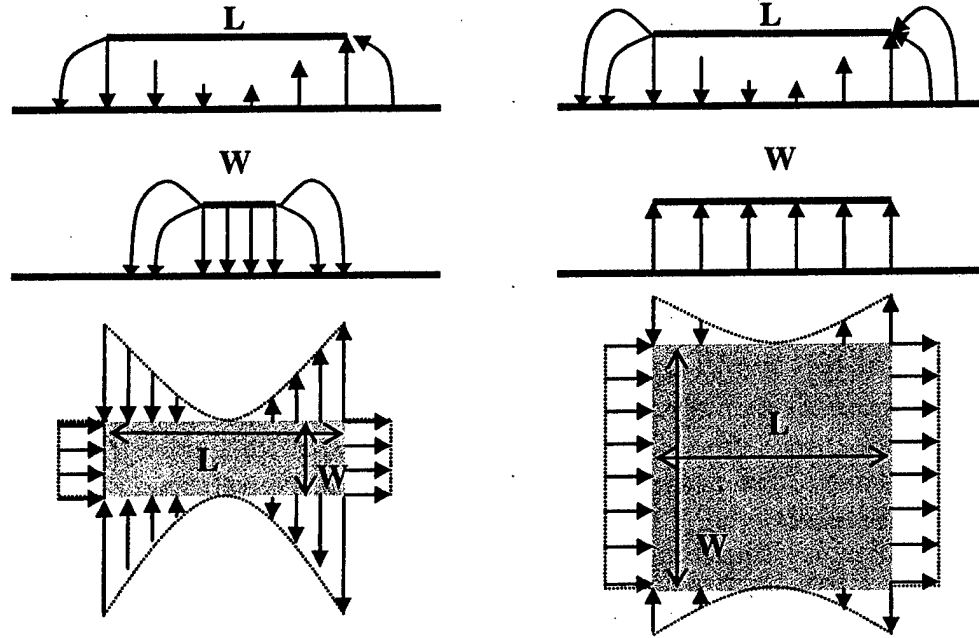


Figure 2. Field distribution (top) and equivalent slots (bottom) for a 0.5λ high impedance (left) and low impedance (right) microstrip line operating in the patch mode.

3.1.3 Cavity Model of the High Impedance Long Microstrip Radiator

The analysis begins first by constructing the appropriate cavities formed by all desired variations of the antenna and resulting electric field distributions. The geometric variations responsible for reconfiguration are created from the in-line switches discussed in Section 2. Next, a set of appropriate wave functions is identified for all of the cavities, which can individually satisfy Laplace's Equation (Equation 1) and the appropriate local boundary conditions (Equation 2). Using these wave functions, the radiating mechanisms can be approximated using radiating slots and a basic description of the operation with respect to frequency can be attained.

$$\bar{\psi}(\nabla^2 + k^2) = 0 \text{ with } \bar{\psi} = \hat{z} \psi(x) \quad (1)$$

$$\frac{d\bar{\psi}(x)}{d\hat{n}} = 0 \text{ (magnetic) and } |\hat{n}\bar{\psi}(x)| = 0 \text{ (electric)} \quad (2)$$

To obtain the radiation characteristics of the antenna, all of the resonant behavior found from the cavity analysis are included and projected onto the ground plane of the antenna, as a properly phased and polarized pair (or pairs) of radiating slots.

To analyze this behavior, a process using commercially available software has been explored which provides a quick approximation to the radiating slots in [1, 5]. The physical interpretation of these slots is the modal distribution of the fringing fields, or the vertical magnetic current ribbon along the dimensions of the geometry. In conjunction with this, the microstrip structure can also provide a quick transmission line equivalent circuit, which incorporates the cavity and radiating slot impedance. However, the primary focus of this work will be on the radiating properties of the antenna, and a calculation of impedance will be handled in future work.

For this particular antenna, two further steps can also be made prior to analysis that can simplify the process. First, the antenna can be modeled as a thin microstrip line ($W < h$ and $W \ll L$), which can be unwrapped into linear geometries and later re-wrapped without significantly disturbing the wave function. It is along these unwrapped linear dimensions that the modal behavior will be considered. Second, the SMA probe feed used to excite the antenna can be modeled as short circuit of the same dimension in the microstrip line in lieu of a forced (or hard) boundary condition, and hence will resemble an electric boundary condition in the cavity analysis when this is the case.

3.2 Endfire Configuration

The endfire configuration is examined first. With this geometry unwrapped counterclockwise, two cavities can be formed having the lengths L_1 and L_2 , shown in Figure 3. These represent the section of line from the open circuit to the grounding via and the length of line from the probe feed to the open circuit at e' , respectively. The first length L_1 is negligible in comparison to L_2 and λ_d , so contributions from this cavity can be neglected in the absence of an excitation for this section. The boundary conditions for this remaining cavity C_2 are magnetic at $x = 0$ where the open circuit resides (standing electric field is at a maximum), and electric at $x = x_1$ from the probe's appearance as a short circuit (standing electric field is at a minimum). The wave function which satisfies these two boundary conditions is given identified in Equation 3, with $L = L_2$. This configuration is operated in the TM_{05} mode.

$$\psi_m(x) = \cos(k_m x) \text{ with } k_m = \frac{m\pi}{2L} \text{ and } m = 1, 3, 5, \dots (\text{odd}) \quad (3)$$

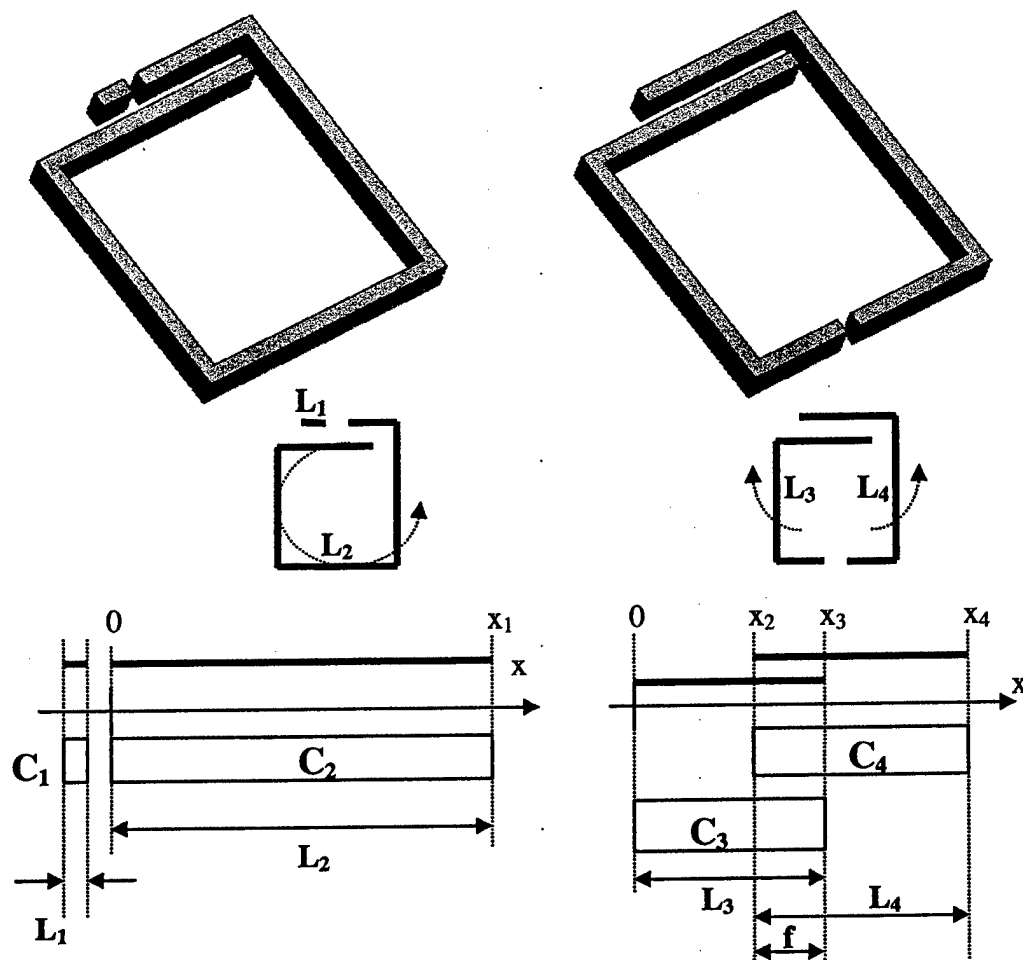


Figure 3. Endfire (left) and broadside (right) reconfigurable radiation configurations. The resulting cavities (top) can be decomposed into similar sets of inner and outer slot geometries (middle), and unwound according to arrow direction (only the general shape is shown), which can be approximated by the cavity cross sections (bottom).

3.3 Broadside Configuration

For the broadside configuration, the geometry is unwrapped (Figure 3) such that the probe fed section is opened up clockwise toward the negative x -axis and the section of line with the via to ground opened up counterclockwise toward the positive x -axis. The antenna can then be modeled as two cavities C_3 and C_4 , representing the probe fed section of line of length L_3 and the parasitic section of line with the via to ground for length L_4 . For the cavity C_3 the associated

boundary conditions are magnetic at $x = 0$ (open circuit), and electric at $x = x_3$ (short circuit from probe), similar to the endfire configuration. The cavity C_4 is similar to the endfire configuration as well (reversed), with electric boundary conditions (the via to ground) at $x = x_2$ and magnetic (open circuit) at $x = x_4$. The resulting wave function for these cavities is Equation 3 with $L = L_3$ and Equation 4 with $L = L_4$ for C_3 and C_4 , respectively. Further, to facilitate a better impedance match with these capacitively coupled lines and limit its effects on radiation, the length L_3 is set slightly inductive (smaller in comparison to resonant length of L_4).

$$\psi_m(x) = \sin(k_m x) \text{ with } k_m = \frac{m\pi}{2L} \text{ and } m = 1, 3, 5, \dots (\text{odd}) \quad (4)$$

3.4 Cavity Representation of Coupling

3.4.1 Broadside Configuration

In the broadside configuration, the coupling across the contiguous spiral section (length f , separated by s) is essential to achieving the desired operation. The probe fed cavity C_3 is coupled to the parasitic cavity C_4 through the resonant behavior along the length f (Figure 3), which is set to $\sim 0.5 \lambda_d$. This behavior can also be modeled as a resonant structure in an analysis similar to [7]. This cavity is of length f and width s , and is formed by impressing the boundary conditions from the two neighboring cavities, creating electric walls of width s at x_3 and x_4 . For these walls, it is assumed that the electric walls at x_2 and x_3 (especially the shorting via) will greatly influence the local field behavior across the distance s ($\sim 0.04 \lambda_d$), which will also be in the vicinity of a voltage minima when the cavity is resonant. A magnetic wall on the surface of the substrate completes the cavity geometry, and is created by assuming the electric field is primarily coupling in a differential mode across s and along f (from the probe fed section to the parasitic section). The wave function for this cavity is in Equation 5, with $L = f$; where coupling is greatest when this cavity shares resonance with the other two neighboring cavities, C_3 and C_4 . This can be extended to include a phase delay δ (Equation 6) for the argument in Equation 4, associated with the transient effects of coupling onto the parasitic section.

$$\psi_m(x) = \sin(k_m x) \text{ with } k_m = \frac{m\pi}{L} \text{ and } m = 1, 2, 3, \dots (\text{all}) \quad (5)$$

$$\delta = \frac{2\pi s}{\lambda_d} \quad (6)$$

3.4.2 Endfire Configuration

In the endfire configuration, the coupling from the contiguous portion of the spiral (length f , separated by distance s) can also be taken into account, but the effects are not as pronounced as in the broadside configuration. This is due to: (1) a voltage minima (in the cavity) at the location of the short when the cavity is resonant and (2) the isolation of the shorting via created by the open circuit at e' , which perturbs the cavity and prevents the resonant coupling behavior seen in the broadside configuration. However, some interaction will occur from differential mode coupling and can be accounted for by superimposing a second wave function in the cavity (identical to Equation 3) with the additional phase delay δ (Eq. 6) in the argument. Without the resonant coupling, the effect of the superimposed wave function has a decreased magnitude and will be minimal. In a transient analysis, this interaction is responsible for the ringing this geometry experiences, along with the higher Q (or lower bandwidth) similar to a spiral inductor.

3.5 Reconfigured Frequency

After the appropriate wave functions have been determined, the resonant frequencies of the cavity can be calculated. Using the wave number k_m found in the previous sections, an approximate resonant frequency can be calculated using Eq. 7, where ϵ_d is the dielectric permittivity. Using this process in reverse (identical to the process determining rectangular patch dimensions), one can easily obtain approximate dimensions of similar reconfigurable antennas. A continuation of this topic will be addressed in future work.

$$k_m = \frac{m\pi}{2L} = 2\pi f_m \sqrt{\mu\epsilon_d} \quad (7)$$

4. Radiating Slots: Representation and Evaluation

To validate the cavity model and its resonant behavior of the radiation reconfigurable antenna, a method using commercially available software has been used. It provides an approximation to the physical mechanisms of the cavity model that is responsible for the radiation behavior. In this approach, the radiating slots used to represent the fringing electric fields are modeled using features common to many full wave electromagnetic solvers. To model the slots directly, the representative slot areas residing at the appropriate physical locations on the ground plane can be excited as if they were radiating apertures. The

polarization, phase and magnitude of these apertures can be tailored within the program, and may also incorporate local boundary conditions to force the electric field distribution in the slot to a modal (TEM behavior described in Section 3) or non-modal profile. While this approach provides useful information about the radiation features without including all of the geometric features, it does not accurately model the impedance due to the ambiguity of the excitation with regard to a specific feed location.

For this work, HFSS 9.1 has been used to model the radiating slots. Within the framework of the software, the radiating slots of the microstrip antenna can be modeled as "wave port" excitations, located where the slots would be projected onto the ground plane of the antenna geometry. To accommodate this excitation, the ground plane of the antenna must first be extruded into a volumetric element of finite conductivity (copper was used for this study) and nominal thickness below the substrate. For all of the results obtained in this work, the ground planes have been given a thickness of 0.25 mm. This must be done as to not allow energy to enter or exit through the back of the wave port (passive, 1 port device). Next, the planar geometries of the radiation slots are created on the interface between the substrate and ground plane. These slots are then excited as a wave port and polarized accordingly. In this orientation, the boundary conditions around the port geometry will be electric by default due to its location on the surface of the conductive slab. If a magnetic boundary condition is required (as is the case with an open circuited line), a nominally small area (or appropriate vertex) can be created and assigned as such, along the desired dimensions tangent to the polarization of the slot.

4.1 Example: Rectangular Microstrip Patch

To evaluate the wave port representation of the radiating slots, a probe fed (probe dimensions same as reconfigurable antenna) rectangular microstrip patch antenna designed to operate at 5.775 GHz ($L = 8.2$ mm and $W = 14$ mm) has been modeled and fabricated on a finite ground plane and substrate (Duroid 6006, $\epsilon_r = 6.15$ and $h = 2.54$ mm). To approximate the radiating slots, the patch is replaced by two slots (wave ports) with the appropriate orientation, spacing, and polarization determined by the patch dimensions and cavity model. For the patch, the field distribution within the slot is approximately uniform, so magnetic boundary conditions are enforced at the opposing ends of each slot. The layout for both the patch and the slots can be seen in Figure 4.

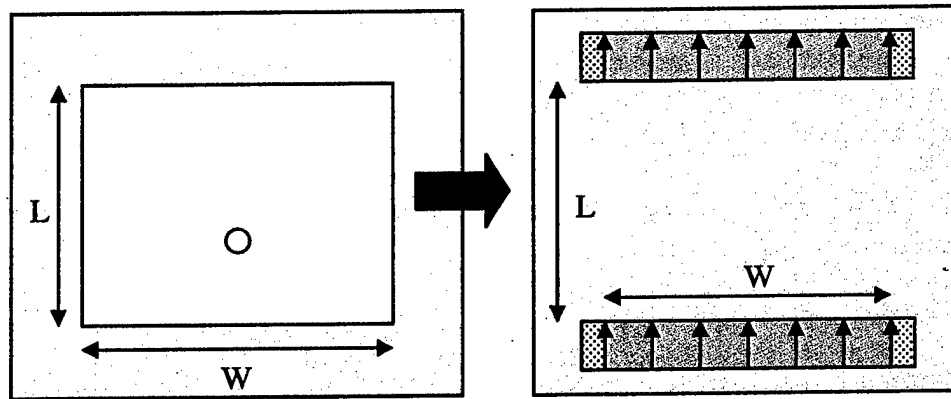


Figure 4. Patch antenna (left) and equivalent radiating slot model using wave ports in HFSS (right). The ground plane is light gray, the slot (wave port) is dark gray, hatched areas outside the slot represent magnetic boundary conditions, and arrows indicate slot polarization.

4.2 Results: Rectangular Microstrip Patch

Measured and simulated radiation patterns from this patch can be seen in Figure 5. Examination of these patterns demonstrates the wave port's ability to provide a good representation of the physical radiating mechanism associated with microstrip antenna patch-mode. It should be noted that effects from the finite ground plane are present with the wave port approximation, shown by the development of back-plane radiation that closely matches the measured antenna behavior. Using this as verification for the accuracy of the model approximation, the results obtained for the reconfigurable antenna can be interpreted.

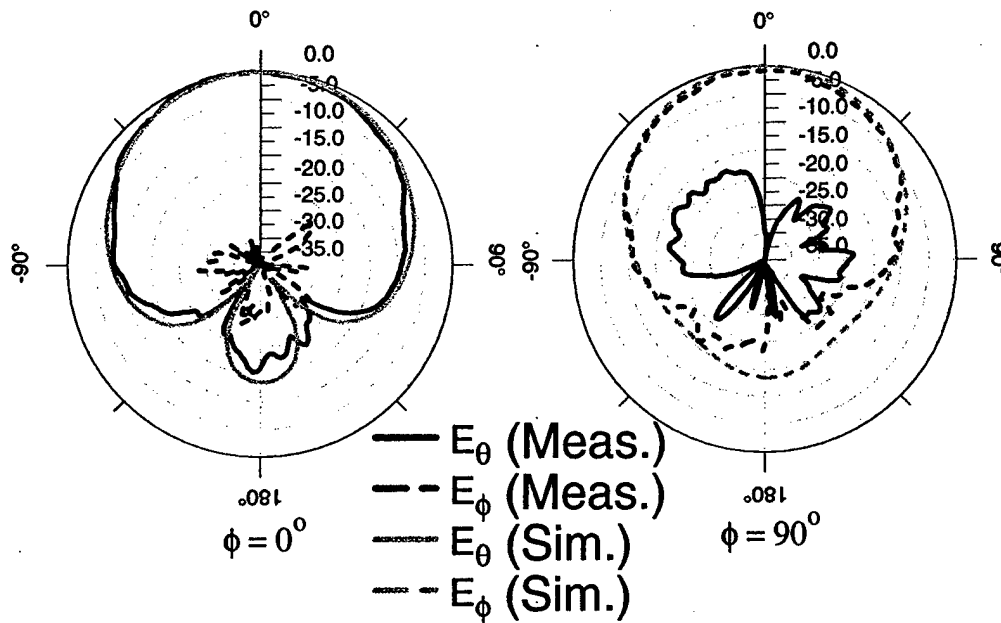


Figure 5. Measured (black) and simulated radiating slot (gray) radiation patterns for the microstrip patch example.

4.3 Reconfigured Radiating Slots

For the radiation reconfigurable antenna discussed in this work, an approximate radiating slot distribution can also be obtained according to the description in Section 3. The polarization and phasing of these slots must be representative of the physical electric field distribution, so special attention must be given to the individual slots to ensure the accuracy of the model. After creating these slot pairs transverse to the length of the line segment(s) that bound the cavity or cavities, the proper boundary conditions are created along the end of the slots according to the cavity analysis. For these full-length slots, the modal distribution will develop according to the imposed boundary conditions and will be used in the following sections to model the antenna's radiation.

5. Measured and Simulated Radiation Characteristics

Measured and simulated results for the reconfigurable antenna can be seen in Figures 6 and 7. To achieve the reconfigured radiation over a common impedance bandwidth, the endfire configuration is operated in the TM_{05} mode and the broadside configuration is operated in the TM_{03} mode (both sections). At the corresponding frequency (~ 6.9 GHz) for these modes, both configurations will

exhibit resonant behavior and the impedance will be dominated by the radiation resistance of the antenna (this topic will be addressed in future work). In both configurations, the measured and simulated radiation patterns have been normalized independently and show good agreement between the simulated equivalent slots and the measured results. In Figure 6, the results for the endfire configuration show the development of nulls in the broadside direction that are very close in depth and direction. In the dominant polarization E_θ , the agreement is very close. In the orthogonal polarization E_ϕ , the level of agreement between the simulated and measured is not as precise, but the general characteristics and shaping of the radiation is similar. This effect on the non-dominant polarization can be attributed to the idealistic conditions of the two parallel slots with opposite tangential polarizations, which does not completely model the interaction of those fringing fields. Specific to this case, the superposition of the fields with ideal slots effectively cancel each other better in the far field, more so than the fabricated antenna. Additionally, no corner effects are captured in this configuration as the modal field distribution has maxima along the straight edges.

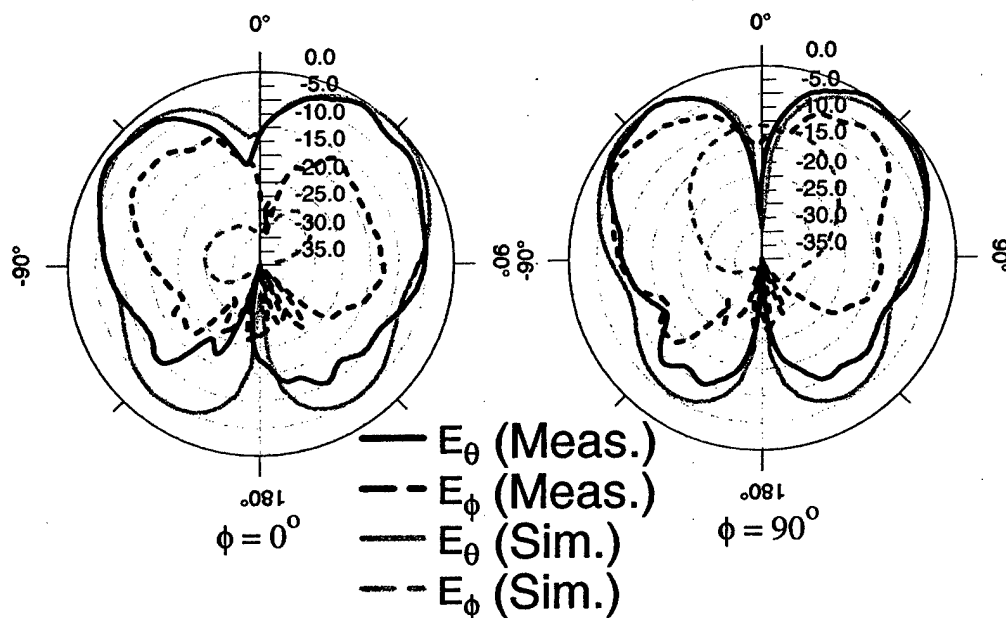


Figure 6. Measured (black) and simulated radiating slot (gray) radiation patterns for the endfire configuration.

In the broadside configuration (Figure 7) the general behavior of the radiating slots accurately describes the antenna. In this case there exists the effects of fringing fields (e.g. the tilting of the beam) associated with the coupled line

section. In this configuration the electric field distribution is shifted by $0.25 \lambda_d$ due to the shorted section (with respect to the endfire configuration) that creates maxima located closer to the corners of the antenna, providing a slight imbalance in the field distribution between the inner and outer apertures. This effectively keeps the opposing polarizations from completely canceling each other (as in the case of the endfire configuration) and creates the broadside radiation characteristics.

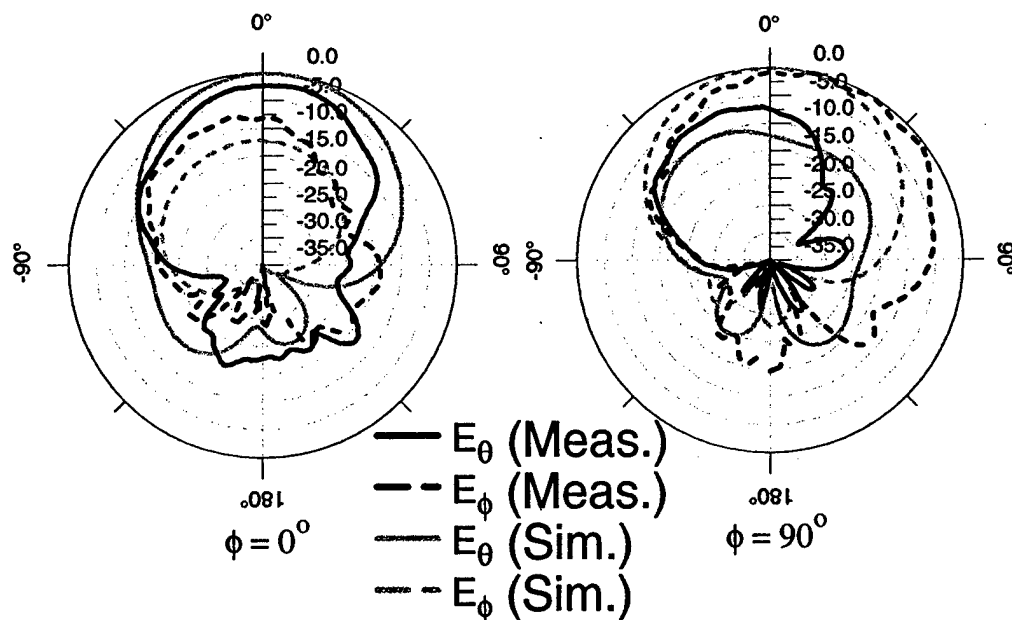


Figure 7. Measured (black) and simulated radiating slot (gray) radiation patterns for the broadside configuration.

6. Conclusions

In this work we have applied the cavity model originally developed for rectangular patch antennas to a thin line ($W \ll L$) spiral microstrip radiation and frequency reconfigurable antenna. A method for approximating the radiation of the cavity model for complex geometries has also been successfully explored using commercially available software, and has been used to verify the operation of the antenna in a higher order patch-mode. With this knowledge of the physical radiating mechanism, scaling in both substrate and frequency can be achieved. Future work will focus on the development of design equations based on the fundamental cavity relationships obtained from this analysis.

7. Work Cited

- [1] Y. T. Lo , D. Solomon, and W. F. Richards, "Theory and experiment on microstrip antennas," *IEEE Transactions on Antennas and Propagation*, vol. 27, no. 2, March 1979, pp. 137 – 145.
- [2] G. H. Huff, J. Feng, and J. T. Bernhard, "Small array of boresight to endfire radiation reconfigurable antennas," *Proc. 2003 Antenna Applications Symposium*, Allerton Park, Monticello, Illinois, 2003, pp. 147-161.
- [3] G. H. Huff, J. Feng, S. Zhang, J. T. Bernhard, "A novel radiation pattern and frequency reconfigurable single turn square spiral antenna," *IEEE Microwave and Wireless Components Letters*, vol. 13, no. 2, pp. 57-60, Feb. 2003.
- [4] G. H. Huff, J. Feng, S. Zhang, and J. T. Bernhard, "Directional reconfigurable antennas on laptop computers: simulation, measurement, and evaluation of candidate integration positions." Accepted for publication in *IEEE Transactions on Antennas and Propagation*.
- [5] W. Richards, Y. T. Lo, and D. Harrison, "An improved theory for microstrip antennas and applications," *IEEE Transactions on Antennas and Propagation*, vol.29, no. 1, pp. 38-46, Nov. 1981.
- [6] J. Gomez-Tagle and C.G. Christodoulou, "Extended cavity model analysis of stacked microstrip ring antennas," *IEEE Transactions on Antennas and Propagation*, vol. 45, no. 11, pp. 1626-1635, Nov. 1997.
- [7] H. Himdi, J. P. Daniel, and C. Terret, "Analysis of aperture-coupled microstrip antenna using cavity method," *Electronics Letters*, vol. 25, no. 6, pp. 391 – 392, March 1989.
- [8] R. E. Munson, "Conformal microstrip antennas and microstrip phased arrays," *IEEE Transactions on Antennas and Propagation*, vol. 22, pp. 74-78, Jan. 1974.
- [9] A. Derneryd, "Linearly polarized microstrip antennas," *IEEE Transactions on Antennas and Propagation*, vol. 24, no. 6, pp. 846-851, Nov. 1976.
- [10] A. Derneryd and A. Lind, "Extended analysis of rectangular microstrip resonator antennas," *IEEE Transactions on Antennas and Propagation*, vol. 27, no. 6, pp. 846-849, Nov. 1979.

[11] D. Chang, "Analytical theory of an unloaded rectangular microstrip patch," *IEEE Transactions on Antennas and Propagation*, vol.29, no. 1, pp. 54-62, Nov. 1981.

[12] S. Mutlu and M. I. Aksun, "Hybrid model for probe-fed rectangular microstrip antennas with shorting pins," *2000 IEEE Antennas and Propagation Society International Symposium*, vol. 3, 16-21 pp. 1448 -1451, July 2000

32-CHANNEL X-BAND DIGITAL BEAMFORMING RECEIVE ARRAY HARDWARE

William H. Weedon¹, David D. Curtis² and Capt Ryan W. Thomas²

John Burroughs¹, Daniel Spendley², 2dLt Joseph D Rosal²

¹Applied Radar, Inc., 210 Airport Street, N. Kingstown, RI 02852

²Air Force Research Lab. 80 Scott Road, Hanscom AFB, MA 01731

Abstract: Hardware for a 32-channel digital beamforming (DBF) receive array operating at X-band with 15 MHz instantaneous bandwidth is presented. The digital receive system consists of a 32-channel processor backplane with 9 field-programmable gate arrays (FPGAs), 1 GB of RAM, and a USB 2.0 interface for applying digital complex weights in real time and transferring multi-beam digital data to a remote computer. A plug-n-play architecture is employed with 32 identical X-band digital receive modules that plug into the processor backplane. The receive modules each contain a single-stage downconverter tunable throughout the X-band range, an A/D converter, and an internal FPGA that implements a digital equalizer and a digital demodulator to generate I/Q baseband data. In principle, the DBF processor can be re-used in such a way that the X-band receive modules are replaced with other receive modules, such as those operating at UHF, L-band or EHF frequencies. Scalability features have also been designed into the DBF processor so that a larger array can be built by stacking multiple DBF arrays side-by-side.

1.0 Introduction

Digital beamforming (DBF) is becoming increasingly popular for phased-array radar and communications applications [1-2]. Advantages include multiple simultaneous beams on receive, ultra-low sidelobes through the use of dynamic calibration, jam suppression, etc. Multi-function apertures are also enabled by DBF technology. Multiple simultaneous narrow-beam communications channels could exist at the same time on different beams. Multiple-input multiple-output (MIMO) communications utilize multiple beams for increased efficiency [3]. Radar and communications functions could also potentially be performed simultaneously using the same aperture.

There is a big push to reduce the number of antennas on airborne, ship-based and vehicular platforms, so a single aperture that can perform multiple functions is quite attractive. Satellite-based radar and communications antennas also benefit

from DBF. The ability to rapidly re-configure the multiple aperture beams adds a high degree of flexibility and allows the most effective utilization of a valuable antenna aperture for both military and commercial applications.

Despite the numerous advantages of DBF, there are still a number of challenges associated with the implementation of this technology. The biggest technical obstacle is cost. At X-band, implementation of a DBF receiver requires a downconverter and A/D for every channel. Generally speaking, the cost of implementing DBF at the element-level (downconverter and A/D at every element) for a moderate-sized array of 1000 elements is prohibitive for all but the most critical applications. For this reason, DBF may more practically implemented at the sub-array level. Although sub-array DBF still requires phase-shifters at the element-level, the cost is substantially reduced.

There are also a number of technical issues associated with the implementation of DBF. The first is the implementation of a downconverter and A/D at every channel. At low frequencies (UHF and possibly L-band), direct sampling of the RF signal is possible. At X-band, a downconverter is necessary to shift the RF signal frequency within the range of the A/D. This means that local oscillator (LO) signals must be provided to each channel. A single-stage downconverter requires only one LO, but the dynamic range is limited due to spurious image tones. A two-stage receiver would typically have more performance, but requires two separate LO signals to be routed to every input channel. Plumbing the various LO signals in coax is less than desirable. Another hardware option is to implement a frequency synthesizer for every input channel, phase-locked to a common low-frequency source. This cuts down on the RF plumbing, but adds to the hardware complexity.

In addition to the downconverter and A/D required at every input channel, a digital processor is required in order to perform the actual digital beamforming. The use of field-programmable gate array (FPGA) hardware makes the processor implementation practical and allows many of the details of the actual beamforming to be implemented in firmware. Nevertheless, there are many details associated with the data timing and synchronization that must be carefully considered. Very careful attention to circuit layout must be considered due to the number data busses and the potential for cross-talk and simultaneous switching noise problems.

Although many high-performance FPGAs are available with over 1000 pins, the I/O pins get used up quickly by the input channel data, output data, and control

busses. The DBF hardware that we present here uses parallel busses for the input channels and output beams. As a result, we were limited to 4 input channels per FPGA, and multiple FPGAs were required to implement the full array with 32 input channels. A total of 9 FPGAs were used on our DBF processor, 8 for performing the beamforming (CMULT FPGAs), and 1 more (TCOP FPGA) for directing the data to RAM and the output interface. Synchronizing multiple FPGAs in real-time is a challenging task, but if feasible if the clock and data lines are implemented correctly in hardware.

In our previous paper [1], the design of our 32-Channel DBF receive array was discussed. The concept of a "plug-n-Play" array presented, where the receive modules are form-fit to a 4x4 subarray of X-band elements, and located directly behind the array. At that time, the DBF modules were fabricated but not tested, and the DBF processor was not built. All of this hardware has since been built, tested, and delivered to the Government. While we do not yet have antenna patterns to show, we have collected measurement data from the DBF modules and processor hardware on the benchtop, and show that the hardware performs as designed. The antenna pattern measurements will be deferred to another paper, once we have had a chance to perform the full-system measurements with an antenna array.

2.0 Plug-n-Play Architecture

Figure 1 illustrates the architecture of the 32-channel DBF receive array. A total of 32 X-band digital receive modules sit behind a 512-element aperture of microstrip patch elements. Although the modules physically fit beneath a 4x4 group of array elements, each module is electrically connected one to a column of 16 elements. In this manner, the digital beamforming is performed in azimuth only. Mechanical scanning may be used to scan the elevation direction if necessary.

The 32 modules also plug directly into a DBF processor backplane that also sits beneath the footprint of the 512-element array. Digital data is passed from the digital receive modules to the DBF processor, which is responsible for performing the actual beamforming operations. A remote computer connects to the processor to control the array and to extract digital beam data.

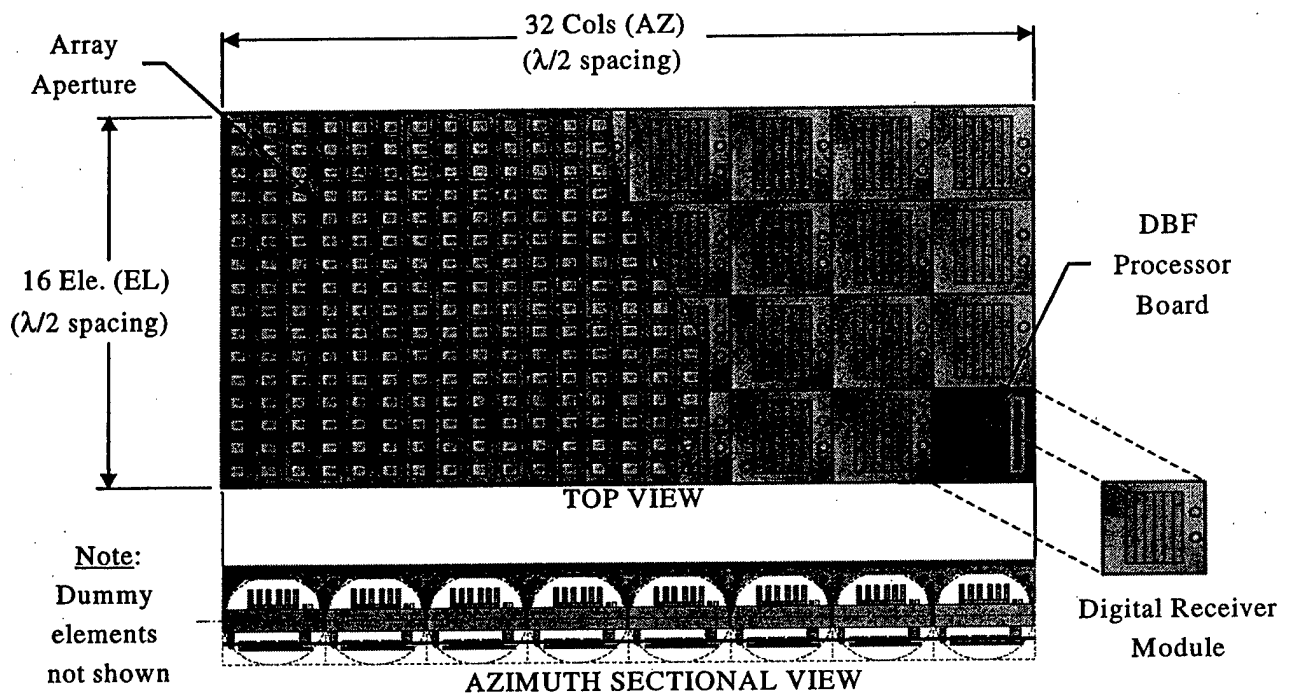


Figure 1: Illustration of digital beamforming (DBF) plug-n-play array configuration.

3.0 X-Band Digital Receive Modules

The digital receive modules shown in Figure 2 consist of an RF downconverter and a data acquisition module (DAM). The RF inputs to this module consist of a LO input tunable over 8 – 12 GHz and the RF input. A digital connector is provided at the bottom of the module to supply power from the DBF processor as well as to provide digital control signals. Digital data is extracted through this same connector.

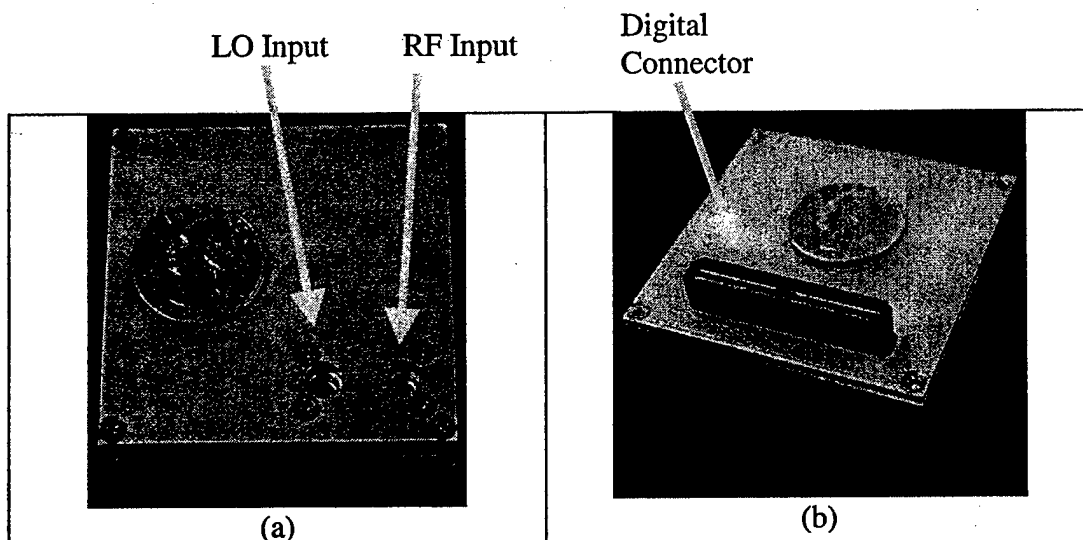


Figure 2: X-band digital receive module: (a) top side, (b) bottom side. The module measures 2.5"x2.5"x1.0".

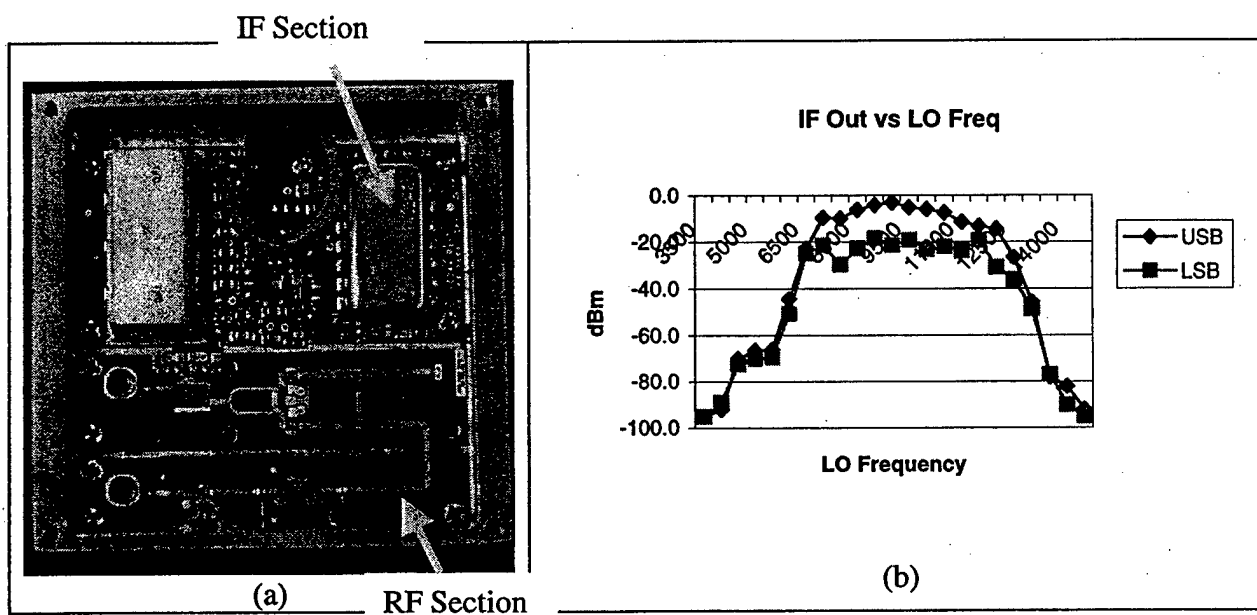


Figure 3: RF downconverter: (a) hardware, (b) IF output vs LO frequency.

3.1 RF Downconverter

Figure 3(a) shows a picture of the RF downconverter consisting of the RF and IF sections sitting side-by-side. The blue coaxial cable connects the IF output to the digital section on the bottom side. The downconverter employs a single-stage image-reject mixer architecture to simplify the RF electronics and minimize the required LO plumbing. A block diagram of the RF downconverter signal chain is shown in Figure 4.

Figure 3(b) shows the upper and lower sideband outputs (USB/LSB) from the RF downconverter as the LO is tuned across the 8 – 12 GHz band. The difference between the USB and LSB signal levels indicates the image rejection of about 18 dB in the center of the band. Typically, the LSB signal is terminated in 50 Ohms, and the USB signal is fed to the IF amplifier/filter chain. Our measurements indicate approximately 90 dB of dynamic range from the minimal detectable signal (MDS) to the 1dB compression point.

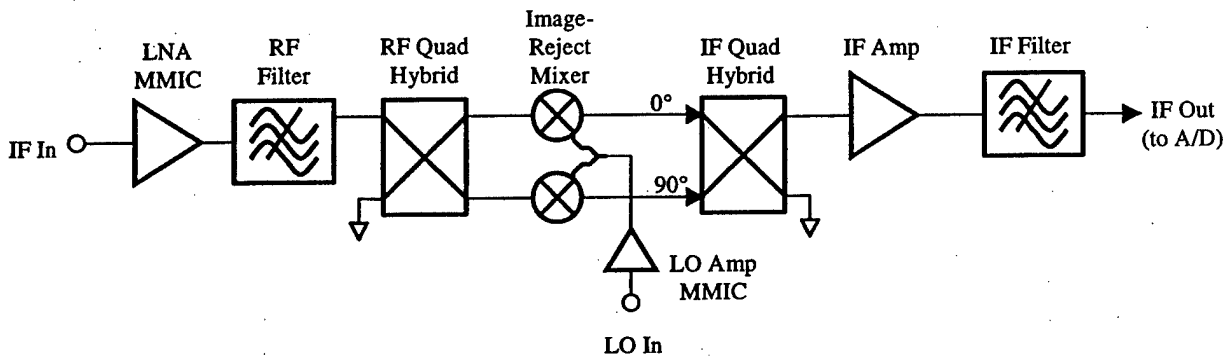


Figure 4: Block diagram of the RF downconverter signal chain.

3.2 Data Acquisition Module (DAM)

Figure 5 shows a photograph of the top and bottom sides of the DAM board. A block diagram of the data flow is shown in Figure 6. The IF data is sampled with a 14-bit A/D at 60 MHz. Data is then passed to an Altera FPGA which performs real-time equalization of the channel followed by a digital demodulation. A 10-tap non-symmetric FIR equalization filter is used to calibrate out any channel-to-channel amplitude and phase deviations as a function of frequency.

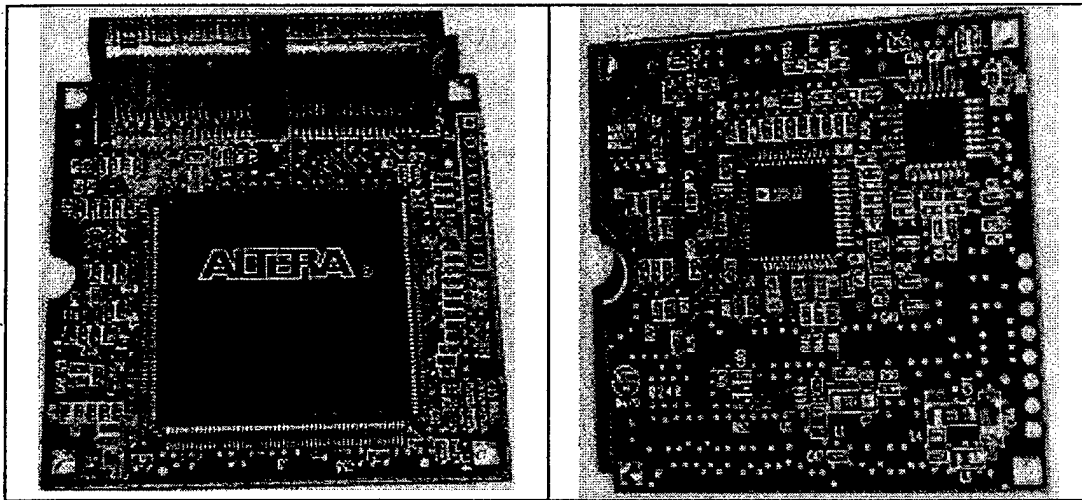


Figure 5: Photograph of (a) top and (b) bottom sides of data acquisition module (DAM).

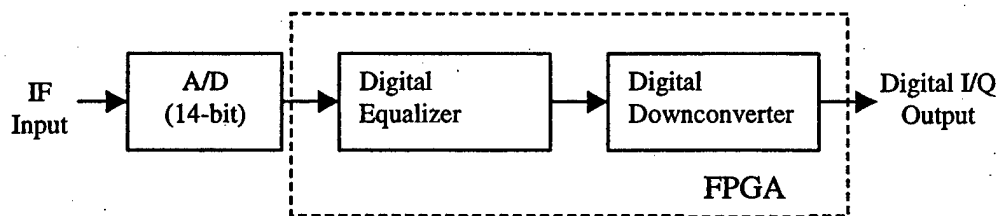


Figure 6: Block diagram of DAM data processing.

4.0 DBF Processor

Figure 7 shows a block diagram of the DBF processor. There are a total of 8 complex multiply (CMULT) FPGAs, each of which accepts 4 input channels (digital receive modules). Each CMULT feeds its 4 parallel output beams to the adjacent CMULT, with the exception of the last one, which feeds to the traffic-cop (TCOP) FPGA.

Beam input and output connectors are present at the beginning and the end of the CMULT chain to allow additional DBF processors to be used in a scalable array. Alternately, the beam output connector can be used to connect to an external RAID array for real-time data storage.

The TCOP FPGA accepts data from the CMULT chain and directs data between the SDRAM and a USB 2.0 interface. The real-time data rate is:

$$\text{Output Data Rate} = 60 \text{ MHz} \times 4 \text{ Beams} \times 16 \text{ bits} = 3.84 \text{ GBPS}$$

The USB 2.0 interface is only capable of a maximum of 480 MBPS. Hence, data needs to be stored in SDRAM and buffered out through the USB 2.0 interface for quasi-real-time operation. In a radar application, data could be collected, stored, and transferred between every transmit pulse. If real-time data is required, a daughter card could be connected to the beam output connector with a fiber-channel connection to a RAID array.

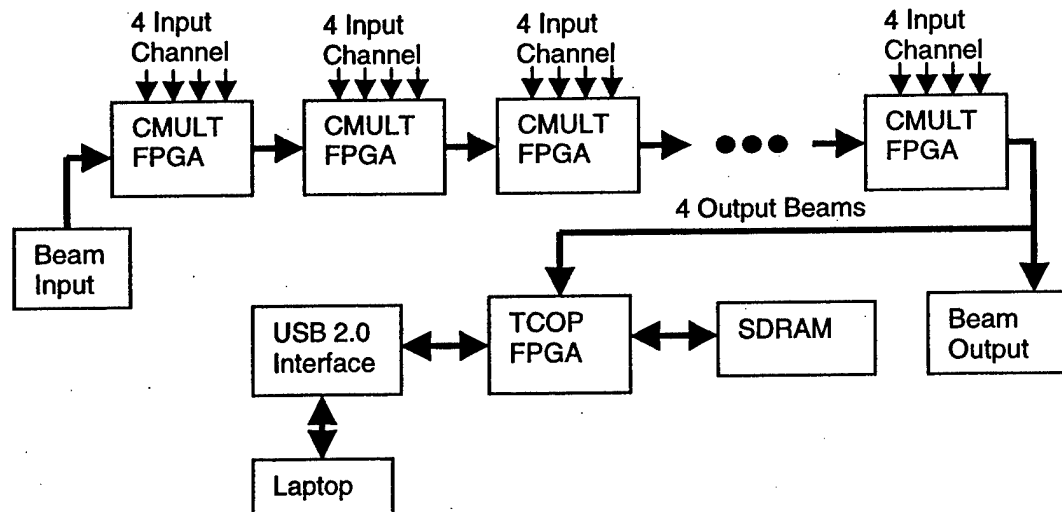


Figure 7: Signal flow block diagram of DBF processor.

Figure 8 shows several pictures of the complete DBF processor unit. In (a), the top side of the bare board is shown with 5 digital receive modules populated. In (b), the bottom side is shown, with the various FPGAs, USB chip and SDRAM. A 3D CAD drawing is shown in (c), while a photo of the complete DBF processor is shown in (d).

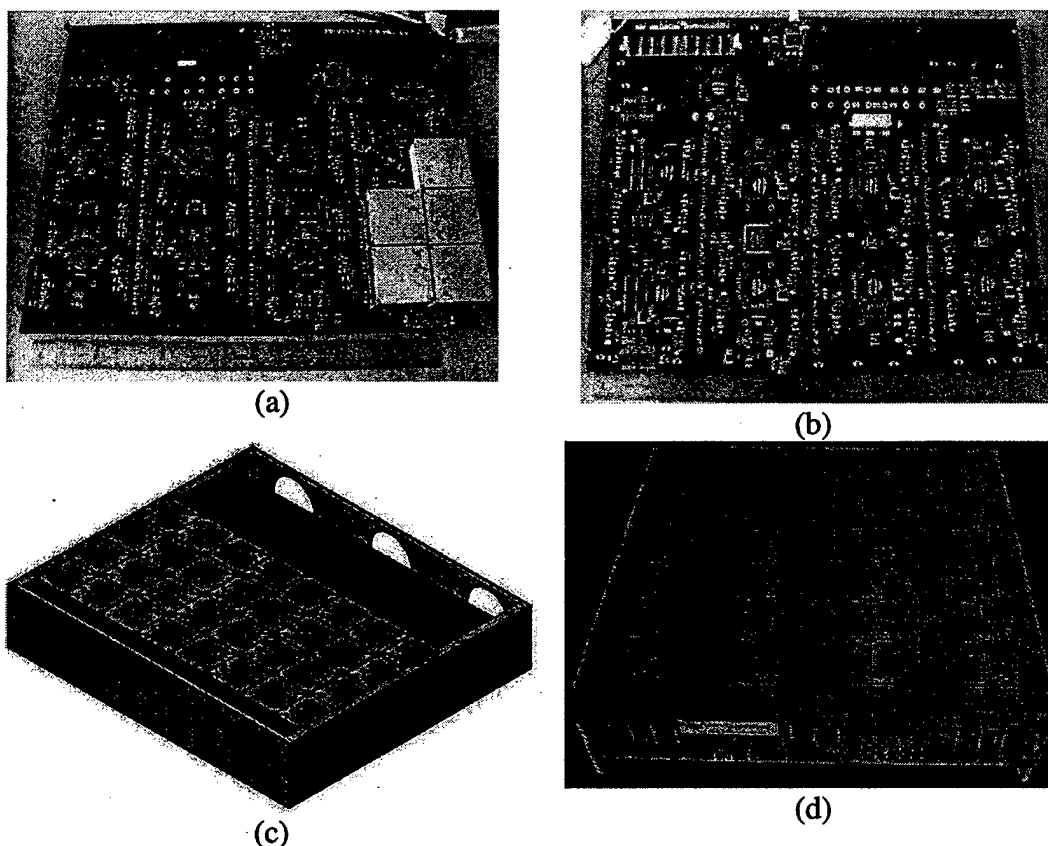


Figure 8: DBF processor. In (a), the populated board is shown outside the processor housing with 5 digital receive modules plugged in. The 32 module connectors are visible in the photo. In (b), the bottom side of the processor is shown, along with the 9 FPGAs. A 3-D CAD drawing is shown in (c), while a photo of the fully-populated DBF receiver is shown in (d).

Figures 9 and 10 below show the output of the DBF processor hardware for a simple 2-channel beamforming test case. Two DAM modules without the RF downconverters were inserted into two DBF processor slots. A 1 MHz signal was fed to a power splitter and injected directly into the DAM IF inputs.

In the beamformer, one channel was supplied a unity DBF weight, while the second channel was assigned a complex weight that varied with time about the unit circle with unity amplitude. Figure 9 shows the time-domain results, while Figure 10 shows the frequency-domain amplitude and phase of the beamformer output. Also shown in Figure 10 are the beamformer weights vs time.

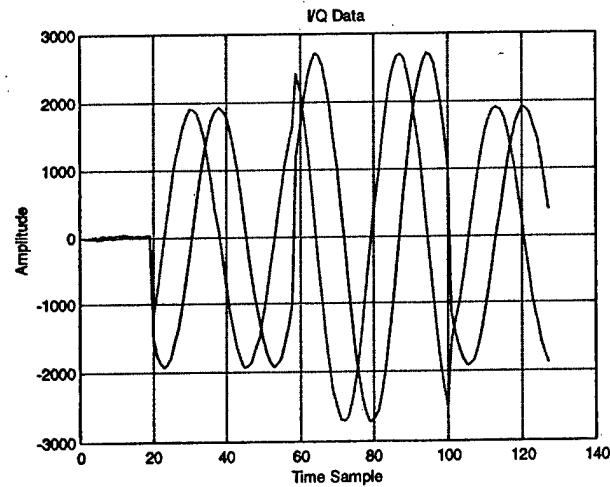


Figure 9: Time-domain data representing I and Q components at the output of the two-channel digital beamforming operation. One channel's beamforming coefficient is fixed with a constant amplitude of 1, while the second channel's complex coefficient rotates with time around the unit circle in 90-degree intervals. The coefficients are shown in Figure 10 below.

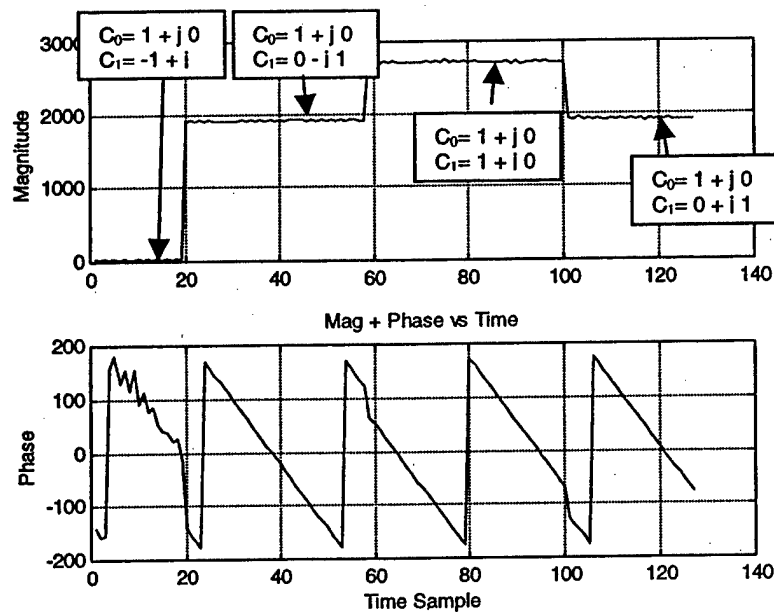


Figure 10: Time-domain data representing the magnitude and phase from Figure 9 at the output of the two-channel digital beamforming operation. One channel's beamforming coefficient is fixed, while the second channel's coefficient changes with time.

5.0 Conclusions

A 32-Channel DBF receive array has been designed and fabricated. Preliminary test data indicates that the hardware is performing as designed in all respects. Further tests including antenna pattern measurements are underway. Software development to enable all of the hardware features built into the DBF array continues as well.

Acknowledgement

This work was sponsored by the US Air Force Research Lab (AFRL/SNHA) at Hanscom AFB, MA.

2.0 References

- [1] D. Curtis, R. Thomas, W. Payne, W. Weedon, M. Deaett, "32-Channel X-Band Digital Beamforming Plug-and-Play Receive Array," *IEEE International Symposium on Phased-Array Systems and Technology*, October, 2003.
- [2] H. Steyskal, "Aspects of Digital Beamforming," Tutorial Session at *IEEE International Symposium on Phased-Array Systems and Technology*, October 17, 2003.
- [3] A. Hajimiri et. al., "Phased Array Systems in Silicon," *IEEE Communications Magazine*, Aug. 2004

NON-FOSTER COUPLING AND MATCHING IN ARRAYS

R. C. Hansen
Consulting Engineer
P.O. Box 570215
Tarzana, CA 91357
www.rchansen.com

Non-Foster circuit elements (Non-Foster Circuits) were first used circa 1930 to offset loss in long distance telephone lines) open a new capability for arrays. These elements can be used in matching (positive capacitance) or in coupling of contiguous collinear dipoles (negative inductance) in a planar array. This paper compares the two over a 10:1 frequency range. A square array of dipoles is modelled, with dipole lengths from $.05\lambda$ to $.5\lambda$. A Moment Method simulation of a 20×20 array, with and without ground screen provides current distributions, Scan Impedance, and Scan Element Pattern (gain per element). At mid and low band the Non-Foster coupling provides current continuity across the array, thus approaching for the first time the ideal current sheet Gedanken of Wheeler. Plots of Scan Element Pattern, current distributions, and Smith Charts of Scan Impedance are shown.

1.0 INTRODUCTION

We antenna engineers have done what is possible by rearranging the wires; future significant advances will come through use of new low loss materials, and through use of circuits. Circuits that produce negative inductance or positive capacitance can be used to offset the normal behavior of antenna impedance with frequency. These impedances are Non-Foster, as they circle the Smith Chart with frequency the wrong way. Thus they violate Foster's reactance theorem for passive circuits. Such circuits are also called Negative Impedance Converters (NIC). NICs were used prior to World War II for reducing loss in telephone equipment. Positive feedback is used to obtain these properties. As shown in [1], the transistor quickly replaced the vacuum tube in NIC circuits. Applications include raising the Q of filters using negative resistance; and negative and positive inductors at microwave frequencies, where conventional inductors are less attractive [2, 3]. The MTT Transactions contains many papers on filter applications. See [4] for an extensive reference list. Papers on NIC topology include [5-6]. These concepts were applied to antennas by Mayes and Poggio in 1970. Negative impedance units were placed in series at several locations with the arms of a dipole [7-8]. This work was extended in a MS thesis under Mayes [9], using Op Amps. Subsequently,

transistors with much improved characteristics became available, allowing operation at microwave frequencies.

A large planar array of dipoles, with and without a ground plane, is simulated by the Moment Method. This simulation provides current distributions on the dipoles, Scan Impedance, and Scan Element Pattern [10].

Computer simulation is important as it is difficult to measure Scan Impedance [11]. All elements must be excited with the appropriate amplitude and phase, but a direct measurement requires a technique such as the load pull method recently suggested [12].

2.0 THE COMPUTER SIMULATION

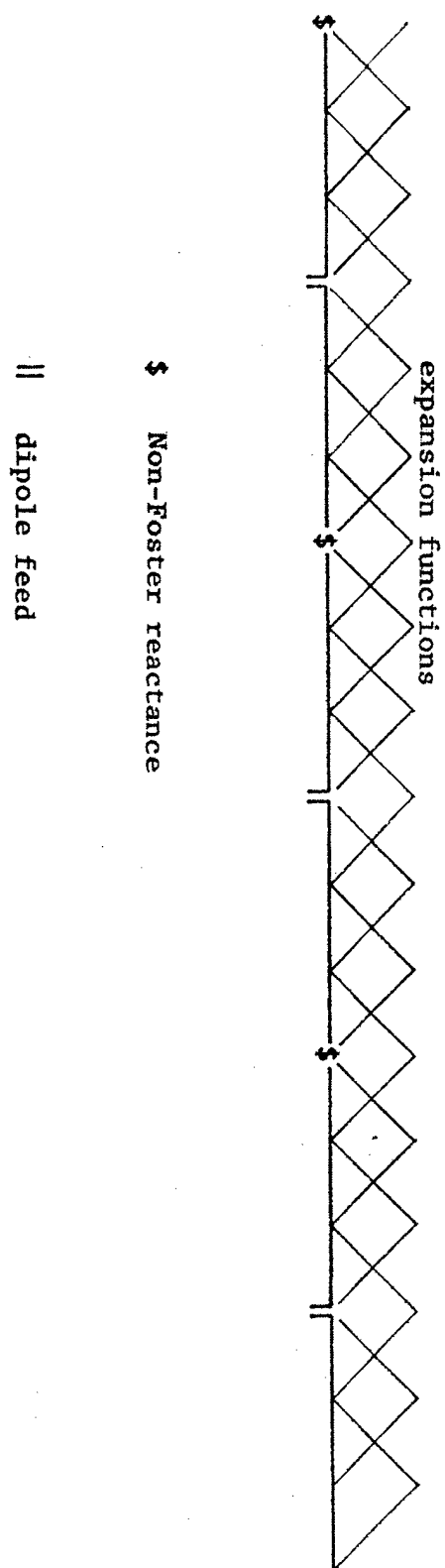
The array is square, with N elements per row and N columns; the dipoles are equi-spaced. Dipoles are moderately fat. Piecewise sinusoidal expansion and test functions are used in a Galerkin Moment Method formulation. Because all dipoles and images in the array are straight and parallel, the Carter mutual impedances are used. A double precision version of a compact code [13] is used; requisite Sine and Cosine Integrals are computed using a double precision routine involving Chebyshev polynomials [14]. The array lattice is square, and the dipole length equals the lattice spacing. Each dipole has a feed point at its center. Contiguous collinear dipole ends are open

(matching case), or connected by a negative inductance (coupling case). Ground plane effects are simulated by out of phase images as usual. All dipoles are excited with unity amplitude; drive phases correspond to scanning in any desired plane. The matrix equation consisting of this drive voltage vector and the array impedance matrix is solved for the current vector. From this, the Scan Impedance is immediately available. Scan Impedance behavior is critical, as any impedance mismatch to the transmitter or receiver results in a loss of gain. For the finite arrays the Scan Impedance is obtained directly from the currents. Scan Element Pattern is obtained by calculating radiated power and the array pattern.

As mentioned, measurement of Scan Impedance is difficult but in a computer model all quantities are available. The load resistance is applied at the center (feed point) of each dipole and is added to each feed self impedance term. Total power is calculated by taking the real part of the summation of $V I^*$ over the current at the center of each piecewise sinusoidal expansion function. Load power is found from the summation of $I I^*$ over the dipole feed points, multiplied by the load impedance Z_0 (real). Finally radiated power is equal to total power minus load power. Scan Element Pattern (gain per element) is calculated from the intensity at the main beam peak,

divided by radiated power, times the impedance mismatch loss $(1 - |\Gamma|^2)$, divided by the number of elements. All calculations are in double precision. Results of the code are validated against codes for conventional dipole arrays by inserting large values of resistance (10^5 ohms) in place of the coupling impedances, thus simulating a conventional planar array. The simulation code allows results to be calculated for a number of angles with a specified feed spacing, or for a number of feed spacings in wavelengths at a specific scan angle. Parameters calculated are the magnitude and phase of a current distribution along the wire, the impedance at the center element and the gain per element (Scan Element Pattern).

Six piecewise sinusoidal expansion and test functions are used per dipole; expansion functions extend across one dipole to the next contiguous dipole, allowing current to flow between dipoles. Thus a row of 10 collinear dipoles utilizes 59 unknowns. The 20 x 20 array has 119 unknowns per row, for a total of 2,380 unknowns. Calculations are made for a 10:1 bandwidth, for dipole lengths from $.05\lambda$ to $.5\lambda$. Thus the array length over the bandwidth, is 1 to 10 wavelengths, for the 20 x 20 array. Fig. 1 Sketches a portion of the dipole, and expansion functions, in one row of the planar array.



PORTION OF ONE ROW OF PLANAR ARRAY

Fig. 1

Adding the load resistance to the feed terms in the impedance matrix makes no difference in dipole arrays. However for connected arrays, it does markedly change the shape, magnitude and phase of the currents, and the Scan Impedance and Scan Element Pattern. This is probably due to the resonant edge currents on connected arrays as seen in the current amplitude plots that follow, and the ability of currents to flow from one feed to another.

The expectation is that the array will be multi-octave, so the center frequency is chosen such that the dipoles are $\lambda/4$ long, allowing an octave up to $\lambda/2$ length, and one or more octaves to $.125\lambda$ and shorter. Grating lobes appear above $.5\lambda$ length upon scan, so $.5\lambda$ is a useful upper limit. Dipole length/diameter is 125; for 6 segments per dipole this allows segment length/diameter to be a comfortable 10.4.

3.0 NON-FOSTER MATCHING

It took a few years for Non-Foster concepts to penetrate the antenna community; applications were matching of electrically small antennas. The paper by Bahr [15] was followed by patents by Albee [16], Ryan [17], Baekgaard [18], Sutton [19], and Skahill, Rudish, and Piero [20, 21]. This paper is concerned with

phased arrays, a more complex problem.

In a large array of dipoles the broadside Scan Resistance is nearly constant over many octaves [22], thus it is only necessary to match out the reactance change with frequency. This reactance is of course negative (capacitance), so a Non-Foster match using positive capacitance will provide an excellent match over a wideband.

Using dipole length of $.25\lambda$ as band center, the reactance at each dipole feed is calculated. An equal positive reactance, varying inversely with frequency, is applied at each feed point. The Z_0 used is that found for $.25\lambda$. Fig. 2 shows Scan Element Pattern at broadside for a 10:1 frequency range, with dipole lengths from $.05\lambda$ to $.5\lambda$. SEP includes impedance mismatch. The dashed line represents area gain. $2\pi A/N^2\lambda^2 = 1.96$ dB, where the array is $N \times N$. When a ground plane is added the Scan Resistance is no longer nearly constant. It decreases as f^2 . Fig. 3 shows Scan Element Pattern for this case.

The current across the center row of the array is shown in Fig. 4 for $\lambda/2$. As expected each dipole has essentially the current shape that an isolated dipole has. At the bottom of the 10:1 band the $.05\lambda$ dipoles

show the triangular current distribution, see Fig. 5. Later these current distributions will be contrasted with those for the Non-Foster coupled array.

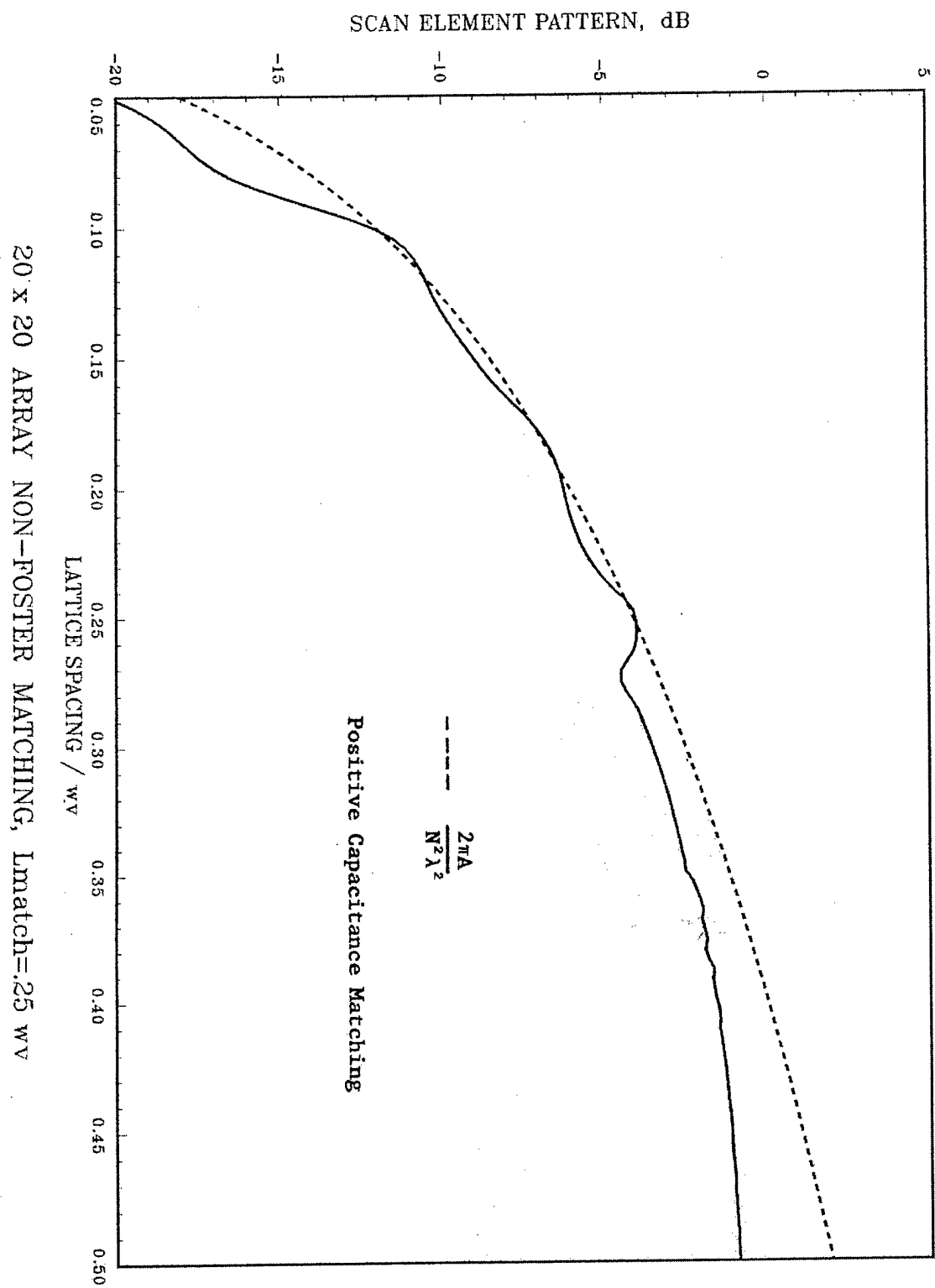
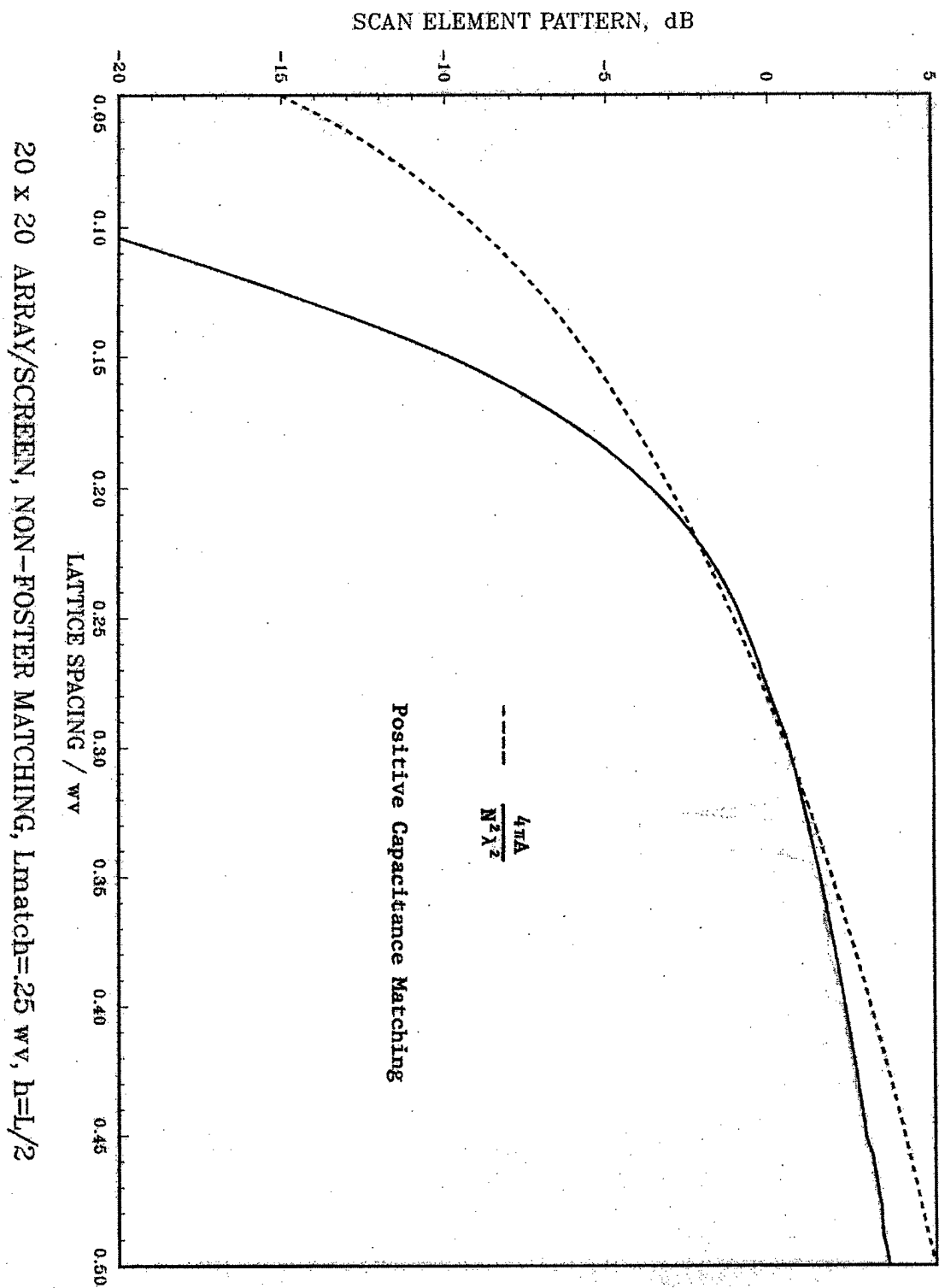


Fig. 2



20 x 20 ARRAY/SCREEN, NON-FOSTER MATCHING, $l_{match}=.25 wv$, $h=L/2$

FIG. 3

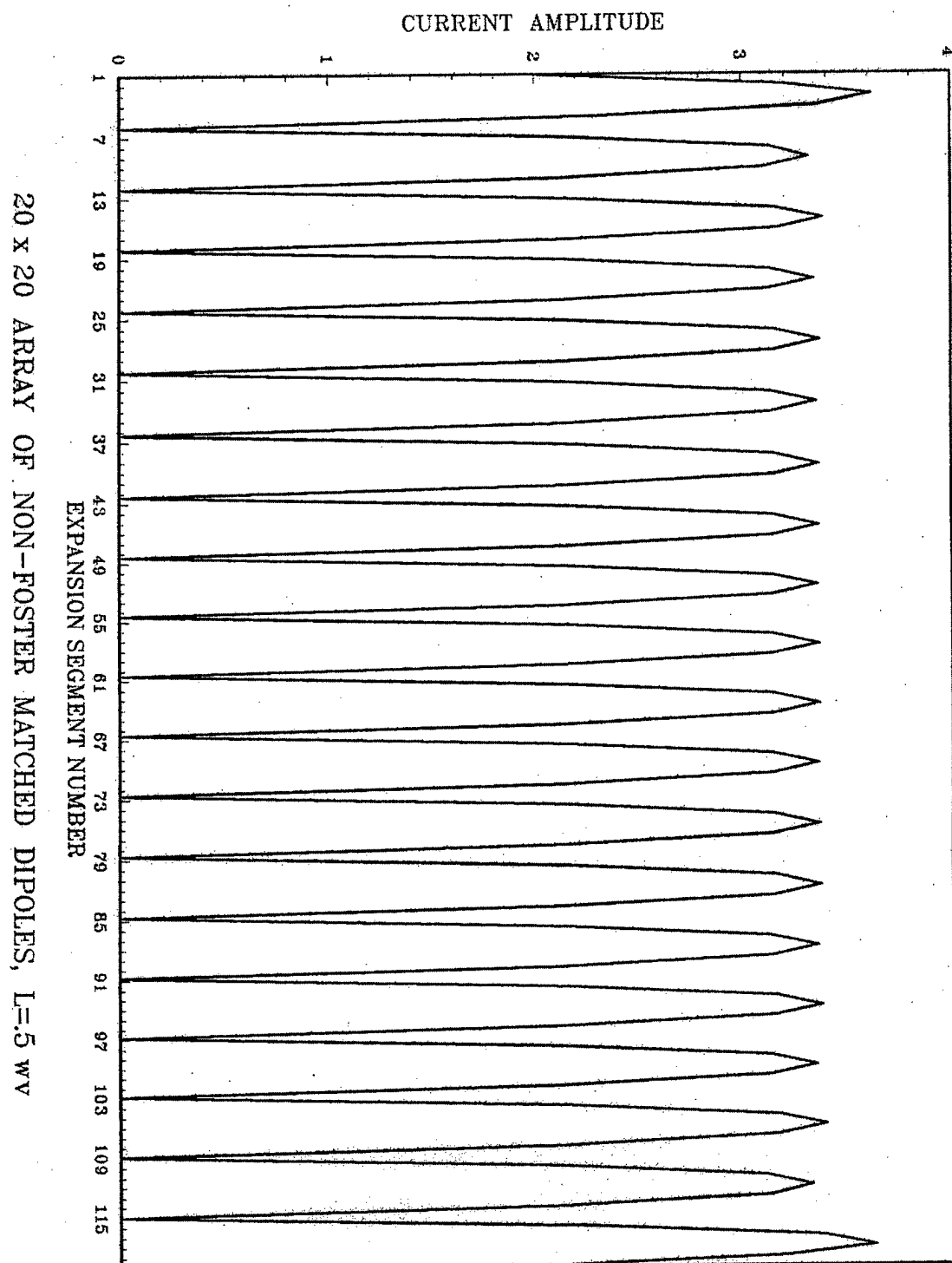


Fig. 4

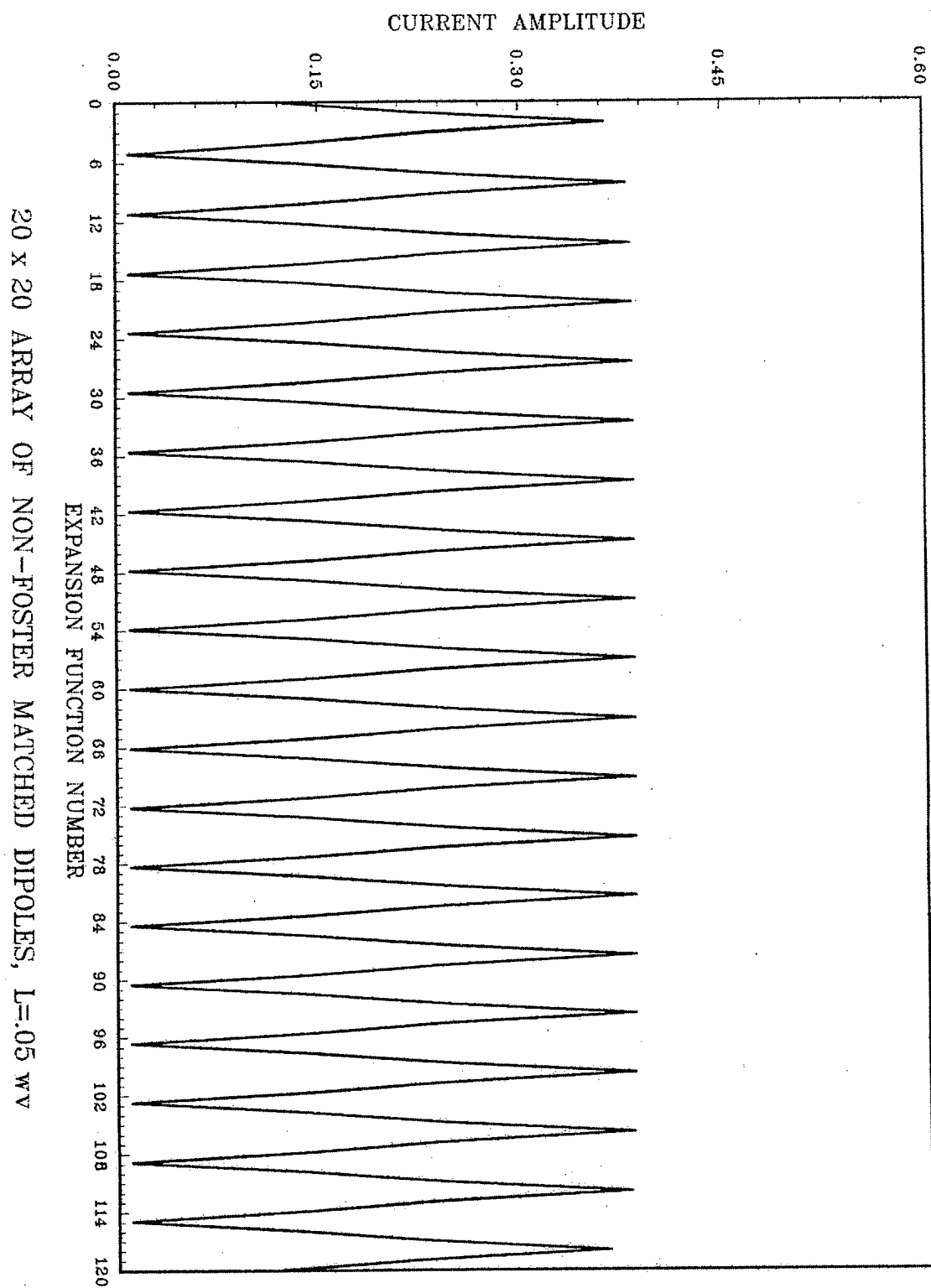


Fig. 5

4.0 NON-FOSTER COUPLING

At frequencies where the dipoles are short, with each having a large reactance, it is desirable to couple contiguous collinear dipoles so as to make each collinear row a single longer dipole. As the frequency increases toward dipole half-wavelength, the dipoles work well when unconnected. The coupling then should be a negative inductance [23]. Scan Reactance (at broadside) is matched for dipole length $\lambda/4$; the matching reactance is -429 ohms. Fig. 6 shows Scan Element Pattern over the $.05\lambda$ to $.5\lambda$ band of 10:1. It is remarkable that the performance is very close to area gain per element over most of the band, with only a 2 dB drop at the upper end. These results used a characteristic impedance of 200 ohms; for reactive coupling this provides best overall performance. The Non-Foster negative inductance cancels the Scan Reactance except near $\lambda/2$ where the Scan Reactance no longer varies as $1/f$. When a ground plane is added the performance below about $.2\lambda$ drops as expected. Near $.5\lambda$ the performance is improved, as seen in Fig. 7.

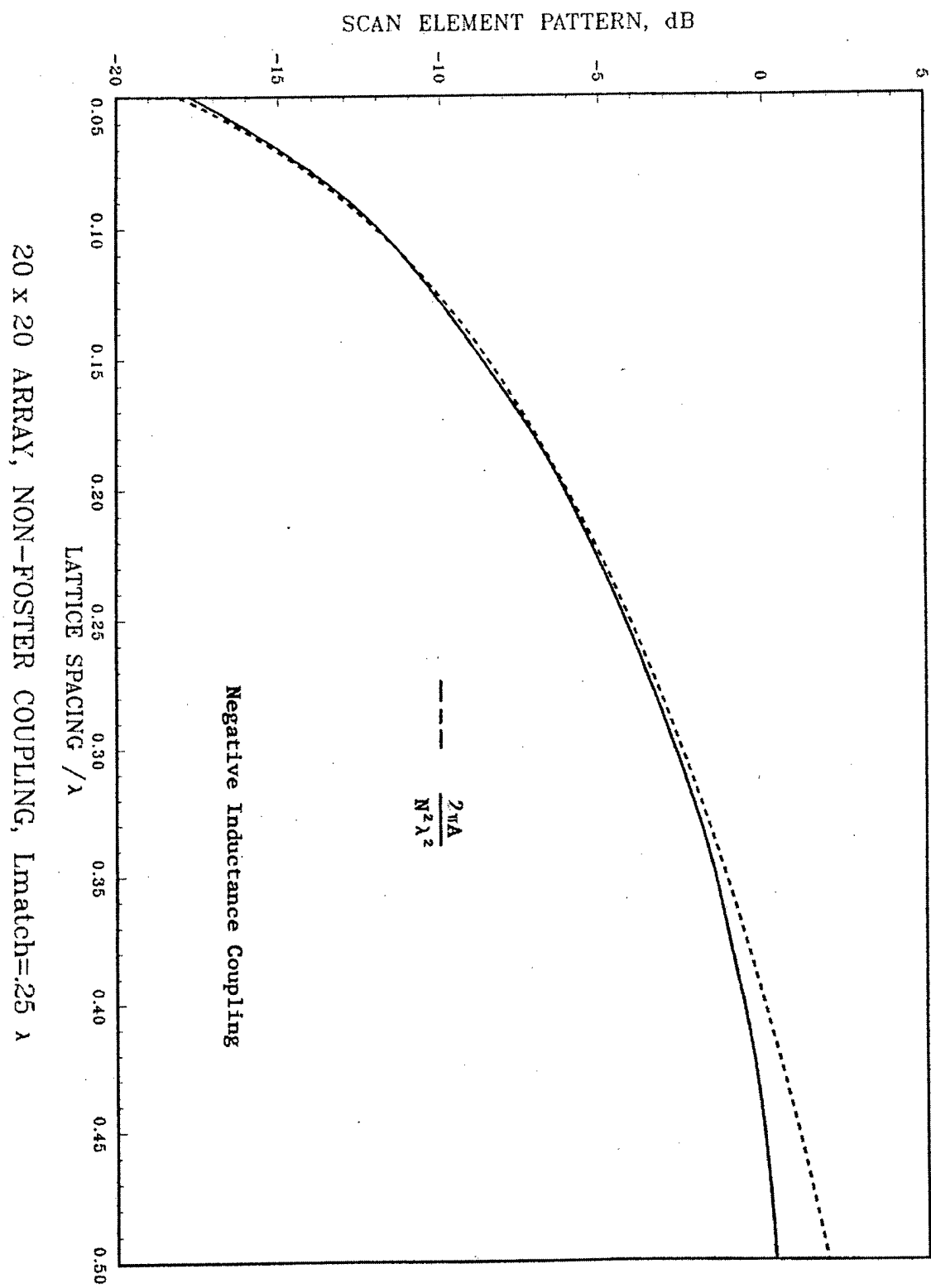
Fig. 8 shows the Smith chart locus, and the VSWR is below 2 over an 8:1 bandwidth, starting at $.05\lambda$ up.

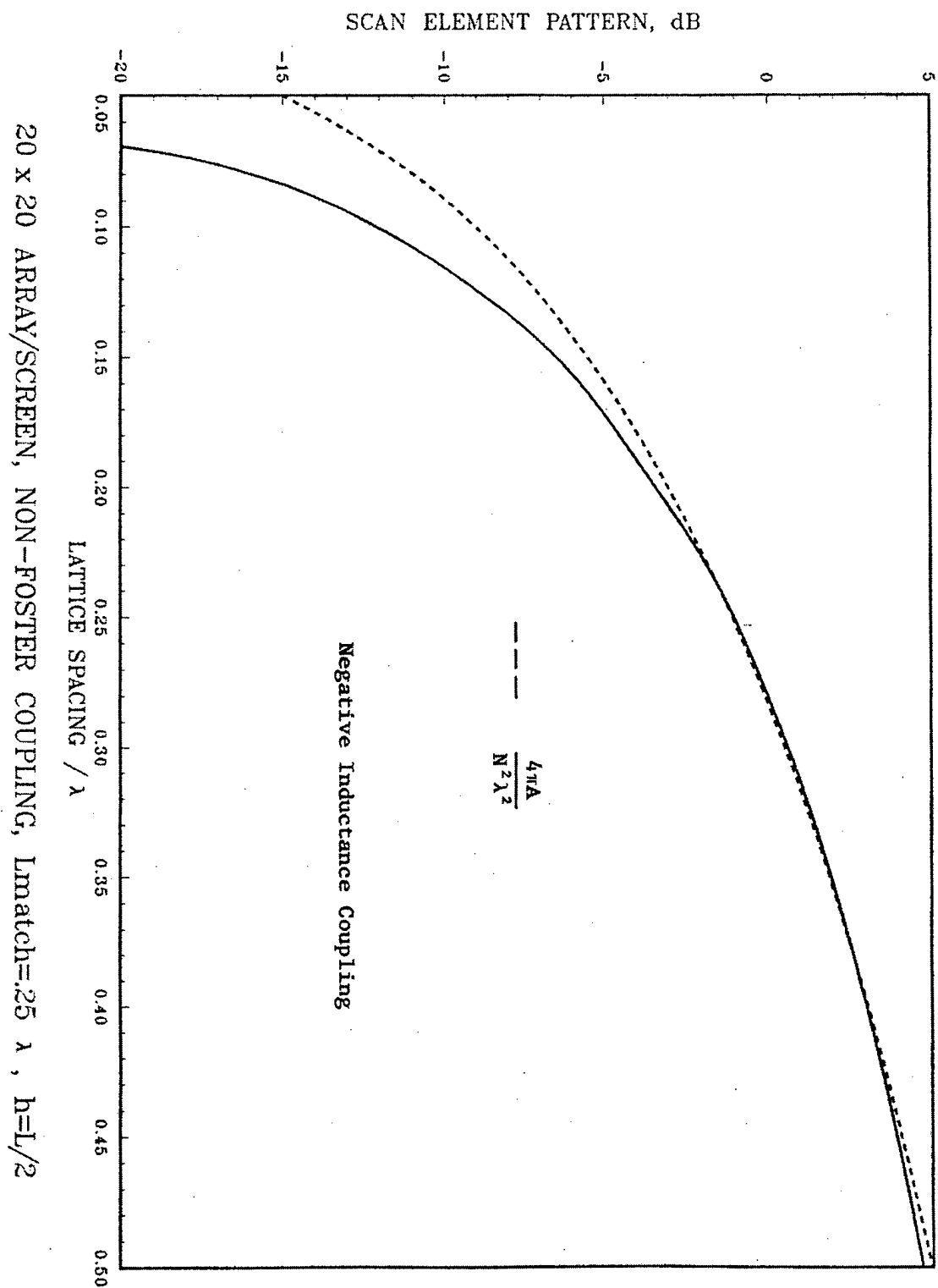
When the ground screen is added the impedance is poor at low frequencies, as seen in Fig. 9. Now the VSWR is

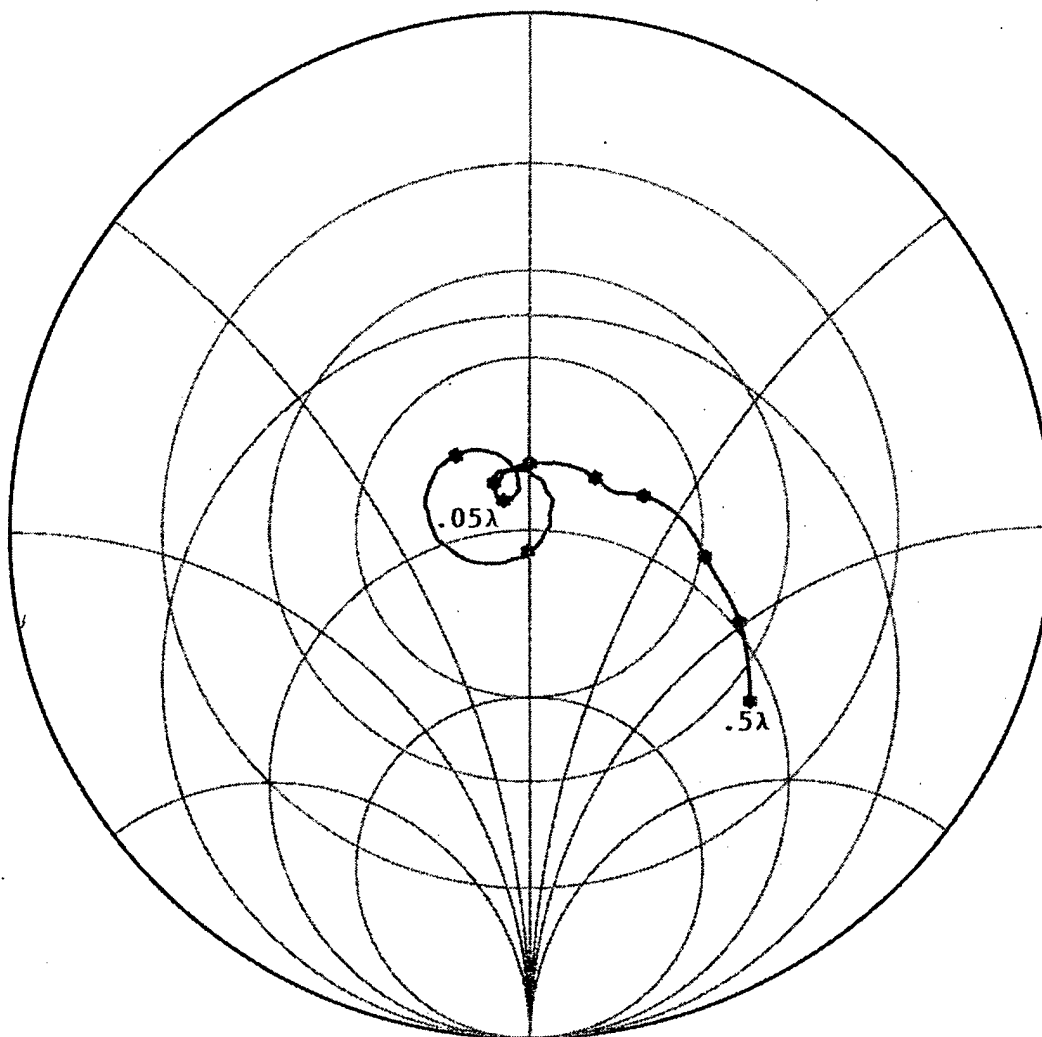
below 2 over a 2.5:1 bandwidth, starting at $.5\lambda$ down.

The concentric circles represent
VSWR = 2 (.51 dB loss), VSWR = 3 (1.25 dB loss), and
VSWR = 5 (2.55 dB loss). Scan Impedance is critical,
as studies have shown that SEP is approximately given
by area gain decreased by the impedance mismatch loss.

Plots of the current distribution along the center
row are illuminating. In Fig. 10 for dipole length
 $.05\lambda$ the current is nearly constant over the entire 1λ
long array. Thus the Non-Foster coupling does indeed
produce the Wheeler current sheet [24] at low
frequencies. Fig. 11, for $.1\lambda$ dipoles, shows a modest
dip, but the current continuity is maintained. Finally
at $.5\lambda$ dipole length, the results are close to isolated
dipole currents, except for some edge effects [25].



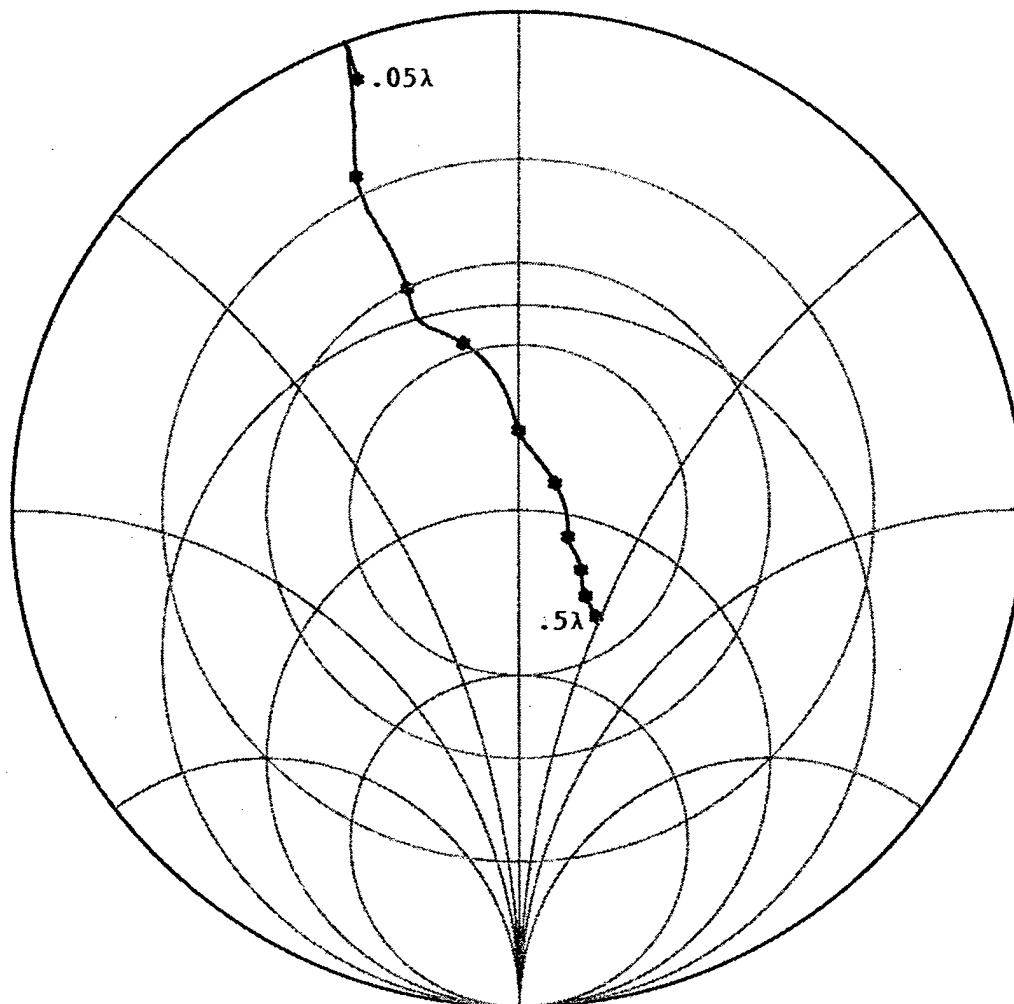




20 x 20 NON-FOSTER COUPLED ARRAY

BROADSIDE

Fig. 8



20 x 20 NON-FOSTER COUPLED ARRAY/SCREEN

BROADSIDE, $H = L/2$

Fig. 9

5.0 CONCLUSIONS

Use of Non-Foster matching and coupling elements to make a phased array broadband have been compared. Although the Non-Foster matching is more attractive, as each element will be connected to a preamp/poweramp module which could contain the Non-Foster circuit, the Scan Element Pattern performance is less good than that of the Non-Foster coupled array. Without screen the coupled array shows a 10:1 bandwidth for $VSWR \leq 3$. The coupling produces a continuity of current at low frequencies, that improves gain, and for the first time, approximates the current sheet antenna used by Wheeler as a scan gedanken. Clearly the Non-Foster coupling is superior to Non-Foster matching, and allows multi-octave performance. With screen a drop off occurs at the low end of the band, but it is less than that for the Non-Foster matched array.

Future work should be on the Non-Foster circuits: system trades on dynamic range (IP2 and IP3), noise figure, stability criteria, and use of switching (Class E) amplifiers to increase DC efficiency.

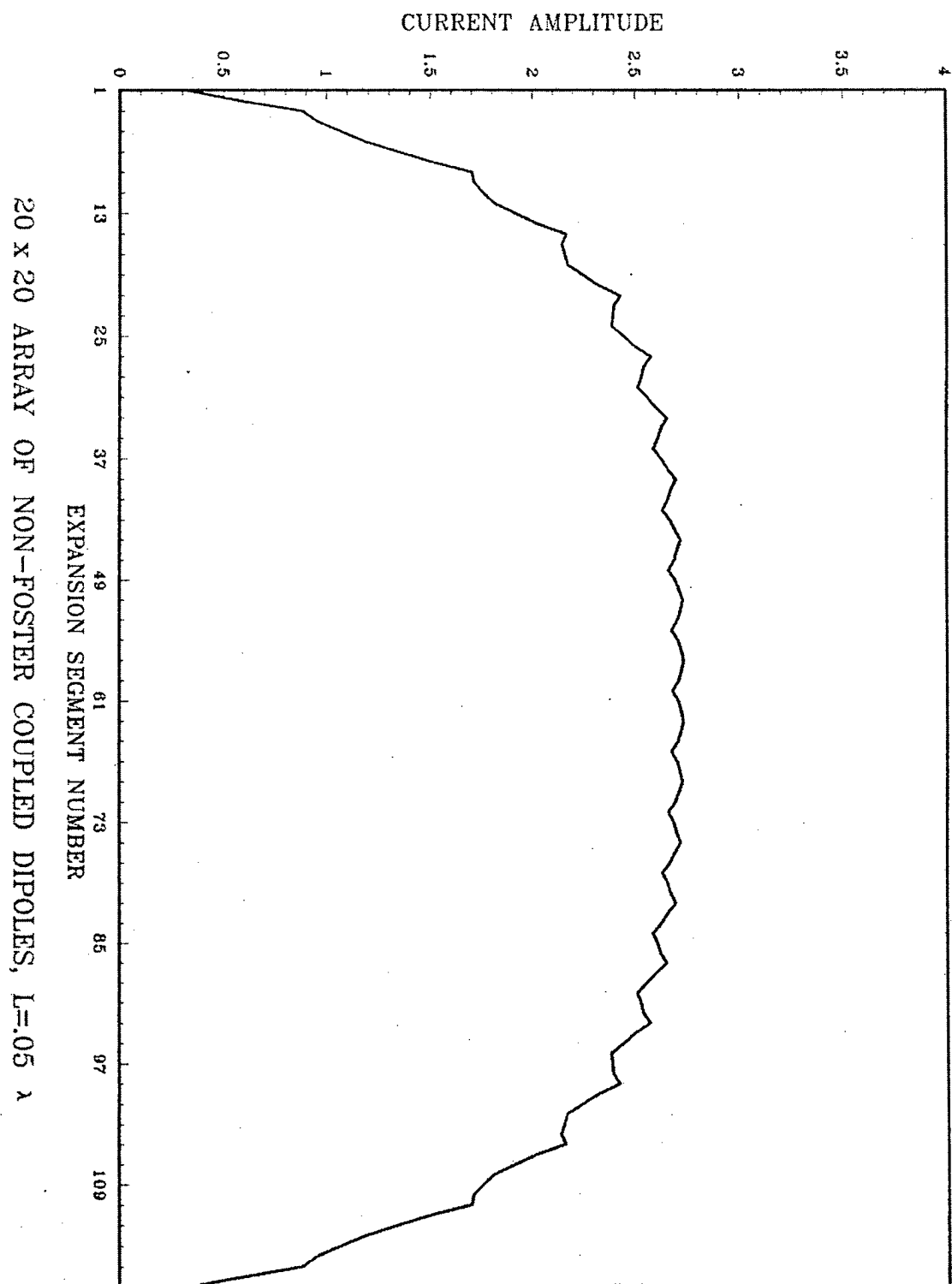
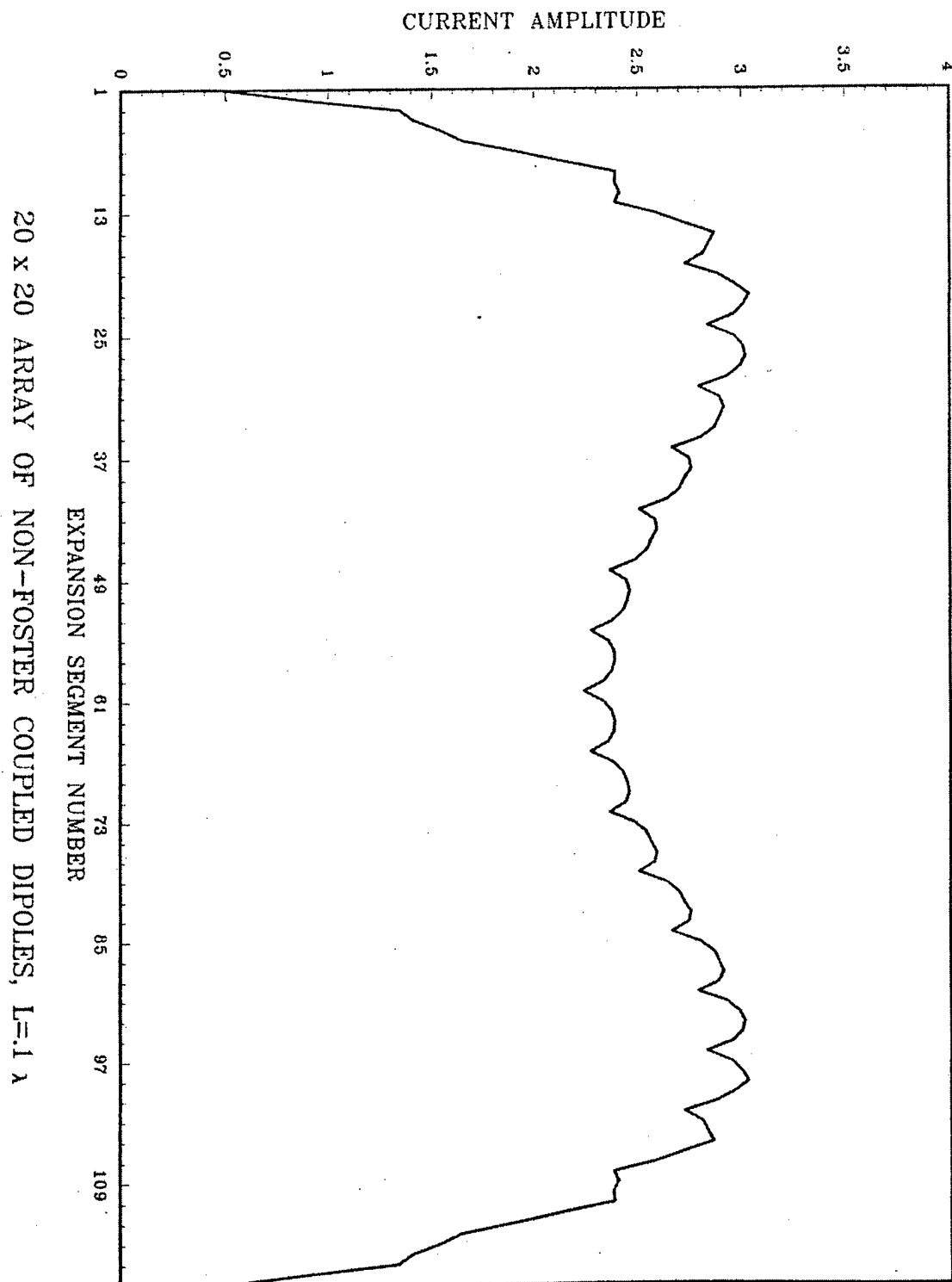


Fig. 10



20 x 20 ARRAY OF NON-FOSTER COUPLED DIPOLES, $L=1 \lambda$

Fig. 11

6.0 REFERENCES

- [1] J. G. Linvill, "Transistor Negative-Impedance Converters," *Proc. IRE*, Vol. 41, June 1953, pp. 725-729
- [2] S. Hara et al, "Broad-Band Monolithic Microwave Active Inductor and Its Application to Miniaturized Wide-Band Amplifiers," *Trans. IEEE*, Vol. MTT-36, Dec. 1988, pp. 1920-1155
- [3] S. El Khoury, "The Design of Active Floating Positive and Negative Inductors in MMIC Technology," *IEEE Microwave and Guided Wave Ltrs.*, Vol. 5, Oct. 1995, pp. 321-323
- [4] S. E. Sussmann-Fort, "Gyrator-Based Biquad Filters and Negative Impedance Converters for Microwaves," *Int. J. of Microwave and Millimeter-Wave Computer Aided Engineering*. Vol. 6, 1998, John Wiley & Sons, pp. 86-101
- [5] H. Tek and F. Anday, "Voltage Transfer Function Synthesis Using Current Conveyors," *Electronics Ltrs.*, Vol. 25, 9 Nov. 1989, pp. 1552-1553
- [6] J. H. Sinsky and C. R. Westgate, "A New Approach to Designing Active MMIC Tuning Elements Using

Second-Generation Current Conveyors," *IEEE Microwave and Guided Ltrs.*, Vol. 6, Sept. 1996, pp. 326-328

- [7] P. E. Mayes and A. J. Poggio, *Wire Antenna Multiply-Loaded with Active Element Impedances*, U. S. Patent No. 3,716,867, 13 Feb. 1973
- [8] A. J. Poggio and P. E. Mayes, "Bandwidth Extension for Dipole Antennas by Conjugate Reactance Loading," *Trans. IEEE*, Vol. AP-19, July 1971, pp. 544-547
- [9] J. D. Quirin, *A Study of High-Frequency Solid-State Negative-Impedance Converters for Impedance Loading of Dipole Antennas*, MS Thesis, Univ. of Illinois at Urbana-Champaign, 1971
- [10] R. C. Hansen, *Phased Array Antennas*, John Wiley & Sons, 1998
- [11] R. C. Hansen, "Measurement of Wideband Arrays," *Proc. AMTA 2002, Cleveland, OH*, pp. 242-246
- [12] R. C. Van Wagoner and R. C. Hansen, "Measurement of Phased Array Scan Impedance by Load Pull," *Electronics Ltrs.*, Vol. 39, 24 July 2003, pp. 1101-1102

- [13] R. C. Hansen, "Formulation of Echelon Dipole Mutual Impedance for Computer," *Trans. IEEE*, Vol. AP-20, Nov. 1972, pp. 780-781
- [14] Y. L. Luke, *Mathematical Functions and Their Approximations*, Academic Press, 1975, Table 4.4
- [15] A. J. Bahr, "Application of Active-Impedance Matching to Electrically Small Receiving Antennas," *Proc. ECOM-ARO Workshop on Electrically Small Antennas*, Ft. Monmouth, NJ, Oct. 1976, pp. 199-204
- [16] T. K. Albee, *Broadband VLF Loop Antenna System*, U. S. Patent No. 3,953,799, 27 April 1976
- [17] P. A. Ryan, *Low Profile Electric Field Sensor*, U. S. Patent no. 4,383,260, 10 May 1983
- [18] K. E. Baekgaard, *Antenna Circuit of the Negative Impedance Type*, U. S. patent No. 4,442, 434, 10 April 1984
- [19] J. F. Sutton, *Active Antenna*, U. S. Patent No. 5, 311, 198, 10 May 1994
- [20] G. Skahill, R. M. Rudish, and J. Piero,

"Electrically Small, Efficient, Wide-Band Low-Noise Antenna Elements," *Proc. 1998 Antenna Applications Symp., Allerton, IL, Sept 1998*, pp. 214-231

- [21] G. Skahill, R. M. Rudish, and J. A. Piero, *Apparatus and Method for Broadband Matching of Electrically Small Antennas*, U. S. Patent No. 6,121,940, 19 Sept. 2000
- [22] R. C. Hansen, "Dipole Array Scan Performance over a Wide-Band," *Trans. IEEE*, Vol. AP-47, May 1999, pp. 956-957
- [23] R. C. Hansen, "Wideband Dipole Arrays Using Non-Foster Coupling," *Microwave and Optical Tech. Ltrs.*, Vol. 38, 20 Sept. 2003A, pp. 453-455
- [24] H. A. Wheeler, "Simple Relations Derived from a Phased-Array Antenna Made of an Infinite Current Sheet," *Trans. IEEE*, Vol. AP-13, July 1965, pp. 506-514
- [25] R. C. Hansen, "A Gibbsian Model for Finite Scanned Arrays," *Trans. IEEE*, Vol. AP-44 Feb. 1996, pp. 243-248

POLARIZATION CHARACTERIZATION OF WIDEBAND ARRAY ELEMENTS

Joel C. Roper, R. Thomas Dover
Raytheon Space and Airborne Systems
Advanced Products Center, McKinney, Texas

Abstract

As the need for wideband phased array apertures has grown, so has the need for understanding their polarization properties over scan volume. This paper describes the measurements and analysis of the antenna elements of a dual-polarized decade (10:1) bandwidth flared notch array. The element pattern measurements covered a large scan volume at a fine frequency increment. The analysis focused on the polarization characteristics of the tapered notch array element. Most elements change polarization with scan, and the notch element changes more than most due to the geometry of the currents on the notch. For most applications, this change of polarization with scan angle is acceptable. Of specific interest for this study is the orthogonality of the dual-polarized notch elements over the scan volume.

1. Introduction

The DARPA Reconfigurable Aperture (RECAP) Program funded Raytheon to develop a decade bandwidth phased array antenna. The need was for a wideband phased array aperture for both government and industry applications. Multi-mission roles from a single aperture required an array that either achieves wide instantaneous bandwidth or that can be quickly reconfigured. After investigating both options, Raytheon chose to pursue the wide instantaneous bandwidth approach. As part of this program, Raytheon engineers developed a new design process that allows substantial increases in the bandwidth of tapered notch elements. The result was the Decade Bandwidth Tapered Notch Array (DTNA) [1].

Raytheon built a Demonstration Array based on the DTNA design. What is unique about this array is that it achieves a 10:1 bandwidth over a wide scan volume ($\pm 60^\circ$ E- and H-plane) with dual-polarized elements. The scan impedance of the element in an infinite array as predicted by the HFSS model is shown in Figure 1.

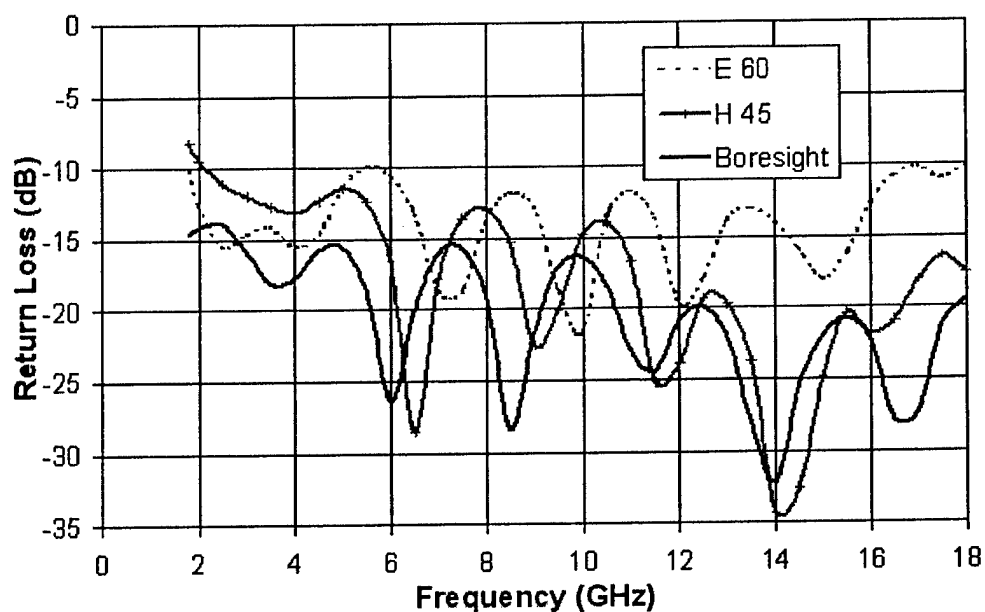


Figure 1 - HFSS Predicted Scan Impedance

The demonstration array consists of 32 x 64 dual-polarized elements housed in a rigid mounting fixture. A single row of elements along the centerline of the array was connectorized (both polarizations) and the remaining elements were terminated. The measured swept gain for this linear array of the V-polarized elements at boresight is presented in Figure 2.

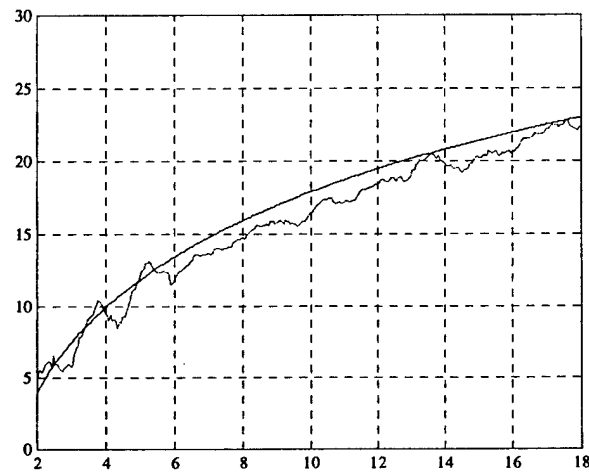


Figure 2 - Measured Swept Gain

2. Measurement Plan

The purpose of the measurements was to characterize the RECAP Demo Array elements over scan volume and frequency range. So the element patterns only (no array patterns) were measured. The measurement consisted of conical azimuth cuts over $\pm 90^\circ$ in 1° steps (ϕ coordinate) at multiple elevation angles from -20° to $+60^\circ$ with steps ranging from 2.5° to 10° (θ coordinate) – see Figure 3.

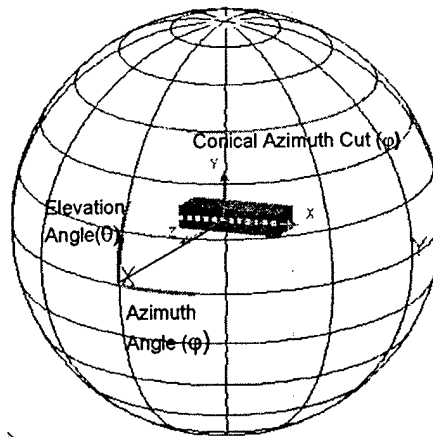


Figure 3 - Angular Definitions

The frequency plan ranged from 2 to 18 GHz in 50 MHz increments (321 frequencies). The range source polarizations were Vertical and Horizontal. Both amplitude and phase were recorded at every position and frequency.

For these measurements, four pairs of center elements and eight pairs of edge elements were selected. The array elements are numbered horizontally from 1 to 64. The center elements selected were 25, 29, 32, and 36. On the edges, elements 1-4 and 61-64 were chosen (see Figure 4).

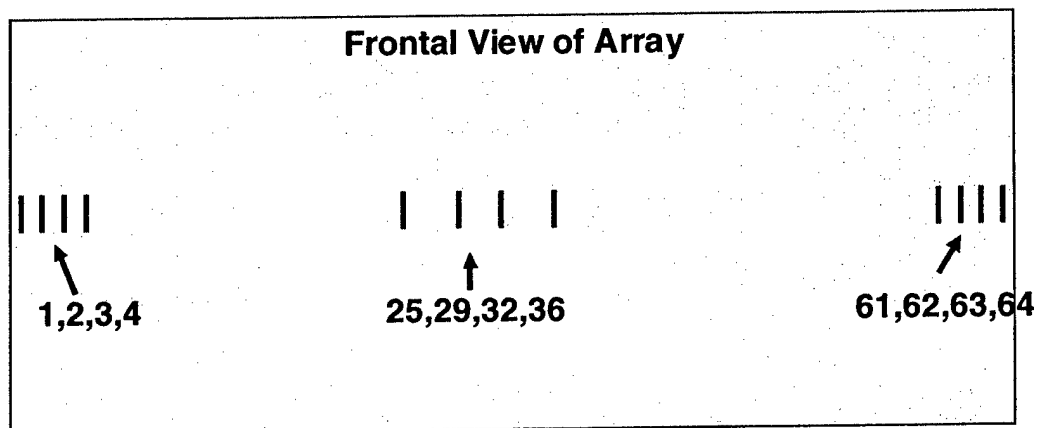


Figure 4 - Array Element Selection

The angles presented with the data are positioner angles. In Azimuth, the positioner angles are the negative of the antenna angles. In Elevation, the positioner angles are the same as the antenna angles.

3. Embedded Element Patterns

Patterns were measured on the array as described in the previous section. This data was combined in a number of different ways, the first of which produced the embedded element gain. The embedded element gain plots illustrate the swept gain for different azimuth angles at a fixed elevation angle (in this case, 0°). The embedded element patterns show the array main beam gain roll-off over scan angle and demonstrate all of the mutual coupling effects.

This data is compared to the HFSS (infinite array) prediction for a center element (32) in Figure 5. As can be seen, there is excellent correlation between the measured data and the HFSS prediction. The "V" indicates a vertically polarized element, and the "H" denotes a horizontally polarized element. The actual measured peak gain is nearly 5 dBi at the highest frequency, as expected, where element spacing is approximately $\lambda/2$. Peak element gain at the lowest frequency is 15 dBi, as expected.

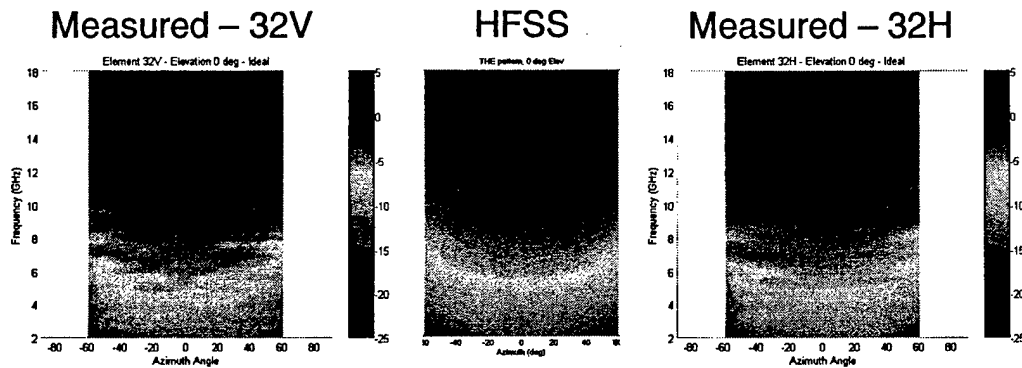


Figure 5 - Embedded Element Gain

The measured embedded element gain for the edge elements (Figure 6) shows the edge effects that begin to alter the pattern at the larger scan angles. However, the overall pattern level remains high for these elements.

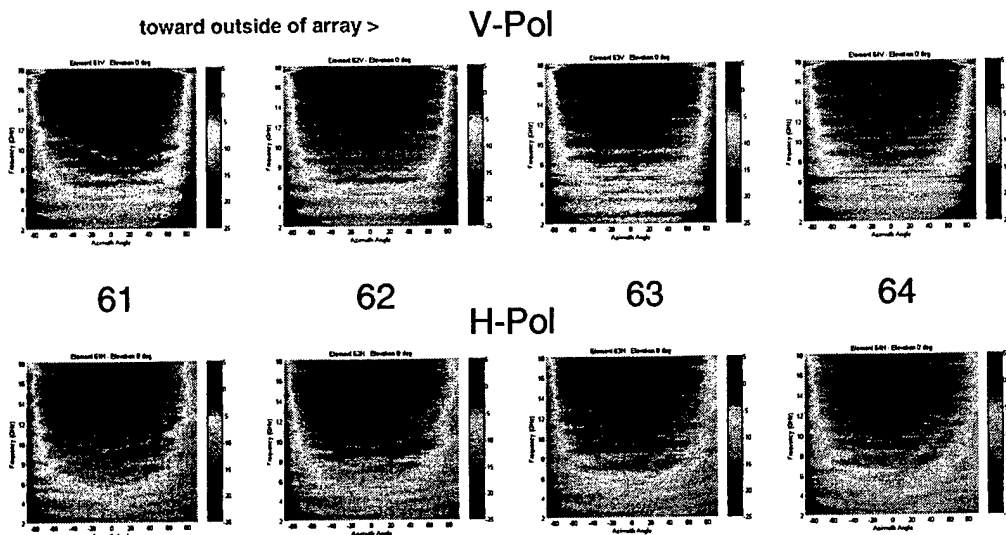


Figure 6 - Embedded Element Gain - Edge

Additionally, from the embedded element gain data, azimuth cuts at selected frequencies at 0° elevation were extracted for both center and edge elements. These patterns are plotted in Figure 7 and Figure 8. The difference in gain for these cuts is because the gain varies as a function of frequency. Notice in the edge element patterns how the pattern is altered in the direction of the edge of the array.

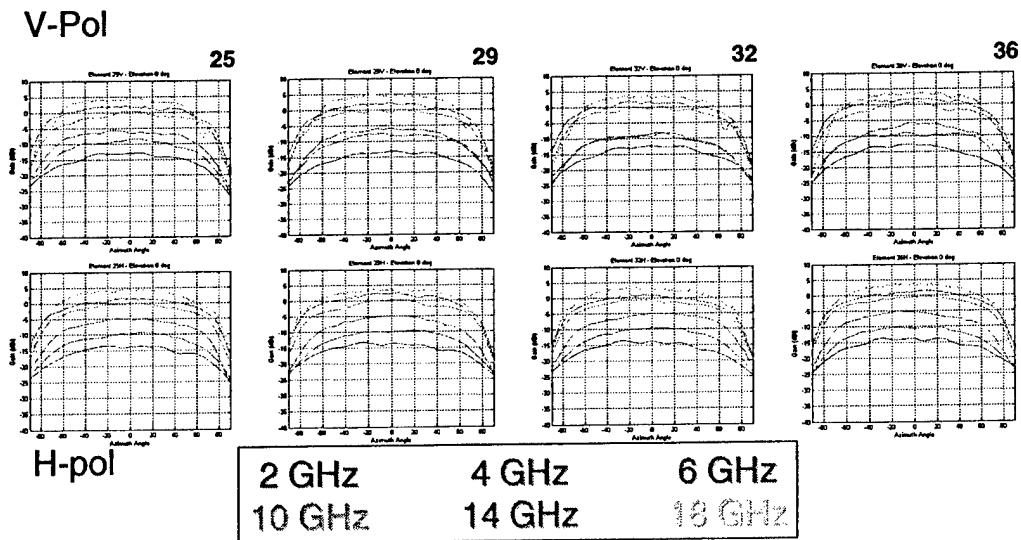


Figure 7 - Azimuth Element Patterns - Center

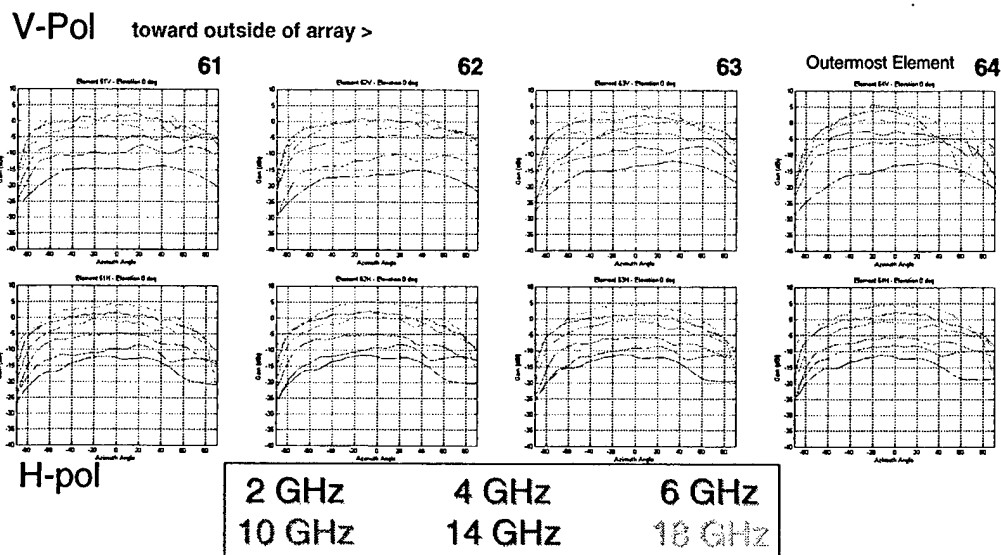


Figure 8 - Azimuth Element Patterns - Edge

The embedded element patterns (in dBi) for a pair of center elements at selected frequencies are presented in Figure 9 and Figure 10. These are k-space representations of the measured azimuth v. elevation data. The amplitude scale is consistent for all of the plots. These well-behaved patterns indicate the broadband nature of the RECAP array element.

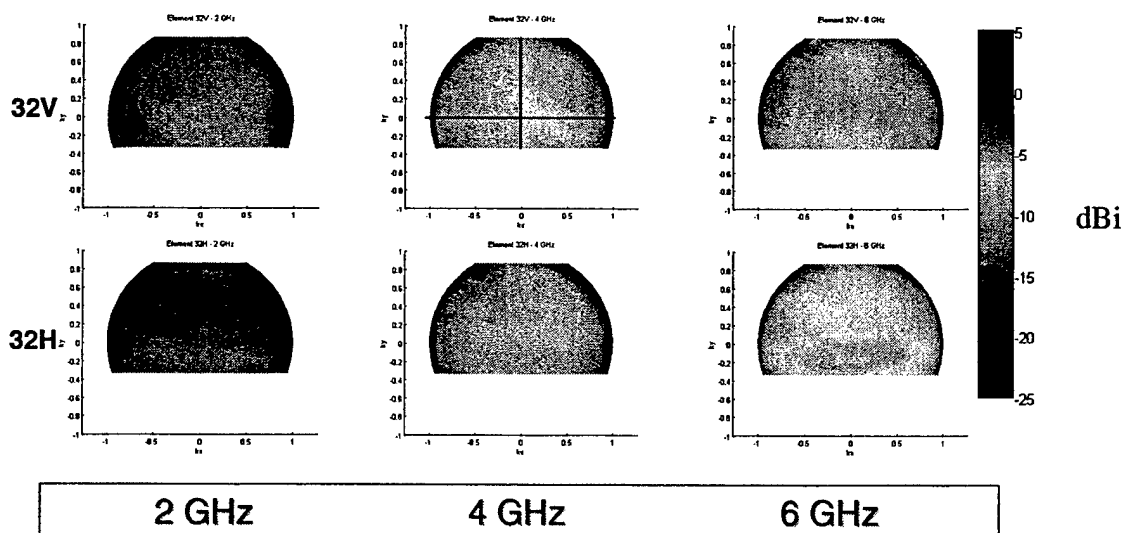


Figure 9 - Embedded Element Patterns (2-6 GHz)

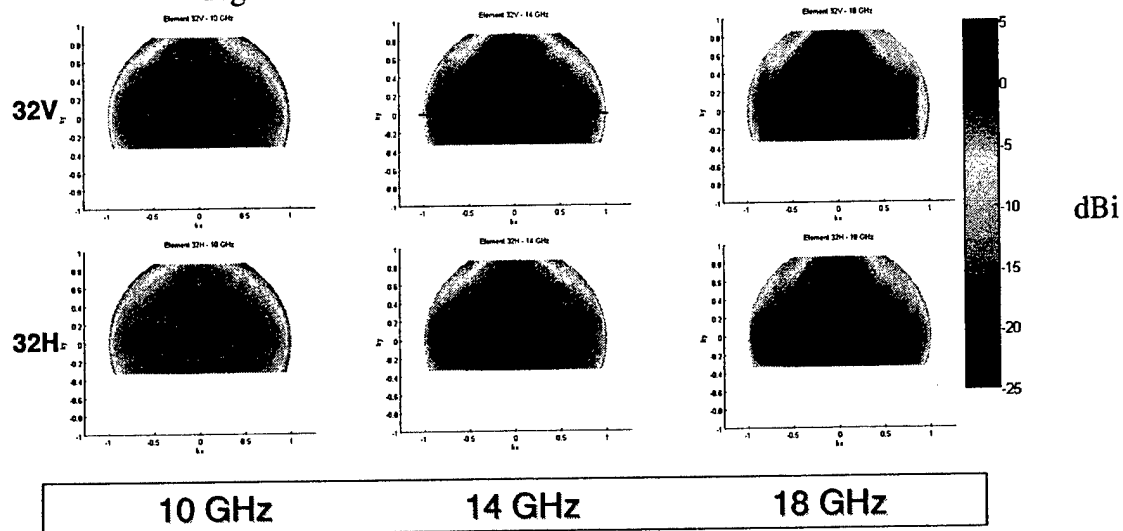


Figure 10 - Embedded Element Patterns (10-18 GHz)

4. Orthogonality Analysis

The analysis focused on the polarization characteristics of the dual-polarized tapered notch array element. Most elements change polarization with scan, and the notch element changes more than most due to the geometry of the currents on the notch [2]. For most applications, this change of polarization with scan angle is acceptable. Of specific interest for this study is the orthogonality of the dual-polarized notch elements over the scan volume.

The Orthogonality analysis encompassed three main divisions: Cross-polarization Discrimination, Axial Ratio, and Orthogonality.

The Cross-Polarization Discrimination (XPD) analysis illustrated the shift in the element polarization as a function of scan angle as is typical of flared-notch radiators. The Axial Ratio analysis explained the nature of this polarization shift. The Orthogonality analysis proved that the two physically orthogonal elements remain electrically orthogonal throughout the scan volume.

4.1 Cross-Polarization Discrimination

Cross-polarization discrimination is defined as the ratio of the signal level at the output of the receiving antenna that is nominally co-polarized to the transmitting antenna to the output of the receiving antenna that is nominally orthogonal to the transmitting antenna [3].

$$XPD_V = \frac{|V_{VV}|^2}{|V_{HV}|^2} \quad XPD_H = \frac{|V_{HH}|^2}{|V_{VH}|^2} \quad (1)$$

XPD plots are presented in colored images of azimuth vs. elevation. The XPD of the RECAP tapered notch array can be misleading if left to stand on its own. Taken together with the axial ratio plots, it hints at the orthogonal characteristics of the DTNA element. (The orthogonality of this element is described in Section 4.3 of this report.)

The measured XPD data is compared to the HFSS predictions at five frequencies with good correlation (Figure 11). Negative (red) values indicate that the “cross-pol” term is higher than the “co-pol” term. In fact, though, it is simply a matter of the polarization shifting away from linear to elliptical.

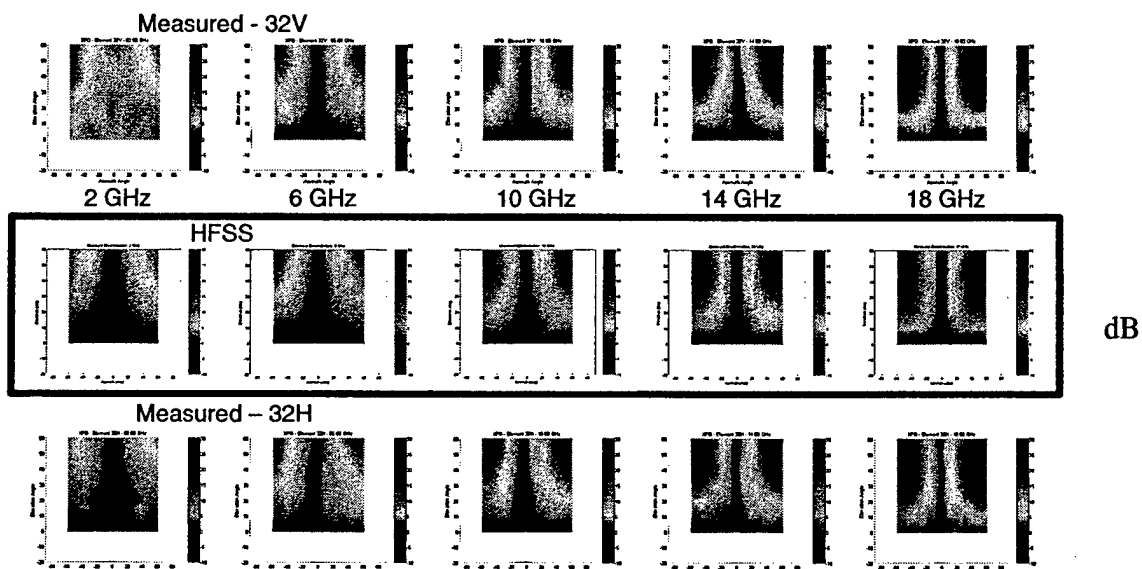


Figure 11 - Cross-Pol Discrimination

4.2 Axial Ratio

Axial ratio quantifies the shape of the polarization ellipse and is computed from the circular polarization (CP) component magnitude (IEEE Std 149-1979) [4].

$$R = \frac{E_{RO} + E_{LO}}{E_{RO} - E_{LO}} \quad (2)$$

For left-hand (LH), $R < 0$.
For right-hand (RH), $R > 0$.

At the extremes are

LHCP ($E_{LO} = 1, E_{RO} = 0$)
Linear ($E_{LO} = 1, E_{RO} = 1$)
RHCP ($E_{LO} = 0, E_{RO} = 1$).

The tilt angle (τ) of the polarization ellipse is defined as [5]

$$\tau = \frac{\pi}{2} - \frac{1}{2} \tan^{-1} \left[\frac{2E_x E_y \cos(\Delta\phi)}{E_x^2 - E_y^2} \right] \quad (3)$$

where

$$\Delta\phi = \phi_y - \phi_x$$

Axial ratio plots are presented in colored images of azimuth vs. elevation. This data is compared to the HFSS predictions at five frequencies with very good correlation (Figure 12). In this case, the HFSS model corresponds to the H-pol measured element. For all plots, the scale ranges from -1 (LHCP - red) through 0 (Linear - green) to $+1$ (RHCP - blue). The plots indicate that the V- and H-pol elements have relatively orthogonal elliptical responses off of the principal planes, as discussed in the next section. In other words, when the V-pol element goes to red (left-hand), the H-pol element goes to blue (right-hand).

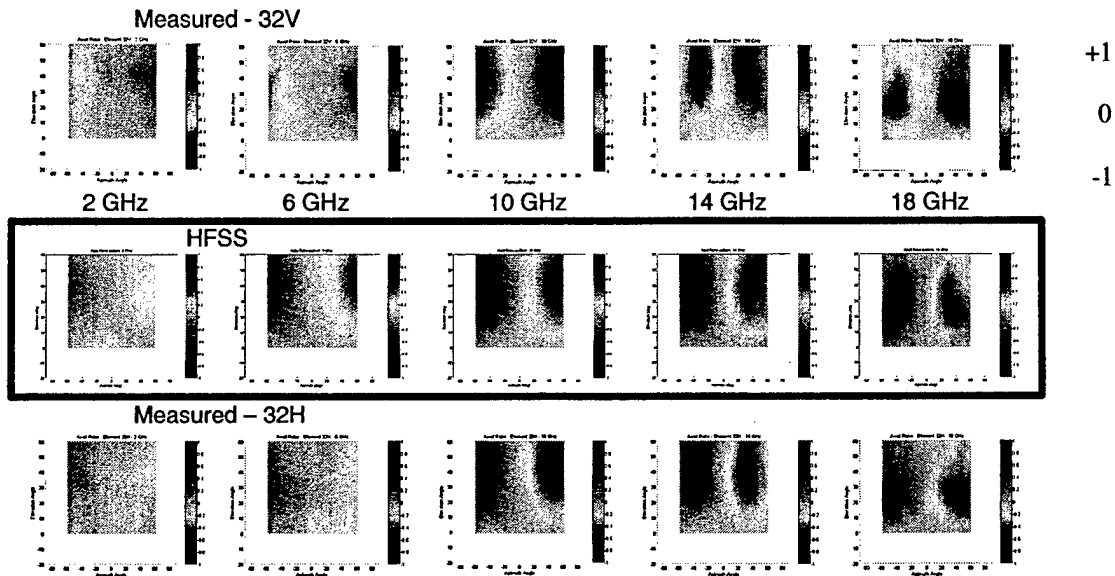


Figure 12 - Axial Ratio

4.3 Orthogonality

Notch-type elements do not remain linearly polarized at angles off of the principal planes. Off of these planes, the polarization of these elements becomes elliptical, thus causing the (linear) XPD levels to change significantly. By computing the Axial Ratio of these elements, it becomes obvious that the element becomes Left-Hand (LH) polarized along one diagonal and Right-Hand (RH) polarized along the other. In the dual-polarized RECAP array, the orthogonal orientation of the V and H elements causes the V element to be RH when the H element is LH, thus maintaining a high degree of orthogonality.

Polarization orthogonality is important over the scan volume. On a receive antenna, orthogonal components allow the antenna to receive any incoming signal polarization. In transmit mode, two orthogonal components allow the antenna to provide any required polarization by setting the relative amplitude and phase of the element V and H pair.

This orthogonality is quantified by computing the polarization efficiency of the two elements from the axial ratios and tilt angles [6].

$$p = \frac{1}{2} + \frac{4R_V R_H + (R_V^2 - 1)(R_H^2 - 1)\cos(2\Delta\tau)}{2(R_V^2 + 1)(R_H^2 + 1)} \quad (4)$$

Where

R_V is the axial ratio of the V-pol element

R_H is the axial ratio of the H-pol element

$$\Delta\tau = \tau_V - \tau_H + \pi/2.$$

$$ortho = 10 \cdot \log_{10}(p) \quad (5)$$

For orthogonality purposes, this data is interpreted inversely of typical polarization efficiency:

$p = 1.0$ ($ortho = 0$ dB) is worst case.

$p = 0.0$ ($ortho = -\infty$ dB) is best case.

Orthogonality plots are presented as colored images in k-space in 1 GHz steps (Figure 13) for the entire measured volume ($\pm 90^\circ$ azimuth, -20° to $+60^\circ$ elevation). The orthogonality values are generally very good except at the outer edges of the measured volume ($\pm 90^\circ$), but this is beyond the desired scan volume ($\pm 60^\circ$). At the low end of the band (2 GHz), the orthogonality values, while still acceptable, are not as good as at the higher frequencies. This may be due to the size of the demonstration array, which is shorter than $4\lambda_0$ below about 2.1 GHz, thus not meeting the criteria set forth by Chio, et. al. in [7].

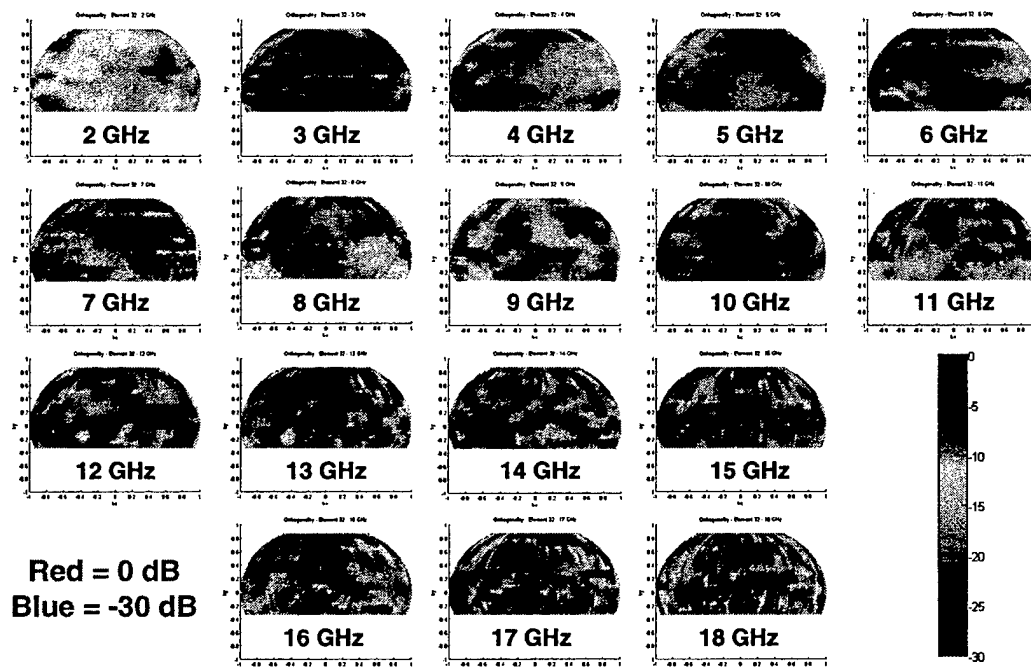


Figure 13 - Orthogonality in 1 GHz Steps

The Cumulative Distribution as a function of scan volume ($\pm 60^\circ$ in both azimuth and elevation) was computed across the entire frequency band. Plotted in Figure 14 are the 75% and 95% lines. There is some variation with frequency in this data, but overall, 75% of the scan volume maintains better than -15 dB orthogonality. With the exception of one glitch, 95% of the scan volume orthogonality is better than -10 dB and is typically better than -13 dB. For ESM applications, orthogonality levels on the order of -5 to -10 dB are generally deemed acceptable.

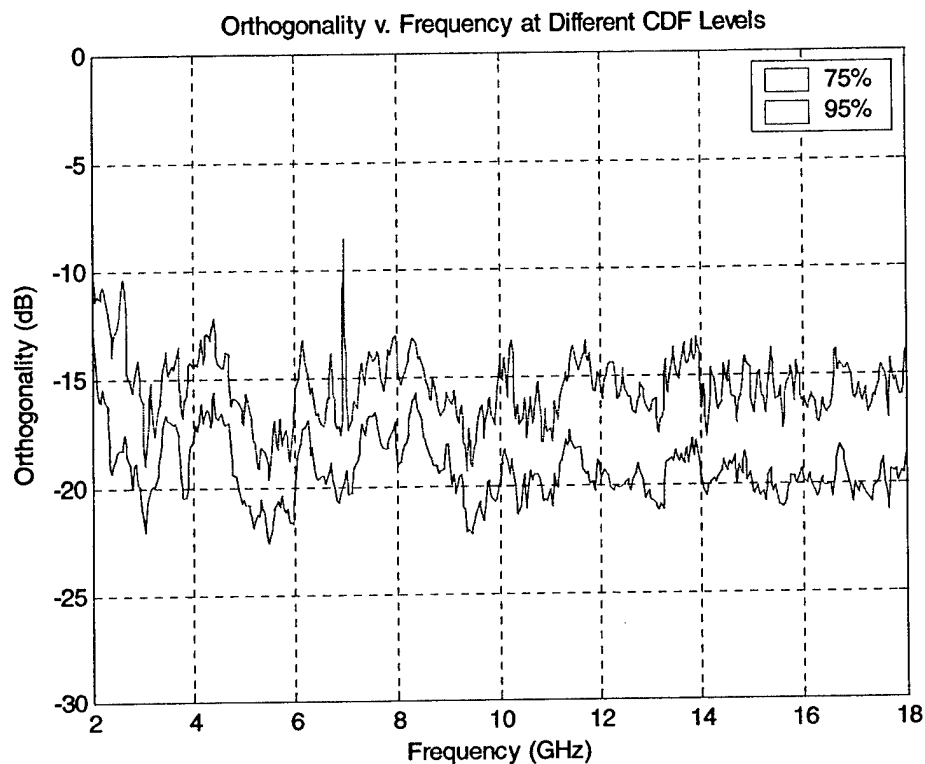


Figure 14 - Cumulative Distribution of Orthogonality

5. Summary and Conclusions

At the conclusion of the test, conical patterns at 13 elevation angles had been measured over the 2-18 GHz band. In total, approximately 250,000 patterns were gathered.

Analysis included embedded element gain and patterns, followed by cross-polarization discrimination, axial ratio, and orthogonality calculations.

The Raytheon RECAP array elements maintain excellent patterns over the 2-18 GHz range and $\pm 60^\circ$ scan volume. The measurements also confirmed the HFSS infinite array predictions through excellent correlation with the demonstration array.

Both measured and calculated data clearly demonstrate that the RECAP element polarization response shifts from linear to elliptical as a function of scan angle and frequency (typical of flared-notch elements). This dual-polarized element maintains excellent polarization orthogonality, however, throughout the

scan volume and frequency range. This polarization characteristic meets the requirements of most applications.

6. Appendix

6.1 Data Display Methods

These measurements generated a huge amount of data, and one question that emerged was how to display the results in a meaningful manner. Several methods are presented to solve this. All processing was performed on a PC running MATLAB.

The first method is the Embedded Element Gain, which illustrates the swept gain of the element in the array for different azimuth angles at a fixed elevation angle. This is displayed as a colored image plot of element gain on an azimuth v. frequency axis.

A similar method was employed for the Embedded Element Pattern plots. But in this case, the element gain is plotted as a color image on an azimuth v. elevation (or k_x v. k_y) axis. The Cross-Polarization Discrimination (XPD), Axial Ratio, and Orthogonality plots were all generated in this fashion.

The biggest challenge was how to display the 4-dimensional data, such as XPD v. azimuth v. elevation v. frequency. To solve this problem, a series of 3-D plots (XPD v. azimuth v. elevation) was generated for all frequencies. Each plot was stored and then sequenced together in a movie file. The movie files were then converted into AVI files to be inserted into PowerPoint. This allows the user to observe frequency-related changes that occur in the data without having to view all 321 plots individually.

Additionally, the 4-D orthogonality data was histogrammed to compute the cumulative distribution across scan volume for all frequencies. A contour plot of this data was generated with contour levels of 75% and 95%.

7. References

- [1] N. Schuneman, J. Irion, and R. Hodges, "Decade Bandwidth Tapered Notch Antenna Array Element", *Proc. 2001 Antenna Applications Symposium*, pp. 280-307, September 2001.
- [2] D. T. McGrath, N. Schuneman, T. H. Shively, and J. Irion, "Polarization Properties of Scanning Arrays", *IEEE International Symposium*, October 2003.

- [3] W. L. Stutzman, Polarization in Electromagnetic Systems, p. 157, Boston: Artech House, 1993.
- [4] Ibid., p. 28.
- [5] C. A. Balanis, Antenna Theory: Analysis and Design, p. 51, New York: Harper & Row, Publishers, 1982.
- [6] Stutzman, p. 126.
- [7] T-H. Chio, D. H. Schaubert, and H. Holter, "Experimental Radiation and Mutual Coupling Characteristics of Dual-Polarized Tapered Slot Antenna (TSA) Arrays", *1999 Antenna Applications Symposium*, September 1999.